

Dissertation

**Material Inspections with Low Energy  
Neutrons and  
3D Image Reconstruction**

ausgeführt zum Zwecke der Erlangung des akademischen Grades eines Doktors der  
technischen Wissenschaften unter der Leitung von

o. Univ. Prof. Dipl. Ing. Dr. Helmut Rauch  
E141  
Atominstitut der Österreichischen Universitäten


eingereicht an der Technischen Universität Wien  
Technisch – Naturwissenschaftliche Fakultät

von

**Menekse Bastürk**

Mart. Nr.:9800103  
Uchatiusgasse 10/1/3  
A-1030 Wien

Wien, am 29.09.2003



*To  
my parents Ayse and Ishak Bastürk,  
my grandfather Durmus Bastürk,  
and  
my aunt Menekse Bastürk, whom I have never seen.*

## Abstract

The non – destructive neutron radiography (NR) and neutron tomography (NT) methods are favored mostly by the industry for quality assurance and improvements of products. In this study, investigation of different materials by means of NR and NT, automation and further improvements at the NR – II facility at ATI – Wien are presented. The suitable radiographic – methods related to the materials and geometry of the samples are discussed. In addition to common thermal NR, cold NR and X – ray radiography were also used in the inspection of some materials. Different interesting materials for the nuclear technology were inspected such as boron – alloyed steels as neutron shielding material, fiber reinforced structural and insulation materials in fusion technology, visualization of inner details and also defects in ancient samples to restore them, manufacturing defects in TiAl turbine blade, e.t.c. Energy Selective Neutron Radiography was utilized in our material inspections because of the strong dependence of material cross-sections on the neutron energy. A portable neutron detection system, JEN-3, which is used for routine neutron transmission measurements through shielding material by the Austrian Steel Production Company Böhler – Bleche GmbH, was analyzed by MCNP simulations in order to define its principle. Of specific interest was the use of MCNP (Monte Carlo Neutron Particle Transport) code to simulate the neutron transmission measurements of shielding materials. Secondary factors in the neutron transmission measurements of strong absorber materials, which were estimated by means of MCNP simulations, are discussed in detail. The NR II facility was upgraded to provide sufficient place for the inspection of bigger samples, and a 10 cm thick lead plate was installed at the back end of the CCD light tight box in order to reduce gamma radiation dose. A 3 dimensional image reconstruction program, which is based on the IDL software, was developed for NT applications performed at NR II facility. Finally, first NR images taken during the TRIGA Mark II research reactor pulse are presented.

## Kurzfassung

Die zerstörungsfreie Neutronenradiographische (NR) und Neutronentomographische (NT) Abbildungsmethode wird hauptsächlich von der Industrie zur Qualitätssicherung eingesetzt. In dieser Arbeit werden Untersuchungen verschiedener Materialien mittels NR und NT, Automatisierung und weitere Verbesserungen an der NR II Anlage am Atominstitut der Österreichischen Universitäten - Wien vorgestellt. Die geeigneten radiographischen Methoden werden in Abhängigkeit von Materialien und Geometrien diskutiert. Neben der konventionellen thermischen NR wurden die Röntgenradiographie und NR mit kalten Neutronen eingesetzt. Verschiedene interessante Materialien für die Nukleartechnologie wie zum Beispiel borierte Stähle als Neutronen Abschirmungsmaterialien, Faser-, Struktur- und Isoliermaterialien in der Fusionstechnologie und Untersuchung archäologischer Proben, Homogenitätsverteilung im TiAl Turbine Blatt u.s.w. wurden untersucht. Es ist von besonderem Interesse, die Homogenitätsverteilung von Absorbermaterialien mittels radiographischen Methoden quantitativ zu definieren. MCNP (Monte Carlo Neutron Partikel Transport) Simulationen wurden ausgeführt, und mit Neutronen Transmissionsmessungen von Neutronen Abschirmungsmaterialien verglichen. Ein transportables System, JEN - 3, das von der österreichischen Stahlproduktionsfirma Böhler - Bleche GmbH für alltägliche Neutronen Transmissionsmessungen von Materialien verwendet, wurde mittels MCNP Code analysiert, um dessen Funktion genau zu definieren. Sekundärfaktoren, die starke Einflüsse auf den Transmissionsmessungen von Absorbermaterialien haben, wurden ausführlich mittels MCNP Simulationen analysiert. Die energiselektive Neutronenradiographie mit kalten Neutronen wurde wegen der starken Abhängigkeit des Wirkungsquerschnittes von der Neutronenenergie ebenfalls in unseren Untersuchungen verwendet. Die NR II Anlage wurde verbessert, um genügend Platz für die Untersuchung größerer Proben bereitzustellen. Dazu wurde eine 10 cm dicke Bleiplatte am Kollimatorausgang (hinter der Betonabschirmung) installiert, um die  $\gamma$ -Abschirmung zu verbessern. Ein dreidimensionales Bildrekonstruktion Programm basierend auf der IDL Software wurde für NT Anwendungen an NR II Anlage entwickelt und optimiert. Schließlich wurde zum ersten Mal NR während des Pulsbetriebes von der TRIGA Mark II Reaktor realisiert.



## Table of Contents

<b>1</b>	<b>Introduction .....</b>	<b>1</b>
<b>2</b>	<b>NDT (Non – Destructive Testing) Methods.....</b>	<b>4</b>
2.1	Radiographic Inspection.....	7
<b>3</b>	<b>Neutron Radiography .....</b>	<b>9</b>
3.1	Characteristics of Neutron Radiography Beam.....	11
3.1.1	Illuminator .....	11
3.1.2	Beam Aperture .....	11
3.1.3	$\gamma$ -Beam Filter .....	11
3.1.4	$\gamma$ -Shielding and $\gamma$ -Content .....	11
3.1.5	Collimator Walls .....	12
3.1.6	Filling Gas .....	12
3.1.7	Collimation Ratio (L/D).....	12
3.1.8	Beam Divergence .....	13
3.1.9	Neutron Flux .....	13
3.2	NR Imaging Methods .....	13
3.3	Position Sensitive Neutron Radiography Detectors .....	16
3.3.1	Basic Characteristics of CCD Camera .....	18
3.3.1.1	Detectable Quantum Efficiency .....	18

## Table of Contents

---

3.3.1.2	Readout and Charge Transfer Efficiency .....	20
3.3.1.3	Signal-to-Noise Ratio .....	21
3.3.1.4	Spatial Resolution .....	22
3.3.1.5	Dynamic Range .....	23
3.3.1.6	Linearity and Sensitivity .....	23
3.3.1.7	Dark Current and Cooling of the CCD Chip .....	23
3.4	Cold Neutron Radiography .....	25
3.5	Thermal NR Facilities at the Atoinstitute of Austrian Universities in Vienna ...	27
<b>4</b>	<b>Neutron Tomography .....</b>	<b>36</b>
4.1	Experiment .....	39
4.2	FBP based Image Reconstruction Program supported by IDL Software .....	40
4.2.1	Preparation of Images for the Reconstruction Program .....	42
4.2.1.1	Searching of the Sample Rotation Axis .....	43
4.2.1.2	Open & Dark Beam Correction and White Spots Removal .....	44
4.2.1.3	Flat Field Correction .....	45
4.2.1.4	Generation of Raw Sinograms .....	45
4.2.1.5	Filtering of Sinograms .....	45
4.2.1.6	Back-Projection of the Filtered Sinograms (FBP) .....	46
4.2.1.7	Removing of Ring Artifacts .....	47
4.2.2	3-Dimensional Demonstration of Reconstructed Image .....	47
<b>5</b>	<b>Investigation of Fusion Relevant Materials .....</b>	<b>49</b>
5.1	TAURO Blanket Concept .....	50
5.1.1	Structural Materials for TAURO Blanket Module .....	52
5.1.1.1	Fiber reinforced Silicon Carbide (SiC/SiC <sub>f</sub> ) .....	53
5.2	Investigations of SiC/SiC <sub>f</sub> composites by thermal Neutrons .....	54
5.2.1	Motivation .....	54
5.2.2	Thermal NR and NT Measurements .....	56
5.3	Investigations of SiC/SiC <sub>f</sub> composites with cold Neutrons .....	59
5.3.1	Experimental Set – Up of Energy Selective Cold Neutron Radiography Facility – PGA at PSI .....	59

## Table of Contents

---

5.3.1.1	Detection System.....	60
5.3.1.2	Velocity Selector.....	61
5.3.2	ESNR Measurements.....	64
5.4	Investigation of SiC/SiC <sub>f</sub> composites with X – Ray Radiography.....	68
5.5	Investigation of Insulation Materials of the ITER Toroidal Field Coils.....	70
5.5.1	Radiographic Inspections.....	70
<b>6</b>	<b>Portable Non-Destructive Material Testing System “ JEN-3 ”.....</b>	<b>72</b>
6.1	Principle of JEN-3 Detection System.....	72
6.2	Monte Carlo Neutron Transport Program (MCNP <sup>TM</sup> ).....	73
6.2.1	MCNP Input File Organization.....	74
6.3	Characterization of the JEN-3 System with the Help of MCNP Simulations.....	74
6.3.1	Simulation of the Detector Response of JEN-3 System.....	75
6.3.2	Thermal Neutron Flux Distribution within the Paraffin Desk.....	77
6.3.3	Thermal Neutron Distribution on the Paraffin Surface.....	78
6.4	Optimization of the Detector and Sample Distance.....	80
<b>7</b>	<b>Quantitative Analysis of Shielding Materials: Neutron Transmission through Boron-alloyed Steels.....</b>	<b>83</b>
7.1	Neutron Transmission Measurements by NR.....	84
7.2	Neutron Transmission Measurements by JEN-3.....	86
7.3	MCNP Simulations of Neutron Transmission Measurements.....	87
7.3.1	Effect of the multiple scattered neutrons on NR Images.....	89
7.3.2	Analysis of Secondary Factors.....	91
7.3.2.1	Beam Hardening Effect.....	91
7.3.2.2	Heterogeneous Structure Modelling of Boron – alloyed Steel Plates.....	93
7.3.2.3	Background Effect.....	96
7.4	NT Investigations of Boron – alloyed Steel Rods.....	98
7.4.1	Measurements.....	99
7.4.2	Correction of the Secondary Effects on the NT Measurements.....	100

Table of Contents

---

<b>8</b>	<b>Conclusion.....</b>	<b>104</b>
<b>9</b>	<b>Appendix I – 3D Image Reconstruction Program.....</b>	<b>107</b>
<b>10</b>	<b>Appendix II – Further NR and NT Applications of ATI – Wien.....</b>	<b>125</b>
	10.1 Nuclear Applications.....	125
	10.2 Ancient Samples from Austrian Museum of National History.....	128
	10.3 Electro Motors.....	130
	10.4 TiAl Turbine Blade .....	131
	10.5 Upgrading of NR II Facility at ATI-Wien .....	132
	10.6 NR during TRIGA Mark II Reactor Pulse .....	134
<b>11</b>	<b>References .....</b>	<b>135</b>
<b>12</b>	<b>Acknowledgment .....</b>	<b>142</b>

# 1

## Introduction

Neutron radiography (NR) is a very efficient tool to analyze materials and investigate inner structural defects non-destructively. By the installation of the digital imaging system at NR – II facility in 1999, which is based on a slow scan CCD camera and neutron sensitive scintillator detection system, a neutron tomography (NT) system has been commissioned. The main tasks in this study are respectively development of a 3D image reconstruction program, investigation of materials by means of NR and NT, automation and further improvements at the NR – II facility at ATI – Wien. NR and NT method is favored mostly by the industry for testing and improvements of products. Different interesting materials for the nuclear technology were inspected such as boron – alloyed steels as neutron shielding material; fiber reinforced silicon carbide as structural material in fusion reactor blanket, different types of insulation materials for ITER toroidal field coils in fusion reactors. In addition to common NR, it is also applied to the X – ray radiography with high spatial resolution in the inspection of some materials, which have small thickness. X – rays do not possess high penetration ability into the materials having high atomic number. Elements having small atomic number like  $^1\text{H}$ ,  $^2\text{D}$ ,  $^6\text{Li}$ , etc. cannot give contrast with X – ray radiography contrary to neutron radiography.

A three – dimensional image reconstruction program optimized for the NT investigations at NR – II facility at ATI – Wien was developed in the first step of this work. This program being based on the IDL software fulfills the whole image processing steps: opens a window for input parameters, prepares projections taken from all views between  $0 - 180^\circ$ , searches rotation axis, corrects white spots and fluctuations, creates sinograms, filters sinograms and reconstruct slices using filtered back-projection method. After generation of all slices of an object, it stores a 3D volume file as output file. The software “IDL – *the Interactive Data Language*” for data analysis, visualization, and cross – platform application development was employed. IDL combines all of the tools what we need for any type of project, interactive analysis, and display to large – scale commercial programming projects.

## 1. Introduction

---

The SiC/SiC<sub>f</sub> composite is considered as an attractive material for a breeding blanket due to its high thermal stability, high performance, and chemical inertness. Therefore, this material is of high scientific value for the investigations concerning its macroscopic structure inhomogeneity and radiation resistance. Neutron radiography was utilized to investigate these interesting samples. The neutron cross section of materials depends strongly on the neutron energy, and this property was exploited in our inspections of the SiC/SiC<sub>f</sub> composites. The SiC/SiC<sub>f</sub> composites are very transparent for thermal neutrons. It means, it has low neutron attenuation coefficient. As a result of this, material structure could not be visualized sufficiently. Therefore, these composites and their bonding with metal pads were inspected at discrete neutron energies of cold neutrons using a mechanical velocity selector, which is called Energy Selective Cold Neutron Radiography. It allowed getting better contrast between fiber bundles and porosity within the composites. The bonding of SiC<sub>f</sub> with a metal pad was also investigated. Neutron tomography investigations of the samples using a set of 200 projections were performed for the most interesting cases with thermal neutrons at the Atominstutute – Vienna (ATI) and with cold neutrons at PSI – Switzerland to position the defects and also inhomogeneity of the glue binder.

The super – conducting fusion magnets in ITER (International Thermonuclear Experimental Reactor) fusion device require high – quality performance of the insulation material due to its exposure to a neutron and gamma environment, and due to the high – mechanical stresses at cryogenic temperatures [Tsuji01, Mitc01]. Basically, the insulation systems, Kapton/R – glass manufactured in Italy and Alstom/R – glass manufactured in France, are glass fiber reinforced plastics (GFRPs) consisting of different fibers and matrix materials, like multi – component epoxy resins or similar compositions. The stability and the lifetime of the insulation systems, which determines the lifetime of magnetic coils, will change under the demanding performance conditions of the ITER fusion device. Therefore, the structural change and swelling problem of these newly developed fiber reinforced composites under high irradiation was investigated with radiographic methods. The tomographic inspection failed because of the insufficient number of projections for such a thin samples (~ 2 mm).

For material characterization, it is of specific importance to define the homogeneity distribution of strong absorbing elements within shielding materials quantitatively. Boron is an important absorber used for the production of boron – alloyed steel to serve in long – term storage of spent nuclear fuel or nuclear waste disposals. Due to the high neutron absorption of boron compared to steel, the neutron radiography is a powerful tool for the nondestructive investigation. Thermal neutron transmission measurements have been performed for boron-alloyed steel plates having different thickness. The Austrian Steel Production Company Böhler Bleche GmbH, which uses natural and <sup>10</sup>B enriched boron in the form of boron carbide within the steel matrix, has supplied investigated samples. MCNP simulations were performed for better understanding and interpretation of the obtained experimental results. A portable commercial neutron detection setup, JEN-3, which was developed mainly for routine neutron transmission measurements of shielding materials by the Austrian Steel Production Company Böhler Bleche GmbH was analyzed by means of MCNP (Monte Carlo Neutron Particle) simulations to define its working principle. In this part of the work, we focused on the quantitative estimations of secondary effects on the neutron transmission measurements through thermal neutron shielding materials, such as beam hardening, background, and inhomogeneous absorber distribution within the samples, which decrease the neutron attenuation in absorber materials. The beam hardening factor, which is a shift of the mean

## 1. Introduction

---

neutron energy to the higher energy region, causes sharp decreases of the effective total macroscopic cross sections of strong neutron absorber materials having  $1/v$  behavior –  $v$  is neutron velocity with increasing material thickness.

Additionally, NR and NT were utilized in the inspection of the cellulose solutions, visualization of inner defects and material composition in ancient samples from Austrian museums in order to restore them, visualization of inner details of electro motors, e.t.c. The 250 kW TRIGA Mark II research reactor can be pulsed a maximum of 12 times per hour. During the pulse, the power reaches 250 MW with a pulse duration of 40 ms. We tried to synchronize reactor pulse and CCD camera exposure time, and we could realize an NR image during one reactor pulse. This could be utilized in future to perform investigations of dynamical processes.

# 2

## NDT (Non – Destructive Testing) Methods

Non – Destructive Testing (NDT) is one of the major tools of quality control, and it provides information about the inner condition of samples without destroying them. NDT examines materials and reveals the defects within the sample. There are several established NDT methods, which are currently used in quality programs of industries such as aerospace, automotive, defense, pipeline, power generation, preventative maintenance, pulp and paper, refinery, nuclear technology and shipbuilding. New methods are being constantly developed, and many of the established techniques have their effectiveness and efficiency enhanced by conversion to electronic, computerized, or robotic operation. Seven basic NTD methods [Smit96, Büyü98, Esto99] are: Visual Inspection, Liquid Penetrant Inspection, Magnetic Particle Inspection, Eddy Current Inspection, Ultrasonic Inspection, Thermographic Inspection (Infrared Imaging) and Radiographic Inspection. This study is based on the radiographic inspection of materials with neutrons, but it would be reasonable to give some general information about other NDT methods before going to radiographic inspection.

*Visual inspection* is a quick, economical method and the primary evaluation method of many quality control programs detecting various types of defects before they cause failure. Its reliability depends on the experience of the inspector and it requires good vision, good lighting and the knowledge of what to look for. The inspector must know how to search for critical defects and how to recognize areas where failure could occur. Visual methods can provide a simple and speedy way to assess questionable components and can help in deciding what to do next. Visual inspection can be enhanced by various methods ranging from low power magnifying glasses through to borescopes (integrated endoscopes). These devices can also be used with television camera systems. Visual inspection can be done in many ways either directly or remotely by using borescopes, which works by forming an image of the viewing area with an objective lens, or video cameras. Photography or digital imaging can obtain permanent records if necessary. The main disadvantage of visual inspection is that the surface to be inspected must be relatively clean and accessible to either the naked eye or to an



## 2. NDT (Non – Destructive Testing) Methods

---

optical aid such as a borescope. Typically, visual inspection lacks the sensitivity of other surface methods of inspection, which can identify defects that are not easily seen by the eye. It can identify where a failure is most likely to occur and identify when failure has commenced.

*Liquid penetrant inspection* is the easy method to apply surface breaking defects and highly sensitive and it reveals the surface defects by a *colored* or *fluorescent* penetrant. In manual operation, it uses simple equipment to detect defects open to the surface and it can be used for almost any material which surface is not extremely rough or porous. Metals (Al, Cu, Steel, Ti, etc.), Glass, Rubber and Ceramic materials are commonly inspected materials with liquid penetrant inspection method. As penetrants, petroleum or water – based liquids that are colored by a dye are used. The technique is based on the ability of a liquid to penetrate into a clean surface-breaking defect or void by capillary action. After a period of time, excess surface penetrant is removed and a developer applied. This acts as a blotter. It draws the penetrant from the defect to reveal its presence. While colored (contrast) penetrants require good white light, fluorescent penetrants require a darkened condition to be used with an ultraviolet black light. Before the application of this method, it is essential that the material surface should be carefully cleaned. Otherwise the penetrant will not be able to get into the defect. If surface penetrant is not fully removed, the measurements also don't show the exact result. The disadvantages of this application are the following:

- Only surface – breaking defects can be detected
- Only materials with a relative nonporous surface can be inspected.
- Pre-cleaning is critical (contaminants can mask defects)
- The inspector must have direct access to the surface being inspected
- Surface finish and roughness can affect inspection sensitivity
- Multiple process operations must be performed and controlled
- Post cleaning of acceptable parts or materials is required
- Chemical handling and proper disposal is required

In a *magnetic particle inspection*, magnetic fields are generated using electrical equipment. Magnetic particle inspection tests only metals that can be magnetized. Magnetic particle inspection is a method that can be used to find surface and near surface defects in ferromagnetic materials such as steel and iron. It works best for defects, which are elongated rather than round. An internal magnetic field is generated in the tested specimen. In locations where defects (non – magnetic voids) exist, some of the field will leak off the specimen and bridge the voids through the air. In theory, it is a relatively simple concept. When a bar magnet broken in the center of its length, two complete bar magnets with magnetic poles on each end of each magnet will result. If the magnet were cracked but not broken completely in two, a north and south pole will form at each edge of the crack, just as though the break had been completed. If iron particles were then sprinkled on this cracked magnet, these particles will be attracted not only to the ends of the magnets poles but also to the edges of the crack. Their buildups form a defect indication, but surface irregularities and scratches can give misleading indications. Therefore, it is necessary to prepare surface of the investigated materials carefully, before magnetic particle inspection is applied.

*Eddy current inspection* instruments are small and portable. This method can only be used on electrically conductive materials and it can be applied to a small area at a time. An energized

## 2. NDT (Non – Destructive Testing) Methods

---

electric coil induces a magnetic field into the tested specimen. The fluctuating magnetic field generates an electric eddy current. The presence of a flaw increases the resistance to the flow of eddy currents. This is indicated by a deflection on the instrument's voltmeter. Its applications range from crack detection, to the rapid sorting of small components for either defects and size variations, or material variation. Commonly, it is used in the aerospace, automotive, marine, and manufacturing industries. These currents setup magnetic field, which tends to oppose the original magnetic field. The impedance of coil in the closeness to the specimen is affected by the presence of the induced eddy currents in the specimen. When the eddy currents in the specimen are distorted by the presence of the defects or material variations, the impedance in the coil is altered. This change is measured and displayed in a manner that indicates the type of defect or material condition.

*Ultrasonic inspection* uses complex electronic equipment. The basis of the method is derived from the quantitative determination of shape and size of defects in ultrasonic inspection area. Any material that transmits mechanical vibrations can be tested. Ultrasonic inspection detects both linear and non – linear defects and permits three – dimensional interpretation. Evaluation is often difficult. The ultrasonic inspection instrument converts electrical pulses into mechanical vibrations or pulses. These pulses travel across the tested specimen and they are reflected from defects because of their different acoustic nature. In short, every material has a different acoustic nature. The returning reflected pulses are reconverted to electric energy and displayed as signals on a cathode ray tube (CRT). The position and size of these signals correspond to the position and size of the defects. Ultrasonic inspection uses sound waves of short wavelength and high frequency to detect defects or measure material thickness. Usually pulsed beams of high frequency ultrasound are used via a handheld transducer, which is placed on the specimen. Any sound from that pulse, which returns to the transducer like an echo, is shown on a screen that gives the amplitude of the pulse and the time taken to return to the transducer. Defects anywhere through the specimen thickness reflect the sound, back to the transducer. Void or defect size, distance, and reflectivity can be interpreted.

*Thermography or thermographic inspection (Infrared Imaging)* is used to detect thermal defects and air leakage in buildings. It also measures surface temperatures by using infrared video and still cameras. These tools see light in the heat spectrum. Images on the video or film record the temperature variations of the building's skin with gray value, ranging from white for warm regions to black for cooler areas. The resulting images help to determine whether insulation is needed. They also serve as a quality control tool to ensure that insulation has been installed correctly. Infrared imaging (thermography) is a non – contact optical method where an accurate two – dimensional mapping of steady or transient thermal effects is constructed from the measurement of infrared energy emitted by the target. The physical phenomena behind active infrared inspection can be visualized by following propagation and detection of an induced thermal perturbation. An induced thermal wave front can be imagined to flow from the exposed surface into the material. For a defect – free, homogenous material, the wave front of heat passes through uniformly. However, where there are defects, such as cracks (filled with air or an oxide), these create higher thermal impedance to the passage of the wave front. Physically, when the defects are near to the surface, they restrict the cooling rate due to an insulation blocking effect, and thereby produce hot spots. When a thermal imager views this surface, temperature differences arising from the defect's presence become clearly visible shortly after the deposition of the heat pulse. Similarly, on the opposite (non – pulsed) side, because the defect impedes the passage of heat that warms this surface, the

defect appears as a cold spot against the background heat that arrives. Thermography can be considered and performed as active thermography or transmission approach, where the imager views the side opposite the surface receiving the pulse of heat, and the reflective or single-sided approach, where the surface that receives the pulse of heat is also observed by the thermal imager. Since they give differing representations of the same defect, they can furnish much complementary information on variations of thickness, material content, and defect dimensions. The equipment required to perform active thermography falls into two separate areas: the heating source and the thermal imaging/analysis system. The typical heating sources utilized are pulsed quartz lamps. Cooling the target instead of heating can also perform thermographic analysis. In this case, cold water can be used to generate thermal changes necessary for detection of structural defects. The new developments in infrared technology, specifically development of high – density – imaging sensors has opened a new level of applications of this technology. Coating defects such as blistering and sub – surface corrosion spots, and the variations in the coating thickness can be detected in infrared images by the differences in the thermal diffusivity of the defective and non – defective areas.

### 2.1 RADIOGRAPHIC INSPECTION

Among nondestructive testing methods, radiographic inspection is the most effective method to investigate the samples interior and to visualize the inner details and defects in the material. The inspection methods discussed above are not capable to indicate inner details of a thicker object; they can give information about inner materials near the surface. Radiography uses the attenuation of radiation by the materials within the specimen and depends on the density and thickness of materials as indicated in Eq. (2.1). The denser or thicker materials will absorb more radiation. The specimen is placed between a source of radiation and a sheet of radiographic film or nowadays often – used CCD camera based digital scintillator/camera detection system (a neutron converter is necessary for neutron radiation). A defect present anywhere within the specimen will often absorb less radiation than the specimen itself. The location of the defect will be indicated on the film by an area of higher or darker exposure and on a CCD camera based imaging system by an area of lower or brighter intensity. Radiography can be categorized according to the radiation used such as X – ray radiography, gamma – ray radiography, and neutron radiography. These are complementary methods in the material inspection, because the attenuation properties of materials change due to the radiation and its energy. In order to investigate materials sometimes only one method couldn't give sufficient information, for this reason other complementary methods must be applied. Neutrons interact with nuclei contrary to X – ray, which interacts with the electron clouds around the nucleus. In order to give information about the difference of the attenuation coefficients for thermal neutrons and X – ray is demonstrated in Fig. 1. Some elements such as boron and hydrogenous materials are strong attenuators for neutrons contrary to X – ray. X – ray radiography visualizes microstructures of suitable materials with a thickness limitation, while neutron radiography inspects macrostructures of these materials. X – ray is suitable for thin samples. That means, with neutron radiography macro – samples such as oil circulation in a motor, components of refrigerators, shielding materials and nuclear fuels can be investigated without doubt. Neutron radiography and its application are explained in details in the following chapters.

## 2. NDT (Non – Destructive Testing) Methods

$$I = I_0 e^{-\mu \cdot d} \tag{2.1}$$

- $\mu$  : Attenuation coefficient of included materials within a sample
- $d$  : Sample thickness
- $I$  and  $I_0$  : Transmitted and incident beam intensities.

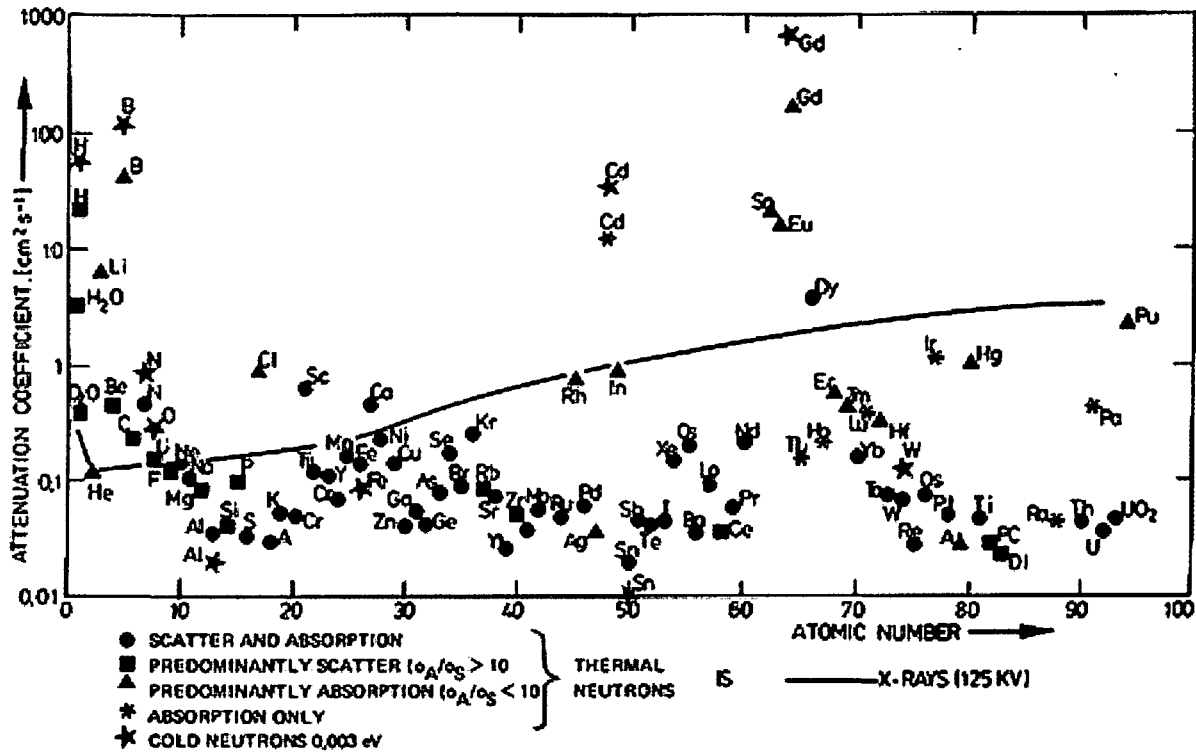


Fig. 2.1: Attenuation coefficients of materials for neutrons and X – rays.

# 3

## Neutron Radiography (NR)

At the present time, NR is one of the main nondestructive techniques, which is able to satisfy the quality – control requirements in order to give quantitative information about the spatial distribution of different elements and isotopes in the investigated samples. In conventional NR, a neutron beam penetrates sample and it is attenuated through the elements within the sample. The transmitted neutrons can be detected using different detection methods: such as film/converter or scintillator based digital CCD camera system. The neutrons react with the converter material producing photons and the generated photons are recorded on a position sensitive detector (film or in digital camera system like slow scan CCD camera). The output of the detector is an image representing the attenuation behavior of the sample. Using the position sensitivity of the detectors the interior elements within the sample can be visualized and determined. NR can be grouped into three categories depending on the neutron beam energy: such as cold, thermal, and fast NR.

The probability of neutron interaction varies depending on the type of reaction involved, and also the probability of a particular reaction occurring between a neutron and a nucleus is called the microscopic cross section ( $\sigma$ ), which depends strongly on the energy of the neutron. The microscopic cross section may also be regarded as the effective area of the nucleus for the particular neutron reaction. The larger is the effective area, the greater is the probability for the reaction. That means, the microscopic cross section is an area and therefore it is expressed in units of area ( $\text{cm}^2$ ) or commonly in terms of barns ( $1 \text{ barn} = 10^{-24} \text{ cm}^2$ ). The interaction of neutrons with a certain volume of material depends not only on the microscopic cross section of the individual nuclei but also on the number of nuclei within that volume or atom density of materials. Therefore, it is necessary to define another kind of cross section known as the macroscopic cross section ( $\Sigma$ ). The macroscopic cross section is the probability of a given reaction occurring per unit travel of the neutron, and if sample consists of several different elements, the total macroscopic cross-section is given by the sum of the total macroscopic cross sections of each element as in Eq. (3.1).

### 3. Neutron Radiography

---

$$\Sigma = \sum N_i \cdot \sigma_i = \sum \Sigma_i = \Sigma_1 + \Sigma_2 + \Sigma_3 + \dots \quad (3.1)$$

$\sigma$  : Microscopic cross section, [ $\text{cm}^2$ ]

$N$  : Atom density of material, [ $\text{atoms} \cdot \text{cm}^{-3}$ ]

The difference between the microscopic and macroscopic cross sections is important and is restated for clarity. The microscopic cross section ( $\sigma$ ) represents the effective target area that a single nucleus presents to a bombarding particle. The units are given in barns or  $\text{cm}^2$ . The macroscopic cross section represents the effective target area that is presented by all of the nuclei contained in a  $1 \text{ cm}^3$  of the material and its unit is  $\text{cm}^{-1}$ . A neutron interaction with an atom of the material can be taken place in two ways: it interacts through either a scattering interaction or an absorption reaction. The probability of a neutron being absorbed by a particular atom is the microscopic absorption cross section ( $\sigma_a$ ). The probability of a neutron being scattered by an interaction of particular nucleus is the microscopic scattering cross section for scattering ( $\sigma_s$ ). The sum of the microscopic absorption and scattering cross sections gives the total microscopic cross section ( $\sigma_t$ ) as given in Eq. (3.2).

$$\sigma_t = \sigma_a + \sigma_s \quad (3.2)$$

In NR, neutron beam is attenuated according to the basic law of radiation attenuation depending on the isotopes, geometry, and density as in Eq. (3.3). Neutron cross sections of isotopes of an element may vary over several orders of magnitude like boron isotopes, B – 10 and B – 11.

$$\Phi(x,y,E) \equiv \Phi_0(x,y,E) \cdot e^{-\Sigma(x,y,E) \cdot d} \quad (3.3)$$

$\Phi_0(x, y, E)$ : Incident neutron flux, [ $\text{cm}^{-2}\text{s}^{-1}$ ].

$\Phi(x, y, E)$ : Transmitted neutron flux through the sample, [ $\text{cm}^{-2}\text{s}^{-1}$ ].

$d$  : Thickness of the sample, [cm].

$\Sigma$  : Total macroscopic cross-section (absorption and scattering), [ $\text{cm}^{-1}$ ].

The absorption of a thermal neutron in most materials is much more probable than the absorption of a fast neutron. The neutron absorption cross sections of considerable number of nuclides is inversely proportional to the neutron velocity ( $v$ ), therefore this region is frequently referred to as the "1/v region".

### 3.1 Characteristics of NR Beam

#### 3.1.1 Illuminator

The aim of an illuminator is to provide a uniform neutron source for NR. Typical illuminator in NR facility is a graphite block near the core for a radial beam and near the flux centerline for a tangential beam. The typical illuminator thickness is between 10 – 15 cm thick in the beam axial direction, because the excessive illuminator in the NR installation reduces the neutron flux and also increases the gamma-ray intensity [Lehm96, Silv01].

#### 3.1.2 Beam Aperture

The beam aperture is one of the important components in the collimator design in NR, and it limits neutrons entering the collimator. Thermal neutrons except through the hole or collimator inlet has to be prevented with an aperture made out of strongly absorbing materials. Most radiography apertures are round but there are also square apertures that are used nowadays in several beam guides. The aperture should be made as a sandwich of several different materials such as lead (Pb) and boron – based materials ( $B_4C$ ). Boron based materials absorb the neutrons with little gamma – ray emission, an indium layer is to capture some of the epithermal neutrons and a lead layer is to remove the gamma-rays generated within the materials. Gd and Cd can also be used to provide sharp aperture-hole edges, but boron – based materials should be between these materials and illuminator in order to minimize the amount of gamma rays produced.

#### 3.1.3 $\gamma$ – Beam Filters

Beam filters are used to remove the undesirable gamma rays from the beam and they act as a scattering source. Typical gamma ray filters are lead (Pb) and Bismuth (Bi). Filters absorb neutrons and gamma rays in addition to scattering neutrons. The gamma rays filter must be placed between the illuminator and the aperture – hole. Common used filter for gamma rays in NR is Bi crystal, because its neutron – attenuation is lower than Pb, while they have identical gamma-attenuation. Bi crystal could be used single- or polycrystalline. By using a single crystal Bi filter instead of an equated polycrystalline, an improvement can be obtained in the neutron intensity. However, the cost of a single – crystal should be considered, and it must be also well cooled to retain its monocrystal characteristics under high irradiation.

$Al_2O_3$  and  $SiO_2$  are sometimes used to reduce higher energetic neutrons from the beam, to reduce the amount of shielding materials for fast neutrons required at the external end of the collimator. These should be single – crystal to be effective and must be properly oriented, but cooling is not usually required.

#### 3.1.4 $\gamma$ – Shielding and $\gamma$ – Content

Gamma shielding is needed at the aperture to prevent the entrance of gamma rays to the collimator. The typical gamma shielding is based on Pb, but also include heavy concrete or

### 3. Neutron Radiography

---

other materials. Gamma shielding should be placed at every step change in neutron collimator dimension in order to reduce  $\gamma$  - ray flux. For biological shielding, the energy distribution of gamma rays must be carefully considered, as well as the intensity. In an optimal design, the collimator components generate low energy gammas so that they can easily be shielded. Nevertheless, primary gamma rays from the reactor core in a radial beam require additional shielding. The intensity of gamma radiation in the beam affects the amount of biological shielding and it determines whether direct radiography method is possible. However, the relative contribution of gamma rays has an important effect to the generation of the image. The gamma ray content in an image reduces the quality of the images causing white spots in the image. The images, which contain more white spots, need a good image processing suitable filters. Every filter application to the image causes some information lost, therefore a useful characteristic of a neutron beam is the neutron/gamma ratio. The typical neutron to gamma ratio should be greater than  $10^8$  n.cm<sup>-2</sup>.mSv<sup>-1</sup>.

#### 3.1.5 Collimator Walls

Collimator walls are very important in the collimation design, because it defines the NR beam. It should be constructed from a purely neutron absorbing material (alpha emitter) to prevent neutron scattering from the walls. Neutron scattering at the collimator walls must be as small as possible, therefore boron - based material with minimal hydrogen content should be chosen. If neutron - absorbing materials cannot be used in the collimator walls, then wall materials having small scattering cross sections should be selected. By this way, neutrons, which travel through the collimator with an acceptable divergence limit, are allowed to reach to the sample position at a radiography facility.

#### 3.1.6 Filling Gas

If it is possible, the collimator should be either evacuated or filled with He to gain neutron intensity at the sample position preventing the neutron scattering with N in air. The scattering neutrons yield interactions with the collimator walls that require shielding, and they also cause degradation of the sharpness of the images. 4 % more neutrons at the sample position can be gained using He filling for every meter of collimator length [Doma92, Silv01].

#### 3.1.7 Collimation Ratio (L/D)

Collimation ratio (L/D) is the ratio of the collimator length to the effective diameter of the aperture hole. This parameter or ratio directly determines the image quality depending upon the beam collimation. An optimal collimated neutron beam generates sharpest images. It affects directly spatial resolution of the radiography images related to the Eq. (3.4) and Eq. (3.5).

$$\Phi_{\text{detector}} = \frac{\Phi_{\text{aperture}}}{16 \cdot \left(\frac{L}{D}\right)^2} \quad (3.4)$$



$$U_g = L_f \left( \frac{D}{L} \right) \quad (3.5)$$

- L** : Collimator length  
**D** : Aperture diameter of the collimator  
**L<sub>f</sub>** : Sample to detector distance  
**Φ<sub>detector</sub>** : Neutron flux at the collimator exit or image plane  
**Φ<sub>aperture</sub>** : Neutron flux at the collimator aperture  
**U<sub>g</sub>** : Geometric unsharpness

#### 3.1.8 Beam Divergence

The beam divergence is one of the important measures of the beam usefulness for the NR. If the neutron beam diverges very rapidly to a large size, then the images will suffer significant distortion. That means the spatial resolution becomes worst that will be explained in further chapters. A small aperture and/or longer collimator length (long beam) generate small beam divergence and increase spatial resolution or image sharpness. The divergence is stated as  $2\theta$  and the half angle is shown in Eq. (3.6).

$$\theta = \tan^{-1} \left( \frac{t}{2L} \right) \quad (3.6)$$

- θ** : Half angle of the divergence  
**t** : Maximum dimension of the image plane (diagonal)

#### 3.1.9 Neutron Flux

The neutron flux determines the exposure time and availability of the NR facility for other experiments such as real – time NR, phase contrast NR, for which high neutron flux is necessary. If insufficient neutron flux is used, generated images have low contrast. Exposure time and neutron flux are linear proportional related to the used linear detector. Neutron intensity increases with increasing the exposure time.

The Cd – ratio, which is a measure of epithermal neutron content of the beam, will impact the effectiveness of the beam in penetrating certain materials such as nuclear fuels. The content of epithermal neutrons in the beam has an advantage and also a disadvantage. The disadvantage is the moderation process by thermal interactions within the sample, if the inspected sample contains hydrogenous materials [Lehm96]. Deciding about Cd – ratio depends on the demands of the experiment.

### 3.2 NR Imaging Methods

It is necessary to give short information about main imaging techniques. Most NR images are commonly generated using one of the following methods:

### 3. Neutron Radiography

---

- ***Direct Method***

In this technique, photographic film based neutron converter foils are used. A neutron converter foil and photographic film is placed together in a vacuum cassette and put behind the object into the neutron beam. Gd is a common neutron converter material because of its high conversion efficiency (high neutron absorption cross section). They should be placed in a vacuum cassette, because direct contact of the converter and film is very important to get higher spatial resolution. The disadvantage of this method is the gamma sensitivity of Gd foils and X – ray films. Gamma radiation causes second image in the film then image will be blurred. Because of gamma emission, this technique is not suitable for radioactive objects.

- ***Indirect Method***

Dysprosium, Indium and Gold are most common converters or image recorders in the indirect imaging method considering fast activation with neutrons and fast decay time to produce subsequent images on the photographic film. The converter is placed behind the object and it records the image by the neutron activation. After specific exposure time, the converter foil is contacted with a photographic film. In this way, the registered image is transferred to this film by the decay radiation of the activated foil. This method is very suitable to investigate the highly activated materials, and it is also not sensitive for gamma radiation from the beam and inspected objects.

- ***Track – etch Method***

An ionizing particle passes through a dielectric material, the transfer of energy to electrons results in a trail of damaged molecules along the particle track.  ${}^6\text{Li}$  and  ${}^{10}\text{B}$  foils are well-known track – etch detectors or converters, which are used for the direct imaging of objects and emit alpha particles with neutron reactions. They are used in conjunction with a material that register alpha particle. Alpha particles emitted by the foil produce an image in the nitrocellulose film by creation of small defects or tracks. Then, this nitrocellulose film is etched in a strong acid or base solutions to make the tracks then visible. The etching process enhances the tracks visibility. It is used commonly to radiography very activated materials and also insensitive for gamma radiation and light.

- ***Scintillator based Digital Imaging Method***

Nowadays, the most effective technique is direct imaging with digital image detection system. In this direct method, instead of converter foil scintillator and instead of the film a digital CCD camera is used. Processing time is saved due to short exposure times and development process is not necessary. The scintillation process is one of the most useful methods to detect a wide assortment of radiations. An ideal scintillator should fulfill following main conditions [Fuen59]:

1. It should convert the kinetic energy of charged particles to detectable light with high scintillation efficiency. The scintillation or conversion efficiency of any scintillator is the number of generated particles per incident particle energy, which is converted into visible light.
2. It should give best light output and good linearity; the converted light must be proportional to initial radiation.

### 3. Neutron Radiography

3. It should not absorb its own emission (self absorption). If the absorption spectra and emission spectra of a scintillator quite separated, then this scintillator is transparent for its own fluorescence emission.
4. The decay time of induced luminance should be short, so that, fast signal pulse can be generated.

Inorganic scintillators are preferred for NR, because the inorganic scintillators have better light output and linearity than organics.

The fluorescence is the emission of visible light from a substance. For a good scintillator, the scintillator material should convert incident radiation energy to fluorescence rapidly and with a large fraction. In the scintillators, the scintillation process depends on the energy of the conversion electrons of the scintillator material. The required charged particle energy to create one electron-hole pair in the scintillator material and the resulted amount of photons determine its scintillation efficiency.

The scintillation mechanism in inorganic materials depends on the energy states, which are determined by the crystal lattice of the material. The energy band structure of a scintillator consists of three parts, valence, conduction and a band gap or forbidden band between conduction and valence band where electrons cannot be found, as shown in Fig. 3.1. Electrons in the valence band can cross the forbidden band, and can migrate to the conduction band with energy absorption. They emit photons by the return to the valence band, if the resulting photon would have high energy to lie in the visible range. Small amount of impurity, which is called activator such as Cu, Ag, or Au elements, is added to inorganic scintillator to enhance the probability of visible photon emission. They create energy states within the forbidden band or band gap to increase visible photon, if the energy is less than full forbidden gap. If emission and absorption spectra overlap, it causes self – absorption in the scintillator. In a pure crystal, approximately the same energy would be required to excite an electron – hole pair as in the emission when they recombine. However, in an activated scintillator the emission occurs in the activator states where the energy transition is less than the absorption energy to create electron – hole pair.

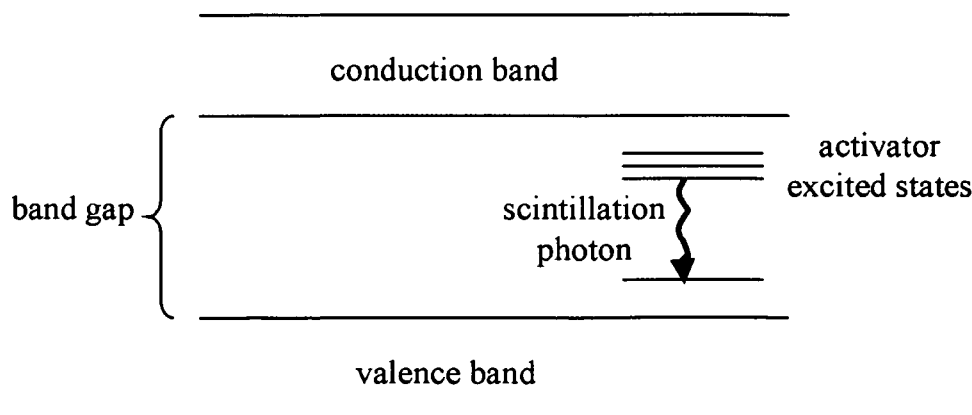


**Fig. 3.1:** Energy band structure of a scintillator with activator material.

Owing to the high scintillation efficiency, activated scintillators are used in NR facilities. Lithium – containing scintillators are quite common as slow neutron detectors because of its

### 3. Neutron Radiography

---

low gamma sensitivity and high light output. Nevertheless, it should be thin as possible considering the opacity problem to its own light. Most common inorganic activated scintillator material is silver activated ZnS. Sometimes more than one material, stands as Ag, Cu and Au can be used as the activator. The ZnS(Ag) powder is mixed with an organic binder to form a scintillator layer. Production of the scintillation light increases with decreasing scintillator layer thickness. On the other side, thin layer thickness causes poor neutron detection efficiency [Care01].

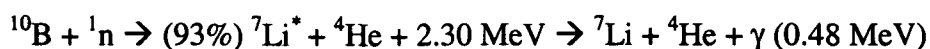
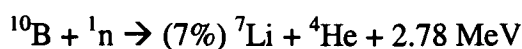
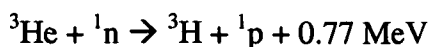
The common 2D scintillator screen of NR consists of a mixture of  ${}^6\text{LiF}$  and ZnS(Ag). Neutrons incident on the screen react with the  ${}^6\text{Li}$  to produce a triton and an alpha particle. Ionization of these charged particles cause the ZnS(Ag) to scintillate at a wavelength of approximately 450 nm – 640 nm depending on the activator. The general mass ratio for  ${}^6\text{LiF}:\text{ZnS (Ag)}$  is 4:1. The neutron detection efficiency of these scintillators is between 10 – 15 %, 177000 photons per detected neutron [Schil01-3]. For more information about the imaging techniques, see in [Doma92, Koer00].

### 3.3 Position Sensitive NR Detectors

The purpose of the position sensitive NR detectors is to measure the neutron field in two dimensions perpendicular to the beam direction. Therefore, the detector area should be in the order or larger than the beam cross section. Further boundary conditions are the spatial and time dependent resolution of the detector, which can be very different among the existing detectors systems. An overview about these parameters will be given in the following chapters for the most common systems. The inherent detectors properties are mainly given by the detection process, which is a nuclear reaction initiated by the neutrons. Neutrons have no electric charge and cannot cause ionization directly; therefore, they need conversion reaction to be detected. The primary conversion reaction for thermal neutrons is mainly neutron capture reaction by an absorbing material emitting secondary radiation. For a good neutron converter materials must fulfill following requirements:

- a. Large neutron cross section for charged particles
- b. Range of charged particle should be large compared to neutron absorption length
- c. Large energy of the reaction products
- d. Low gamma sensitivity
- e. Good mechanical and chemical stability

The most important reactions for low energy neutron detection (for thermal and cold neutrons) are:



### 3. Neutron Radiography



Detectors, which are used in NR, are X – ray film based converter, imaging plate, amorphous silicon flat panels, and scintillator based digital CCD cameras. They are characterized by the minimum required exposure time per radiography image, dynamic range, spatial resolution, and digital format in the generated radiography images.

*X – ray film based neutron converter detection system* is the oldest method in the radiography. The highest quality and resolution radiographs can be obtained with X – ray film. A thin Gd foil is placed next to the film and produces X – rays proportional to the local neutron flux. The x-rays expose the film. It has typically 20 – 50  $\mu\text{m}$  spatial resolution and 5 – 10 minutes exposure time depending on the beam characteristics [Lehm00]. Its dynamic range is  $10^2$  and has a nonlinear proportionality with exposure time. The exhausting development of X – ray films and their processing takes lots of time (reproducibility problem). It is 8 – bit of dynamic range and it makes 256 gray values for a resulted image by the film based converter method.

*Imaging Plates (IP)* have inherent advantages compared to other imaging detectors, such as no accumulation of intrinsic dark signals during the exposure, high dynamic range, short exposure time, high efficiency, and high resolution. Imaging plates consist of  $\text{BaFBr:Eu}^{2+}$ , which is used as a photo-stimulated luminescence material, neutron converter and an organic binder [Thom99-1, Thom99-2]. Image plates are able to store information in the form of locally trapped electron-hole pairs as a latent image. By optical stimulation with a focused HeNe – laser the information can be read out point by point. Thereby, the trapped electrons recombine with holes, emitting photons, which are detected by a photomultiplier. This process is known as photostimulated luminescence. The number of photons is proportional to the stored information. After the readout process, the residual information on the image plates can be erased by irradiation with intense light and the image plate can be reused. At the beginning, imaging plates have been produced for X – ray radiography; they were not sensitive to neutrons. Afterwards, they have been modified to neutrons using neutron converter materials  $^{157}\text{Gd}$  and  ${}^6\text{Li}$  as strong neutron absorbing material. Imaging plates with  ${}^6\text{Li}$  converter show more photo-stimulated luminescence than with the same thickness of  $^{157}\text{Gd}$  converter because of the high energetic conversion radiation, which excite the photo-stimulated luminescence phosphor layer ( ${}^6\text{Li}$  produce 2.05 MeV  $\alpha$  – particles and 2.74 MeV tritium,  $^{157}\text{Gd}$  produces  $\sim 70$  keV internal conversion electrons [Taka96]). Other disadvantage of  $^{157}\text{Gd}$  is the  $\gamma$  – sensitivity in comparison to  ${}^6\text{Li}$ , but the quantum efficiency of  $^{157}\text{Gd}$  is higher than  ${}^6\text{Li}$  because of the high neutron capture cross section. It has 25 – 100  $\mu\text{m}$  spatial resolution and  $10^5$  dynamic ranges. It shows also a good linearity with increasing exposure time. Typical exposure time per projection is 20 s and resulted image has a 16 – bit digital format ( $2^{16} = 65536$  gray values) [Lehm99]. Imaging plates have a greater advantage in the imaging over large areas with high spatial resolution. The gamma sensitivity of image plates is unfortunately very high, which results from the high amount of heavy elements in the image plate material. For more information about imaging plates, see [Raus92, Wilk92, Büch93, Niim94, Taka96, Thom97].

*The amorphous silicon detector* was designed to replace conventional film based radiography. Digital radiography is an excellent candidate for replacing many of the film – based radiography methods. Therefore, the main advantage of the amorphous silicon detectors compared to X – ray film is the digitization of the image with high dynamic range and better

### 3. Neutron Radiography

---

detector quantum efficiency (DQE). The thickness of amorphous silicon flat panel is between 127 – 750  $\mu\text{m}$  and it generates images with  $10^3$  –  $10^5$  dynamic ranges and 12 – 14 bit (4096 to 16384 gray values) nonlinear digitization [Neut01]. Its typical exposure time depends on the application changing from 40 ms to 10 s, which is much lower than conventional film technique. It works well in a radioactive environment, such as inside a nuclear power plant. Image processing is easily managed; to get good images background can be subtracted independent of the ambient radiation. They can be exposed directly to the radiation beam without any significant degradation, which with a conventional CCD device cannot be done. The amorphous silicon serves as a platform for thin film transistors, which are the key components of each light – sensing pixel. It is also possible to make amorphous silicon in larger sizes than crystalline silicon wafers. It consists of a scintillator layer converting the radiation into the visible light and a two dimensional array, where the photosensitive element in each pixel is an amorphous hydrogenated silicon photodiode. The light generates a current striking each photodiode and then the current is integrated in the device's self-capacitance [Koer00, Fort95]. The photocharge level is subsequently transferred to the external drive electronics by a matrix of amorphous hydrogenated silicon switching devices. Amorphous hydrogenated silicon is very sensitive to visible light and produces a low thermal noise or dark current in the semiconductor. Amorphous silicon is a semiconductor, like crystalline silicon, but it is much less susceptible to degradation from exposure to radiation. The radiation damage probability, which is caused by neutrons, is very low for the amorphous silicon detectors compared to crystalline silicon.  $\text{Gd}_2\text{O}_2\text{S:Tb}$  is used as a neutron converter for NR.

Digital CCD cameras provide more conveniences in NR. One of its conveniences is its reproducibility in the tomographic applications and real time imaging. The CCD camera provides faster and more practical, while its spatial resolution is not very high like in film or IP's. The resolution of scintillator based digital CCD camera is between 100 – 500  $\mu\text{m}$  with  $10^5$  dynamic ranges with good linearity. The typical exposure time is of 1 ms – 10 s level. The recorded image format is 16 – bit (65536 gray values).

#### 3.3.1 Basic Characteristics of a CCD Camera

There are many advantages of charged coupled slow scan CCD cameras in the imaging systems, such as low noise, low dark current, high spatial resolution, high dynamic range, good linearity and fast read – out rate to generate an image.

##### 3.3.1.1 Detectable Quantum Efficiency

The quantum efficiency (QE) of a sensor describes its response to different wavelengths of light. The fraction of the interacted photons to the incoming photons gives the QE or it can be described as the ability to convert photons into electrons. Detective quantum efficiency (DQE) is the ratio of average number of neutrons that were detected and the number of neutrons that entered the detector. The QE of the CCD sensors (back – illuminated and front – illuminated) depending on the light wavelengths is shown in Fig. 3.2.

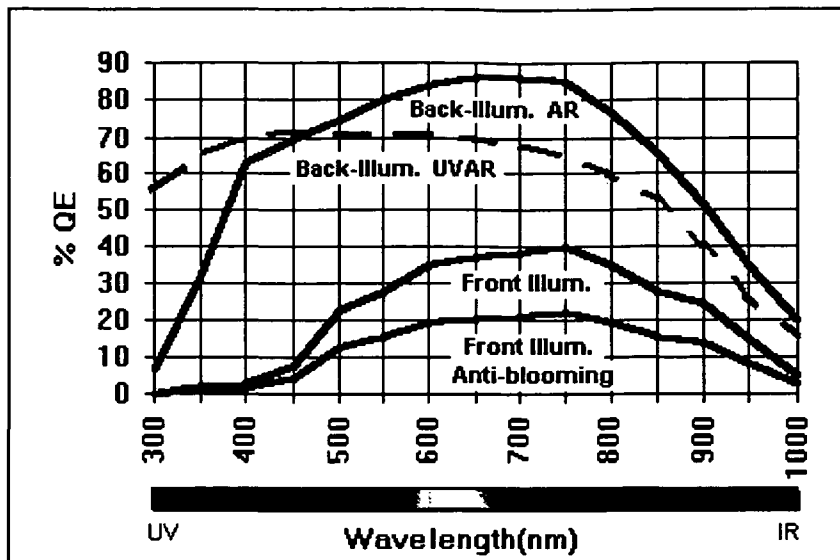


Fig. 3.2: The quantum efficiency of different CCD sensors [Astr98].

The CCD chip consists of a semiconductor material (silicon). Silicon exhibits an energy gap of 1.14 eV. Incoming photons with energy greater than 1.14 eV can excite valence electrons into the conduction band. Photons that are absorbed at different depths in the silicon depending on their wavelength produce electron – hole pairs. Nevertheless, not all the photons that reach the CCD chip can generate electron – hole pairs. The generated electron – hole pairs diffuse through the silicon lattice structure. The average lifetime for these carriers is 100  $\mu$ s. After this time, the electron hole pair will recombine. The back – illuminated sensors allow an increase in the quantum efficiency and also better sensitivity in the blue and in the ultraviolet (UV) regions of the light spectrum. If the sensor is a front – illuminated one, the photons must cross the region of the electrode (the silicon dioxide layer is transparent). Many photons will be absorbed or reflected in this layer and the quantum efficiency of the sensor will be reduced. The problem is serious for the short wavelengths, which are in the blue and in the UV, where the silicon absorbs strongly. The photons are absorbed directly on the silicon substrate in the back-illuminated sensor. If this substrate is thin enough, 10 – 20  $\mu$ m, it will be possible to force the collecting of the photo-generated electrons in the potential well under the electrode without loss as shown in Fig. 3.3. Standard front – illuminated sensors are more sensitive to green, red, and infrared wavelengths (500 – 800 nm) than to blue wavelengths (400 – 500 nm).

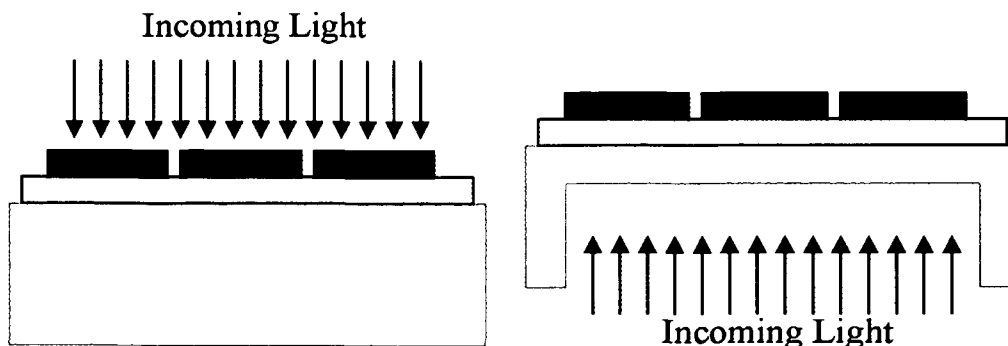
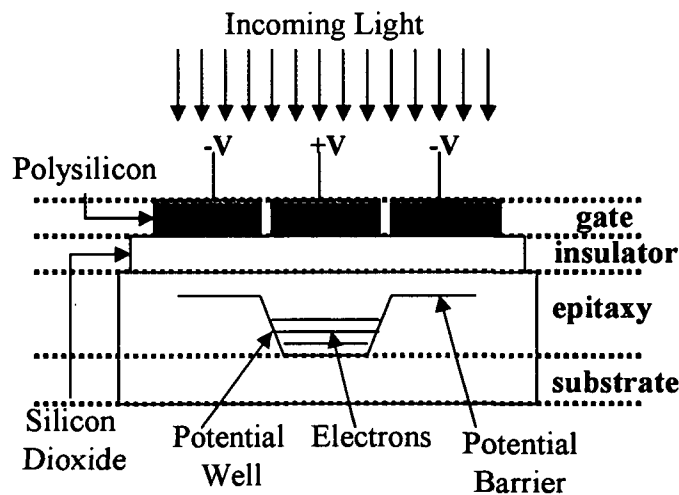


Fig. 3.3: The difference between front – (left) and back – illuminated (right) CCD sensors.

### 3.3.1.2 Readout and Charge Transfer Efficiency

CCDs follow the principles of basic Metal Oxide Semiconductor (MOS) device physics. A CCD MOS structure consists of a vertically stacked conductive material (doped polysilicon) overlying a semiconductor (silicon) separated by a highly insulating material (silicon dioxide). The chips of a CCD camera, which are made from p-doped silicon, collect photo-generated electrons in the potential well. When a photon penetrates into the p-type semiconductor, an electron-hole pair is generated. Then, the generated electrons are drawn towards the gate. However, the oxide layer (insulator) prevents the electrons reaching the gate. Consequently, a potential well is developed. The potential charge held in this well will be proportional to the incident light and also to the time of collection. The charge within the well can be transferred when a suitable potential is applied to the gate. The gate (electrode) is normally highly doped polycrystalline silicon and called polysilicon. It has a metal contact and connected to an electrical potential. The insulator consists of silicon dioxide and a silicon nitride layer. That prevents the arrival of the electrons to the gate and electron charge can be held in the well. The epitaxy is photoactive part of a CCD camera and it consists of p-doped silicon. Its typical thickness changes between 10 – 20  $\mu\text{m}$ . The substrate is a mechanical support, and also consists of p-doped silicon. Its typical thickness is 0.5 mm. Some of the incoming photons can reflect from the surface and a few others may get absorbed deep in the silicon substrate, but most hit the MOS capacitor and create electron-hole pairs. As long as light reaches the MOS capacitor, electrons continue to collect in a charge well (see Fig. 3.4) formed by potentials applied to the CCD gate. The holes are conducted to ground through the silicon substrate by the applied voltage, which creates an electric field through the oxide layer and repels holes.



**Fig. 3.4:** A layout of the CCD MOS structure.

A CCD chip is an analog device. In order to obtain a digital signal, an analog-digital converter is required. CCD sensor level specification describes the transfer efficiency of charge, which is produced in the CCD semiconductor chip converting photons into electrons. The image from a CCD is read out by transfer of rows into a horizontal register, followed by transfer of pixel charge along the horizontal register towards the output node as shown in Fig. 3.5. From the output node, they are transferred into the A/D converter. This is done until one field or frame is read out during the active image period. This method of transporting the image



charge through the image area to the image storage area takes hundreds of microseconds while light is still generating image charge.

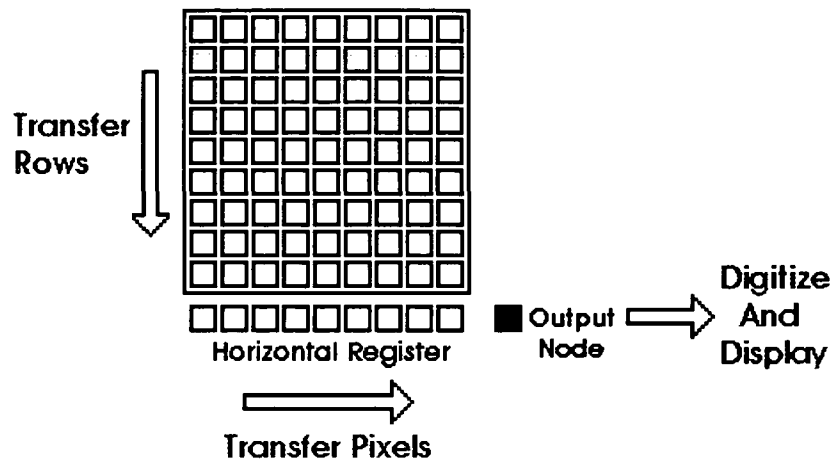


**Fig. 3.5:** Data transfer and registration

Not every electron will be carried along with perfect efficiency. Charge Transfer Efficiency (CTE) is the percentage of charge transferred from one pixel to the next. To transfer the charge in the well at least 3 gates are necessary. By changing the applied voltages to the gates the charge can be transferred to the next. Readout rate determines the speed of the charge transfer per pixel or readout speed of pixels per second. If the readout rate of charge increases, the number of trapped charges increases and also causes an increase of readout noise. Depending on the readout rate the readout noise can be minimized. A 16 – bit A/D converter has a conversion time of  $10^{-6}$  seconds. If it manages to read 100,000 pixels a second for 512 x 512 pixels in a CCD chip, the image processing time (to see the image on the monitor) can be calculated in second with the following expression:  $t = (512 \times 512) / 100000 = 2.62$  s.

#### 3.3.1.3 Signal – to – Noise Ratio (SNR)

Thermal and electrical effects always produce electrons. When the camera shutter is closed, dark currents cause some electrons to get trapped in charge wells. When the shutter opens to capture an image, the dark – current electrons add to those produced by any incident light, thus adding noise to the image information. The noise reduces the CCD's dynamic range, which is a measure of its ability to accurately resolve changes in light levels.

The ratio of the CCD's maximum output signal to the dark current signal represents the SNR of the device. SNR is one indicator of a measurement. In CCD imaging, SNR refers to the relative magnitude of the signal compared to the uncertainty in that signal on a per – pixel basis. Specifically, it is the ratio of the measured signal to the overall measured noise at that pixel. In order to calculate SNR, all noise sources, such as Photon (light +  $\gamma$ ), Readout, and Dark noise, must be taken into account. Photon noise refers to the inherent natural variation of the incident photon flux. Photon noise is the square root of signal and always present in an image. Readout noise refers to the uncertainty introduced during the process of quantifying the electronic signal on the CCD. Readout noise is described both for the CCD sensor and the total system. It comes from the system electronics and CCD sensor. Readout noise can be

### 3. Neutron Radiography

reduced when a slow readout rate in the CCD control program is selected and it is normally proportional to the square root of the readout rate. Dark noise arises from the statistical variation of thermally generated electrons within the silicon layers comprising the CCD. Dark current describes the rate of generation of thermal electrons at a given CCD temperature. Dark noise is also the square root of the number of thermal electrons generated within a given exposure. The SNR for a CCD camera can be calculated taking all together as given in Eq. (3.7) [Rope00]:

$$\frac{S}{N} = \frac{QE.t}{\sqrt{(QE.t + N_d + N_R)}} \approx \frac{t}{\sqrt{t}} = \sqrt{t} \quad (3.7)$$

- I : Photon flux (photons/pixel/second)
- QE : Quantum efficiency
- t : Integration time (seconds)
- N<sub>d</sub> : Dark Current (electrons/pixel/sec)
- N<sub>R</sub> : Read noise (electrons RMS/pixel)

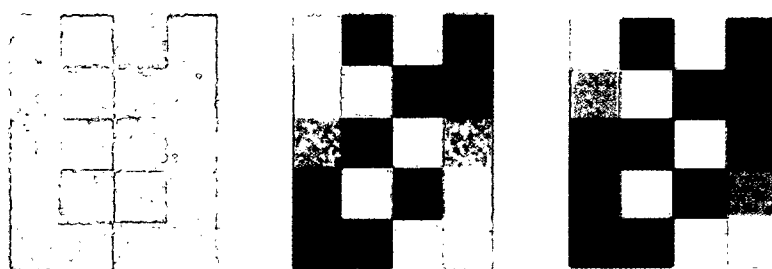


**Fig. 3.6:** Effect of SNR (Signal – to – Noise ratio) to the generated images (left image with lowest and right image with highest ratio) [Rope00].

#### 3.3.1.4 Spatial Resolution

The dimension of an image pixel is called pixel resolution. Spatial resolution is related to image details. It indicates how much detail an image can discern about an individual object and how good it can distinguish between two objects. The higher the spatial resolution is, the greater is the ability of pixels or an image to distinguish smaller details. An other main reason for the necessity to know the spatial resolution of a system is to understand image blurring and to distinguish it from scattering effects in the sample.

There are several ways to determine the spatial resolution of an image, such as PSF (point spread function), LSF (line spread function, which is a Gaussian function), MTF (modulation transfer function) and ESF (edge spread function). LSF is the derivative of ESF. ESF can be derived taking a line profile on the edge of a strong absorber foil like thin Gd – foil. The advantage of ESF is to determine the overall instrument resolution. PSF contains complete information about the spatial resolution. To express the spatial resolution most common way is to specify by the FWHM (full – width – half – maximum) value. This can be measured again using strong absorbing material foil with a small lock (like point). MTF, which is a

frequency response, can be performed taking two – dimensional Fourier transform of the PSF, for more information see [Smit97].

#### 3.3.1.5 Dynamic Range

Dynamic range is an important parameter characterizing the imaging system. The dynamic range refers to the ability to detect very dim and very bright parts of a single image quantitatively. The dynamic range determines how many gray levels can be resolved on an NR image. The smallest measurable intensity varies depending on the experimental conditions and applications, therefore a specific definition for dynamic range has been adopted, which is independent of how the camera is used. It is defined mathematically by the ratio of full well capacity to readout noise. Full well capacity defines the capacity of the potential well for electrons. It is a measure of the different contrasts of an image. An image with higher dynamic range shows more unique details than with lower dynamic range; a 16 – bit image has 65536 gray values and shows more unique details than 12 – bit image. The higher the bit number the more refined is the quantization of the signal according to a simple relation  $2^n$ . The better CCD is required to capture this detail, and more bits are required to store the numbers representing more range. The dynamic range of an integrating detector is given by the maximum and minimum fluencies that are possible. The background signal and noise level gives the lower limit and the upper limit is given by a 1 % departure from the linear response [Raus96, Diet96]. In fact, the lower limit of the fluency for an integrating detector is also influenced by the flux, because the background signal or noise rises linearly with the integration time.

#### 3.3.1.6 Linearity and Sensitivity

Linearity is the proportionality of the light production, or gray value in an image, to the exposure time. For example, if a 1 second exposure produces 3000 electrons of charge, 10 seconds should produce 30000 electrons of charge. The deviation from this straight line is a measure of non – linearity. It depends on the detector used. The scintillator efficiency affects only on the slope of linearity function. If the scintillator has a high efficiency, the change in the gray values is also high. X – ray films are nonlinear detectors, while CCD cameras and imaging plates have good linearity.

Sensitivity is a measure of the minimum detectable signal that a CCD chip can produce. The sensitivity of a CCD imager to light is determined by quantum efficiency and system noise level (signal – to – noise ratio).

#### 3.3.1.7 Dark Current and Cooling of the CCD Chip

The thermal energy of electrons in the silicon allows some electrons to break away from the lattice and become free to move through the silicon. These electrons constitute the dark current and are seen as a signal, which is present even if there is no light falling on CCD chip. Dark current reduces the performance of the CCD camera. Dark current is basically charge, which accumulates in the CCD pixels due to thermal noise. In general, it increases as temperature rises. All CCD's at some level exhibit the occurrence of dark current. The effect of dark current is to produce an additive quantity to the electron count in each pixel. Therefore, CCD chip should be cooled. Different cooling systems, such as liquid nitrogen and

### 3. Neutron Radiography

Peltier cooling, are used to enhance the performance of CCD camera reducing dark current to insufficient level. The typical cooling for charged coupled device is performed by liquid nitrogen utilization, which cools the CCD camera to approximately  $-130\text{ }^{\circ}\text{C}$ . The minimum operating temperature of a digital CCD camera to take a NR image with a good quality (low dark current) is  $-120\text{ }^{\circ}\text{C}$  [Koer00]. By liquid nitrogen cooling, the dark current can be reduced from  $10,000\text{ e}^-/\text{pixel}/\text{sec}$  to  $1 - 3\text{ e}^-/\text{pixel}/\text{sec}$ .

In addition to liquid nitrogen cooling, PC (Peltier Cooling) can also be used for the cooling of CCD sensors. Thermoelectric cooling system is known as "The Peltier Effect". The sample is connected to a large heat bath by an electric circuit built of two conductors as seen in Fig. 3.7. The Peltier heat is absorbed from the sample at one junction, and transferred to the heat bath at the other. The temperature difference achieved between heat bath and sample also depends on the magnitude of the electric current. The Peltier heat is the balance of the heat flows towards and away from the interface. The electron flow velocities depend on the energies of the conduction electrons. The CCD chip is cooled transferring the heat to the heat sink by conductors and the heat sink is cooled by liquid or air. The temperatures of the CCD chip can be reduced to  $-10\text{ }^{\circ}\text{C}$  to  $-50\text{ }^{\circ}\text{C}$  by PC. It corresponds to a few ten of  $\text{e}^-$  per pixel in one second.

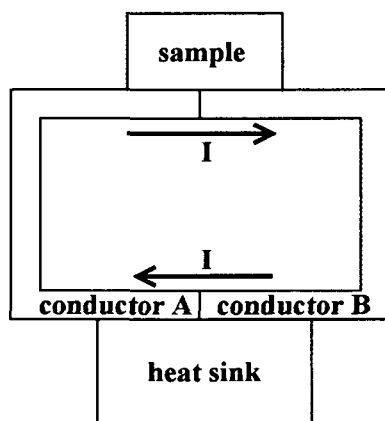


**Fig. 3.7:** Thermoelectric cooling of a sample and Peltier effect between two conductors with an electric current  $I$ .

#### 3.4 Cold Neutron Radiography (CNR)

NR is generally carried out at reactors where a steady – state source produces neutrons within a broad energy range. It is important to define the most suitable method for radiographic investigations. Therefore, in addition to the standard thermal NR, neutrons in other energy regions, such as fast and cold energy, are used in nondestructive material testing. As a result of the strong energy variation of neutron cross sections of nearly all the nuclides, neutron transmission measurement over a broad range of neutron energies can be used to give chemical composition and spatial distribution about an object. CNR offers specific advantages; one advantage is the inspection of rather thin layer of materials, which is one of the many NR problems. For this problem, very cold neutrons offer an advantage over thermal neutrons because of the  $1/v$  dependence ( $v$  refers velocity) of the material cross sections with neutrons. Other advantage of cold neutrons in the investigations of strong absorbing materials is that beam – hardening problems disappear. Another advantage is the fact that cold neutrons can much more easily penetrate thick samples than thermal neutrons due to the reduced cross section for neutron energies below the Bragg cutoff. The Bragg cutoff energies for different solid materials are different (e.g. Bragg cutoff energy for graphite is from 1 meV – 20 meV). Below neutron energy of a few meV (the exact energy depends on the material), there is an abrupt drop in the scattering cross section when the wavelength reaches twice the largest  $d$  spacing of the crystalline materials. The energy level, at which an abrupt drop occurs, is referred to as the Bragg cutoff. The cross sections of neutrons change quite drastically at the Bragg cutoffs due to this step – like behavior of coherent neutron scattering cross section for crystalline materials [Santi01]. The Bragg cutoff value for each crystalline material depends on its lattice constant. Neutrons with a wavelength larger than the lattice constant do not experience coherent scattering within the crystal, which results in a distinct decrease in neutron cross section below some specific neutron energy. This behavior is not used in most research reactor facilities, because the steady state nature of the neutron source is not favorable to separating neutrons of different energies. However, using mechanical velocity selector as monochromator, radiography can be realized in an energy dependent fashion. The abrupt change of the coherent neutron scattering cross sections disappears for very cold neutrons, because the material cross section increases at even smaller neutron energies [Whit83]. So, Bragg cutoff energy cannot be exploited for strong absorbing materials because of the  $1/v$  dependence.

Sometimes the change in the total cross section for the corresponding element is significant and this fact can be used for achieving a material discrimination in radiography images by changing the spectrum of the used neutron beam. A sample can be investigated to make material discrimination at neutron energies below and above the Bragg cutoff energy of the corresponding element within the sample. Then, radiography images of sample with different contrast are performed owing to different neutron energies. In addition to the radiography, three – dimensional imaging of samples can be obtained at these wavelengths by using tomographic image reconstruction techniques.

Radiography images at specific cold neutron energies could be produced using different techniques of neutron monochromatization [Kard01]. The most frequently used techniques can be classified in the following three groups:

- a) Polycrystalline filters,

### 3. Neutron Radiography

---

- b) Monochromator crystals and mirrors,
- c) Time of Flight (TOF) instruments.

A compromise between the energy resolution and the output neutron flux must be made for all monochromatization methods. In most cases, the achievement of a high – energy resolution (very narrow neutron energy spectrum) is connected with a loss of intensity. For NR experiments, a high neutron flux is recommended. Therefore, an optimization of experiment set up in the case of energy selective NR is important. A good example for such an optimization is the so – called Time Gated Energy Selected (TGES) neutron radiography reported recently by [Dona99] and [Buec94]:

- In [Dona99] experiment, short and intense neutron pulses produced in the spallation source (LANSCE) were used in a combination with a time of flight technique. This method gives a very narrow neutron output spectrum and a sufficiently high neutron flux of  $2.1 \times 10^6 \text{ n.cm}^{-2}.\text{s}^{-1}$ .
- In the Buecherl experiment [Buec94], Bragg reflection from different crystals was used in order to monochromatize the neutron beam, and some energy selective tomography experiments were performed at the reactor FRM of Technical University of Munich.

Unfortunately, these methods have disadvantages like long measurement times. Alternative method for neutron monochromatization is the utilization of a mechanical neutron velocity selector in contrast to the above mentioned methods; it will be discussed in chapter 5.3. A high neutron flux is required for this technique, but in a reasonable measuring time. The mechanical velocity selector causes neutron flux loss.

### 3.5 Thermal NR Facilities at the Atoinstitute of Austrian Universities in Vienna

At the ATI – Wien materials are investigated using NR and NT, USANS (Ultra Small Angle Scattering), neutron interferometry, NAA (Neutron Activation Analysis) by a fast pneumatic transfer system, depolarization analysis. All neutron beam lines and positions of the experimental setups at the TRIGA Mark II research reactor are shown in Fig. 3.8.

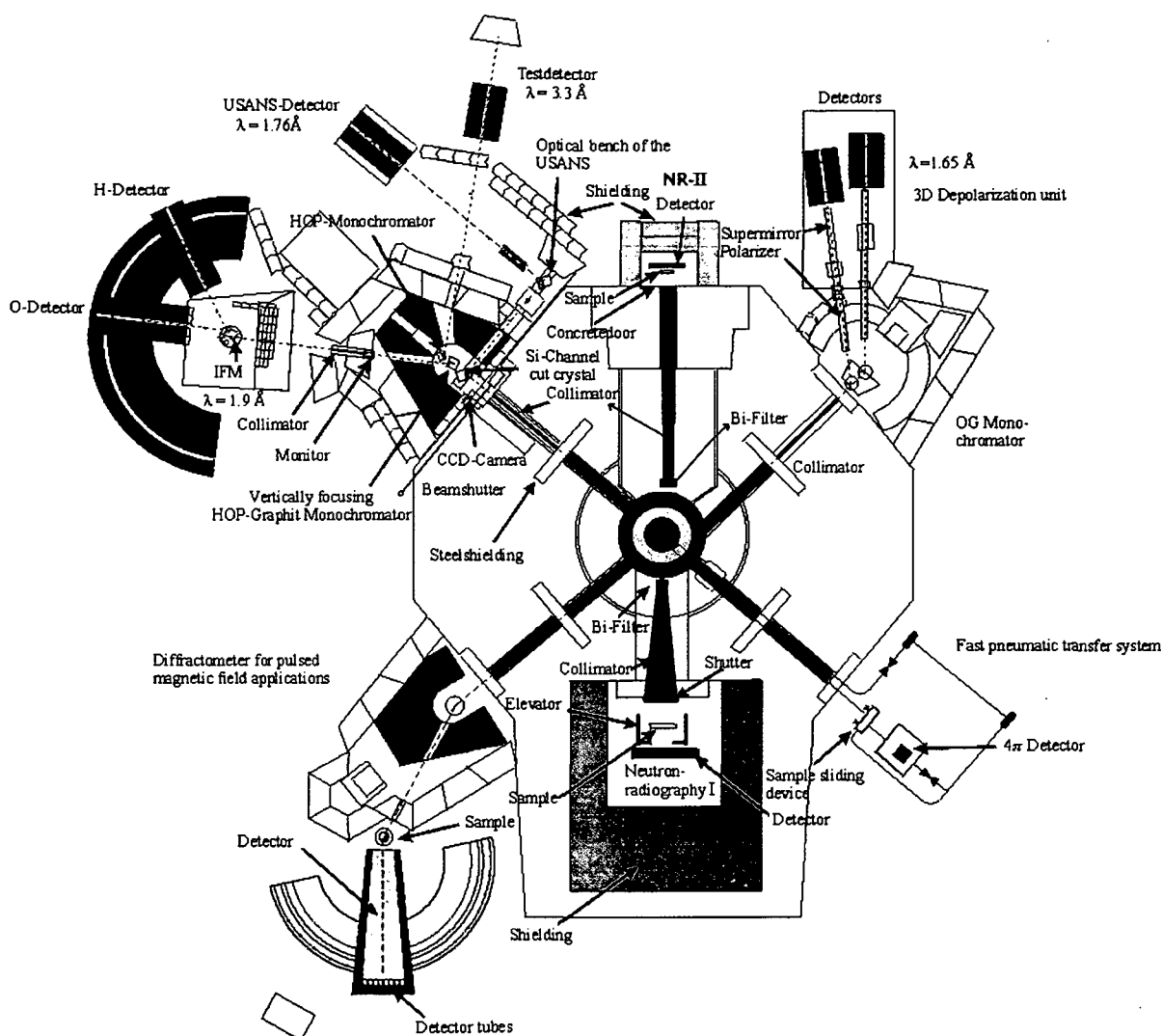


**Fig. 3.8:** The neutron beam lines at the TRIGA Mark II research reactor.

Two beam lines are dedicated to the experimental facilities of thermal NR, NR I and NR II. Neutron tomography set up was installed at the NR II beam line. The components of both NR facilities are depicted in Fig. 3.9.

### 3. Neutron Radiography

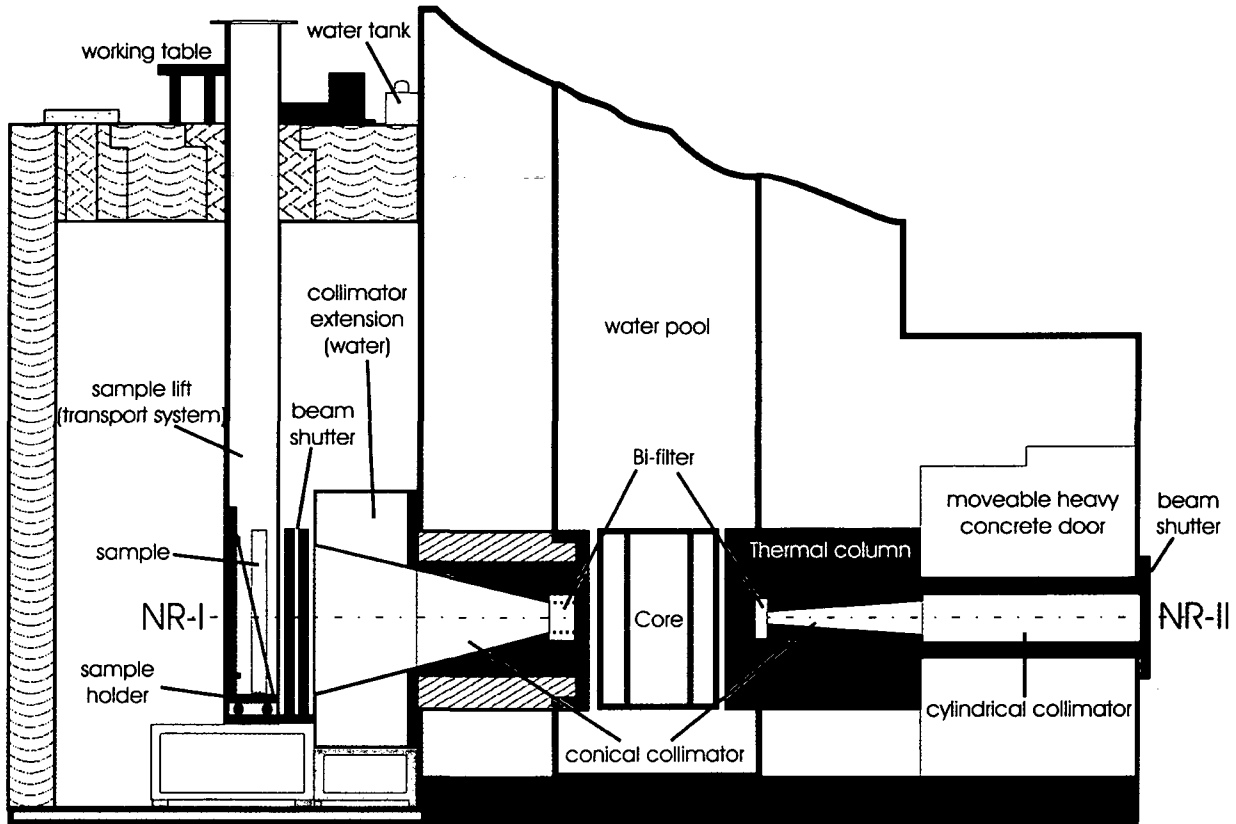


Fig. 3.9: NR facilities at TRIGA Mark II research reactor.

M. Hajek and W. Schöner at ATI have measured the neutron energy spectra of NR I and II beam lines using Bonner Sphere Spectroscopy (BSS) method [Haje01, Haje02]. High density polyethylene ( $\text{CH}_2$ )<sub>n</sub> is an ideal neutron moderating material to loose more kinetic energy per elastic collision due to the high concentration of low - Z elements such as hydrogen and carbon. The detector material in the center of sphere can detect it. Applying spheres of different diameters such as 2 to 10, 12, or 15 inches, a detector response in a wide energy range can obtain. According to the diameter of the sphere, a certain fraction of neutrons with suitable incident energies gets moderated until thermal equilibrium is reached with the atoms of the surrounding medium. A  ${}^6\text{Li}(\text{Eu})$  - scintillation counter, by which thermal neutrons are detected with the  ${}^6\text{Li}(n, \alpha){}^3\text{H}$  - reaction, has been used optically coupled to a photo multiplier tube with connected preamplifier, and a single channel analyzer counts the pulses.

The energy distribution of neutrons after moderation in the graphite block of the thermal column can be approximated by a Maxwellian distribution as given in Eq. (3.8) that gives the number of neutrons  $dn$  per volume element with energies between  $E$  and  $E + dE$ .

$$dn = n(E) dE = \frac{2 \pi n}{(\pi kT)^{3/2}} \cdot \exp(-E/kT) \sqrt{E} dE \quad (3.8)$$

The experiments with BSS were simulated in Monte Carlo Neutron Transport program to determine the detector responses at different sphere diameters for the same detector material. To be precise, the  ${}^6\text{Li}$  - scintillator measures the density of the thermalized neutrons inside



### 3. Neutron Radiography

the Bonner spheres. A computer code or program was used for the deconvolution of detector responses and experimental data. The neutron fluence,  $\Phi$ , is the quotient of  $dN$  by  $dA$ , where  $dN$  is the number of particles incident on a sphere of cross-sectional area  $dA$ . The neutron fluence rate,  $\phi$ , of neutrons is the quotient of  $d\Phi$  by  $dt$ , where  $d\Phi$  is the increment of neutron fluence in the time interval  $dt$  as shown in Eq. (3.9).

$$\phi(t,r) = \frac{d\Phi(r)}{dt} = \frac{d^2N}{dt dA}, \quad (\text{m}^{-2}.\text{s}^{-1}), \quad \text{and} \quad \phi = \int_0^{\infty} n(v).v.dv \quad (3.9)$$

The unfolded spectrum, which is the conversion of the neutron fluence spectrum into a  $d\phi(E)/dE$  spectrum obtained using the MAXED deconvolution, is a  $dn(E)/dE$  distribution with a maximum at an energy of  $kT/2 = 0.0125$  eV. The spectrum was empirically converted into a  $d\phi(E)/dE$  distribution [Haje02].

**The measured neutron spectrum of NR I beam line (without Cd shutter) with BSS method is shown in Fig. 3.10.**

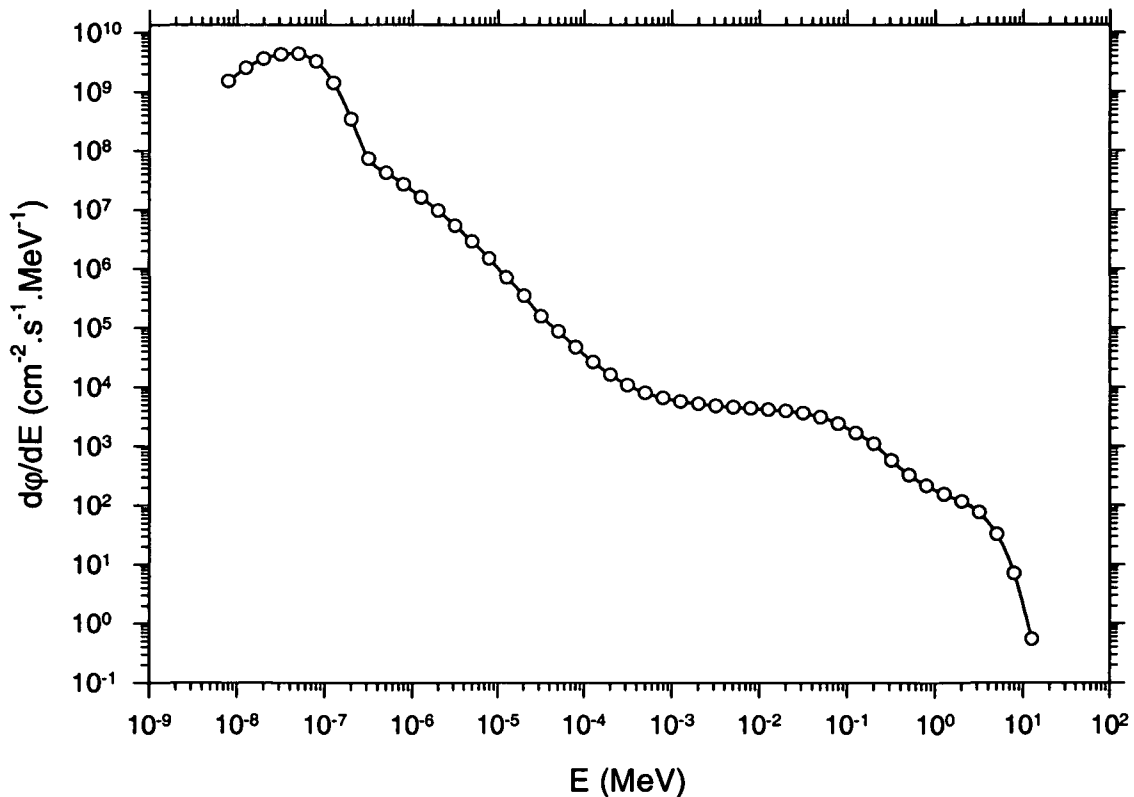


**Fig. 3.10:** The measured neutron fluence rate per energy versus neutron energy of NR I beam line without Cd shutter [Haje02].

**The detection system of NR I facility** is based on the well-known film/converter method. The conical collimator, which has 5 cm aperture and 250 cm length, was installed at this facility. Beside the smaller collimation ratio ( $L/D$ ) of 50, a  $40 \times 40 \text{ cm}^2$  beam size and  $3 \times 10^5 \text{ n.cm}^{-2}.\text{s}^{-1}$  thermal neutron flux, which is approximately 3 times higher than the thermal

### 3. Neutron Radiography

neutron flux of NR II facility, are the main advantages of this facility for the investigation of larger samples with higher neutron flux. A 3 times higher neutron flux means that the exposure time is reduced by a factor of 3. As mentioned previously, the collimation ratio is an important parameter, which describes the beam collimation and will limit the obtainable spatial resolution by the inherent blurring independently from the detector properties. The beam unsharpness,  $U_{\text{beam}}$ , can easily be related to the  $L/D$  ratio as given in Eq. (3.5). The  $L/D$  ratio of 50 is an insufficient value to generate sharp images at NR I facility. A conical collimator was installed at this facility. The conical collimator at NR I facility consists of two parts: First part of the collimator is 150 cm long and second part is 100 cm long. The inner walls consist of 3 mm  $B_4C$  coated rubber Cd. Second part, which is water filled Al tank, acts as an extension of collimator and also a shielding. A 14 cm long single crystal Bi filter reduces gamma content by a factor of 50 and also the thermal neutron flux by a factor of 10 [Buch86]. The gamma radiation is caused by the emission during the free neutron generation process such as fission and by the used moderator (hydrogen or graphite). A water pump, which fills the collimator with water, is used as a beam shutter. Using a lift system, samples can be brought to the irradiation position in 5 minutes.

The measured spectrum of the NR II beam line with BSS method were carried out behind the heavy concrete door at thermal column. Fig. 3.11 shows Maxwellian distribution of neutron fluence and density of NR II beam line and Fig. 3.12 demonstrates the unfolded and fitted neutron spectra at thermal column of NR II facility.

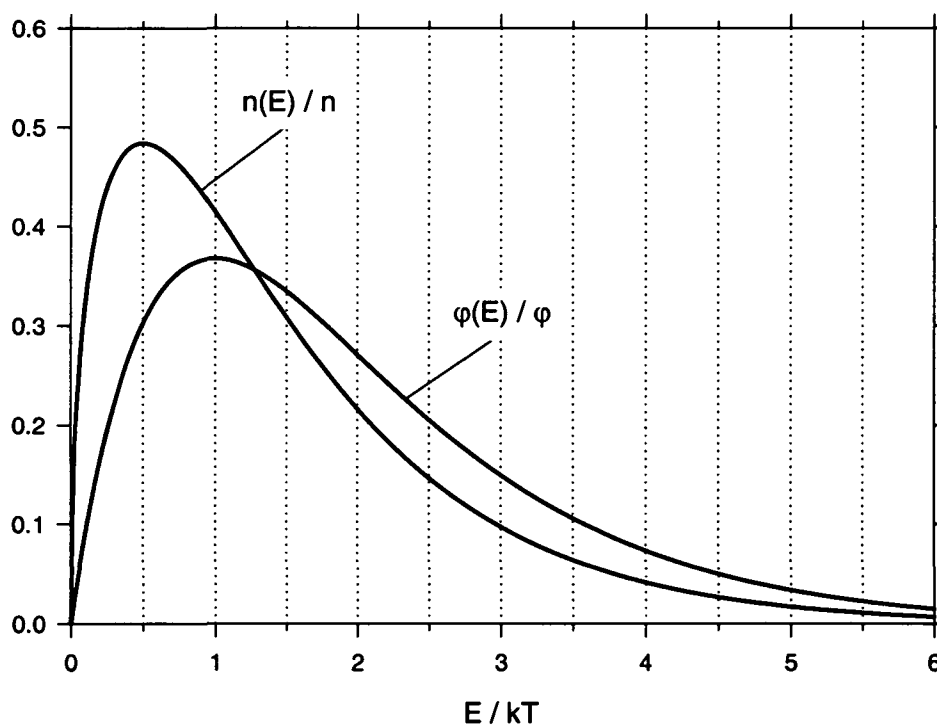
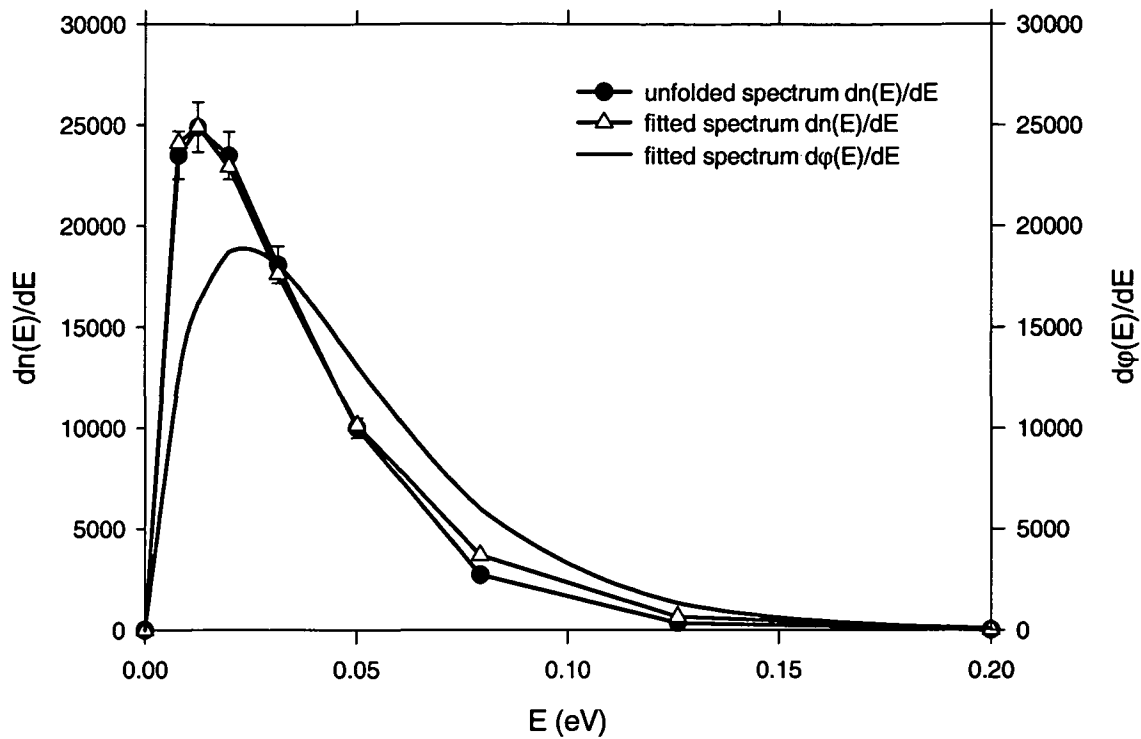


Fig. 3.11: The Maxwellian distributions of neutron fluence and density of NR II [Haje02].

### 3. Neutron Radiography



**Fig. 3.12:** Unfolded and fitted neutron spectra at the thermal column of the TRIGA Mark II research reactor [Haje02].

The calculated values for a thermal power of 250 kW<sub>th</sub> are shown in table I, assuming a linear flux/power relationship. The results show that the contribution of the fast neutrons to total flux is practically negligible. The measurements with the Bonner sphere spectrometer have been carried out in a distance of approximately 35 cm from the graphite surface (behind the door).

**Table I:** Neutron flux at the thermal column of the TRIGA Mark II reactor measured with the Bonner spectrometer [Haje02].

	$\Phi (E < 0.4 \text{ eV})$ ( $\text{cm}^{-2} \cdot \text{s}^{-1}$ )	$\Phi (E < 100 \text{ MeV})$ ( $\text{cm}^{-2} \cdot \text{s}^{-1}$ )
$P_{\text{th}} = 5 \text{ W}_{\text{th}}$	$1.07 \times 10^3$	$1.08 \times 10^3$
$P_{\text{th}} = 250 \text{ kW}_{\text{th}}$	$5.37 \times 10^7$	$5.39 \times 10^7$

**The detection system at NR II facility** is based on the scintillator – digital camera, which was installed considering the beam quality and easy handling previously. Advantages of the camera based detection system are an excellent linearity, high sensitivity, good reproducibility, and fast readout of the information as mentioned in the chapter 3.3. However, every good system has also disadvantages. The disadvantages of this system are high costs of the detector and the lower spatial resolution compared to film and Imaging Plates. The NR II facility contains two collimator parts: The first part of the collimator is conical having a length of 130 cm that was installed in the thermal column. The second part is cylindrical having a length of 127 cm that was installed in the movable heavy concrete door as seen in

### 3. Neutron Radiography

Fig. 3.9. This movable door allows carrying out of some measurements at the thermal column at high neutron flux. First part of the collimator has 2 cm aperture and 6 cm outlet, and it was placed in a 10 x 10 cm outer shell. A 4 cm thick polycrystalline Bi was used as a gamma filter as shown in Fig. 3.13. The second cylindrical part has 8.2 cm inner and 20 cm outer diameter. The inner sides of both collimators were coated with  $\text{CdB}_4\text{C}$ . In order to supply homogeneous neutron distribution for some measurements behind the door at high neutron flux, the first part of collimator can be replaced by a graphite block of the same size.

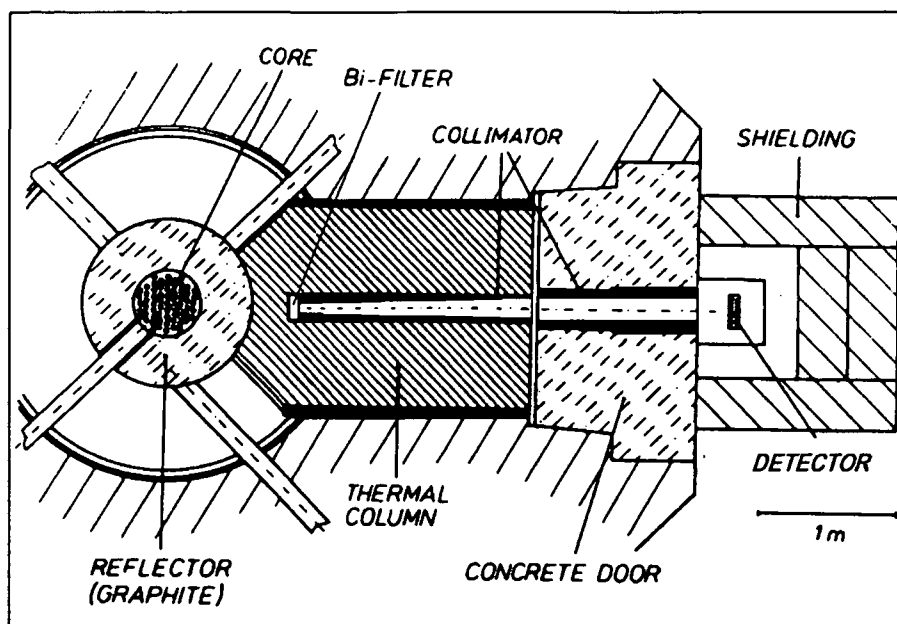


**Fig. 3.13:** The overview of NR II beam line and collimator construction at TRIGA Mark II research reactor.

A 30 cm thick graphite block between the collimator aperture and Al tank of the reactor is an illuminator, which distributes neutrons homogeneously before the neutrons enter the collimator aperture. The 10 – 15 cm thickness of graphite illuminator is a requirement for NR facility. An excess of illuminator causes excess gamma content and also reduction of the neutron flux. There is ~ 20 cm excess graphite at NR II facility and that means factor 4 is the reduction of the thermal neutron flux. The aperture was surrounded with a 3 cm thick neutron and gamma shielding materials in sandwich form, in which three 0.5 cm thick Pb and three 0.5 cm thick  $\text{B}_4\text{C}$  layers were used as shown in Fig. 3.14.

### 3. Neutron Radiography

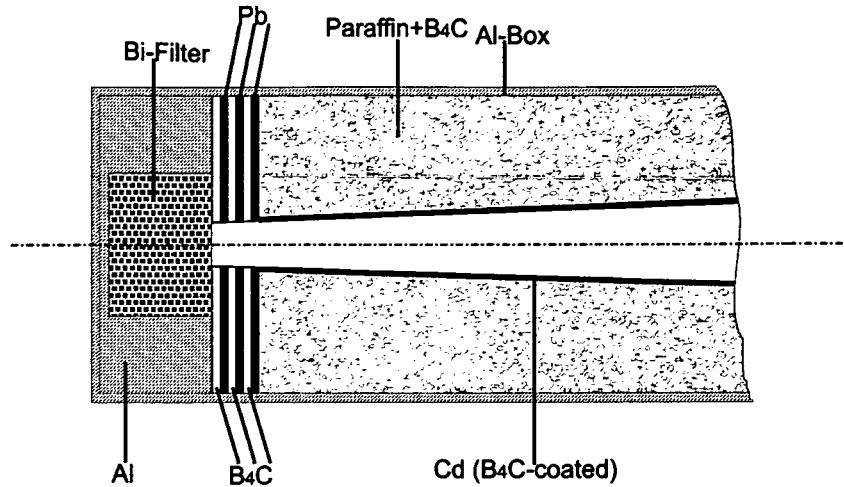


**Fig. 3.14:** The composition of the first part of collimator at NR II facility.

The comparison of the characteristics of neutron radiography facilities, NR I and II at ATI and NEUTRA at PSI (Paul Scherer Institute) in Zurich, are given in table II. For some experiments NEUTRA has preference with a bigger beam size and higher thermal neutron flux and also better collimation ratio in comparison to other NR facilities. Neutrons at NEUTRA – PSI facility come from a highly fluctuating spallation source, contrary to stationary neutron source for NR facilities at ATI.

**Table II:** Basics characteristics of NR facilities at Atominstutute – Wien and NEUTRA – PSI.

	NR I Facility ATI – Wien	NR II Facility ATI – Wien	NEUTRA PSI – Zurich
Neutron flux ( $\text{cm}^{-2} \cdot \text{s}^{-1}$ )	$3 \times 10^5$	$1.3 \times 10^5$	$3 \times 10^6$
L/D (collimation) ratio	50	128	550
Cd-ratio	3	20	100
Beam diameter (cm)	40	9	40
Gamma background (Sv/h*)	0.4	0.045	0.0015
Source strength ( $\text{n} \cdot \text{s}^{-1}$ )	$3.8 \times 10^8$	$7.0 \times 10^6$	$3.8 \times 10^9$
Facilities	NR	NR and NT	NR and NT
Detection system	X – ray film / converter	CCD camera / scintillator	CCD camera / scintillator

\* 1 Sv (Sievert) = 100 rem, 1 Gy (Gray) = 100 rad

**Rem** (Roentgen Equivalent Man) is a unit that relates the dose of any radiation to the biological effect of that dose. To relate the absorbed dose of specific types of radiation to their biological effect, a "quality factor" must be multiplied by the dose in rad, which then shows the dose in rems. For gamma rays and beta particles, 1 rad of exposure results in 1 rem of dose.

**Rad** (Radiation Absorbed Dose) recognizes that different materials that receive the same exposure may not absorb the same amount of energy. A rad measures the amount of radiation energy transferred to some mass of material, typically humans. One roentgen of gamma radiation exposure results in about one rad of absorbed dose.

**R** (Roentgen) measures the energy produced by gamma radiation in a cubic centimeter of air.

### 3. Neutron Radiography

The next important point other than beam quality in a NR facility is the detection system. Neutron sensitive scintillator coupled to digital CCD camera system is the easiest and fastest method among the imaging detectors. The digital format of resultant radiography images can be processed without doubt. The digital camera system was installed at NR II considering all advantages as mentioned in the chapter 3.3. Thermal neutrons penetrate the sample and then the transmitted neutrons from the sample result in photons or visible light in the scintillator screen. A mirror reflects the light to the camera. The distance between the collimator exit and scintillator is 20 cm and a rotary – table was placed in the middle as shown in Fig. 3.15. The Levy – Hill scintillator screen was mounted to the inner side of Al – box positioned at the beam aperture. Approximately a 30 x 30 x 110 cm<sup>3</sup> aluminum light – tight box protects the light sensitive camera. The basic properties of the NR II digital camera system is given in table III, for more information see [Koer00].

**Table III.** Properties and components of the neutron sensitive scintillator coupled to nitrogen cooled digital CCD camera at NR II.

<b>Neutron sensitive scintillator</b>	<b>Levy Hill:</b> 0.4 mm thick ZnS(Ag)- <sup>6</sup> LiF
<b>Camera</b>	Liquid nitrogen cooled Astrocam slow scan CCD camera
<b>Camera chip</b>	<b>Sensitive area :</b> 12.3 x 12.3 mm <b>Sensitive pixel :</b> 512 x 512 pixels <b>Pixel size :</b> 24 x 24 μm
<b>Quantum efficiency (QE)</b>	Up to % 90 with standard AR coating
<b>Digitalization</b>	16 bit digitization with 65535 gray levels
<b>Lenses</b>	Nikon NOKT 58 mm F 1.2 Nikon NOKT 180 mm F 2.8 Nikon NOKT 105 mm F 2.0 (new one)
<b>Mirror</b>	2 mm thick glass plate coated with Al and TiO <sub>2</sub>

The effective spatial resolution of the whole system at NR II station has been measured using a very strong absorber material. MTF (Modulation Transfer Function) was calculated by evaluating the data along a line profile that was taken on one edge of a thin and sharp Gd – plate. It results a spatial resolution of 400 – 500 μm and 180 – 250 μm using two different lenses with 58 mm and 180 mm focal lengths. The current properties of our CCD camera lenses are given in Appendix II. A line profile on a Gd – edge gives faster spatial resolution and called edge response function, but MTF can also be derived using ERF; firstly differentiating ERF function to get line spread function (LSF) and then taking Fourier Transform of LSF function to derive MTF function [Smit97].

### 3. Neutron Radiography

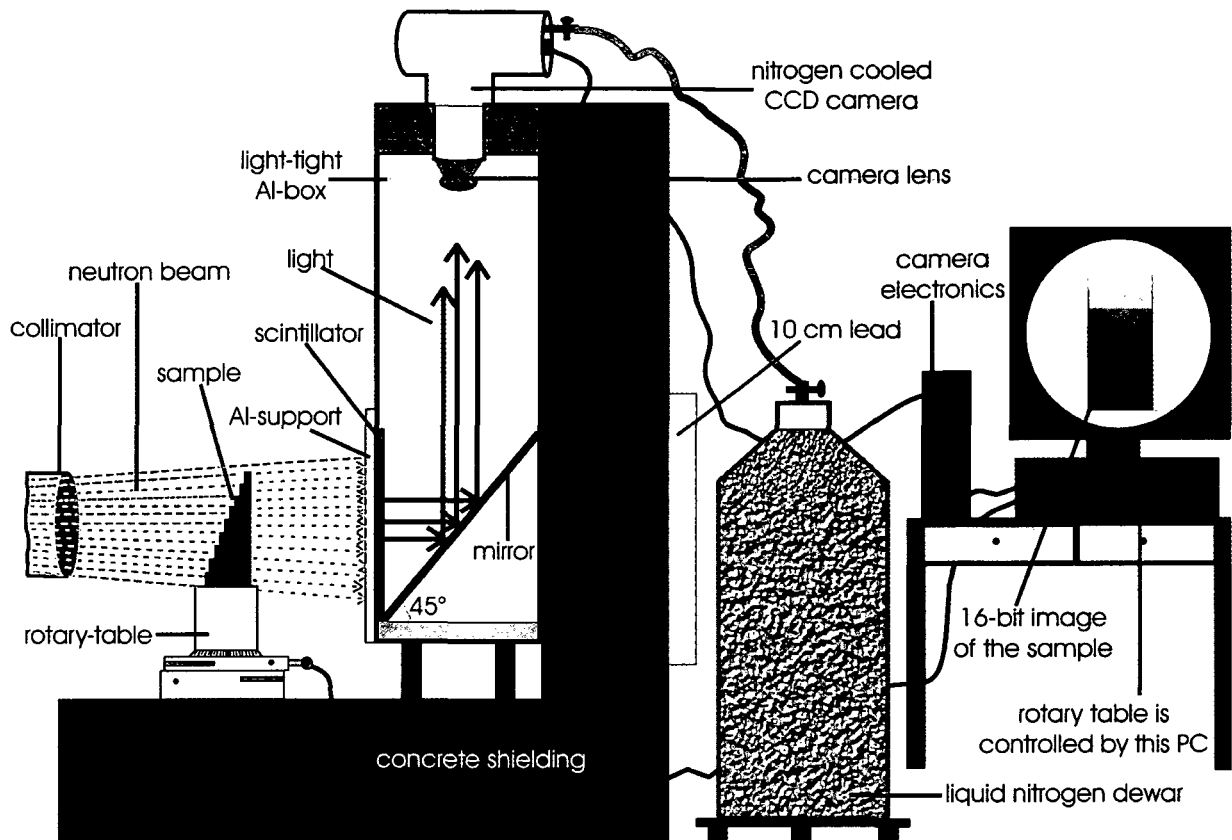


**Fig. 3.15:** The components of the digital detection system at NR II – ATI facility in Vienna.

# 4

## Neutron Tomography (NT)

Computed Tomography (CT) is a completely nondestructive technique for visualizing features in the interior of an opaque object, and for obtaining digital information on their 3D geometries and properties without physically sectioning it. The object being investigated is rotated in the beam in order to make transmission measurements at each angular position. The two dimensional transmission arrays are then reconstructed into images using reconstruction algorithms, by which individual slices of the object can be reconstructed to provide a three-dimensional view of internal and external structural details. Tomography has found widespread application in many scientific fields including physics, chemistry, geophysics, and medicine. By this method the porosity, defects or inner structural details can be determined for a wide range of materials.

A well-collimated parallel beam traverses the object and it is attenuated according to the Eq. 4.1, which describes the result along one projection through the object.

$$I(\theta, t) = I_0 \cdot \exp\left(- \int_L \Sigma(x, y) \cdot ds\right) \quad (4.1)$$

- $I_0$  : Initial beam intensity
- $I(\theta, t)$  : Transmitted beam intensity
- $\Sigma(x, y)$  : Total macroscopic cross section

In NT the distribution of sigma,  $\Sigma(x, y)$ , in the slice being imaged are reconstructed. The Radon Transform of a function is defined as the line integral along a line at an angle,  $\theta$ , from the  $y$  - axis and at a distance  $t$  from the origin.  $P_\theta(t)$  is the projection of an object at angle  $\theta$ . The variables  $(t, \theta)$  define the position of the line  $L$  in the space as shown in Fig. 4.1. For a



#### 4. Neutron Tomography (NT)

given angle in measurement – space,  $t$  can be calculated for each pixel in the  $M \times M$  reconstruction – matrix as in Eq. (4.2).

$$t = x.\cos\theta + y.\sin\theta \quad (4.2)$$

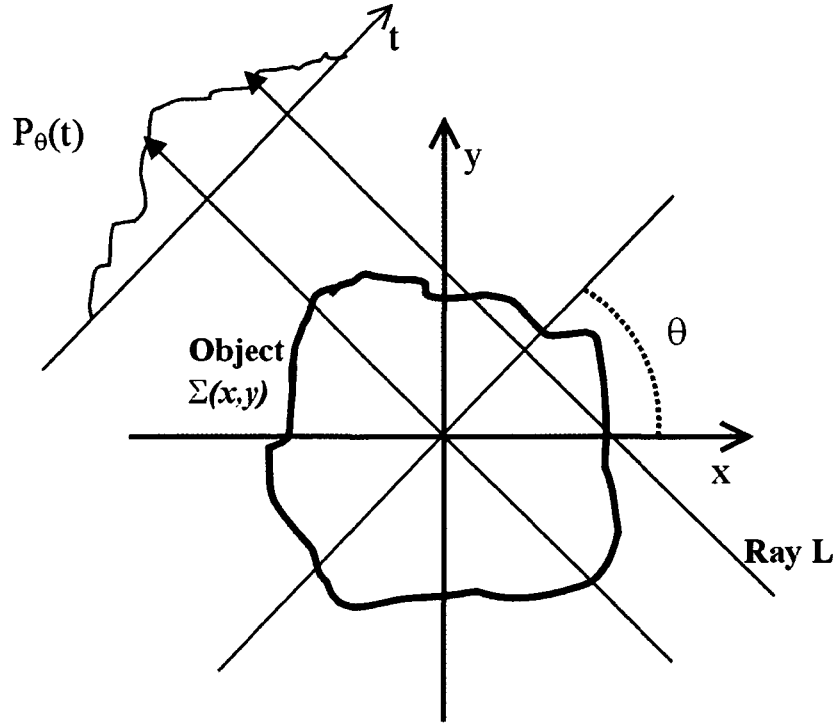


**Fig. 4.1:** Formation of projections; parallel beam projection through an object along beam path L in cartesian coordinate.

The measured intensity profile for a fixed angle  $\theta$  as a function of  $t$  is denominated as projection,  $I_\theta(t)$ . Then, it is transformed into attenuation profile,  $P_\theta(t)$ , taking Radon Transform. The transformation of a function  $\Sigma(x,y)$  into the sinogram  $P(\theta,t)$  is called the Radon Transform, named after Johann Radon [Rado17], the founder of tomographic reconstruction. The Eq. (4.4) is the explicit form of the Eq. (4.3) and it gives the line integral along a beam path (L) (Ray Integral).

$$P_\theta(t) = \ln \frac{I_\theta(t)}{I_0} = - \int_L \Sigma(x,y).ds \quad (4.3)$$

$$P(\theta,t) = \int_{-\infty}^{\infty} \int_{-\infty}^{\infty} \Sigma(x,y).\delta(x.\cos\theta + y.\sin\theta - t).dx.dy \quad (4.4)$$

$P(\theta,t)$  can be obtained stacking all the projections  $P_\theta(t)$  together in 2D array [Dove01]. The angular step is found by dividing total angle  $\pi$  to the number of projections,  $N$ , taken between  $0 - \pi$ . Dirac delta function,  $\delta$ , indicates that the integration is carried out only along the line – L. Using the inverse Radon transform, so that  $\Sigma(x,y)$  is recovered from the projection set

#### 4. Neutron Tomography (NT)

$P(\theta,t)$  a slice can be reconstructed from the Eq. (4.4). There are different reconstruction algorithms; the task of all algorithms is to estimate the distribution of a particular physical quantity in the object using measurements. Image reconstruction in NT is the process of estimating  $\Sigma(x,y)$  from a set of projections  $P(\theta,t)$ : summation of the contributions from all projections to the point  $(x,y)$ . Geometrically, the back projection operation simply propagates the measured sinogram back into the image – space along the projection paths.

If the back – projection is performed without modification, then a crude image is formed. That means the star-like artifacts are occurred in the reconstructed image apparently. As a result of this, the reconstructed image gets blurred and distorted. One would expect that a high-pass filter could be used to eliminate blurring. If the measurement data is first convolved by a filter and then back – projected into x-y plane, this is called FBP (Filtered Back Projection) [Kak88, Herm80]. The measured attenuation is distributed evenly along the line; the problem is the overlapping of all projections from different views around the low frequency regions. In order to control these effects, a high-pass filter can be used to spread the overlapped contributions along the line during the reconstruction of the projections. Fig. 4.2 shows common reconstruction filters that are utilized in FBP. These filters have the effect of filtering out low frequencies and passing high frequencies with corresponding filter behavior (e.g. Ramp filter with a linear behavior). Thus with this filter, contrasting features (high-frequencies) are accentuated, while blurring (low-frequencies) is minimized. The Ramp filter produces a sharper image, but it has also the undesirable effect of passing and magnifying extraneous noise from projection data. The Butterworth filter produces a smoother image than the Ramp filter. The Shepp – Logan filter is a smoothing filter and it suppresses the highest spatial frequency and reduces noise; therefore, it was used in our image reconstructions.

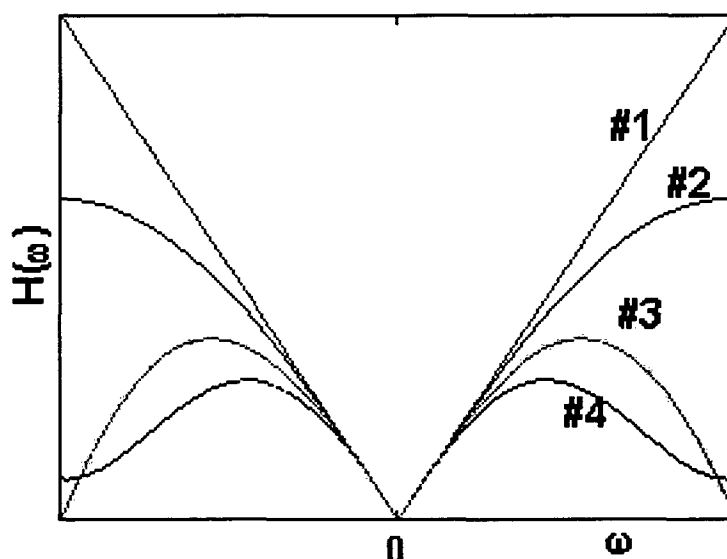


**Fig. 4.2:** Magnitude responses of common back – projection filters in frequency domain: 1 = Ram – Lak (Ramp), 2 = Shepp – Logan, 3 = Cosine, 4 = Hamming [Duke00].

### 4.1 Experiment

In order to perform NT of an object, sufficient projections should be recorded from different views with angular increment by the digital CCD camera. A digital detection system is very useful compared to other imaging devices like IP's and converter/film for tomographic inspections. Our NT detection system was installed at NR II facility at ATI – Wien [Koer00]. Two computers control NT measurements in order to synchronize rotary table and camera control program. After the computer reads out and save the first projection, the next trigger signal is sent to the rotary table, which has been connected to a computerized motion control system. Thus, the sample is rotated a specific angle step, and the next exposure starts automatically. The angle step depends on the projection number being taken from 0° to 180°. The position of the object or rotation axis does not have to change during a NT measurement, otherwise the processing and reconstruction of its projections will be difficult.

One of the important points in a NT measurement is the determination of the total projection number over 180°. In order to reconstruct a slice, a sequence of projections from a sample must be recorded to capture the peaks and troughs of the original waveform. For high frequencies, the points are further apart (far from the origin) resulting image degradation (mission of some information). This phenomenon is called aliasing and appears below and above the Nyquist frequency, which is normally the highest possible frequency. The Nyquist theorem states that the sampling rate\* must be greater than twice of the highest frequency in the input signal [Kak88]. Eq. (4.5) gives approximately the required projection number [Schi99, Schi01-1, Schi01-2]. However, the practical experiences in NR using scintillator/digital camera detector showed that half or one third of the pixel number in one row gives the sufficient projection number for a NT.

$$\frac{N}{B} \approx \frac{\pi}{2} \quad (4.5)$$

**N** : Total projection number

**B** : Number of rays per projection, which implies in our measurements the number of pixels in one row of a projection.

200 projections over 180° are reasonable for the chip format, 512 x 512 pixels, of our CCD-camera, using 58 mm F 1.2 lens for a NT measurement. This means that the sample is rotated by 0.9° angular intervals. In the case of the use 180 mm F 2.8 lens, the number of projections is limited with 60 – 70 projections considering the limited reactor operation time. 180 mm F 2.8 lens needs longer exposure time (2-3 minutes for one projection) to give the same intensity as with 58 mm F 1.2 mm lens for 20 seconds. In a tomograph, one additional image is taken at 180°, which is the reverse projection as taken at 0°. It is necessary to search rotation axis for the image reconstruction. Otherwise, some ring shape artifacts will appear in the reconstructed slice. In the preparation step of the image reconstruction, all projections have to be processed. Some open (without object) and dark (with closed camera shutter) beam

---

\* Sampling rate is the number of times per second the analogue to digital converter measures the incoming signal. The rate of sampling or measurement is the sampling rate and corresponds to the limits of frequency resolution. Current standard is sampling rate of 44,100 Hz with a resolution of 16 bits (96 dB dynamic range).

images must be performed to process images. If the temperature condition of the CCD camera changes during the measurements, the open and dark beams corrections will not be the same for all sample projections. In order to prevent this problem it is better to take average of initial and final open and dark beam images. In our measurements, we have taken 3 open and 3 dark beam images at the beginning of the NT measurement, and then 2 open and 2 dark images at the end.

### 4.2 FBP based Image Reconstruction Program supported by IDL Software

One of the reconstruction algorithms is the FBP image reconstruction technique that is the common method today [Kak88, Herm80, Herm95]; so we have developed our image reconstruction program based on the FBP algorithm in IDL software [Appendix I]. After performing all projections of a sample over 180° and also open/dark beam images, this FBP based image reconstruction program can be used as the following:

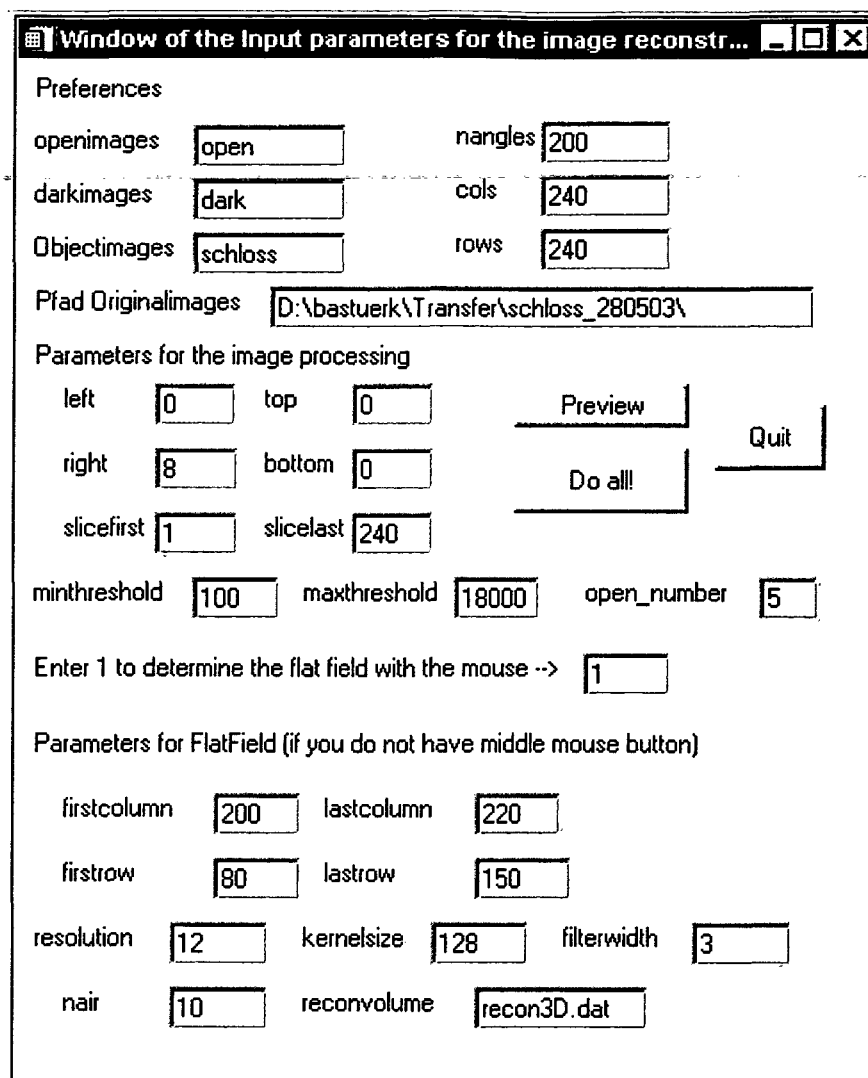
- First of all, the software of IDL 5.2 or higher version must be installed in the computer,
- Open the reconstruction program,
- Compile and run the program,
- A window for the input parameters appears on the monitor as shown in Fig. 4.3,
- Type the names of the open, dark and object images into the corresponding openings in the input parameter window,
- Type the total number of projections for the “nangles” part, and image size for “cols” and “rows” parts,
- Type the initial and final number of being reconstructed slices,
- Type the file path for “Pfad Originalimages” (all projections should be in the same file path). Do not forget to type slash “\” at the end of the file path name as seen in Fig. 4.3.
- Pressing the button “Preview” can check the rotation axis. If rotation axis is not searched, it causes some artifacts in respect of relation to the shift – quantity of the axis from the center. The center of the rotation can be searched cutting images from left-, right-, bottom-, and topsides if necessary. Repeat this process until the resultant image gives approximately dark image, changing the number of pixels to be cut from all projections and Pressing the “preview” button (see also chapter 4.1.2 – searching of the sample rotation axis).

#### 4. Neutron Tomography (NT)

---

- Type minimum and maximum threshold values, which replace the pixel intensities under minimum and over maximum threshold values on the images in order to reduce artifacts.
- Type the number of open and dark beam images for the “open\_number” part on the window; this number is the same for open and dark beam images in our measurements.
- To execute the flat field correction for each image you have to determine flat field area on one of the images where neutrons do not pass through the object in all projections. For this procedure, you have two different choices: one is the determination of the flat field area by using the mouse (you must type 1 for this choice), and other is the determination by typing the matrix positions of the flat field area in the parts of “ firstcolumn, lastcolumn, firstrow and lastrow”.
- Type the resolution, which changes the dynamic range of the reconstructed image; if you type higher values resolution will be better (default value is 10).
- Type kernel size for the reconstruction matrix, it depends on the projections matrix size; it goes 128, 256, 512 e.t.c., for bigger image size type higher one.
- Type the kernel size or width of the image filter (e.g. median filter is a common and faster one); 3 refer 3x3, 5 refer 5x5 and 7 refer 7x7 e.t.c.
- Type “nair”, which determines the number of columns from left and right side of the sinogram matrix; mean value of these columns is used to normalize sinograms.
- Type the output file name for the 3D reconstructed volume data (do not forget to type “.dat” after the name as seen in Fig. 4.3).
- Then, press the button of “Do all!” to perform reconstruction procedure.

## 4. Neutron Tomography (NT)



Window of the Input parameters for the image reconstruction

Preferences

openimages  nangles

darkimages  cols

Objectimages  rows

Pfad Originalimages

Parameters for the image processing

left  top

right  bottom

slicefirst  slicelast

minthreshold  maxthreshold  open\_number

Enter 1 to determine the flat field with the mouse -->

Parameters for FlatField (if you do not have middle mouse button)

firstcolumn  lastcolumn

firstrow  lastrow

resolution  kernelsize  filterwidth

nair  reconvolume

Preview

Do all

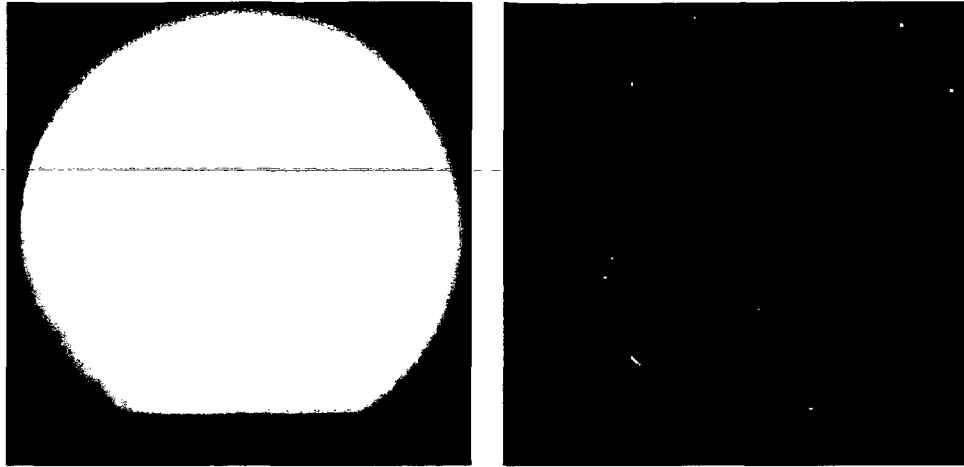
Quit

Fig. 4.3: The window of the input parameters for the image reconstruction.

### 4.2.1 Preparation of Images for the Reconstruction Program

Normally, our camera chip has 512 x 512 active pixels. If we use 58 mm F 1.2 camera lens, the whole chip area is unnecessary. It is limited by the beam size, which has ~ 9 cm diameter at the scintillator screen. The represented images in Fig. 4.4 and Fig. 4.5 contain 240 x 240 pixels. In the investigation of special objects, the 180 mm F 2.8 camera lens is more suitable considering its spatial resolution (e.g. absorber distribution in the boron – alloyed steel matrix) because of better resolution. In that case, entire pixels of the camera chip (512 x 512) should be utilized to visualize objects with ~ 4 x 4 cm<sup>2</sup> size. Some applications of NT in the industry and the properties of these lenses will be given in Appendix II.

In order to demonstrate all steps in the image reconstruction, a pad – lock was used as an example as shown in Fig. 4.5.



**Fig. 4.4:** One open (left) and dark (right) images; white spots on the account of gamma rays can be seen clearly.

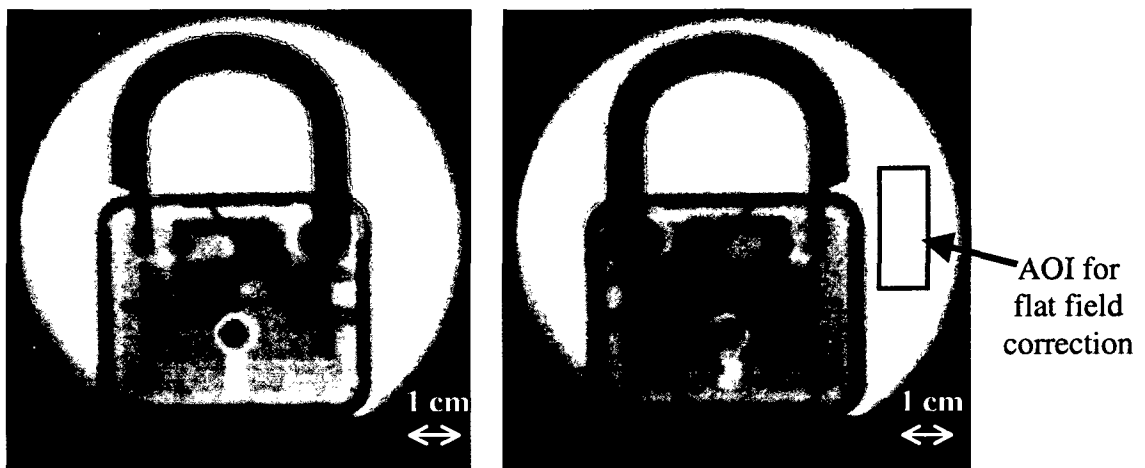


**Fig. 4.5:** First (at  $0^\circ$ ) and last (at  $180^\circ$ ) projection of a pad – lock.

#### 4.2.1.1 Searching of the Sample Rotation Axis

The projections at  $0^\circ$  and  $180^\circ$  should contain the same transmission data, but they are reversed. At this stage, the last projection at  $180^\circ$  is flipped and subtracted from the first projection at  $0^\circ$ . The resultant image must be dark in an ideal case, if not, the images have to be cut from the sides to find center of rotation. It is important to prevent some artifacts in the reconstruction. If the rotation axis is not in the center, white and black stripes will appear as seen in Fig. 4.6 (left). In the pad – lock example, the rotation center was determined cutting 8 pixels from the right side as demonstrated in Fig. 4.6 (right image).

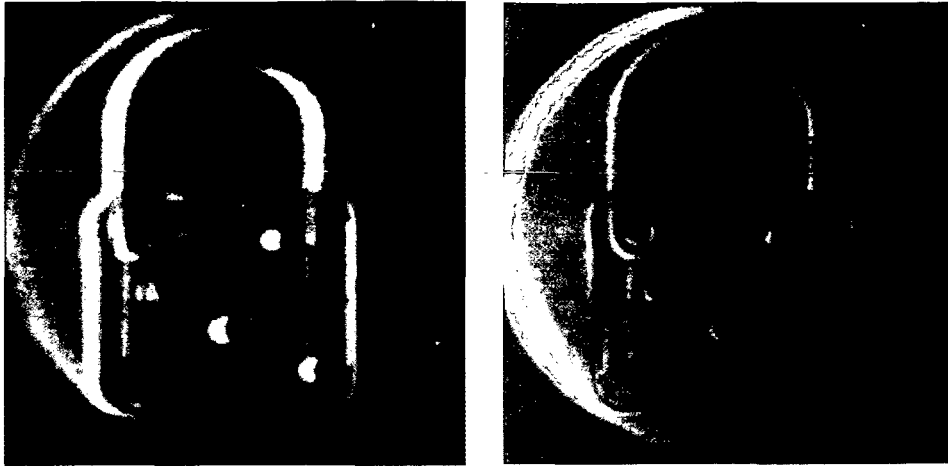


**Fig. 4.6:** The rotation axis is not in the center (left), and in the center (right) after cutting 8 pixels from the left side of the image – matrix.

### 4.2.1.2 Open & Dark Beam Correction and White Spots Removal

The neutron beam is not uniform throughout the NT projections. On that account, they have to be corrected by an open (white) beam image. Each NR image contains also background (dark current) has to be also subtracted from all projections including open beam projections. The reason of the dark current was explained in the previous chapters. Then, all sample projections are divided with the corrected open beam projection (average of 5 open beam images).

White spots caused by gamma radiation can be removed using median filter as seen in Fig. 4.7. The median filter is an easy correction of white spots or noises, where individual pixels are infected, however it declines spatial resolution of images. Therefore, using a small filter kernel is recommended. The neighbouring pixels are sorted due to their brightness and the median value is replaced with the value of the center pixel. If images have less white spots, a small filter kernel (3 x 3) is better; the one is used in our reconstructions. White spots density in an image increases with increasing exposure time [Koer00].

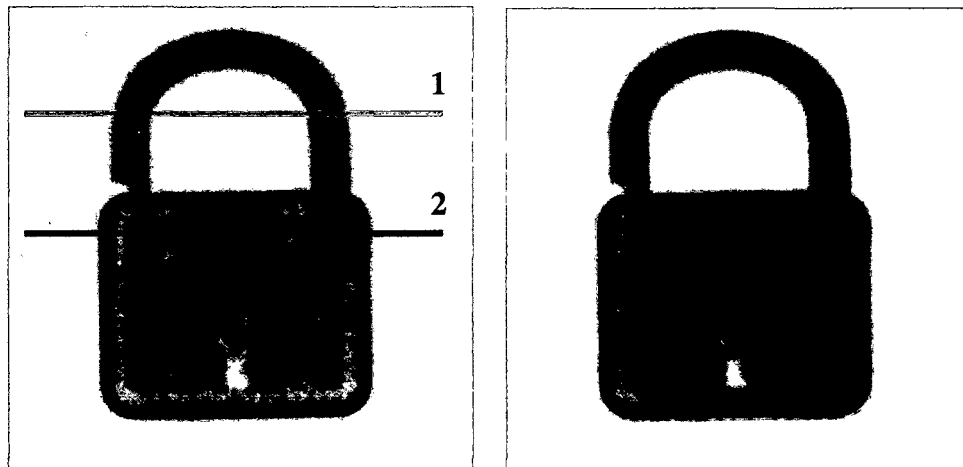


**Fig. 4.7:** Open and dark beam corrected image (left) and white spot were removed using 3 x 3 median filter (right).



### 4.2.1.3 Flat Field Correction

Flat field correction is necessary, if intensity – fluctuations take place in the projections during the tomography experiment. The fluctuations of neutron flux (related to the reactor power) and non – linearity in the scintillator screen can result the intensity – fluctuations on the images. Open beam correction should not be confused with flat field correction. Open beam correction eliminates the neutron beam fluctuations on one image, and flat field correction is to eliminate intensity fluctuations between sequence images. In order to prevent this effect an area of interest (AOI) is taken from one of the projections, where beam could pass unattenuated to the detector in all projections as shown in Fig. 4.5. Then, each projection is divided by its own AOI (open beam part in a sample projection) to remove this effect.

### 4.2.1.4 Generation of Raw Sinograms

All afore mentioned image processing stages were only the preparation of the images for the reconstruction. In order to begin the reconstruction, the attenuation coefficients have to be calculated taking logarithm of the transmission data. The data will have negative values; it must be converted into the positive values, multiplying by  $-1$ . Sinogram, which contains all data collected in relation to a specific slice, is constructed by putting the data from each projection angle into a single row of a new matrix. Fig. 4.8 shows the sinograms of 55<sup>th</sup> and 120<sup>th</sup> slice from the inspected pad – lock. It is called sinogram, because the data show sine function.



**Fig. 4.8:** Raw sinograms of 55<sup>th</sup> and 120<sup>th</sup> slices along the line 1 and 2, which were depicted in Fig. 4.7.

### 4.2.1.5 Filtering of Sinograms

As mentioned the Shepp – Logan filter suppresses the highest spatial frequency and reduces noise. Each row of the sinogram is filtered or convolved using Shepp – Logan filter to emphasize the edges as seen in Fig. 4.9.

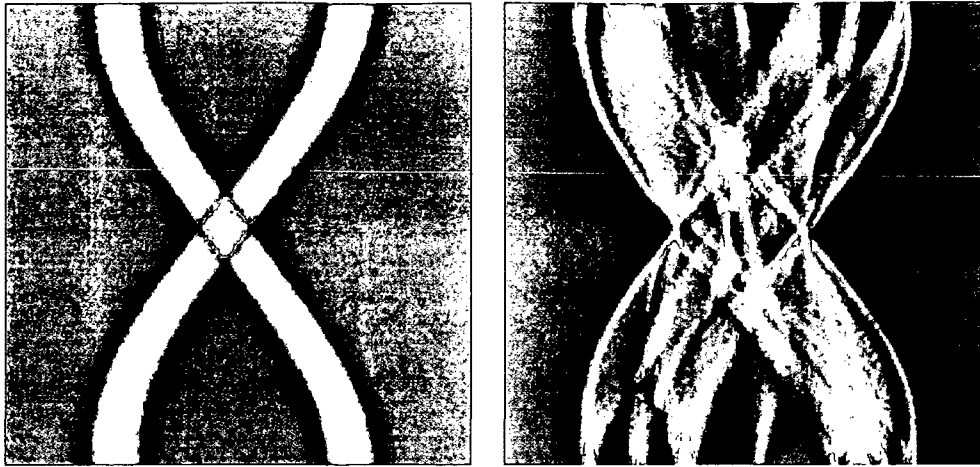


**Fig. 4.9:** Filtered sinograms of 55<sup>th</sup> and 120<sup>th</sup> slices with using Shepp – Logan filter.

#### 4.2.1.6 Back – Projection of the Filtered Sinograms (FBP)

In order to reconstruct the slices from the measured data, the filtered sinograms (e.g. at the line 1 and 2) have to be projected back. Some artifacts that must be removed using some methods can appear. The program computes the 3D volume data matrix (232, 240, 220) for 3D reconstruction of the object. Fig. 4.10 shows the back projections of 55<sup>th</sup> and 120<sup>th</sup> slices among the 220 slices; at the positions of line 1 and 2. The half circles are owing to the fact that the rotation axis of the sample is not directly lined up with the center of the beam, resulting in the rotation axis off. That means the center of rotation must be found.



**Fig. 4.10:** Back projections of 55<sup>th</sup> and 120<sup>th</sup> slices at the position 1 and 2, when the rotation axis is not in the center.

The comparison between Fig. 4.10 and Fig. 4.11 shows clearly the artifacts resulting from the rotation axis. The artifacts were disappeared after the rotation axis correction as seen in Fig. 4.11.

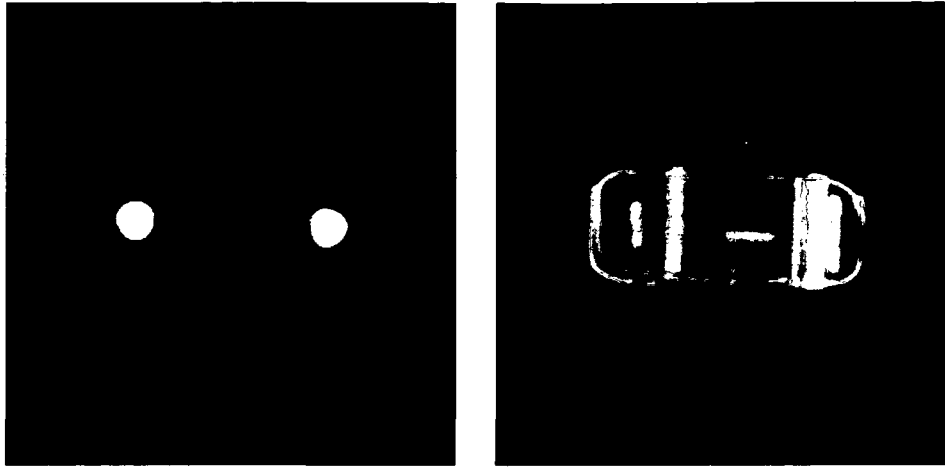


**Fig. 4.11:** Back projections of 55<sup>th</sup> and 120<sup>th</sup> slices, when the rotation axis is in the center.

Some diffraction could appear in the back projections of the slices. The back projected images can be corrected by defining threshold values for upper and lower parts to eliminate such artifacts. The intensities over or under the threshold values can be replaced by threshold values.

### 4.2.1.7 Removing of Ring Artifacts

This image processing is needed, if some ring artifacts appear in the reconstructed image; that means full circles surround the center of the reconstruction, which could be generated by bad detector elements. The simplest way to reduce the ring artifacts used in our reconstructions is as follows:

1. Compute the average row of the sinogram by summing down each column and dividing by the number of rows. The average row should have very little high frequency content, since real objects will be moving in the sinogram, and will be blurred out when computing the average row. Bad detector pixels will show up as spikes or dips in the average row.
2. Compute the magnitude of these detector anomalies by subtracting a smoothed version of the average row from the average row.
3. Subtract the result from step 2, from each row in the sinogram.

### 4.2.2 3 – Dimensional Demonstration of the Reconstructed Image

All reconstructed slices of the sample are saved in a 3D volume matrix at the end of this reconstruction program, which can be demonstrated three dimensionally from desired views by using a 3D visualization program (e.g. VolumeGraphics) as shown in Fig. 4.12.

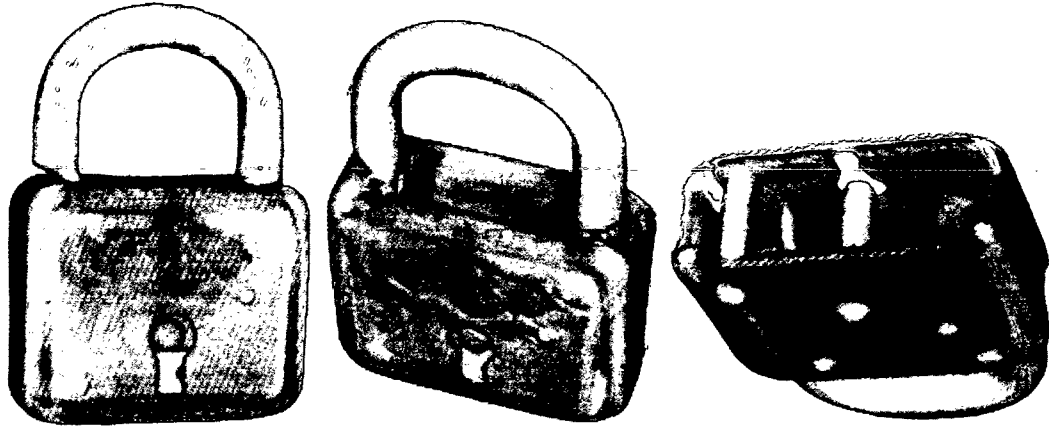


**Fig. 4.12:** 3D visualization of the whole reconstructed slices of the pad-lock with full opacity.

The inner details of the sample (e.g. defects, porosity or material distribution) can be inspected slice by slice as presented in Fig. 4.12 and Fig. 4.13, or changing the transparency – opacity as shown in Fig. 4.14. The histogram is very important contrast enhancement feature, which gives the distribution of gray values in an image. Using the histogram, the desired parts of the sample can be suspended or brought to light as shown in Fig. 4.14 (left and right image).

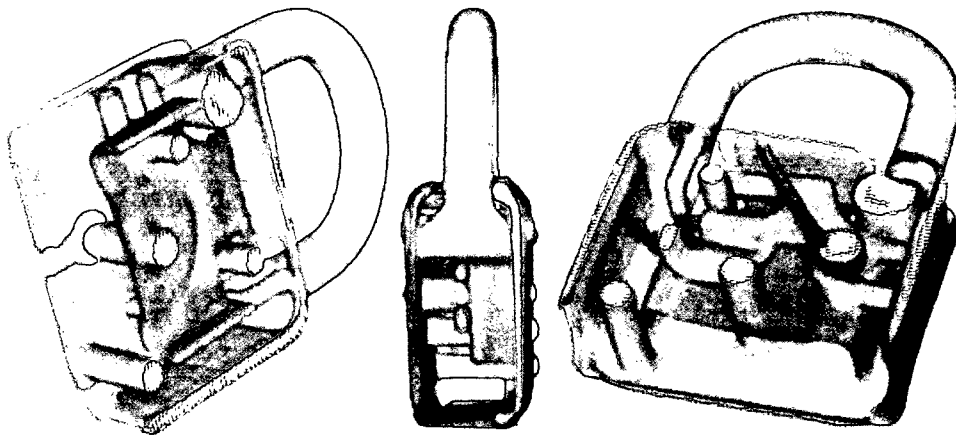


**Fig. 4.13:** Visualization of inner parts cutting the 3D sample slice by slice from the sides.

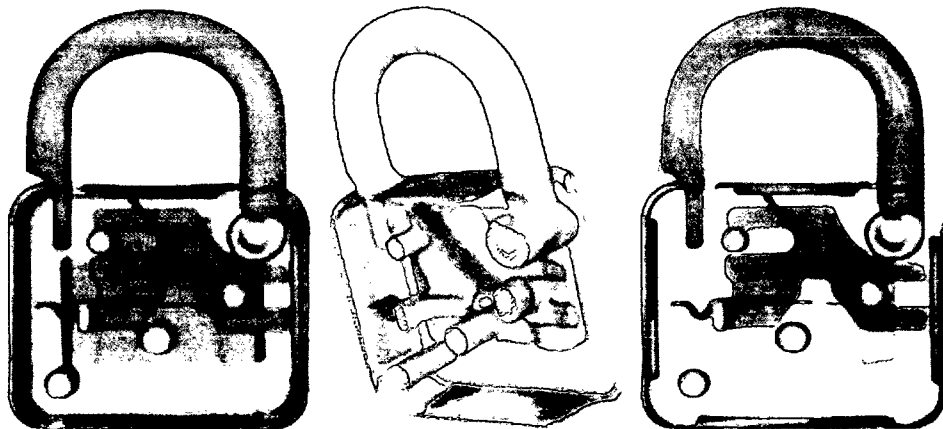


**Fig. 4.14:** Visualization of some parts of the sample at different transparency adjustment.

# 5

## Investigation of Fusion Relevant Materials

ITER (International Thermonuclear Experimental Reactor) is based on the "TOKAMAK" concept, a toroidal (doughnut – shaped) magnetic configuration. Super conducting magnetic coils around a toroidal vessel confine and control a mix of charged particles or ions, the plasma, and induce an electrical current through it. Plasma is the fourth state of matter. It has unique properties like the other states of matter (solid, liquid and gaseous). Just as most substances become solid if cooled sufficiently, any substance will become plasma if heated enough. The hot plasma that generates the fusion reactions is confined by magnetic fields. Fusion reactions take place, when the plasma is hot and dense enough, and contained for long enough to start fusing together. The purpose of the magnetic field is to prevent the plasma from the touching the walls lest it cool down and stop reacting. First wall and blanket (FW – Blanket) design is a crucial element in the performance and acceptance of a fusion power plant. Blanket surrounds the plasma and protects the vessel material from the high radiation. The blanket surface facing the plasma is divided into three functional parts, in which the first wall is only for radiation loads and extends over the majority of the blanket modules [Elio99]. High temperature structural and breeding materials are needed for high thermal performance. A suitable combination of structural design with the selected materials is necessary for D – T fuel efficiency. Whenever possible, low afterheat, low chemical reactivity and low activation materials are desired to achieve passive safety and minimize the amount of high level waste materials. The key characteristics of different advanced high performance FW – Blanket concepts for the fusion technology are presented in Table I [Wong02]. ARIES – AT in USA and TAURO in Europe utilize lead – lithium (Pb – 17%Li or Pb – 17Li) as tritium breeder and coolant, and SiC/SiC<sub>f</sub> (silicon carbide fiber) composite as structural material. In both cases, liquid Pb – 17Li flows in channel boxes of fiber reinforced SiC/SiC composite. All reviewed blanket designs can satisfy most of the necessary design goals. However, further developments are necessary in the first wall and structural material selection, design and improvements of the insulation material of the plasma stabilization TF (Toroidal Field) magnetic coils. One of these advanced blanket modules is the European TAURO – concept,

## 5. Investigation of Fusion Relevant Materials

which is a self – cooled Pb – 17Li blanket. TAURO utilizes Pb – 17Li as breeder – coolant and SiC/SiC<sub>f</sub> ceramic composite as structural material.

**Table I:** Key design parameters of eight – advanced FW – Blanket modules [Wong02].

	1	2	3	4	5	6	7	8
	A-SSTR-2	A-HCPB	TAURO	ARIES-AT <sup>1</sup>	V/Li/He	W/Li/He	EVOLVE	FFHR-2
Application	Tokamak	Tokamak	Tokamak	Tokamak	Tokamak	Tokamak	Tokamak	Tokamak
P <sub>Fusion</sub> , GW	4	4.5	3	1.7	1.9	3.5	3.5	1
FW heat flux, MW/m <sup>2</sup>	1.4 (ave)	0.6 -peak	0.5 (ave) 0.69 -peak	0.26 (ave) 0.34 -peak	0.34	2 -peak	2 -peak	0.09
Neutron wall loading, MW/m <sup>2</sup>	6 (ave)	2.76 (ave) 3.5 -peak	2 2.8 -peak	3.2 (ave)	2.9 (ave)	7 -peak	10 -peak	1.7
Structural material	SiC/SiC <sub>f</sub> composite	SiC/SiC <sub>f</sub>	SiC/SiC <sub>f</sub> composite	SiC/SiC <sub>f</sub> composite	V-4Cr-4Ti	W-alloy	W-alloy	V-4Cr-4Ti
FW thickness, mm	4-6	3	6	4	3	3	3	5
Structural material T <sub>max-allowed</sub> , °C	1100	1300	1300	1000	700	1400	1400	750
FW material, K <sub>th</sub> , W/m-K	10-50	15	15	20	35	85	85	35
Tritium breeder (neutron multiplier)	Li <sub>2</sub> TiO <sub>3</sub> (Be)	Li <sub>2</sub> SiO <sub>3</sub> (Be)	Pb-17Li (none)	Pb-17Li (none)	Li (none)	Li (none)	Li (none)	Flibe (Be)
Fuel form	Pebbles	Pebbles	Liquid	Liquid	Liquid	Liquid	Liquid	Liquid
Coolant (Pressure, MPa)	He (10)	He (8)	Pb-17Li (1.5)	Pb-17Li (1)	He (18)	He (12)	Vaporized Li (0.037)	Flibe (0.6)
<sup>3</sup> T breeding ratio (Li-6 enrichment)	1.37 (local) natural	1.09 „3-D“ optimized	1.37 (local) (90%)	1.1 “3-D” natural	1.4 (local) natural	1.43 (local) (35%)	1.33 (local) natural	1.4 (local) (50%)
Coolant T <sub>in</sub> , °C	600	350	650	654	400	800	1100	450
Coolant T <sub>out</sub> , °C	900	700	860	1100	650	1100	1200	550
Power conversion cycle	CCGT <sup>2</sup>	CCGT <sup>2</sup>	CCGT <sup>2</sup>	CCGT <sup>2</sup>	CCGT <sup>2</sup>	CCGT <sup>2</sup>	CCGT <sup>2</sup>	CCGT <sup>2</sup>
η <sub>th</sub> , %	51	44.8	>47	58.5	46	57.5	58	45

<sup>1</sup>For ARIES-AT the surface heat flux used for temperature and stress calculation was 0.7 MW/m<sup>2</sup>.

<sup>2</sup>Closed Cycle Gas Turbine.

### 5.1 TAURO Blanket Concept

The TAURO design [Pere95] is a self – cooled Pb – 17Li blanket, which is formed by fiber reinforced silicon carbide structural material as depicted in Fig. 5.1. This combination of materials avoids the development of electrically insulating wall coatings, which are normally necessary for the metallic structure and conducting fluid self – cooled design. The TAURO FW – Blanket configuration, which was developed at the French Atomic Energy Center (CEA), is shown in Fig. 5.2 and key parameters are presented in Table I.

The TAURO blanket was designed according to the specifications for a 3000 MW fusion power reactor with ~ 10 m height, which has 16 toroidal field coils, 48 outboard and 32

## 5. Investigation of Fusion Relevant Materials

inboard segments as shown in Fig. 5.2. Each outboard segment is poloidally divided into several straight modules, attached on one common thick back - plate, but cooled independently. The feeding pipes are located behind the module.

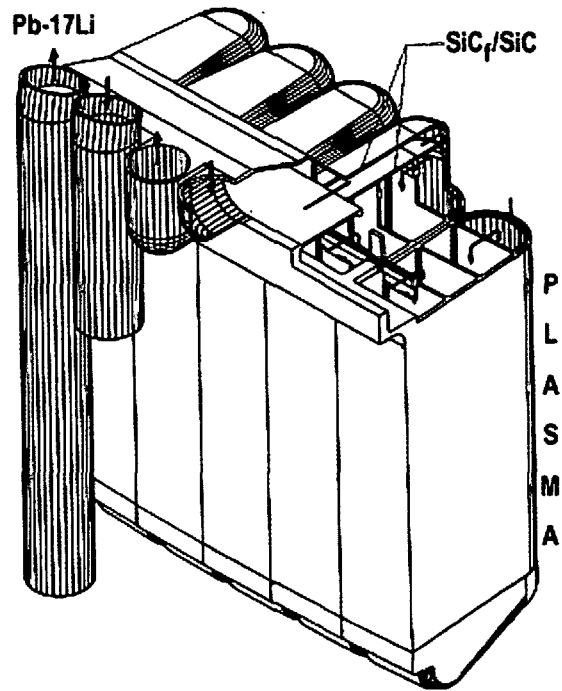


**Fig. 5.1:** Layout of the TAURO blanket module, self cooled Pb - 17Li in low activation structural material, SiC/SiC<sub>f</sub>.

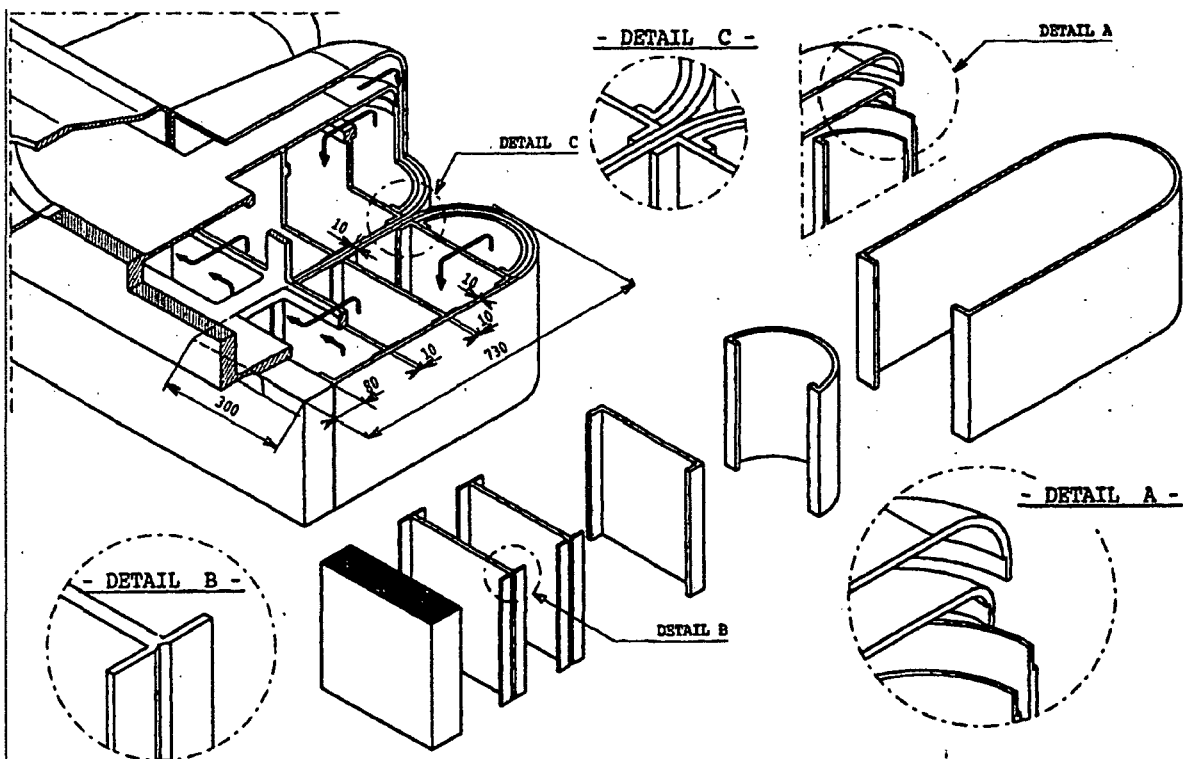
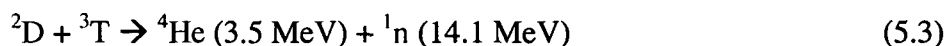
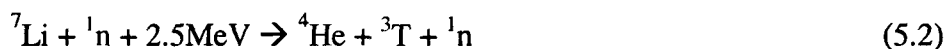


**Fig. 5.2:** Outboard module of the TAURO blanket design.

## 5. Investigation of Fusion Relevant Materials

---

The coolant enters the inlet collector through a single tube and is divided into five sub – flows, one for each sub – module. The Pb – 17Li flows at first poloidally downward in a thin channel located just behind the FW, makes a U – turn at the bottom into a second channel and flows up, and then down into the outlet collector [Pere96, Gian98]. A SiC/SiCf box essentially structures the TAURO blanket, and the cooling process is fulfilled indirectly with the FW material. As mentioned Pb – 17Li is the coolant in this module, which is also tritium breeder and neutron multiplier material, because Li is used simultaneously for tritium production as given in Eq. (5.1) and (5.2). Nuclei of two isotopes of hydrogen, deuterium (D), and tritium (T) react to produce a helium (He) nucleus and a neutron (n). 17.6 MeV energy is liberated by the reaction Eq. (5.3).



The energy released by the fusion reactions is transferred to the first wall and breeding blanket by 14 MeV fast neutrons and  $\alpha$  – particles. A small part (~ 10 %) of the energy of the 14 MeV neutrons will be deposited in the first wall, the remaining energy being transferred mostly to the blanket [Vict01]. Positive charge alpha particle, which deposits energy, interacts strongly with surroundings and heats the plasma. Further increases in plasma temperature can increase the fraction of the collisions with energies greater than 0.11 MeV, and increase the collisions result in the fusion reactions. If the rate of plasma heating by alpha particles equals the rate of the energy leaking from the plasma, the ignition can be achieved and self – sustaining fusion burn occurs.

### 5.1.1 Structural Materials for TAURO Blanket Module

The structural material and the coolant temperature determine the activation, the after – heat, and the waste disposal rating of the materials. Therefore, it plays an important role in the determination of the safety and environmental characteristics in the fusion technology. In order to satisfy the design requirements, low activation materials are necessary. The structural materials should maintain their performance such as activity, fast decay heat under irradiation, and they should be compatible with surrounding materials [Vict01]. These conditions strongly limit the number of available materials that are a few families of alloys, such as titanium alloys, vanadium alloys and fiber reinforced silicon carbide ceramic composites (generically known as low activation materials).

Titanium alloys have a number of properties that make them attractive as structural material candidates for fusion reactors. Some of the favorable properties of titanium alloys are high electrical resistivity, heat capacity, low thermal expansion coefficient, low long – term residual radioactivity, a high corrosion resistance, good compatibility with coolants such as Li, He and water, good weld ability, and commercial availability with established mine and mill capacity [Davi96]. Because of the numerous current applications of titanium alloys in the aerospace and medical domains, there exists an extended properties database and industrial experience on these materials.



Vanadium alloys are also considered [Zink98] because of their low thermal expansion coefficient (low elastic modulus), low thermal stresses, and a high heat flux capability. Their compatibility with pure Li makes them a good choice for a liquid Li coolant – breeder blanket concept. Few percent titanium additions are highly resistant to the irradiation – induced swelling. As a result of this property, it has a potential for long operating lifetime in a fusion first wall applications. Nevertheless, brittle fracture behavior occurs whenever the yield strength exceeds 700 MPa [Smit95]. In addition, the necessity of the electrically insulating walls for coolant channels is a critical issue for self – cooled Li metal systems.

SiC/SiC<sub>f</sub> ceramic composites have superiority among the other candidate materials because of their high performance. The most important characteristic of SiC/SiC<sub>f</sub> ceramic composite is the low activation material and good decay heat properties at short and intermediate decay times. It has high mechanical strength at high temperatures up to ~ 1000 °C [Vict01]. Their microstructure consists of SiC embedded in a SiC matrix through a fiber – matrix produced by using the chemical vapor infiltration (CVI) process. They have a good compatibility with Li and He, which makes them primary candidates for high temperature blanket modules.

### 5.1.1.1 Fiber reinforced Silicon Carbide (SiC/SiC<sub>f</sub>)

SiC/SiC<sub>f</sub> is a key component in the breeder reactor engineering developed by the CERACEP®. This composite has been employed in the studies of the first wall and structural material in fusion reactors such as ARIES in the USA, DREAM in Japan and TAURO in the European Union [Aiel00]. In ARIES, the both materials (first wall and structural material) are silicon carbide fiber composites. The combination of the silicon carbide fiber composites with liquid lithium in TAURO blanket model avoids the development of electrically insulating wall coatings, which is necessary for the metallic structure. Silicon carbide is not an electrical insulator (semiconductor), but its use as structural material can reduce the current flow in a self – cooled blanket to a tolerable level. In this way, there is no need for the additional coatings. From another aspects, SiC/SiC has a low neutron absorption cross section that means it is transparent to the neutrons, which causes additional shielding materials in the vacuum vessel material in the blanket design. Despite the possible increased shielding requirements, the use of SiC/SiC is economically due to the high thermal efficiency, which reduces cost of electricity by 15 % [Tayl01, Gian98, Gian02]. The high temperature properties of SiC/SiC<sub>f</sub> composites improve energy handling capabilities allowing the use of high temperature coolants, which have high potential in the energy conversion systems and yield high thermal efficiency.

The SiC/SiC<sub>f</sub> composite is considered as an attractive material for a breeding blanket due to the hardness, strength, chemical inertness, oxidation resistance at elevated temperatures, high thermal and low electrical conductivity, low coefficient of thermal expansion, and corrosion resistance. All heat deposited to the SiC/SiC<sub>f</sub> structure is transferred into the adjacent Pb – 17Li flow. The high content of oxygen in SiC/SiC<sub>f</sub> composite (Nicolan – 3) causes decomposition of the fiber at high temperature mainly. New advanced SiC/SiC<sub>f</sub> structural material like Nicolan – 4 has been developed reducing the oxygen content. Nicolan – 3 and 4 have different material properties caused by varying the oxygen enrichment within the composites at a constant atomic ratio of C/Si, as shown in Table II. [Hain00] was inspected the performance of Nicolan – 4 under irradiation, and compared with Nicolan – 3. SiC consist of fibers with a diameter of 14 μm, which are inserted in a SiC matrix with a carbon interface.

The fiber structure and netting of this ceramic composite is shown in Fig. 5.3. The present generation of SiC composites, with low oxygen, quasi – stoichiometric SiC fibers of enhanced crystalline perfection seem to have much improved properties after irradiation [Kohy01].

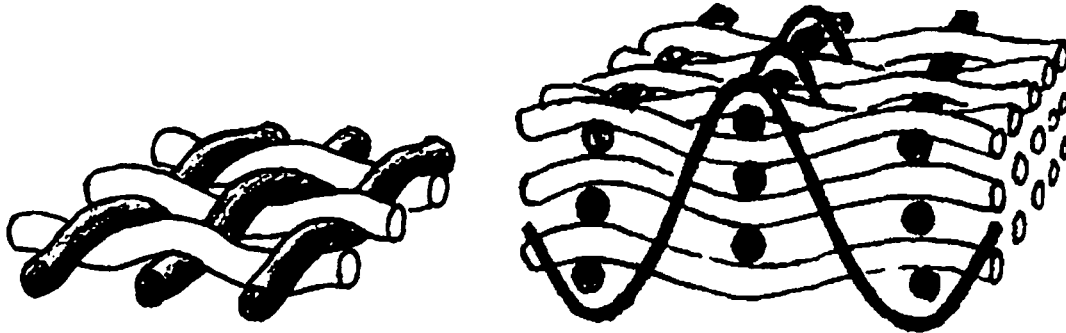


Fig. 5.3: Netting of the silicon carbide fiber composite.

Table II. The composition of the Nicalon – 3 and Nicalon – 4.

Type of SiC/SiC <sub>f</sub>	Percent	Si	C	O	C/Si Ratio
Nicalon – 4 (N4 – 1)	wt %	65.7	33.7	0.6	-
	at %	45.2	54.1	0.7	1.2
Nicalon – 3 (N3 – 1)	wt %	56.6	31.7	11.7	-
	at %	37.4	49	13.6	1.2

The thermal conductivity of silicon carbide composites is dependent on fiber type and netting, temperature and also the fabrication process (e.g. between 20-500 °C temperature 1.5 for Nicalon, ~ 4 for Hi – Nicalon and 18 W/m.K for S type Hi – Nicalon). The SiC/SiC<sub>f</sub> composites are obtained by infiltrating a SiC fiber with a SiC matrix. The available methods of fabricating silicon carbide are chemical vapor deposition (CVD) or chemical vapor infiltration (CVI). By the CVD method high purity and near – zero porosity materials can be produced. CVI is a variant on CVD process. CVD implies deposition onto a surface, whereas CVI implies deposition within a body. CVI, which produces 10% porosity, is a widely used method in the fabrication of fiber reinforced ceramic matrix composites [Ultr00]. The impurities and porosities generated during the fabrication of composites would cause degradation in the conductivity of N3 – 1 SiC/SiC compared to N4 – 1 SiC/SiC [Hain00, Zink98].

## 5.2 Investigations of SiC/SiC<sub>f</sub> composites by thermal Neutrons

### 5.2.1 Motivation

The maximum producible thickness of SiC/SiC<sub>f</sub> structural material considering the maximum allowable porosity of 10 % is 6 mm. Nevertheless, the required thickness for the TAURO blanket concept is between 10 – 15 mm [Hain00]. In spite of the CVI method, which produces low porosity materials, porosity problem emerges in the ceramic composites between the fiber

bundles as shown in Fig. 5.4. The porosity within the composites limits the material thickness in the production process, and also causes a reduction of the material thermal conductivity. For this reason, the investigation of the defects and porosities in the structural material is very important.

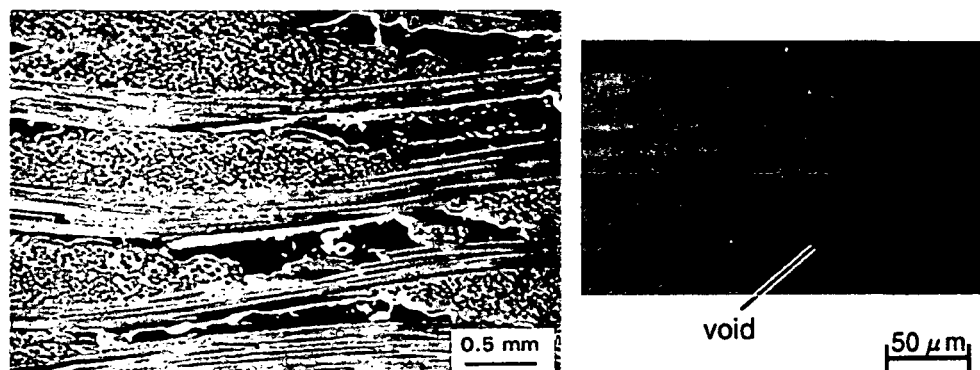


**Fig. 5.4:** In the fabrication process emerged porosity problem between the fiber bundles.

NR and NT inspections of SiC/SiC<sub>f</sub> composites have been carried out addressing to the following problems:

- Void swelling under high temperature and irradiation. Radiation induced swelling in SiC depends on the temperature. At high irradiation temperatures, void swelling occurs. With the help of the radiographic and tomographic analysis, the material structure of the unirradiated and irradiated composites could be visualized, and comparing the results from both conditions, the radiation induced structural change and defects within the ceramic composites could be determined.
- The CVI process produces a microstructure having about 10% porosity, which is permeable to gases. Neutron radiography and small angle neutron scattering experiments are the only way for the investigation of the porosity within the composite, visualization of the inner defects. The defects emerged in the fabrication causes also a reduction of thermal conductivity and low mechanical performance. The thermal conductivity of SiC/SiC<sub>f</sub> composites is strongly dependent on the processing conditions, type of fiber and fiber architecture [Snea92]. The fiber structure could be visualized by means of NR and NT.
- As mentioned before, there is a limit of thickness for producing SiC/SiC<sub>f</sub> ceramic composites. Some joint methods like assembling by sewing at textile stage, sticking and co – infiltration during manufacturing, brazing with evolved special system called BraSiC<sup>®</sup> and pre – ceramic polymer with filler powders have been developed. Joining the composites and to other metal pads is a complicated task. Especially in the joining process of the SiC/SiC<sub>f</sub> some limitations occur in the welding and diffusion bonding techniques [Pere95, Pere96, Gian98]. The quality of joining methods and distribution of the bonding material can be analyzed using NR and NT.

## 5.2.2 Thermal NR and NT Measurements

Different complementary radiographic methods have been performed to get more information based on the comparison of images for the inspection of SiC/SiC<sub>f</sub> composites [Bast02-2]. The neutron radiography represents the total neutron attenuation along beam paths through the sample. Thus, it gives general information about the sample, but not about the position and the size of the defects. It can be observed only with a three dimensional tomographic reconstruction. The NR images of a 3 mm thick CERASEP<sup>®</sup> N3 – 1 composite are shown in Fig. 5.5. Because of the low thermal neutron attenuation properties of Si and C, the radiography image of a 3 mm SiC/SiC<sub>f</sub> composite is extremely transparent, which causes difficulties in its visualization.

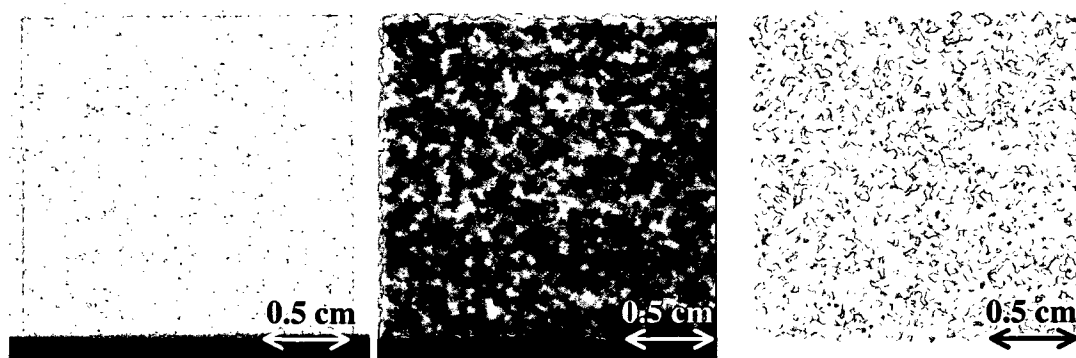


Fig. 5.5: Thermal NR images of a 3mm SiC/SiC<sub>f</sub> composite (left NR image taken at PSI, middle and right images taken at ATI, the left image with enhanced contrast).

In order to assess the joining quality, bonding of two SiC/SiC<sub>f</sub> composites each having 3 mm thickness and bonding of SiC/SiC<sub>f</sub> to a Cu metal pad were investigated where the inhomogeneity of the glue binder was obtained. An 8 mm thick SiC/SiC<sub>f</sub> N3 – 1 composite was bonded to a 2 mm Cu pad by sticking and co – infiltration method. Four different samples were used to visualize the bonding quality. Fig. 5.6 shows the thermal NR inspection of a Cu metal bonded SiC/SiC<sub>f</sub> composite.

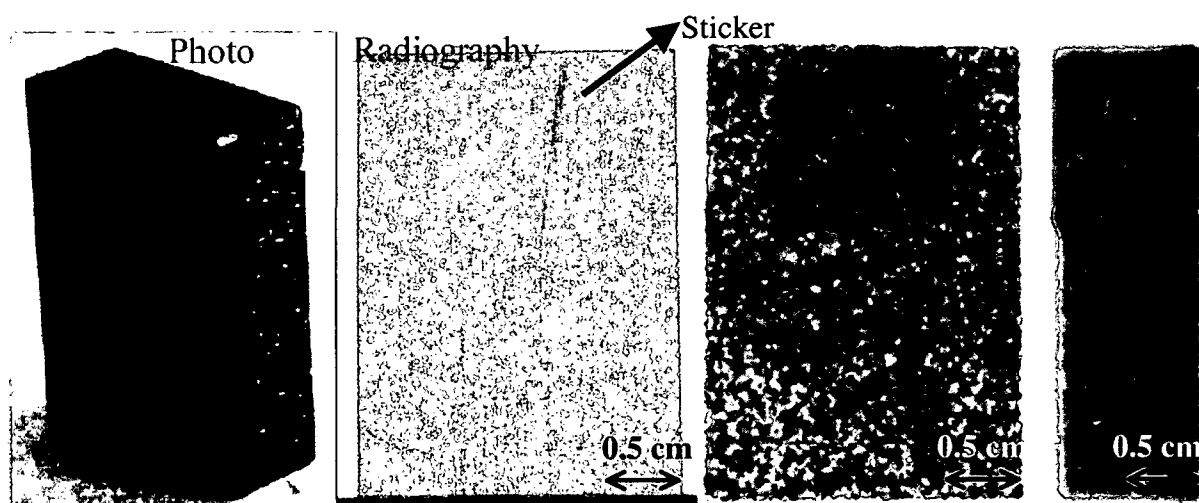
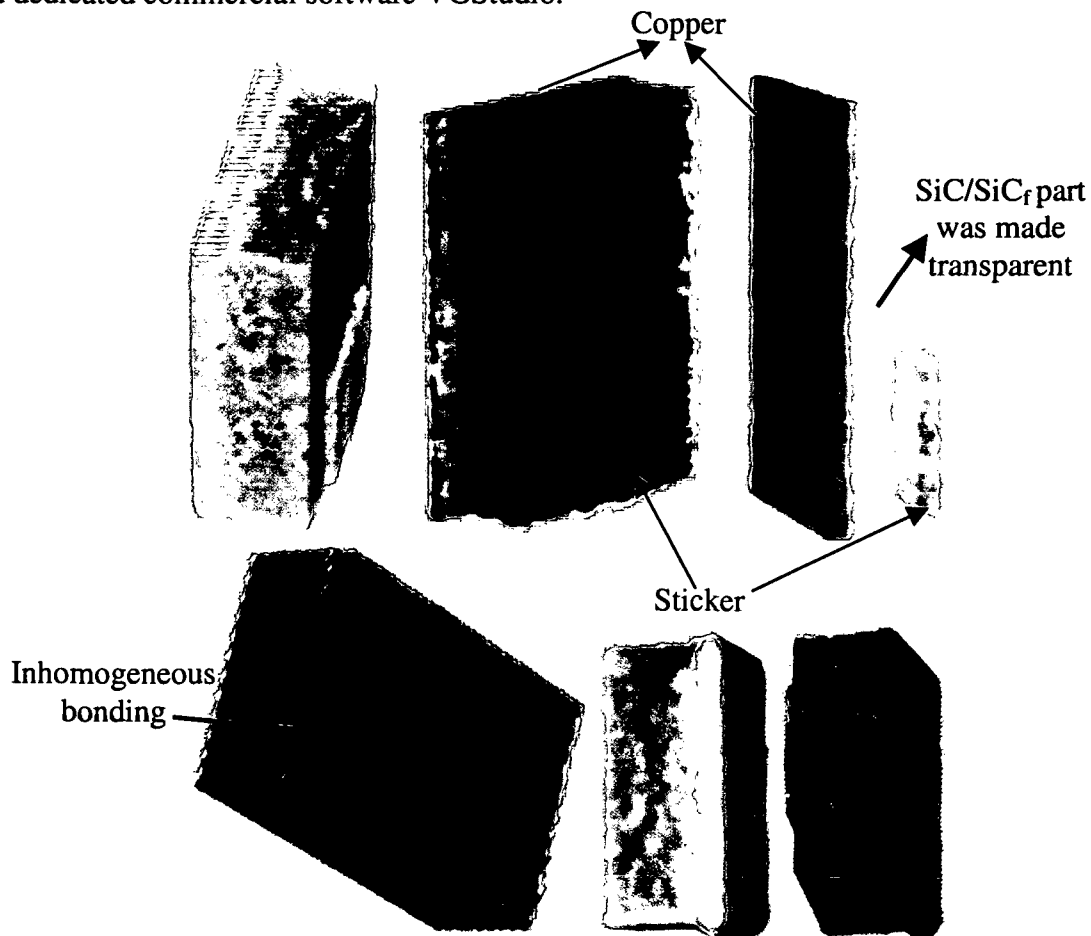


Fig. 5.6: Photo and thermal NR images from front and side of a SiC/SiC<sub>f</sub> fiber bonding with Cu metal pad taken at ATI and PSI.

## 5. Investigation of Fusion Relevant Materials

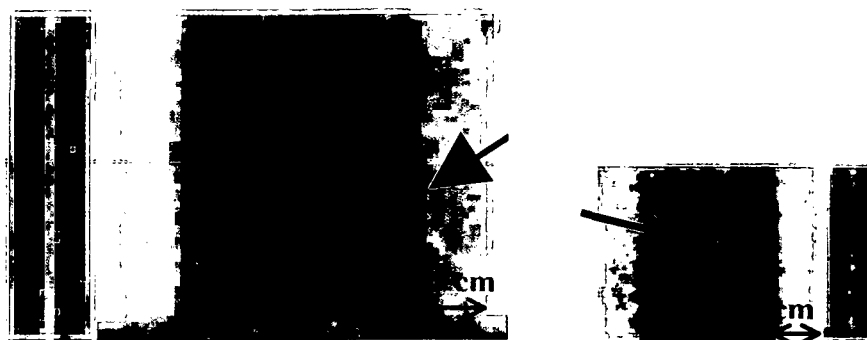
Fig. 5.6 demonstrates the material structure like vertical lines and indefinite distribution of bonding material between the 8 mm thick SiC/SiC<sub>f</sub> composite and 2 mm thick Cu pad. The neutron attenuation of a sticker, which was stuck to number the samples, could also be seen on NR images.

The inhomogeneity of the bonding material between the SiC<sub>f</sub> composite and the Cu metal can be detected in the radiography images but a precise visualization can be done with a NT investigation as shown in Fig. 5.7. For the Computed neutron tomography, 200 projections for 20 seconds exposure time were taken by a CCD camera – based detector system for the most interesting parts at the ATI – Wien. For this measurement, 58 mm F 1.2 camera lens was used. In order to achieve 3D images of the sample, the reconstructed images are assembled in a 3D array that can be treated by IDL; and then demonstrated 3 dimensionally with powerful and dedicated commercial software VGStudio.



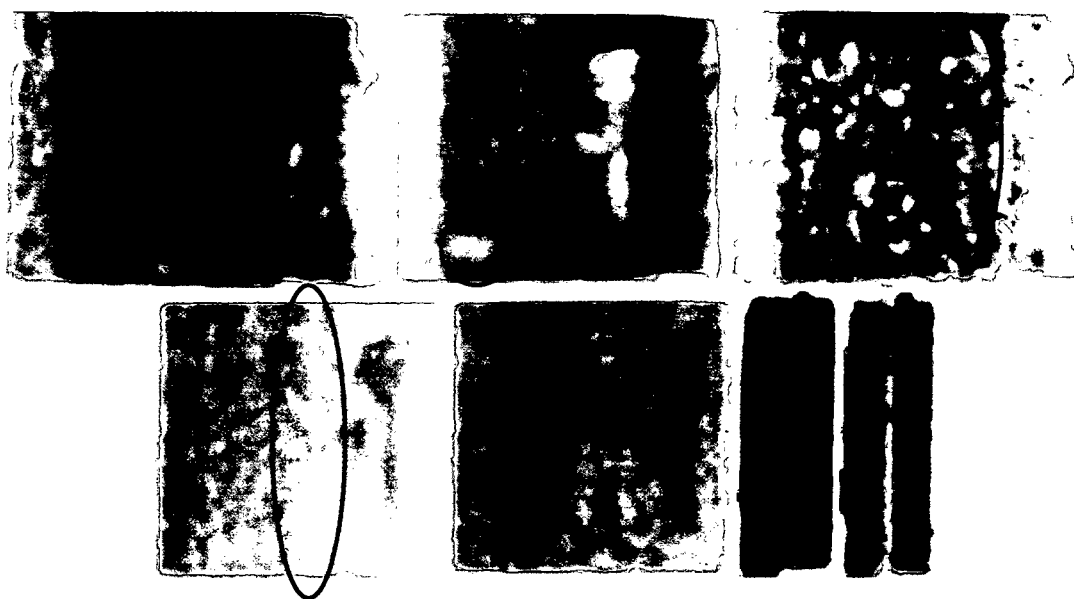
**Fig. 5.7.** The tomographic investigation of the Cu bonding of the SiC/SiC<sub>f</sub> composite with thermal neutrons at NR II – ATI (top right image demonstrates the transparency of the SiC/SiC<sub>f</sub> composite and bottom left image shows joint slice between Cu and SiC/SiC<sub>f</sub> composite).

The BraSiC bonding of two SiC/SiC<sub>f</sub> composites each having 3 mm thickness was inspected with the aid of thermal NR. NR images of the bonding of two SiC/SiC<sub>f</sub> composites cannot give more information. Enhancing the image contrast by the image histogram some inhomogeneities could be visualized as shown in Fig. 5.8.



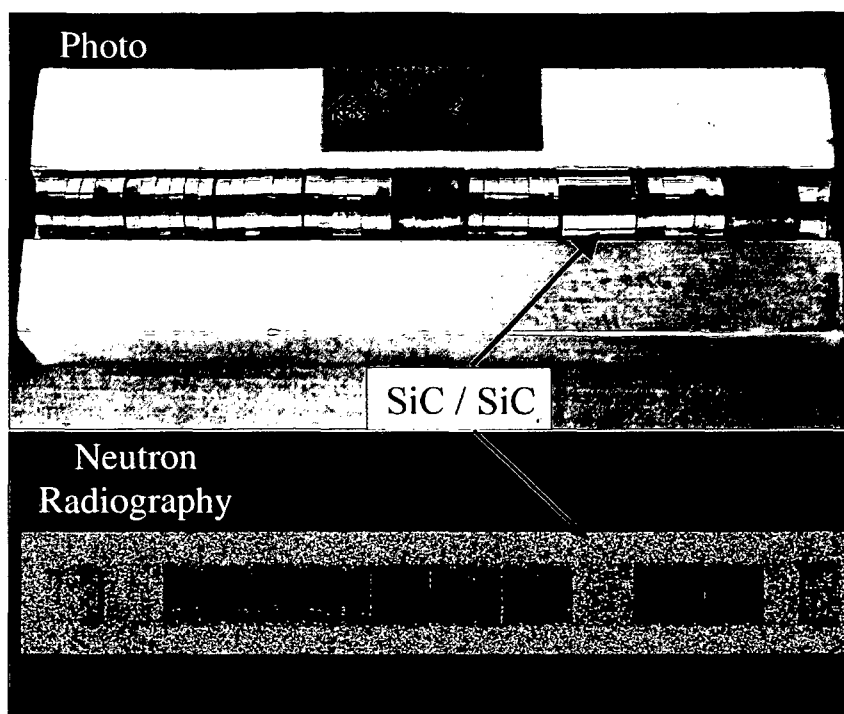
**Fig. 5.8:** The NR of the BraSiC joint between two SiC/SiC<sub>f</sub> composites (right images from the side and front views taken using the 180 mm F 2.8 camera lens, and left images from the front and side views taken using the 58 mm F 1.2 camera lens).

Fig. 5.9 shows the three – dimensional reconstruction of 200 NT projections, which was also performed at NR II working station at ATI – Wien using 58 mm F 1.2 camera lens for 20 seconds exposure time (58 mm refers its local length and 1.2 refers F – number). 3D reconstructed images show more inhomogeneous parts than NR images from different view angles.



**Fig. 5.9:** The reconstructed tomography images were demonstrated from different views with different contrast changing the opacity of the of SiC/SiC<sub>f</sub> composite BraSiC joint (marked areas show inhomogeneous distribution).

Previously, one of the 3 mm thick N3 – 1 composites was placed into the SINQ target (Swiss Spallation Source) shown in Fig. 5.10 and irradiated there for one year under high neutron and proton fluence. This sample received proton and fast ( $E > 0.1 \text{ MeV}$ ) neutron fluencies of about  $2.7 \times 10^{25} \text{ p.m}^{-2}$  and  $5.9 \times 10^{25} \text{ n.m}^{-2}$ . In order to investigate radiation induced structural changes, the SiC/SiC<sub>f</sub> ceramic composite will be measured with NR and NT methods, when the radiation protection policy permits.



**Fig. 5.10:** Photo and NR image of the SiC/SiC<sub>f</sub> composite, which was inserted into the SINQ target [Koer00].

### 5.3 Investigations of SiC/SiC<sub>f</sub> composites with cold Neutrons

#### 5.3.1 Experimental Set up of Energy Selective Cold Neutron Radiography Facility – PGA at PSI

Energy selective neutron radiography (ESNR) was located at the PGA neutron guide as depicted in Fig. 5.11. PGA facility exploits the high neutron flux of  $10^8 \text{ n.cm}^{-2}.\text{s}^{-1}$  at the sample position. Ni coated neutron guide that defines beam divergence delivers the neutrons. Beam divergence is very important to know the characteristic of NR facility depending on the  $L/D$  ratio. Neutron guide causes considerable beam divergence dependent on the neutron energy and it is very effective factor on the quality of the radiography image [Schi01-1]. The relation between the divergence angle  $\alpha$  and the critical reflection angle of the used neutron guide  $\theta_c$  is  $\alpha = 2\theta_c$  and the wavelength dependence is  $\theta_c = 0.1^\circ / \text{\AA}$  for a natural Ni coated neutron guide [Baec02-1, Kard03-1]. The mean wavelength of neutrons at PGA is about 5.5  $\text{\AA}$ .

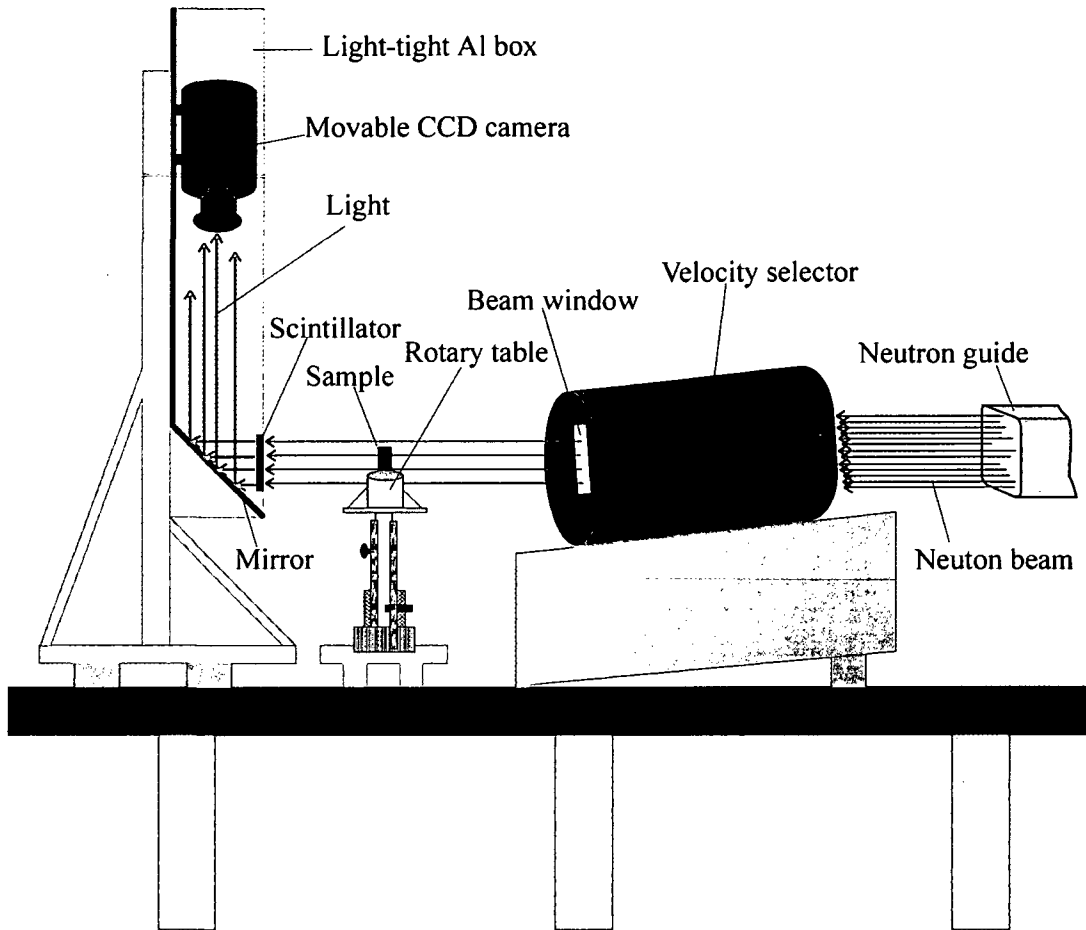


Fig. 5.11: Drawing of the ESNR set up at PGA – PSI.

### 5.3.1.1 Detection System

The beam size at the exit of the guide is 20 mm wide and 50 mm high, but the radiography images were limited generally from the scintillator size of 3 x 3 cm. In this way, only small objects can be investigated. The detection system is composed of a neutron conversion screen, a mirror, digital CCD camera, and an optical lens. The conversion screen consists of a dispersion of ZnS(Ag) – a scintillation material – and  $^6\text{LiF}$  neutron converter in an acrylic binder. The lithium atoms in the scintillator material absorb neutrons penetrating the screen. This results in the ejection of alphas and tritons that interact with the scintillation part to create light events that can be detected by a CCD imaging system. Using a 45° silver free mirror reflected light is imaged an optical lens coupled to a Peltier – cooled CCD camera (Sensicam 1280 x 1024 pixels) with 12 bits image digitization. The whole experimental procedure is performed automatically on a standard PC. A program based on the LabView software controls the camera settings, image displaying and storing, and the velocity selector. The sample is placed on a motorized rotation table and additional step motors allow positioning the sample in the x, y, z directions. The whole set up is placed on rails and can be moved along the beam axis as presented in Fig. 5.11.



### 5.3.1.2 Velocity Selector

The neutron velocity selector is a high – speed rotor and it is widely used in neutron spectroscopy for generating monochromatic neutron beams. A crystal monochromator is set to reflect a chosen wavelength,  $\lambda$ , in the direction  $2\theta_m$  from a set of lattice planes (hkl) according to Bragg law. However, it does not reflect neutrons of only this wavelength,  $\lambda$ , and also its higher harmonics  $\lambda/2, \lambda/3 \dots \lambda/n$  giving rise to a 2<sup>nd</sup>, 3<sup>rd</sup>, ...,  $n^{\text{th}}$  – order contamination in the monochromatized beam. A basic element of neutron velocity selector is the rotor. The neutron absorbing blades inserted in the rotor are made of the twisted carbon fiber in epoxy with 35g  $^{10}\text{B}$  per  $\text{m}^2$  of blade surface at PGA – PSI facility. It has been designed and constructed by Dornier Satellitensysteme GmbH. Blades in the rotor are only transparent for neutrons, which are able to pass the rotor in a specific time interval defined by the selector rotation speed, tilt angle of the velocity selector and selector acceptance. Thus, neutron wavelength can be determined due to the rotation speed of the selector rotor. The wavelength distribution of neutrons is also dependent on the tilt angle of the selector,  $\gamma$ , which is the angle between the rotation axis and the neutron beam. The main parameters of the selector at PGA – PSI are given in Table III, see [Baec02-1, Kard03-1, Frie89] for more information about the velocity selector and its principle.

**Table III:** Velocity selector specifications.

<b>Overall rotor diameter, [mm]</b>	330
<b>Overall rotor length, [mm]</b>	330
<b>Total weight, [kg]</b>	~ 50
<b>Rotor length 'L', [mm]</b>	250
<b>Diameter of the rotor 'D', [mm]</b>	290
<b>Number of blades</b>	72
<b>Speed range</b>	3000 – 28300
<b>Speed constancy, [%]</b>	0.2
<b>Blade thickness, [mm]</b>	0.4
<b>Blade material</b>	Carbon fiber in epoxy with 35g $^{10}\text{B}$ per $\text{m}^2$ of blade surface
<b>Selector window, [mm]</b>	150 x 65
<b>Twist angle of blades, [°]</b>	48.3

The selector transmission  $T_m(\lambda)$  can be derived using Eq. (5.4). In this equation  $L$  is the effective rotor length,  $T_m^0$  is the peak transmission for neutrons parallel to the rotor axis,  $\alpha$  is the beam divergence and  $\beta$  is the selector acceptance or the divergence defined between the adjacent lamellae of the selector turbine.

$$T_m = T(v_0) = \frac{T_m^0 \beta}{\sqrt{\alpha^2 + \beta^2}} \quad (5.4)$$

The collimation ratio with velocity selector is much better than the same measuring position without velocity selector [Schi01-2]. The influence of the velocity selector on the neutron output beam acts as an additional collimator, which improves the  $L/D$  ratio of the radiography setup. This implies that the beam divergence can be changed in some interval limited by the maximal acceptance of the selector blades in case of the utilization of a neutron guide together with velocity selector. The maximum divergence angle  $\alpha_{\max}$  defines the  $L/D$  ratio as given in Eq. (5.5). This selector can be used for radiography purposes to define the desired beam divergence. Consequently, an improvement in the NR image quality can be achieved at harder neutron spectra.

$$L/D = 1/\tan(\alpha_{\max}) \quad (5.5)$$

The neutron spectra obtained with the velocity selector for different rotations per minute (rpm) measured with a standard Time – of – Flight technique (chopper in a combination with a  $^3\text{He}$  detector) is given in Fig. 5.12, in which the circles shows the spectrum without velocity selector [Kard03-1].

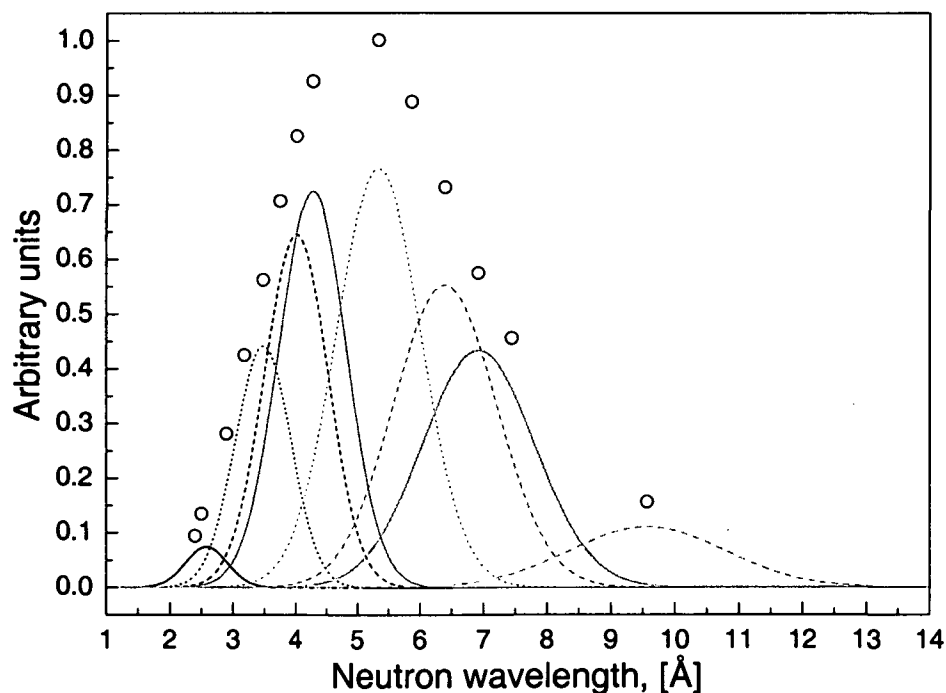


**Fig. 5.12:** Simulated spectra at different angular speeds of the velocity selector at PGA – PSI, the spectral neutron distribution at the PGA guide measured without the velocity selector is marked with circles [Kard03-1].

One vacuum and one cooling systems supported the required conditions for the selector exploitation. The selector was controlled outside the PGA by its control system as it is shown in Fig. 5.13. The rotor temperature was kept in the temperature interval between 15 – 25 °C and the vacuum was under  $10^{-3}$  mbar. More details about the experimental setup can be found in [Baec02-1, Kard03-1].

## 5. Investigation of Fusion Relevant Materials

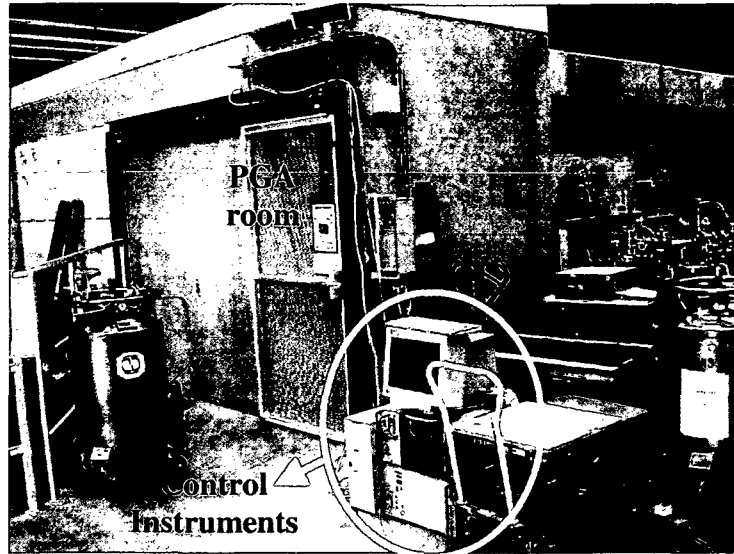


**Fig. 5.13:** The control blocks of the mechanical velocity selector were placed at the PGA bunker.

A special selector holder – table was constructed in order to allow tilting of the selector around its horizontal axis perpendicular to the rotor (Fig. 5.14).

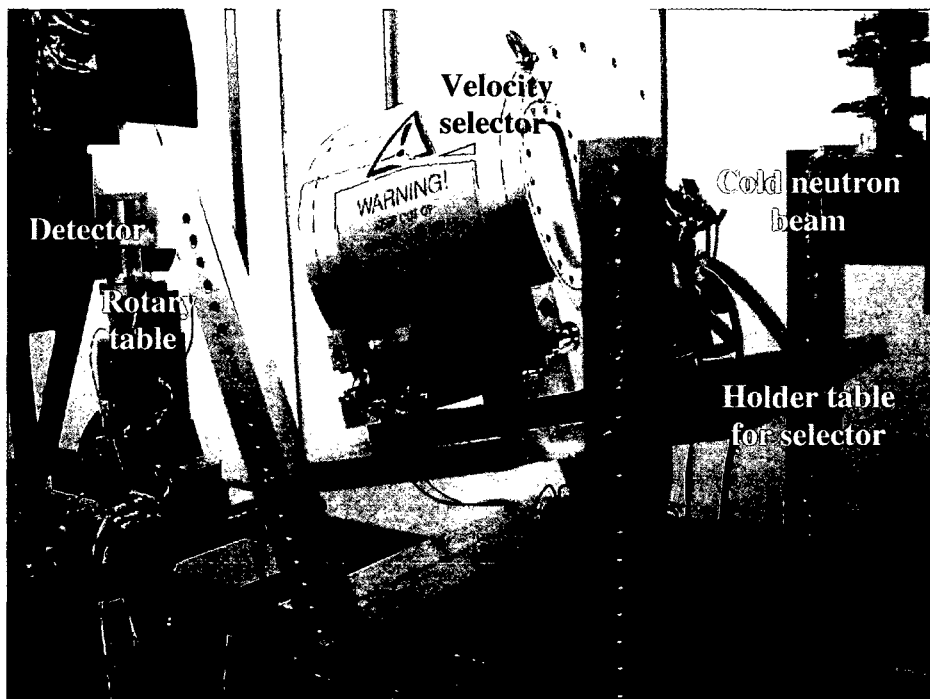


**Fig. 5.14:** A side view from the mechanical velocity selector on the table at PGA – PSI facility.

At PGA – PSI facility, solid materials can be inspected at discrete neutron energy using mechanical velocity selector as a monochromator. The neutron cross sections of the solid materials change abruptly at the Bragg cutoff energies and the samples can be radiographed below and over the Bragg cutoffs. Taking into account the energy spectrum of PGA neutron beam line and the characteristic parameters of the velocity selector, the tilting angle of the

## 5. Investigation of Fusion Relevant Materials

selector was adjusted as  $12.74^\circ$ , which allows a minimum neutron wavelength of  $2.56 \text{ \AA}$  at maximum rotation speed of 27880 rpm. Therefore, the radiography experiments were performed in the wavelength interval from  $2.56$  to  $10.5 \text{ \AA}$ . The rotation of the selector rotor can be adjusted due to desired neutron wavelength, and sufficient exposure time for a radiography image depends also on the rotation speed and desired neutron wavelength because of the decreasing neutron flux owing to the neutron absorption of the rotor blades as given in Table IV. Therefore, the exposure time for a radiography image depends also the rotation speed. Actually, the spatial image resolution becomes worst at longer neutron wavelength due to the energy dependent divergence produced by the neutron guide [Baec02-1].

**Table IV.** The adjustable neutron wavelength versus corresponding rotation speed of the velocity selector for the chosen tilting angle of  $12.74^\circ$ .

Speed, (rotation per minute - rpm)	$\lambda$ ( $\text{\AA}$ )	Exposure time (s)
27880	2.56	50
19398	3.0	35
14414	3.5	21
11468	4.0	14
9700	4.45	11
7500	5.29	10
7109	5.5	10
6309	6.0	11
5672	6.5	12
5151	7.0	15
4718	7.5	17
4400	7.93	20
3530	9.5	38
3321	10.0	45
3136	10.5	50

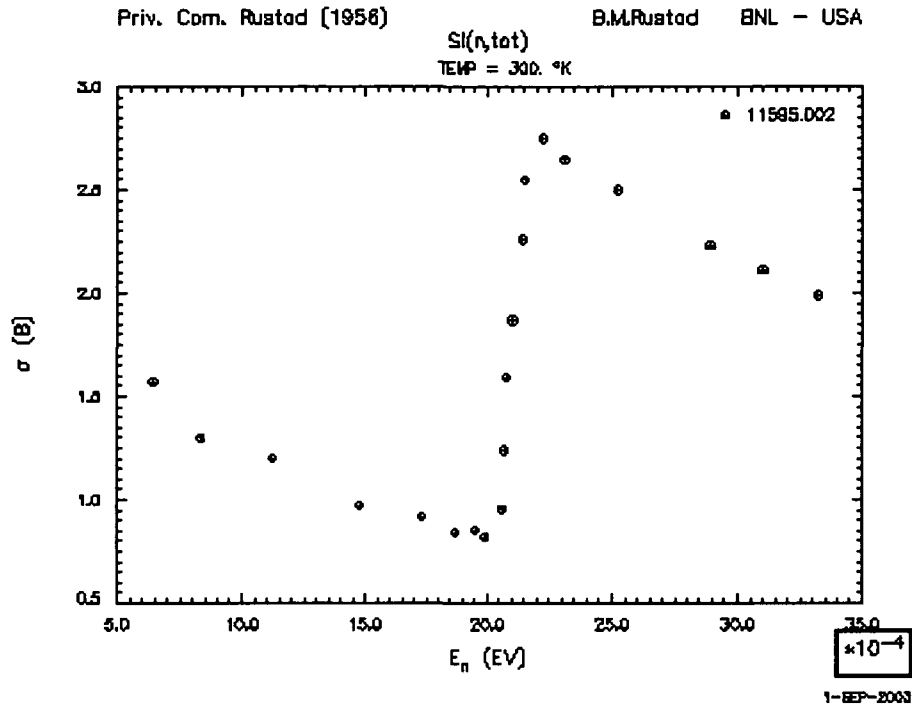
### 5.3.2 ESNR Measurements

The Bragg cutoff energies for some selected materials are given in Table V. Among these Bragg cutoff energies, Si, C and Cu energies were used in our measurements ( $2 \text{ meV}$  or  $6.4 \text{ \AA}$  for Si and C and  $5 \text{ meV}$  or  $4 \text{ \AA}$  for Cu element). The contrast of the fiber structure of SiC/SiC<sub>f</sub> composites could be visualized utilizing abrupt changes of the cross sections below and above the Bragg - cutoff energies for Si, C and Cu elements. The energy dependence of the cross sections for Si, C and Cu is given in Fig. 5.15a, b and c [IAEA].

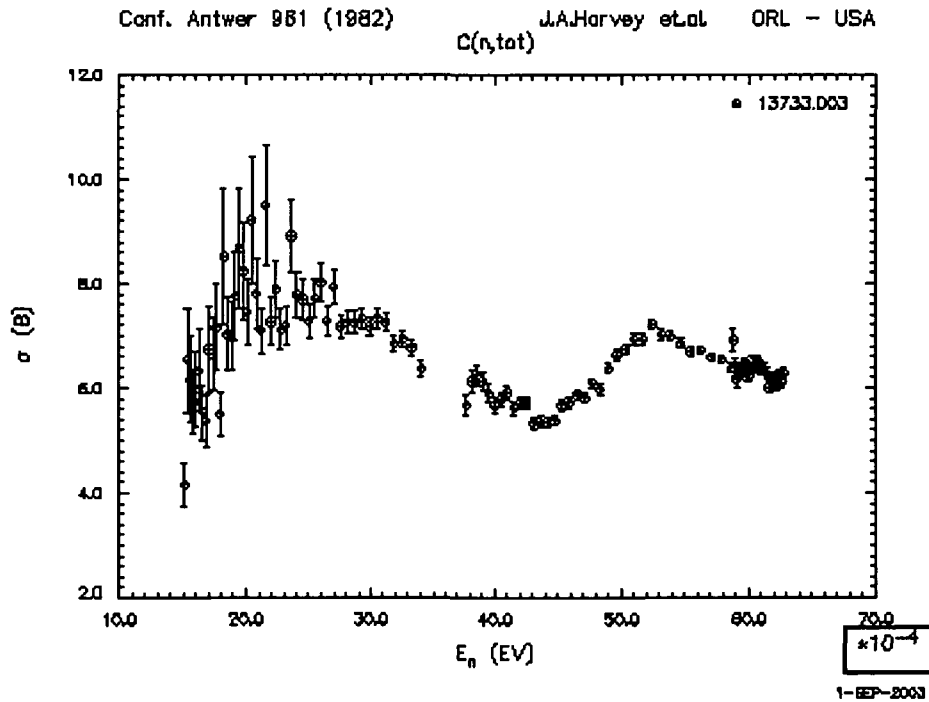
## 5. Investigation of Fusion Relevant Materials

**Table V:** Bragg cutoff energies of some selected materials [McDo99].

Material	Si	C	Cu	Al	Be	Mg	Ni	Pb	Fe	Bi	Zr
Energy, [meV]	2	2	5	4	6	2.6-2.9	5	3	5	2	2.5-3



a)



b)

## 5. Investigation of Fusion Relevant Materials

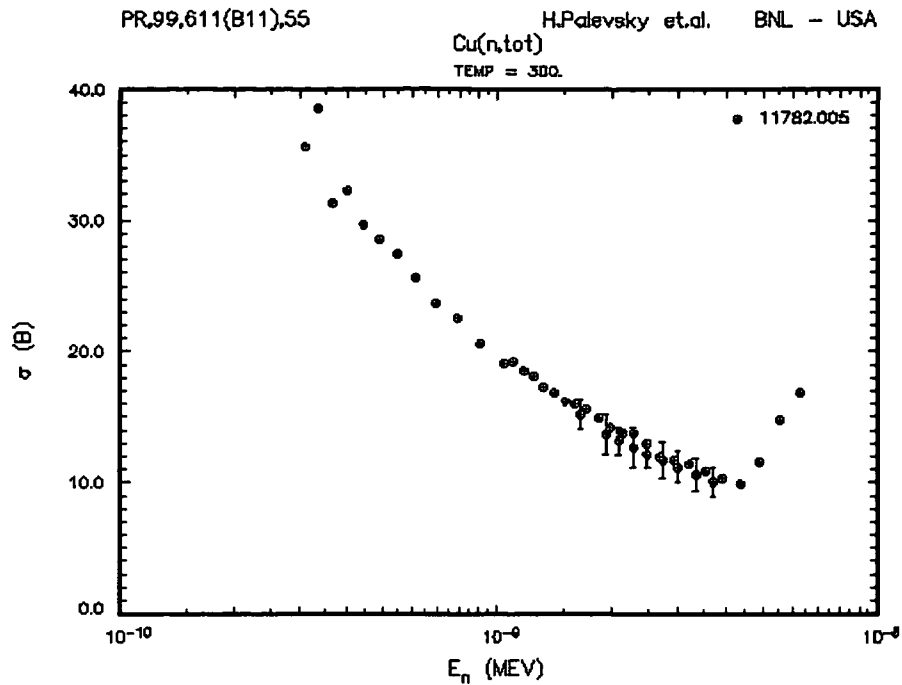


**Fig. 5.15:** The neutron energy dependency of the total cross sections in the low neutron energy range for a) Si, b) C and c) Cu materials [IAEA].

The spatial resolution measured with using edge of a thin Gd foil depends on the neutron wavelength as presented in Fig. 5.16.

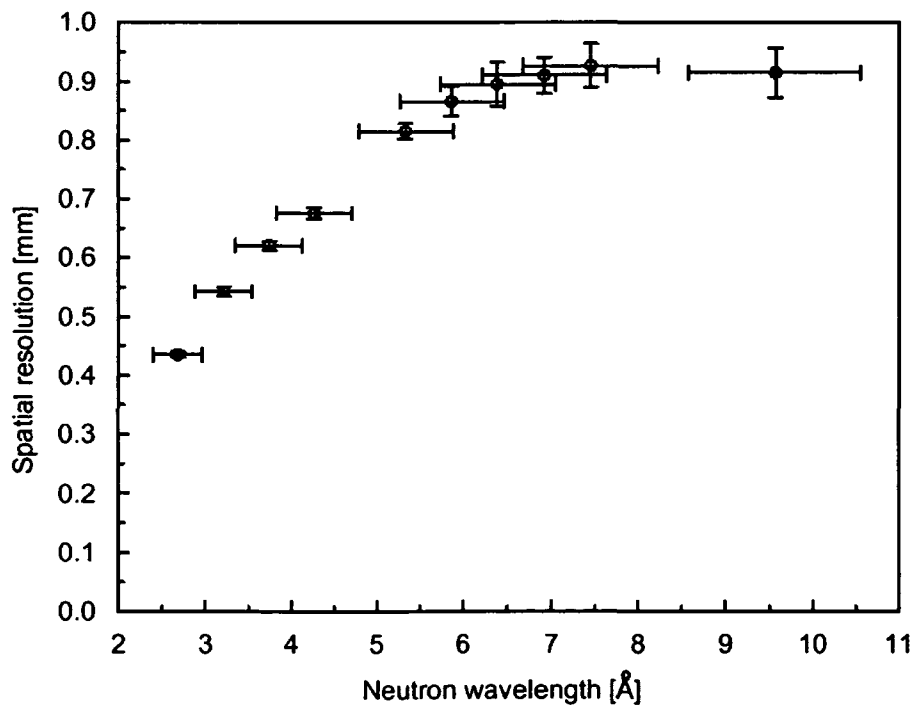


**Fig. 5.16:** The spatial resolution of the ESNR images measured with a 5 cm distance from the scintillator plate [Baec02-1].

## 5. Investigation of Fusion Relevant Materials

The ESNR inspections of the SiC/SiC<sub>f</sub> composites and its bonding yielded more information about the inner structure in comparison to thermal NR. The structure visibility was changed depending on the Bragg cutoffs of Si and C materials. Fig. 5.17 shows the cold neutron radiography images of a 3 mm thick N3 – 1 composite at different neutron wavelengths, in which the fiber structure of silicon carbide ceramic composite could be seen clearly.

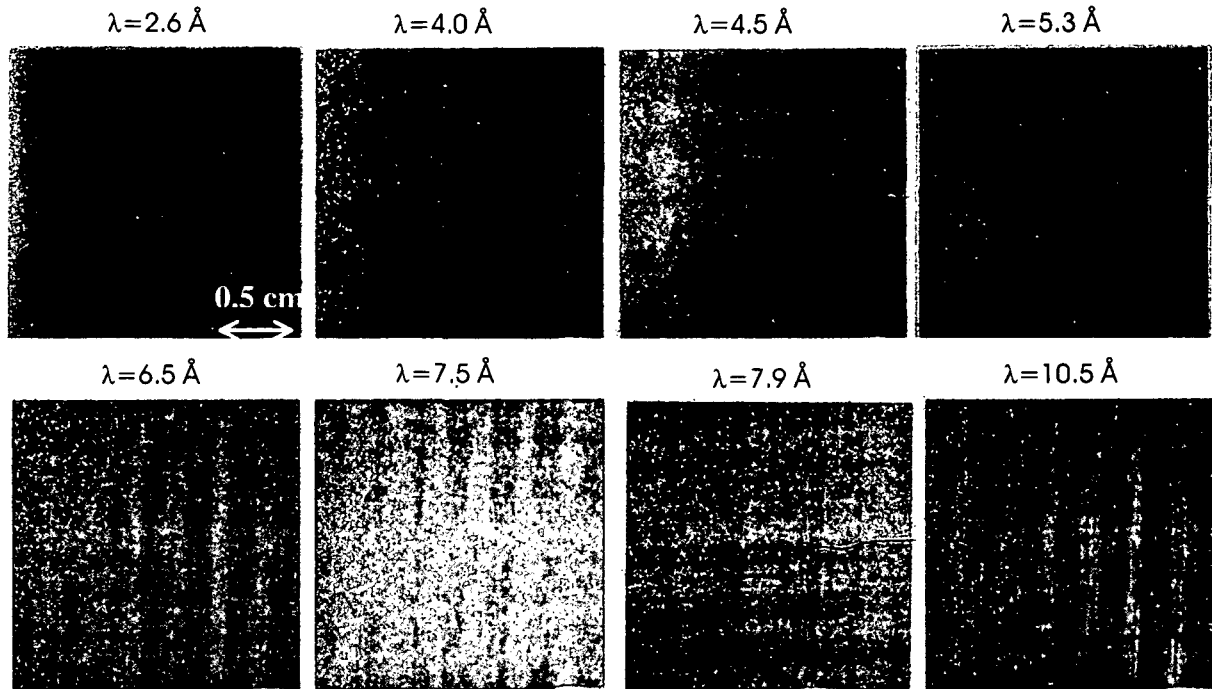


**Fig. 5.17:** ESNR images of the 3 mm thick N3 – 1 SiC/SiC<sub>f</sub> composite taken at discrete neutron wavelengths. The visibility of fiber bundles in the composite could be visualized better at lower neutron energies.

The neutron wavelength for the tomographic inspection was chosen according to the spatial resolution of the radiography images at different neutron energies. In spite of the higher spatial image resolution at 10.5 Å neutron wavelength, 7 Å was chosen owing to short exposure time per projection. Thus, the tomography experiment of 3 mm N3 – 1 ceramic composite was performed at 7 Å where the radiography contrast was still not very bad. The 3D reconstructed images show not only the porosity and defects in the specimen but also the fiber structure as shown in Fig. 5.18.

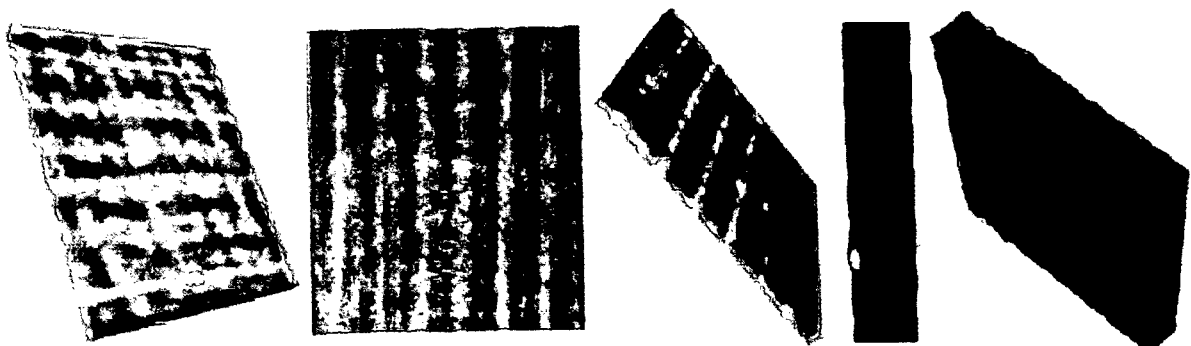
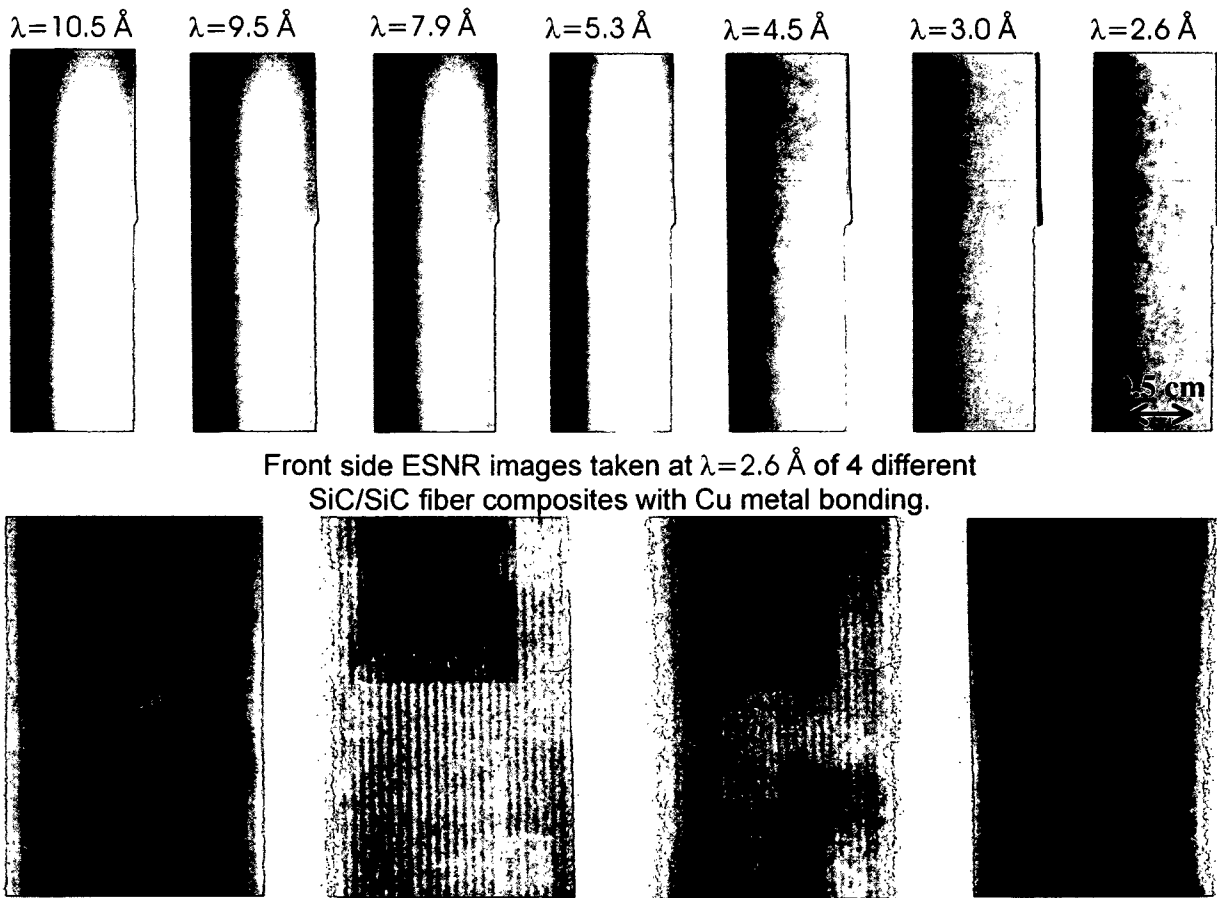


**Fig. 5.18:** The 3D reconstructed NT images of 3 mm thick N3 – 1 composite by ESNR at 7 Å neutron wavelength.

## 5. Investigation of Fusion Relevant Materials

Four different SiC/SiC<sub>f</sub> – Cu samples with the same composition and thicknesses were investigated with ESNR in order to visualize the glue material distribution at joints. The cold neutron ESNR investigation achieved an enhancement in the radiography contrast as seen in Fig. 5.19. The radiographic inspections were done from side views to see the contrast difference between the SiC/SiC<sub>f</sub> and Cu, which gives also information about the spatial resolution. The front view NR images were performed at 2.6 Å neutron wavelengths considering the spatial image resolution of the side view images at different energies as shown in Fig. 5.19. This wavelength will be used for the tomographic investigations of these Cu bonded composites.



Front side ESNR images taken at  $\lambda=2.6 \text{ \AA}$  of 4 different SiC/SiC fiber composites with Cu metal bonding.

**Fig. 5.19:** Radiography images of the four different SiC/SiC<sub>f</sub> composites with Cu metal joints investigated by ESNR at different neutron energies (upper images taken from the sides show the change of the spatial resolution as a function of the neutron wavelength; lower images taken from the front taken at  $\lambda = 2.6 \text{ \AA}$  where the best resolution could be get).

### 5.4 Investigation of SiC/SiC<sub>f</sub> composites with X – Ray Radiography

The principle of X – ray radiography is similar to NR, and is complimentary in the nature of information supplied. Neutrons have high penetration ability contrary to X – rays, however thin samples having small atomic numbers can be investigated with X – ray radiography,



## 5. Investigation of Fusion Relevant Materials

which inspects with better spatial resolution (chapter 2). Elements having very small atomic numbers like H, He, B, Li cannot be seen with X – rays. As shown in Fig. 5.20, the X – ray radiography images demonstrate higher contrast and better resolution than thermal NR for thin SiC/SiC<sub>f</sub> composites but not for 2 mm thick Cu bonded with SiC/SiC<sub>f</sub> sample.

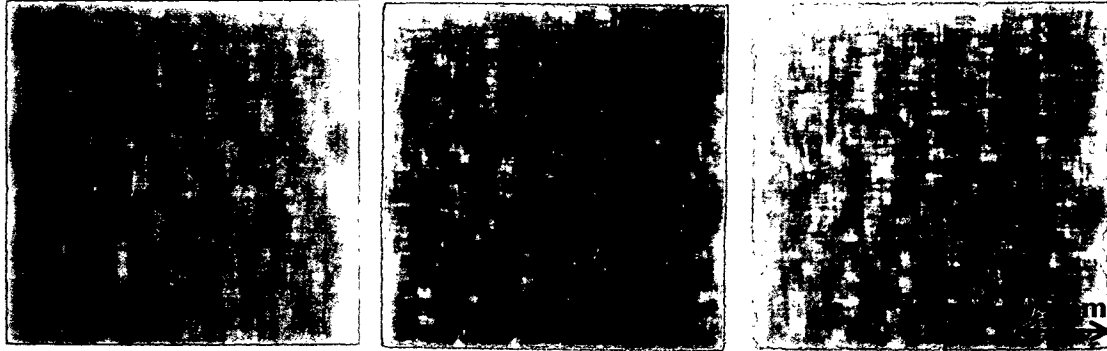


**Fig. 5.20:** X – ray radiography images of 3 mm thick N3 – 1 composite at ATI – Wien (right image taken at 30 kV, 4 mA and for 12 seconds; middle image: at 30 kV, 8 mA and 5 seconds, left image: 30 kV, 8 mA and 12 seconds).

Cu bonding and BraSiC joint of SiC/SiC<sub>f</sub> composites have also been investigated with X – ray imaging as shown in Fig. 5.21. X – ray radiography of Cu bonded SiC/SiC<sub>f</sub> composite did not give any structural information because of the only 2 mm thick Cu metal pad. Cu is a strong absorber material for X – rays because of its high atomic number. The X – ray radiography images of the BraSiC joint between two SiC/SiC<sub>f</sub> composites having each 3 mm thickness gave some complementary information in addition to the thermal NR as presented in Fig. 5.21 (right image).

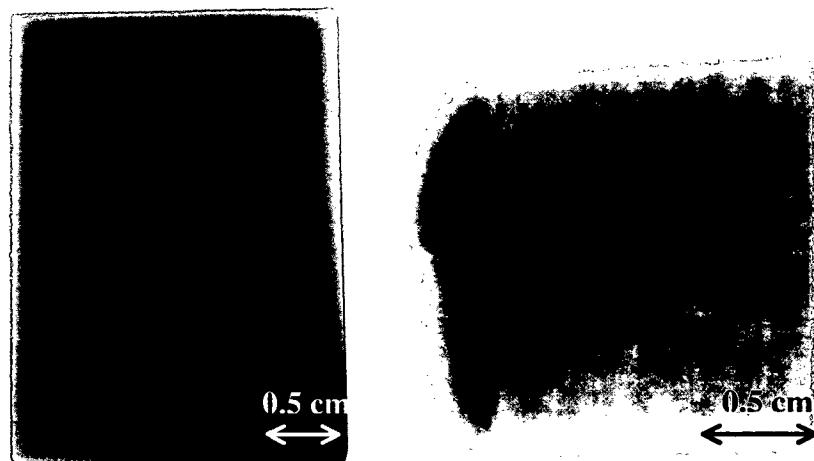


**Fig. 5.21:** X – ray radiography images of silicon carbide composites with Cu metal bonding (left) and with BraSiC joint (right). Cu bonding composite was inspected at 45 kV, 8 mA and for 20 seconds; BraSiC joint at 35 kV, 8 mA and 20 seconds.

## 5.5 Investigations of Insulation Materials of Toroidal Field Coils

The International Thermonuclear Experimental Reactor (ITER) fusion device [Ayma01] is based on the magnet confinement principle in order to control the high – temperature plasma. The fusion magnets require high – quality performance of the insulation material. The insulating materials of super conducting magnet coils for ITER fusion reactor, which are required between coils to avoid eddy current flow from coil to coil, suffer under high mechanical stresses and high radiation environment (neutron and gamma radiation) [Tsuji01, Mitc01]. Basically, these insulation systems are glass fiber reinforced plastic laminates (GFRPs) consisting of different fibers and matrix materials, like multi – component epoxy resins or similar compositions. Alstom/R (manufactured by Alstom – MSA in France) and Kapton/R (manufactured by Ansaldo in Italy) glass tape interleaved are preferred as an insulation material considering the ability to maintain its excellent physical, electrical, and mechanical properties over a wide temperature range. The combination of glass fiber and Kapton – film is the same in both types of the insulation materials (Alstom and Ansaldo) fundamentally. Only specific differences are depending on the manufacturing of fiber – reinforced bundles. The important difference is that Alstom specimen also contains boron element. They are glass fiber reinforced plastic laminate and consist of glass fiber reinforcement tapes; vacuum impregnated in an epoxy system and contain Al, Si and H materials. The mechanical property of these insulation materials under static and dynamic load was investigated at ATI – Wien in earlier works of [Hume00-1, Hume00-2, Bitt02]. However, the stability and the lifetime of the insulation systems, which determines the lifetime of magnetic coils, will change under the demanding performance conditions of the ITER fusion device.

### 5.5.1 Radiographic Inspections

The structural change and swelling problem of these materials of newly developed fiber composites under high irradiation has to be investigated with radiographic methods. The tomographic inspection is not possible because of the insufficient projections from its sides to reconstruct three dimensionally for such a thin samples (~ 2 mm). In order to get about these insulation materials, we utilized thermal NR and X – ray radiography. X – ray radiography for such a thin and light specimen is ideal imaging method.

A comparison between the radiography images of the fiber reinforced Kapton/R glass foils (Fig. 5.22 and Fig. 5.24 taken with thermal NR and Fig. 5.23 and Fig. 5.25 taken with X – ray) represents the difference of the fiber structures. The adhesive distribution between fibers could be inspected with both radiographic methods. Adhesive, which was used in Ansaldo tapes, are unstable under irradiation [Bitt02] and can be seen clearly as vertical stripes in the radiographic images. Fig. 5.23 and 5.25 (X – ray images) show the difference of the fiber structures between two types insulation materials, especially about the fiber connection. However, Fig. 5.22 and Fig. 5.24 (NR images) show necessary information about the inhomogeneous material distribution owing to the boron content within the samples. Under neutron irradiation the boron element with the  $B(n,\alpha)$  reaction emits high energy that damages the glass fibers.

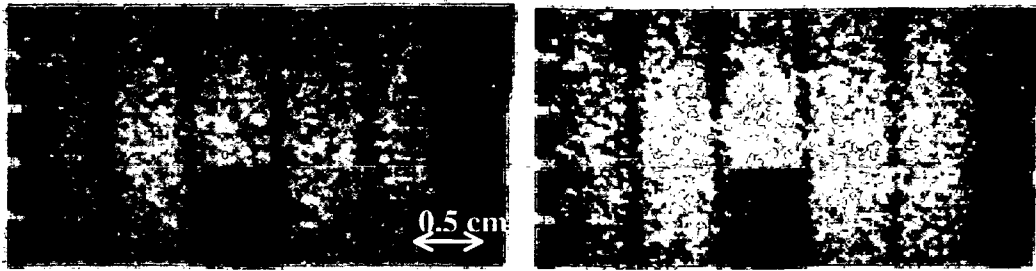


**Fig. 5.22:** NR images with different contrast of the Ansaldo R – glass fiber reinforced tape coil insulation material.



**Fig. 5.23:** X – ray radiography of the same insulation material as in Fig. 5.22.



**Fig. 5.24:** Thermal NR inspection of fiber reinforced insulation material (Alstom R – glass fiber reinforced tape).

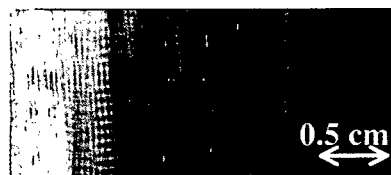


**Fig. 5.25:** X – ray radiography inspection of fiber reinforced insulation material (Alstom R – glass fiber reinforced tape).

The small pieces of fiber reinforced Alstom/R glass foils were irradiated at a fast neutron fluence of  $1 \times 10^{22} \text{ m}^{-2}$  ( $E > 0.1 \text{ MeV}$ ) at TRIGA Mark II [Bitt02]. Radiation causes swelling and plastic materials tend to change their molecular structure owing to the breaking or rearrangement of chemical bonds. The measured swelling percent of these pieces is 0.86 % under the neutron fluence of  $1 \times 10^{22} \text{ m}^{-2}$  in TRIGA Mark II reactor [Bitt02]. Such a small percent of swelling could not be visualized with radiographic methods as shown in Fig. 5.26.



**Fig. 5.26:** Thermal NR (left images) and X – ray (right images) inspection of irradiated Alstom type R – glass fiber tapes (the samples 1 – 1' and 2 – 2' are the same ones).

# 6

## Portable Non – Destructive Material Testing System “JEN-3”

The neutron is an important tool for the investigation of the static and dynamic properties of condensed matter since they distinguish between various elements and isotopes [Doma92]. JEN-3 is a portable nondestructive material testing system, which was developed in France and is used for routine testing of the steel products by the Austrian Stainless Steel Production Company Böhler – Bleche GmbH (BBG). The aim of this study was the analysis of neutron transmission measurements of JEN-3 system. The MCNP code is a very efficient tool to simulate an experimental set up. The JEN-3 system was analyzed by means of MCNP simulations in order to describe its principle and reliability. The JEN-3 system measures neutron transmission through samples having simple geometry such as plate, but it is not a position sensitive detector, only neutron counter.

### 6.1 Principle of the JEN-3 Detection System

The principle of the neutron transmission measurements with JEN-3 system is depicted in Fig. 6.1. A 1 cm diameter small Cf source emits fast neutrons, which are moderated in a paraffin block. The emitted fast neutrons lose their energy by collisions within the paraffin and become thermalized. The backscattered neutrons by the paraffin block penetrate the sample plate that is placed directly above the paraffin block. The transmitted neutrons passing the sample plate are detected with a standard  $^3\text{He}$  neutron counter (3.7 x 3.7 cm) as shown in Fig. 6.1. The detector is shielded from the top and sidewise with 0.2 cm thick Cd plates to form a narrow spatial acceptance angle for the transmitted neutrons. In this way, thermal neutrons from undesired directions cannot be detected. The Cf – source is located 2 cm away from the  $^3\text{He}$  neutron counter in horizontal and vertical direction. Detector and source were installed together in a 20 cm x 20 cm closed black box. The system can be put on inspected sample

## 6. Portable Non – Destructive Material Testing System “JEN-3”

plates with the help of a holder [Boeh97]. The distance between neutron counter and sample is kept to 4 – 5 mm in this system.

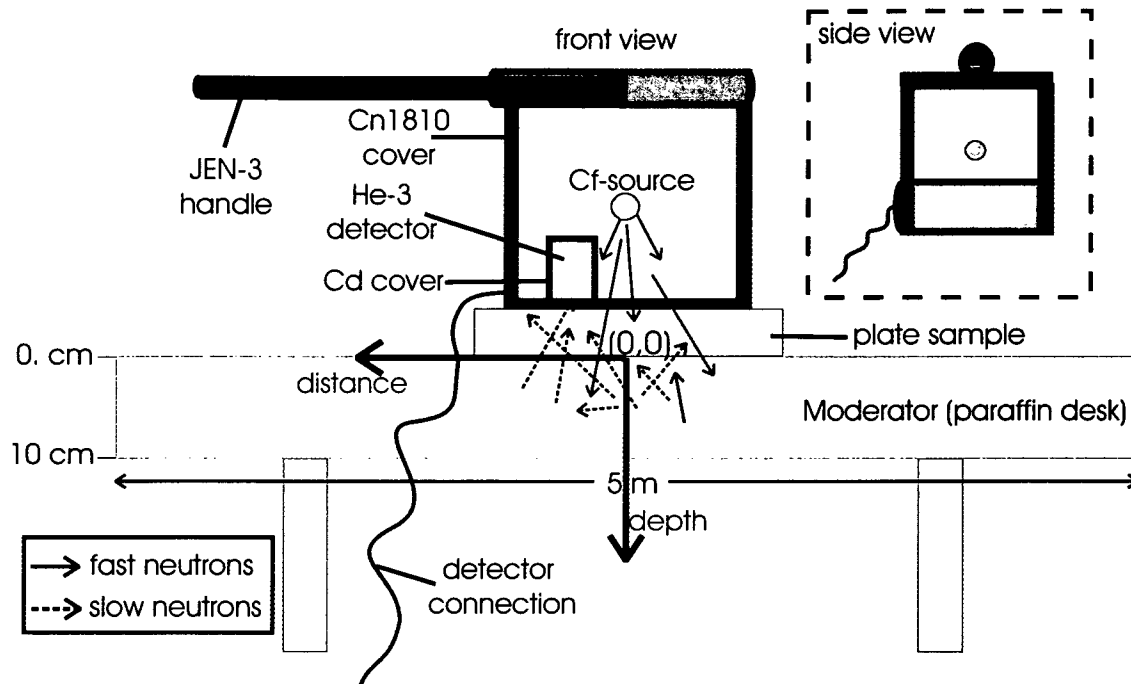


**Fig. 6.1:** The layout of JEN-3 detection system and its measurement principle. Some indications like distance – depth axis and (0,0) center will be often used in JEN-3 analysis (Cn1810 refers stainless steel).

## 6.2 Monte Carlo Neutron Transport Program (MCNP<sup>TM</sup>)

MCNP<sup>TM</sup> (Monte Carlo Neutron Particle transport Code) is a general particle transport code that can be used for a simulation of nuclear particle interactions with materials using evaluated nuclear data. It can be used for neutrons, photons, electrons, also combined neutron/photon, neutron/photon/electron, photon/electron, and electron/photon interactions. In particle transport, the MCNP method is a very realistic method to simulate experimental set – up. The usable neutron energy interval is from  $10^{-5}$  eV to 20 MeV and for photons and electrons from 1 keV to 1000 MeV depending on the available cross section libraries. This code uses nuclear and atomic data libraries, which are evaluations from the Evaluated Nuclear Data File (ENDF) database, the Evaluated Nuclear Data Library (ENDL) and the Activation Library (ACTL) [Brie97]. The MCNP code can be employed for modeling of neutron transport in critical or sub – critical reactors. Neutron histories in arbitrary geometries are tracked from neutron creation to its absorption by the use of evaluated cross sections data libraries for elastic scattering, inelastic scattering and absorption on nuclei present in specified (fixed) materials. The resulting collection of neutron tracks represents the experimental statistics and can be folded track by track with reaction cross sections and heating functions in order to obtain estimates of transmutation rates and power densities, including statistical error estimations. Multiplication eigenvalue calculations can be made in order to find critical configurations, while in sub-critical systems; source neutron multiplication is explicitly modeled. The reliability of its performance depends on the exact descriptions of the system

geometry, used library for material cross sections, and the source characteristics. Position sensitive detectors can be described with tally card, in which the spatial resolution of the detector is adjustable changing the number and size of detector tallies in MCNP input file. All reactions can be defined in an input file and then inserted into the MCNP transport code [Bast02-1, Kard03-2].

### 6.2.1 MCNP Input File Organization

An MCNP input file should contain information about the geometry, the source, the material description, and a selection of corresponding cross section evaluations. The input file is organized step by step as follows:

- Title line
- Cell description
- Blank line
- Surface specifications
- Blank line
- Source characteristics
- Material specifications
- Tally description and reaction types with tallies
- Execution instructions (time etc.).

Comment lines starts with “c” that may be inserted anywhere. First five characters are reserved for the card name or name of instruction/specification. Lines must be shorter than 80 characters. Continuation line is denoted with “&” on previous line. Explanations or comments on line start after “\$” character [Brie97].

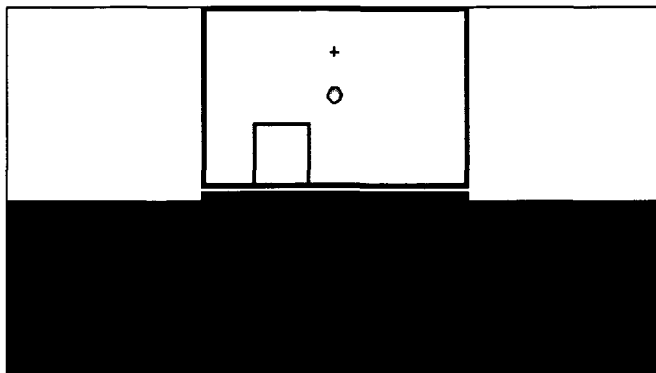
### 6.3 Characterization of the JEN-3 System with the Help of MCNP Simulations

MCNP4b MS – DOS version was used to analyze the JEN-3 detector set up. For this aim, the characteristic parameters of the system were exactly determined to describe the system geometry into the MCNP input file as shown in Fig. 6.2. MCNP input files have been performed to analyze the  $^3\text{He}$  detector response, the distribution of thermal neutrons in the paraffin and on the paraffin surface. The dependence of the neutron cross sections on the material thickness has been tested by MCNP simulations. Meanwhile, an optimization possibility of the distances between the detector and the sample (D – S distance) was also analyzed.

## 6. Portable Non – Destructive Material Testing System “JEN-3”

### INPUT FOR JEN3\_BOELER DESK

```
probid = 05/02/03 12:56:53  
( 1.000000, 0.000000, 0.000000)  
( 0.000000, 0.000000, 1.000000)  
( 0.00, 0.00, 0.00)  
extent = ( 25.00, 25.00)
```



Press enter for prompt

Fig. 6.2: The JEN-3 system geometry, which was described in the MCNP input file.

### 6.3.1 Simulation of the Detector Response of JEN-3 System

The detector response of a system is very important, because the attenuation coefficients of materials depend strongly on the neutron energy. In order to determine the detector response of JEN-3, the detected neutrons by  $^3\text{He}$  counter was analyzed according to their energies. The detected neutrons in each tally can be simulated according to their energies using the corresponding energy card in the MCNP input file. Fig. 6.3 shows a typical thermal energy spectrum for JEN-3 system in a logarithmic scale.

The purpose of the JEN-3 development was especially to measure neutron transmission through steel and boron – alloyed steel plates, whose cross sections depend strongly on the neutron energy and this property of materials is utilised in their investigations with neutron. On this account, the neutron cross-section of B-10 isotope and JEN-3 detector response in linear scale were shown together in Fig. 6.4. The energy dependence of the neutron cross-sections of boron isotope shows typical  $1/v$  behavior where  $v$  refers neutron velocity.

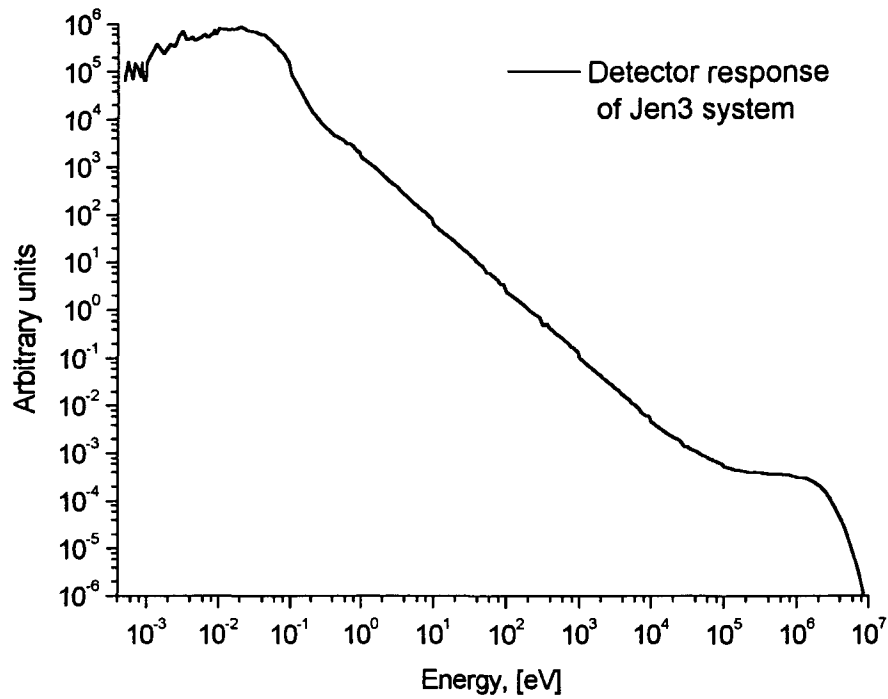


Fig. 6.3:  $^3\text{He}$  detector response in the JEN-3 detection system in logarithmic scale [Bast03].

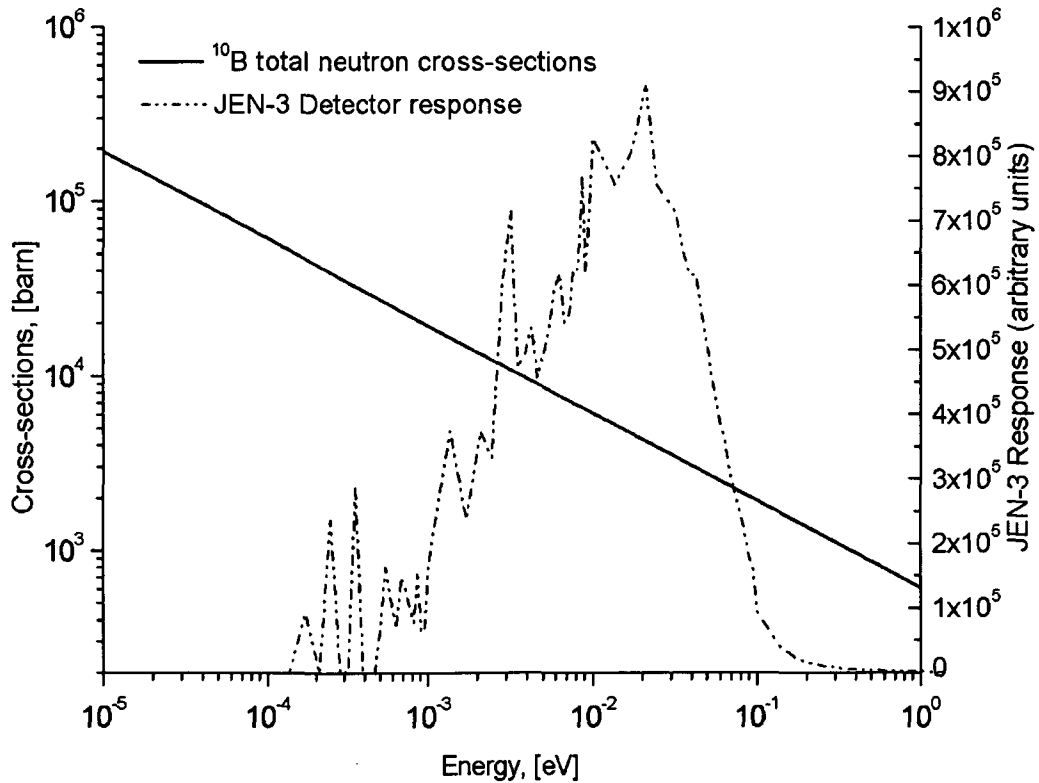


Fig. 6.4: The total neutron cross-section of B-10 isotope [NNDC] and  $^3\text{He}$  detector response of JEN-3 system (in linear scale) are shown as a function of neutron energy in thermal region (natural boron contains 81.5 wt % B-11 and 18.5 wt % B-10 isotopes).



### 6.3.2 Thermal Neutron Flux Distribution within the Paraffin Desk

The total and thermal neutron flux distribution in the paraffin depth of the JEN-3 system (total paraffin depth is 10 cm) was analyzed by means of MCNP simulations. To designate a sufficient moderator thickness in the set – up the neutron energy spectra were simulated at 10 positions within the paraffin in depth (with 1 cm intervals). Analyzing the neutron spectrum of each tally, the required optimal moderator thickness for this system can be determined. The simulated detector responses using  $^3\text{He}$  gas counters for each detector tally are shown in Fig. 6.5; a maximum thermal neutron flux was achieved in the 5<sup>th</sup> detector tally, which means between 5 – 6 cm paraffin depths. The rest of the paraffin block acts role as a reflector to increase the neutron flux on the paraffin surface.

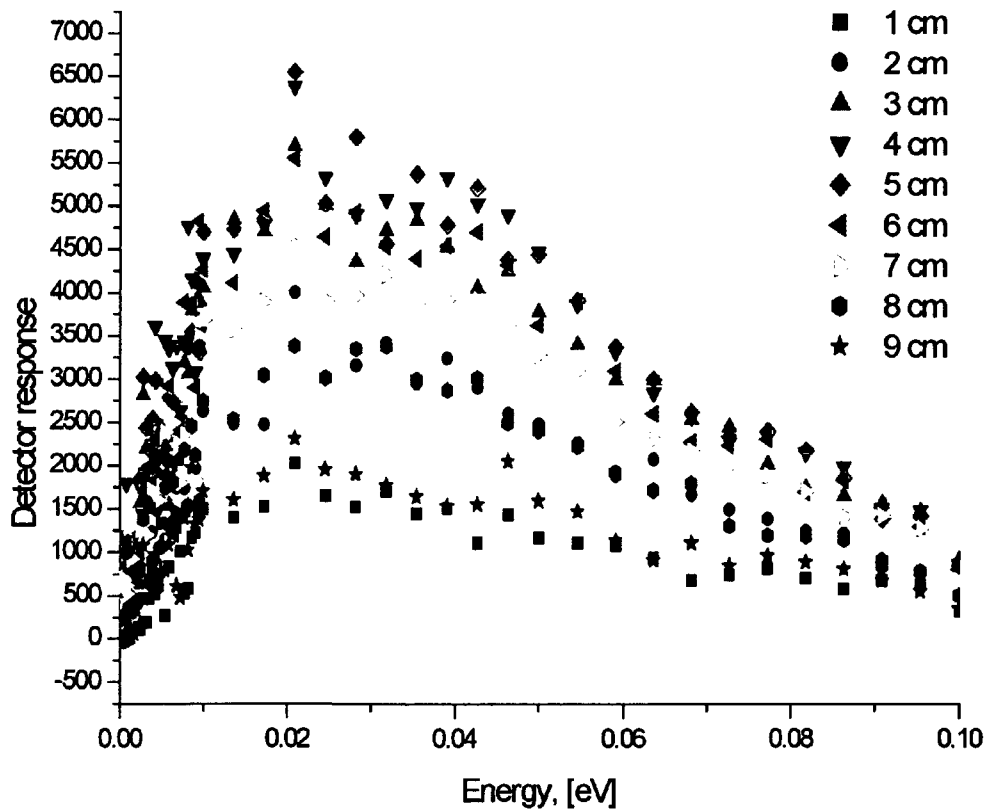
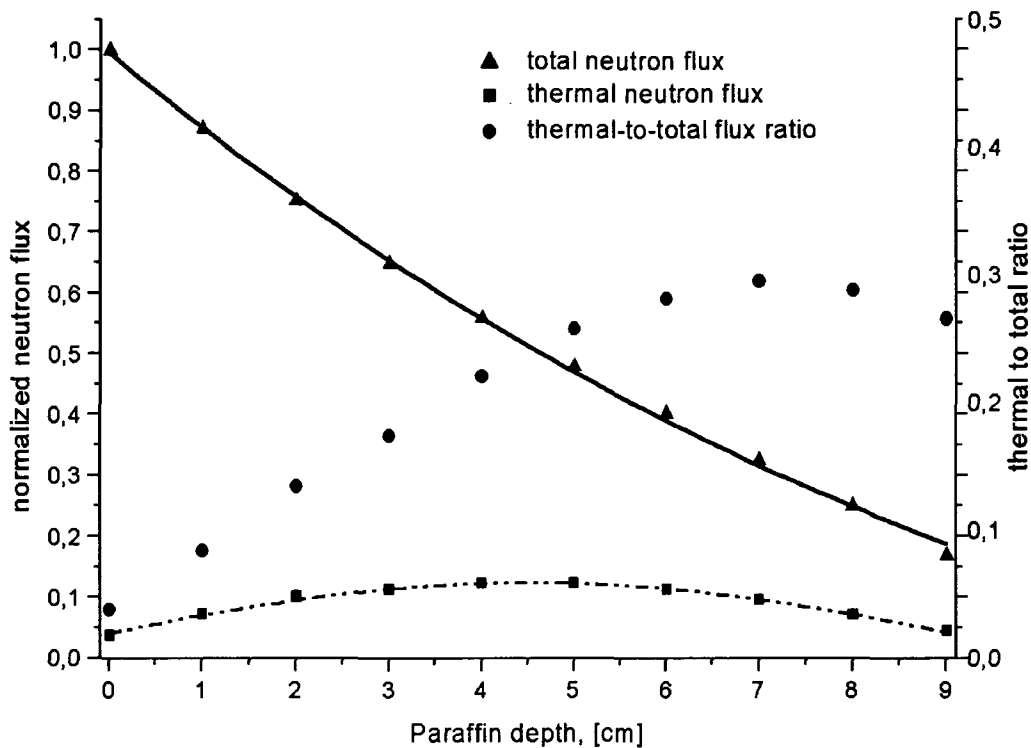


Fig. 6.5: The change of the detector responses as a function of the paraffin – block depth.

The total neutron flux within the paraffin moderator block decreases with increasing paraffin depth as seen in Fig. 6.6, it decrease 16 % from the initial value at the end of 10 cm paraffin depth due to the absorption and the scattering processes in the moderator block. The integrated thermal neutron fluxes, which have neutron energies from 0 to 0.1 eV in each tally position is also shown in Fig. 6.6 where the thermal to total neutron flux ratios for each position (or detector tallies) is also shown. The maximum thermal neutron flux is in the 5<sup>th</sup> position, while the maximum thermal to total neutron flux ratio is in the 7<sup>th</sup> position.



**Fig. 6.6:** The change of the total, thermal neutron fluxes as a function of paraffin – block depth.

### 6.3.3 Thermal Neutron Distribution on the Paraffin Surface

As mentioned, the JEN-3 detector is not position sensitive. However, it can be simulated as a position sensitive detector subdividing into tallies in MCNP input file. The resolution of the detector can be adjusted by changing the tally size in the input geometry. According to the registered neutrons in each tally, the distribution of the detected thermal neutrons could be analyzed. The simulation of a position sensitive counter allows determining the efficient area and the optimal position of the  $^3\text{He}$  counter in the inspection of the samples with the possible homogenous and maximum neutron flux.

Some MCNP simulations have been performed to investigate the thermal neutron flux distribution on the paraffin surface. The paraffin surface has been subdivided into tallies in the input file. Thermal neutrons in each tally were analyzed on the paraffin surface as a function of the distance. Fig. 6.7 shows an inhomogeneous thermal neutron distribution on the paraffin surface without sample. In order to analyze this heterogeneity effect on the neutron transmissions through samples, boron – alloyed steel plates having different thickness were placed between the paraffin surface and detector. The real position of the  $^3\text{He}$  counter in the JEN-3 set up was presented in Fig. 6.7. It is clear that the thermal neutron flux is distributed inhomogeneously on the paraffin surface, and it has maximum value at the center position, which is a vertical projection of the Cf source.

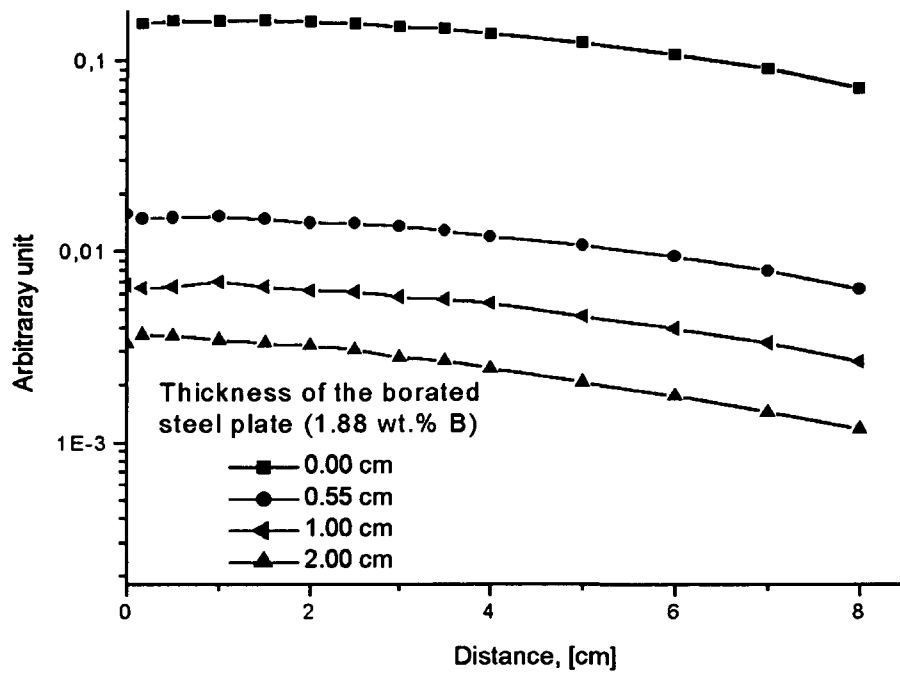


Fig. 6.7: Simulation of the spatial distribution of the transmitted neutrons through boron-alloyed steel with different plate thickness.

The important parameter for shielding material manufacturer is the macroscopic cross sections. On this account, the effective total macroscopic cross sections were calculated from the simulated neutron transmission values as shown in Fig. 6.8.

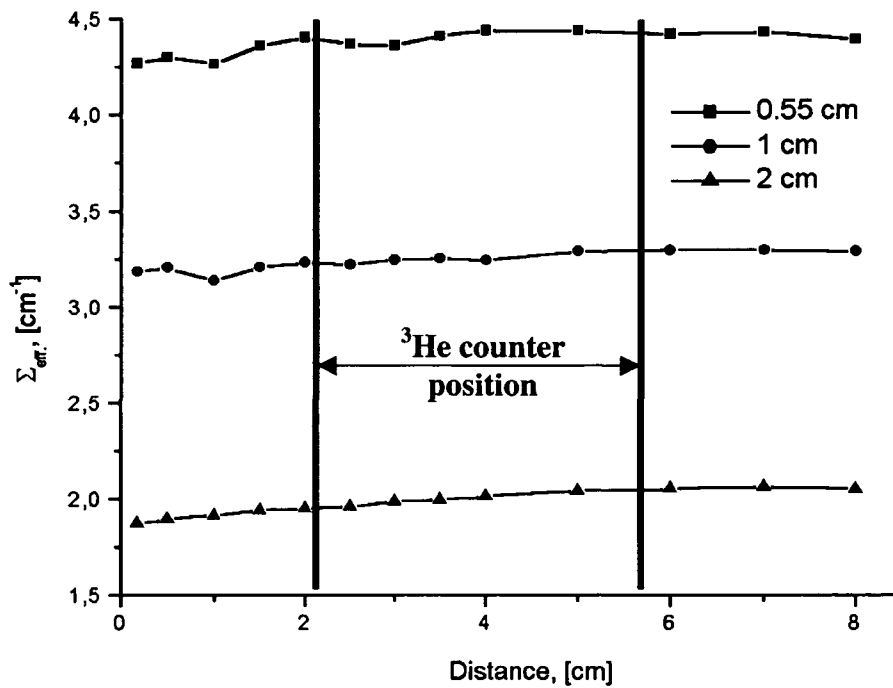


Fig. 6.8: The simulated distribution of the effective macroscopic cross-sections of boron - alloyed steel plates.

## 6. Portable Non – Destructive Material Testing System “JEN-3”

In order to perform a quantitative analysis from materials, the background and fluctuations or inhomogeneities in the neutron beam should be removed. The background for JEN-3 set – up data was performed simulating the system without paraffin desk only using detector and Cf source. The simulation of transmitted neutron flux through boron – alloyed steel plates (d: 0.55, 1.0 and 2.0 cm) was divided by the data without sample (d = 0.0 cm). Before this division, both intensities were corrected subtracting background from each. The effective macroscopic cross-sections of the samples were calculated using the neutron transmissions through the sample as seen in Fig. 6.8. The real position of the  $^3\text{He}$  counter is also marked with vertical lines in Fig. 6.8.

### 6.4 Optimisation of the Detector and Sample Distance

The purpose of this section is to analyze the contribution of multiple scattered neutrons on the neutron transmission measurements through materials. The scattered neutrons cause an increase of neutron transmission, which can be suppressed normally by increasing the detector – sample distance (D – S). However, the D – S distance of JEN-3 system is limited at 4 – 5 mm to prevent neutron intensity loss. With the help of MCNP simulations, the contribution of the scattered neutrons on the transmission results was analyzed. The contribution of multiple scattered neutrons on the transmission data was simulated increasing the D – S distances beginning from the real distance (5 mm) to 55 cm as depicted in Fig. 6.9.

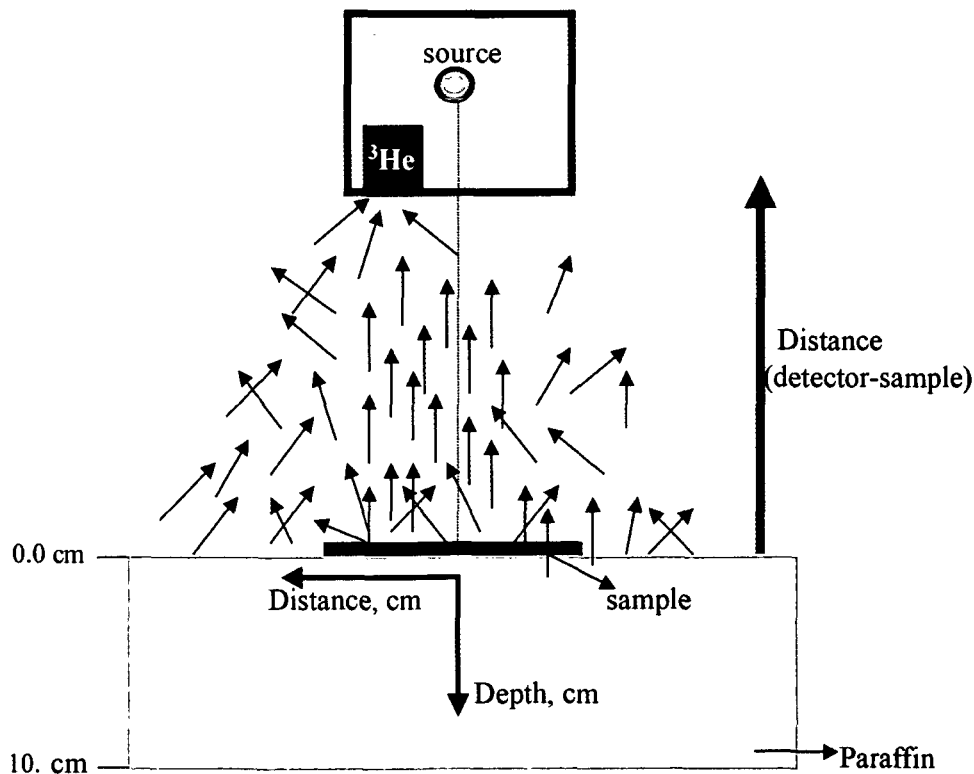


**Fig. 6.9:** Schematic representation of the multiple scattered neutrons on the transmission measurements with JEN-3 system depending on the D – S distance.

## 6. Portable Non – Destructive Material Testing System “JEN-3”

The detected neutrons can be analyzed as total, transmitted and multiple scattered neutrons by MCNP simulations. Therefore, the detected neutrons in  $^3\text{He}$  detector were considered separately depending on whether if they were scattered before their detection or not. The optimal distance between the detector and sample could be estimated analyzing the contribution of multiple scattered neutrons quantitatively, where its contribution is small as shown in Fig. 6.10. Nevertheless, the total neutron intensity decreases with increasing the D – S distance.

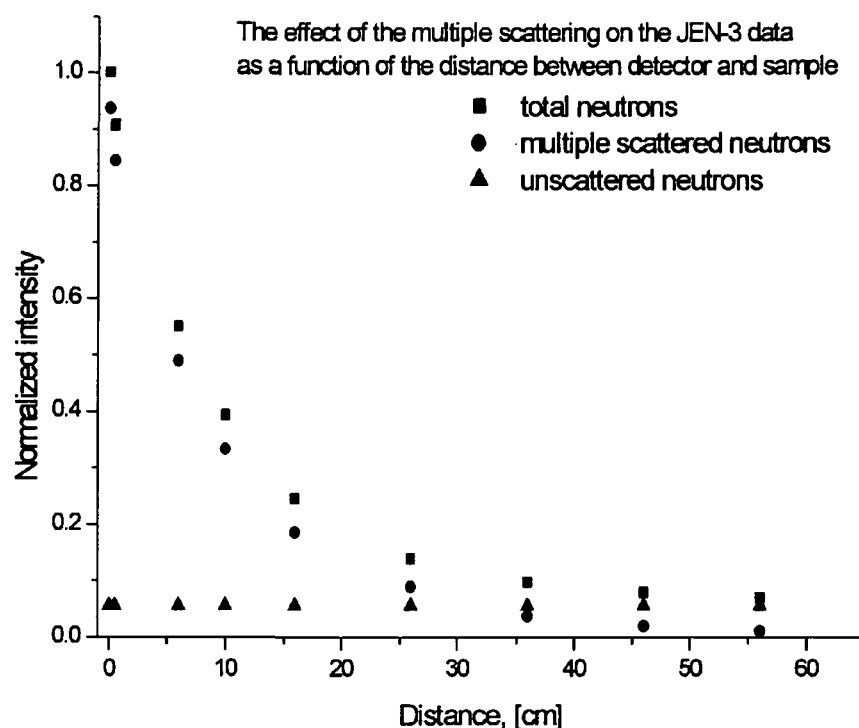


**Fig. 6.10:** Increasing D – S distance the contribution of multiple scattered neutrons decreases, but the neutron intensity decreases also (a 1.88 wt % natural boron – alloyed steel plate having 0.275 cm thickness was used).

The solid angle of the  $^3\text{He}$  detector will be reduced for multiple scattered neutrons from the sample, but the scattered neutrons from the surrounding (e.g. paraffin desk) cause an increase on the neutron transmission, which yields incorrect neutron transmission values in the case of larger D – S distance. That means the detected neutrons contain not only neutrons from the sample also from the surroundings. Consequently, the macroscopic total cross sections of 0.275 cm boron – alloyed steel plate including 1.88 wt % natural boron shows that such an optimization is not possible for this system as seen in Fig. 6.11. Only the position of the  $^3\text{He}$  gas counter can be changed to utilize maximum neutron intensity, which is at the vertical projection of Cf source. Fig. 6.11 shows that 5 mm D – S arrangement in JEN-3 system is optimal in BBG steel inspections.

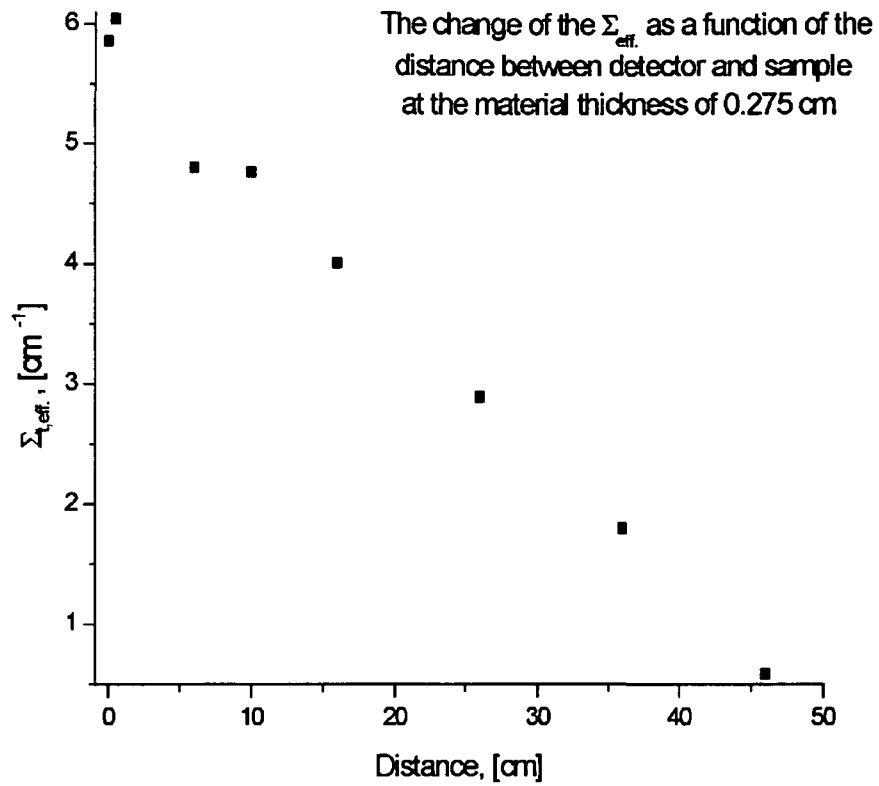


**Fig. 6.11:** The effect of the D – S distance on the effective macroscopic cross section (a 1.88 wt % natural boron – alloyed steel plate having 0.275 cm thickness was used for these MCNP simulations).

# 7

## Quantitative Analysis of Shielding Materials: Neutron Transmission through Boron – alloyed Steels

The main challenge of this work is the appropriate analysis of the transmission data, and the assessment of the neutron attenuation characteristics of strong absorber materials. For material characterization, it is of specific importance to define the homogeneity distribution of strong absorbing elements within shielding materials and the attenuation behavior as a function of thickness quantitatively. Neutron radiography (NR), which involves the attenuation of a thermal neutron beam by the object being radiographed, is also used for the quantitative investigation of the static and dynamic properties of condensed matter like shielding materials. Shielding materials are used for nuclear applications like transportation baskets of fuel storage bins or fuel shipment containers, shielding materials and components for compact storage racks. They have to be corrosion resistant under heavy duty. The most important requirements for the shielding materials are the uniformity of the absorption cross section over the whole volume and maximum thermal neutron absorption capability to perform the required safety functions.

Boron is the dominant absorber used in the production of boron – alloyed steel to serve in long – term storage of spent nuclear fuel or nuclear waste disposals. NR is able to satisfy the quality control requirements in order to give quantitative information about the spatial distribution of different elements and isotopes in the investigated samples due to the high neutron absorption by boron element compared to steel. Thus, the absorption property of the boron – alloyed stainless steels depends solely on the content of  $^{10}\text{B}$  isotope within the natural or enriched boron alloyed stainless steel.  $^{10}\text{B}$  isotope has 3838.1 barns absorption cross-section for thermal neutrons [Doma92, Sear92]. There are some materials whose absorption cross sections exceed boron element such as Sm (Samarium), Cd (Cadmium) and Gd (Gadolinium), but boron is actually the only utilized absorber material for the steel matrix [Vilp74]. Nevertheless, production of homogeneous alloys with boron is not straightforward.

The composition form of the boron powder (e.g. boron is used in boron carbide form) and the type of the steel structure play a big role to get homogeneous distribution of fine boron powders within the steels. According to the type of steel, boron atoms concentrate on grain boundaries, or in the vicinity of grain boundaries [Vilp74].

Neutron transmission measurements using thermal neutrons have been performed for boron – alloyed austenitic stainless steel plates as a function of plate thickness. The investigated samples were provided from the Austrian Steel Production Company BBG, which uses natural boron in the form of boron carbide within the steel matrix. This study concerns quantitative estimations of secondary effects on the neutron transmission measurements through thermal neutron shielding materials such as beam hardening, background, and inhomogeneous absorber distribution within the samples, which decrease the neutron attenuation in absorber materials. The attenuation coefficients of boron – alloyed steels were measured with neutron radiography and JEN-3 system, whose principle was given in chapter 6. The motivation of this study was not to compare two different systems; on the contrary, it was the analysis of attenuation properties of the boron – alloyed steel with the help of the comparison of the experimental results from different systems. In addition to the neutron transmission measurements, MCNP simulations were performed for better understanding and interpretation of the experimental results obtained, from observed differences between experimental results and theoretical predictions.

### 7.1 Neutron Transmission Measurements by NR

NR experiments of shielding materials have been carried out at two neutron radiography facilities having different beam characteristics, NR II at ATI and NEUTRA at PSI (chapter 3). Twenty standard 1.88 wt % natural boron – alloyed steel plates having each 0.137 cm thickness were used for the transmission measurements. One reference plate with a 0.0609 cm thickness was combined with other plates in order to supply a small thickness increment.

The NR images obtained by CCD camera have been corrected using white (without sample) and dark (at closed camera shutter) images. The two – dimensional neutron transmission images of the plates were processed according to the digital image processing steps (see chapter 4). White – dark and flat field corrections were applied to correct spatial fluctuations of the camera sensitivity as well as inhomogeneities of the scintillator and the neutron beam profile. Then, 3 x 3 median filter has been used to remove white spots. The line profile is a very useful tool to extract data from neutron radiography images at a specific position along the sample; it gives transmission data along a line depending on the position in the sample [Koer00, Schi99]. The macroscopic cross sections were calculated from the transmission values through boron – alloyed stainless steel plates with different thickness to describe the shielding material. The measured effective total macroscopic cross sections estimate the neutron scattering and absorption cross sections for a given sample composition as given in Eq. (7.1) and (7.2) where  $\Sigma_{B+Steel}$  is the macroscopic cross section for the boron – alloyed steel and  $d$  the sample thickness.

$$T = \frac{I_s - I_b}{I_o - I_b} = \exp(-\Sigma_t \cdot d) \quad (7.1)$$



## 7. Quantitative Analysis of Shielding Materials

$$\Sigma_{\text{eff.,total}} = -\frac{\ln(T)}{d} \quad (7.2)$$

Instead of macroscopic cross section attenuation coefficients have been used in some definitions, but it does not refer to mass attenuation coefficient. The relation between macroscopic cross section and mass attenuation coefficient is represented in Eq. (7.3).

$$\mu_m (\text{cm}^2 \cdot \text{g}^{-1}) = \frac{\Sigma (\text{cm}^{-1})}{\rho (\text{g} \cdot \text{cm}^{-3})} \quad (7.3)$$

**I<sub>s</sub>**: Attenuated sample intensity

**I<sub>b</sub>**: Background intensity (in the case of closed camera shutter)

**I<sub>o</sub>**: Open beam intensity (without sample)

**d**: Material thickness (cm)

**ρ**: Mass density

**μ<sub>m</sub>**: Mass attenuation coefficient

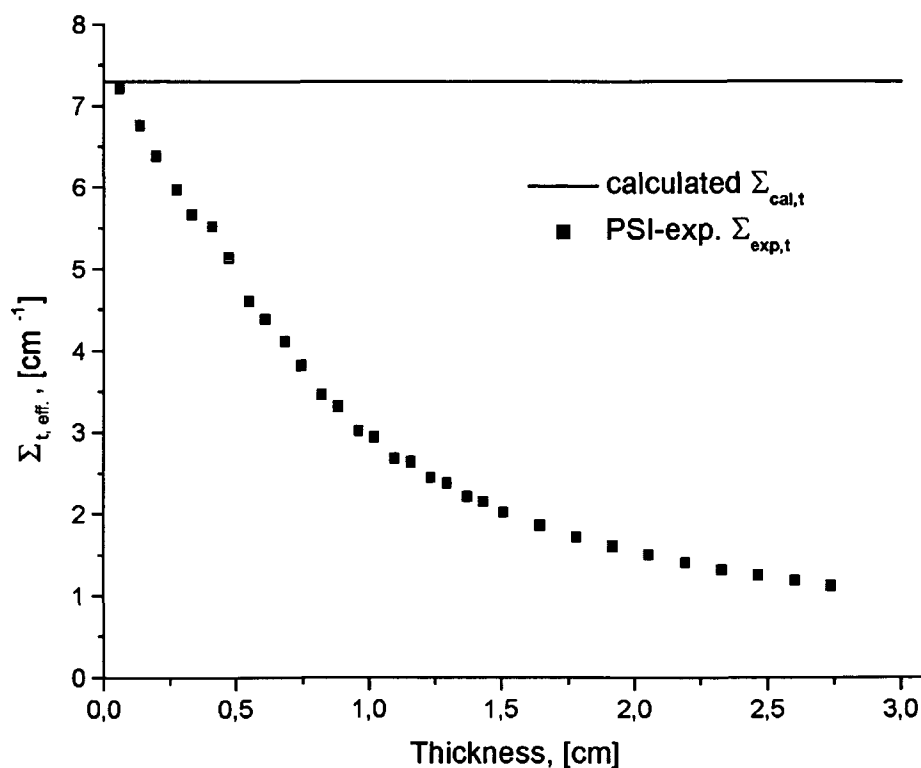


**Fig. 7.1:** The effective macroscopic cross sections of 1.88 wt % natural boron – alloyed steel plates as a function of thickness (neutron transmission experiments were carried out NEUTRA – PSI). The weight percentage of the natural boron 1.88 was calculated from mass spectroscopy analysis delivered by the company BBG.

The transmission measurements show a dramatic deviation from the theoretical calculations for homogeneous boron – alloyed steel as presented in Fig. 7.1. For theoretical calculation of the macroscopic cross section for homogeneous boron – alloyed steel containing 1.88 wt % natural boron, which amounts to  $\Sigma_{\text{B+Steel}} \sim 7.3 \text{ cm}^{-1}$ , the absorption and scattering cross

sections of boron and steel materials were taken at neutron energy of 25 meV (thermal neutrons) [Sear92]. Theoretically, the macroscopic cross section does not change according to the material thickness. However, the experimental results are not in agreement with the theoretical results. The measured effective total attenuation coefficients decrease with increasing the thickness of the shielding plates. The reason of the increasing deviation from the theoretical prediction as a function of the material thickness must be considered in the manufacturing and design of shielding materials.

## 7.2 Neutron Transmission Measurements by JEN-3

The measured transmission data obtained using a standard neutron radiography facility have been compared with results from the JEN-3, which actually is not a radiography system (see chapter 6). The JEN-3 neutron transmissions through the same boron – alloyed steel plates give a good opportunity to analyse the shielding materials by comparing it with the results from NR. The beam characteristics of NR and JEN-3 are completely different: neutron radiography NEUTRA – PSI uses a well-collimated neutron beam contrary to the JEN-3 system. On account of this, JEN-3 system detects scattered neutrons more than transmitted from the sample contrary to NR. The effect of the multiple scattered neutrons on the neutron transmission measurements can easily be suppressed by increasing the distance between detector (scintillator) and sample at NR facility while the D – S distance cannot be enlarged in JEN-3 because of the intensity loss. In order to handle measured data with JEN-3 system, an open beam count without sample was performed. The background from air and ground was performed turning the JEN-3 detector to the air (opposite side of paraffin desk) and putting on the ground in order to remove the background from the transmission data. Then, the mean value of both backgrounds was taken into the calculations using Eq. (7.1).

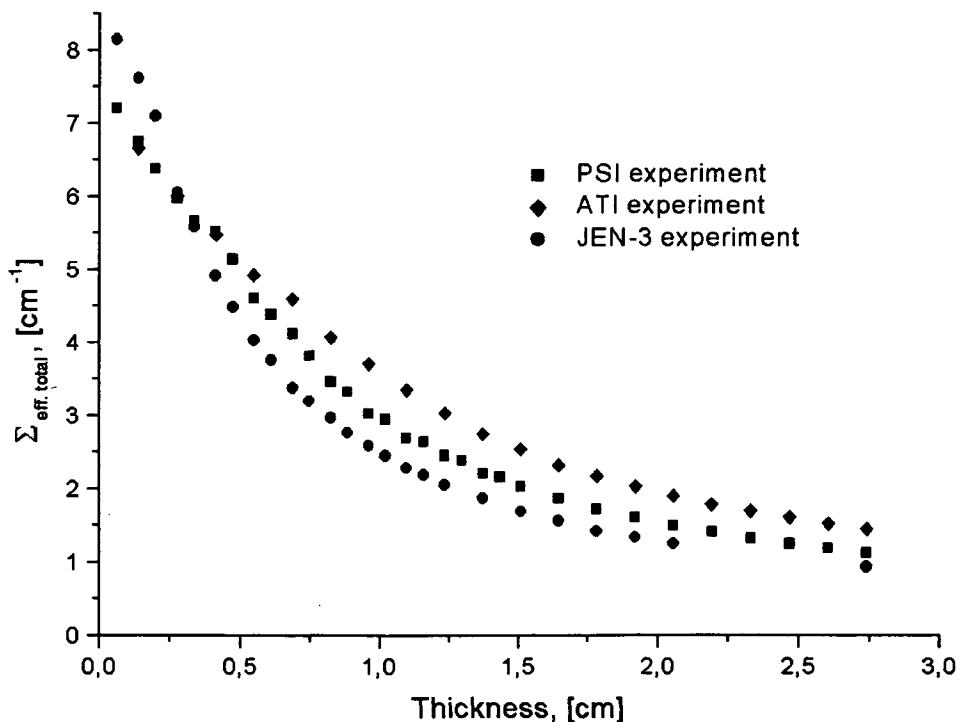


Fig. 7.2: The measured data from industrial set-up JEN-3 and comparison with NR.

Fig. 7.2 shows the effective macroscopic cross sections from the neutron transmission measurements with JEN-3 system and NR facilities. Comparing these results, which show approximately same neutron attenuation behaviour with increasing plate thickness, effective factors on the transmission measurements through strong absorber materials can be estimated. Of course, some deviations on the results come from the influences of different beam characteristics. Surprisingly, the measured data from JEN-3 and NR facilities are comparable despite the systems having different characteristics. From this point of view, it is a fact that other factors affect on all measurements. MCNP simulations of each facility were performed to analyse and define the effective factors.

### 7.3 MCNP Simulations of Neutron Transmission Measurements

As in the previous chapters mentioned, MCNP (Monte Carlo Neutron Particle Transport) code is very efficient software especially in neutron physics, and it uses the experimental cross sections of materials with neutrons or/and photons, electrons. It can be exploited to simulate measurements such as neutron transmission through boron – alloyed steels plates. The necessity of MCNP simulations was to estimate the contribution of negative factors on the transmission measurements. Beam hardening, inhomogeneous boron distribution within the steel matrix, background and additional effects can be assumed as negative factors that take place in neutron transmission experiments. The contribution of secondary effects on the quantitative analysis like scattered neutrons depending on the distance between detector and sample also can be determined by means of MCNP simulations.

At the beginning, boron – alloyed steel plates were assumed homogeneous for MCNP simulations of NR measurements, and the plates were simulated as a function of material thickness. The NEUTRA – PSI neutron energy spectrum and neutron sensitive scintillator screen as a detector was defined in the input file of MCNP simulations. In this model, the sample was assumed as a homogeneous composite consisting of 1.88 – weight percent natural boron and stainless steel. Fig. 7.3 shows a clear deviation between measured and simulated data for a homogeneous model of boron – alloyed steel structure. It is a fact that boron powders are not distributed homogeneously within the steel matrix.

In addition to MCNP simulation of NR, JEN-3 measurements were simulated to verify the influences of estimated factors. The simulations for a homogeneous material composition were repeated using JEN-3 geometry. Using the homogeneous composition assumption for material structure, JEN-3 simulations and measurements of 1.88 wt % natural boron – alloyed steels show a better agreement than the comparison of NR measurement and simulations as presented in Fig. 7.4. It can be related to the different beam characteristics of both detection systems. As mentioned in previous chapters, NR uses parallel neutron beam and can detect micro – heterogeneity in a material contrary to JEN-3 system. As a result of this, the JEN-3 neutron transmission system cannot differ micro – heterogeneity within the samples.

## 7. Quantitative Analysis of Shielding Materials

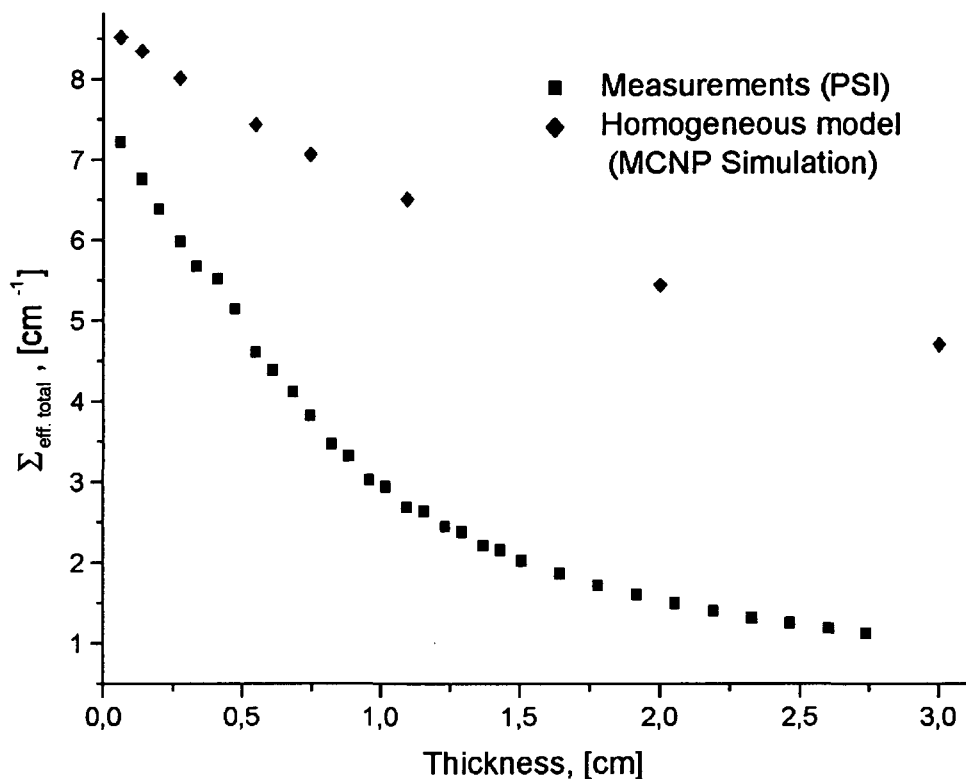


**Fig. 7.3:** Simulation of the material structure assuming that boron powders distribute homogeneously.

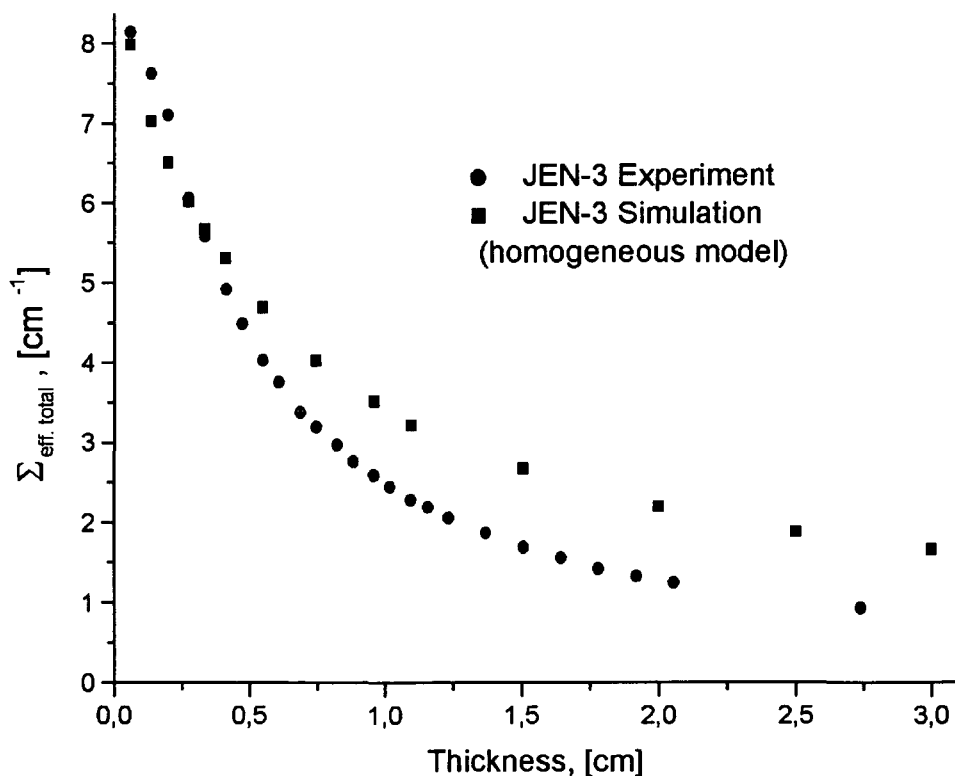


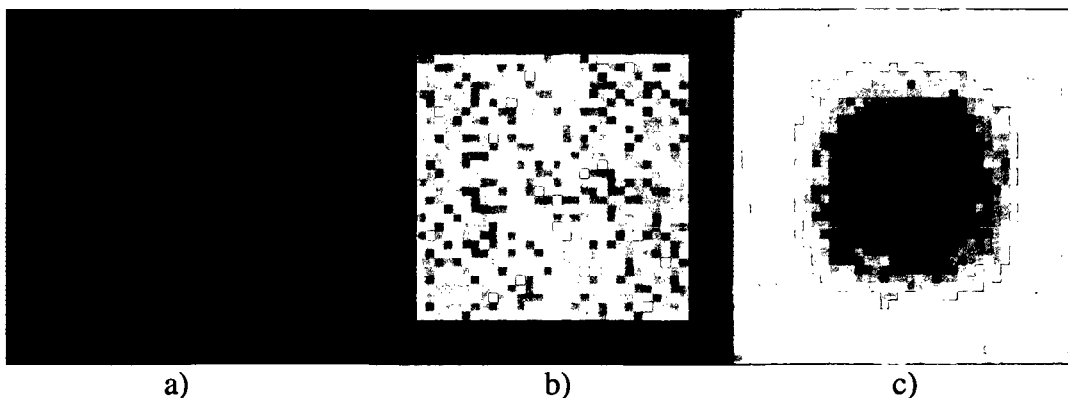
**Fig. 7.4:** The comparison of the macroscopic cross sections from JEN-3 simulations and measurements as a function of plate thickness in JEN-3 system.

### 7.3.1 Effect of the multiple scattered Neutrons on NR Images

Scattered neutrons from samples yield serious problems on neutron radiography images and also computed – tomography (CT). It is especially very important, if quantitative analysis of NR measurements is necessary. This effect should be considered depending on being inspected sample material like steel or hydrogenous materials, which scatter neutrons (e.g. Al element is not a problem). The following problems due to the scattered neutrons can be appeared on the NR and NT [Sear92, Kard03-2]:

- One being the degradation of the image contrast, which makes difficult to define edge determination on CT.
- Other being the deviation from quantitative linearity between density and CT value, which makes it difficult to carry out quantitative analysis inside materials.

The solid angle of the detector for the scattered neutrons from the sample can be reduced increasing the distance between detector and sample in NR facility. In order to demonstrate the influence of scattered neutrons on the NR transmission measurements, 1 cm thick pure steel with a dimension of  $3 \times 3 \text{ cm}^2$  was simulated in MCNP at different D – S distances. With the help of MCNP simulations, the transmitted neutrons can be analyzed separately as detected total neutrons, detected neutrons without being scattered and detected neutrons being multiple scattered during their path within the sample (collided and uncollided and total transmitted neutrons). Fig. 7.5 shows the effect of scattered neutrons on the NR image caused by the 1 cm thick steel sample depending on the D – S distance. We executed simulations at different D-S distances until this effect on the image contrast is negligible. This process is necessary only for quantitative analysis, because normally the spatial resolution (image sharpness) depending on the beam divergence becomes worst with increasing D – S distance as illustrated in Fig. 7.5b and 7.5e. If the spatial resolution is important for the inspected object, then a small D – S is suitable.



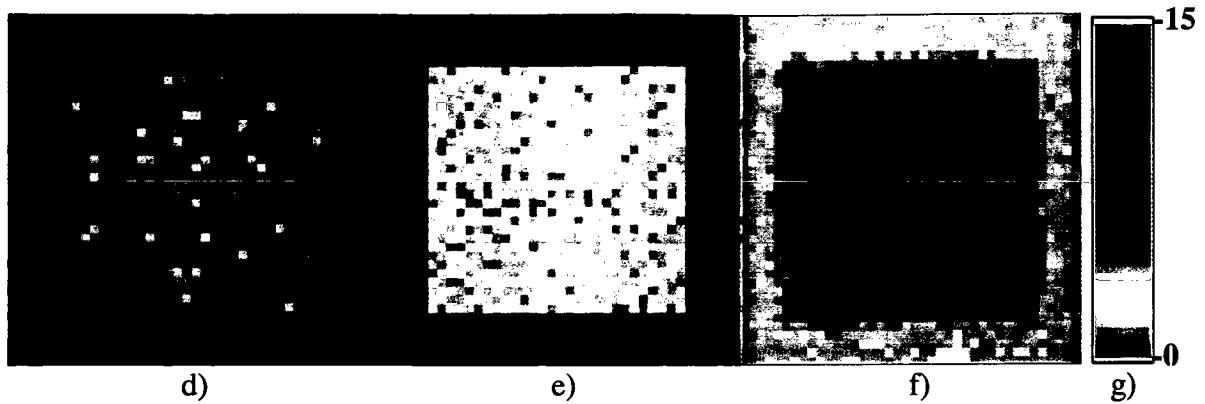


**Fig. 7.5:** Simulation of the effect of the scattered neutrons on the NR images at 0.0 cm and 10 cm D – S distances; a) total neutrons with 0.0 cm D – S, b) transmitted neutrons without being scattered with 0.0 cm D – S, c) multiple scattered neutrons with 0.0 cm D – S, d) total neutrons with 10 cm D – S, e) transmitted neutrons without being scattered with 10 cm D – S, f) multiple scattered neutrons with 10 cm D – S, g) corresponding color bar.

Simulation of the contribution of multiple scattered neutrons gives a possibility to reduce this problem in the experiments. Especially, it can be subtracted from the transmission measurements for simple geometry objects, if quantitative analysis is necessary. The line profile of the neutron transmission shows the effect of multiple scattered neutrons on the neutron transmission through 1 cm thick steel plate as represented in Fig. 7.6. The effect of multiple scattered neutrons on the quantitative analysis can be neglected in the investigations of strong absorber materials, nevertheless the D – S distance was kept to a minimum of 15.0 cm for our NR investigation to reduce problem.

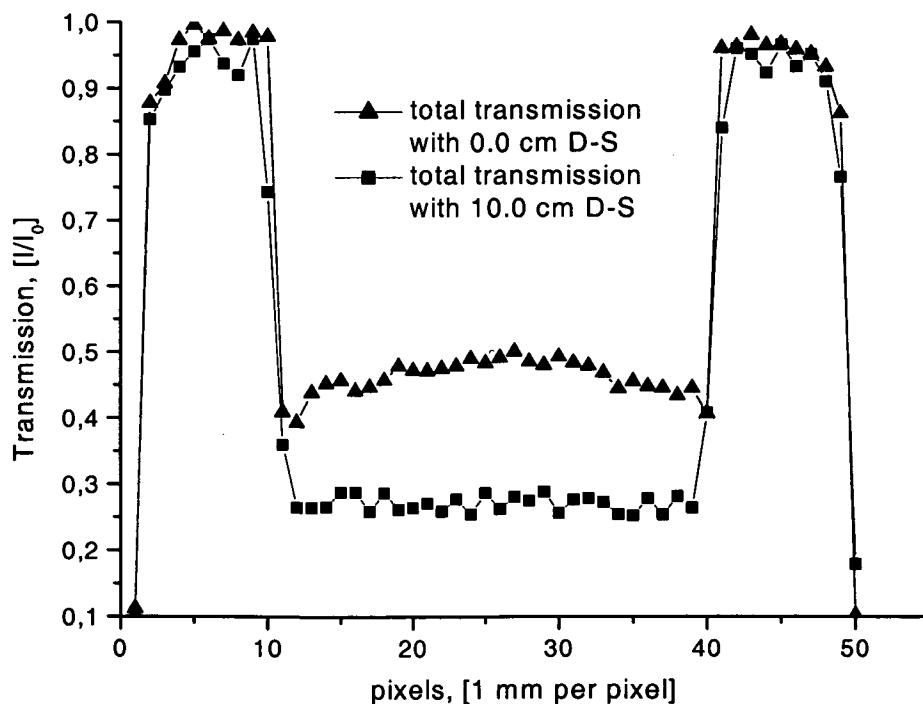


**Fig. 7.6:** The effect of multiple scattered neutrons on the neutron transmission depending on the D-S distance.

### 7.3.2 Analysis of the Secondary Factors

MCNP simulations have been employed to determine the negative factors and their influence on the transmission measurements. All reactions can be defined by an input program and then they are inserted into the MCNP code. The decrease of the effective macroscopic cross sections with increasing sample thickness can be related to well known beam hardening effect; MCNP considers also beam hardening in its calculations. However the disagreement or deviation between simulated and measured values is too large and requires other assumptions about the material structure. We have developed analytical models for each of the problems in this respect to emphasize its own peculiarities. Firstly, a sequence of MCNP simulations has been enforced to show the beam hardening effect. Then, the estimated secondary effects were analysed based on the comparison of the simulated and measured data.

#### 7.3.2.1 Beam Hardening Effect

The shift of the neutron spectrum to the higher energy region by the sample is called beam hardening, which is a well – known phenomenon in X – ray optics and causes an increase of the transmission through the material in the measurements [Herm80, Leli96]. This effect takes place in strong absorbing materials such as Boron ( $\sigma_a/\sigma_s \sim 200$  for thermal neutrons), where neutron absorption of boron depends strongly on the energy and shows a  $1/v$  behavior ( $v$  being neutron velocity). That means the absorption probability of slow neutrons increases with decreasing neutron energy. The first reason is the absorption of low energy neutrons in the first thickness interval of an absorber material, so that the remaining beam becomes richer in high – energy neutrons. As a result of this, the rest of the material cannot attenuate neutrons as in the first thickness interval of a sample, so that the macroscopic cross section decreases with increasing material thickness. Second reason is the inelastic neutron collisions with the materials, which also cause beam shift. It has recently been verified that the beam hardening in strong absorbing materials is the main cause of the deviations from the experimental transmission law. Consequently, the mean energy of transmitted neutrons through such a material will be higher than before the penetration [Bast02-1, Zawi03].

In order to determine the beam hardening contribution of the material itself, a series of simulations have been performed by means of the MCNP code. Neutron detection in a neutron sensitive scintillator is strong energy dependent, and the beam – hardening factor can cause a deviation of the quantitatively estimated neutron detection. Analytical calculations and a simple Monte Carlo model have investigated the thickness dependent effect of the boron – alloyed samples as shown in Fig. 7.7. The agreement between input spectrum of NEUTRA and output spectrum (without sample and scintillator screen) presents the accuracy of these simulations. The shift of the transmitted spectra with increasing material thickness (boron – alloyed steel plates) was analyzed and is demonstrated in Fig. 7.7 and Fig. 7.8. Consequently, absorber materials such as boron cause a strong beam hardening effect, which becomes dominant with increasing material thickness. This is one of the reasons that the measured and simulated effective macroscopic cross – sections decrease sharply. In Fig. 7.7, the simulated intensity of 1.75 cm boron – alloyed steel plates was multiplied by a factor of 50 to show the beam shift in one graph. The detailed representation of beam hardening effect depending on the material thickness is shown in Fig. 7.8 in logarithmic scale.

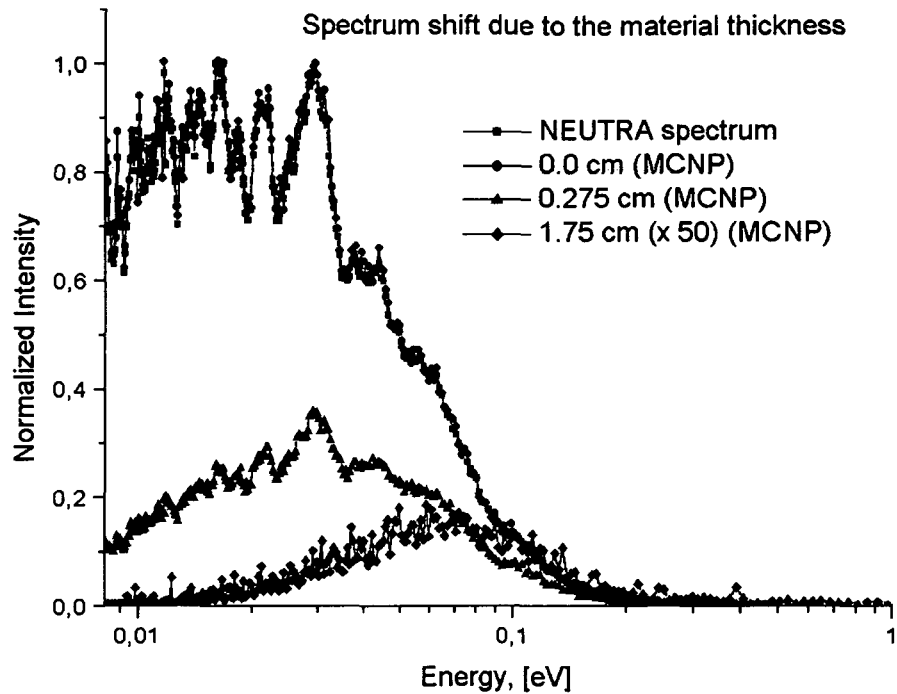


**Fig. 7.7:** Simulation of the beam hardening effect (shift of the neutron spectrum to the higher energy), which is caused strong absorber materials; the transmission through 1.75 cm boron – alloyed steel plate was multiplied with a magnification factor of 50.

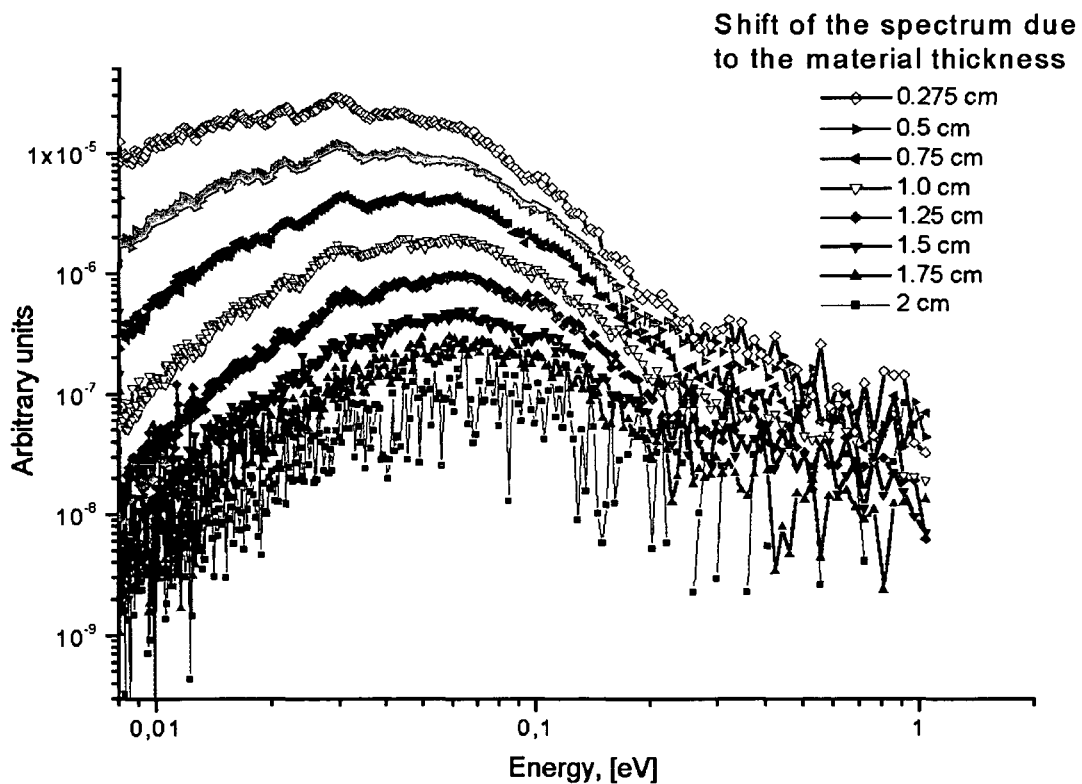


**Fig. 7.8:** The beam hardening with increasing 1.88 wt % natural boron alloyed steel thickness (in logarithmic scale).



### 7.3.2.2 Heterogeneous Structure Modelling for Boron – alloyed Steel Plates

In the first step of MCNP analysis, the boron – alloyed steel plates were assumed homogeneous and that assumption was not in agreement with the measurements. Then, further simulations have been performed to analyze the material structure. We developed specific analytical models on the basis of the SEM (scanning electron microscope) inspection of a slice of boron – alloyed plate [Boeh97], which presents an inhomogeneous boron powder distribution as seen in Fig. 7.9. On this account, different single analytical models were used in the MCNP input files due to the observed differences between experimental results and theoretical predictions. The basis of this structural modeling is to approach the actual structure of boron – alloyed steels and to make accurate comparisons to obtain better precision.

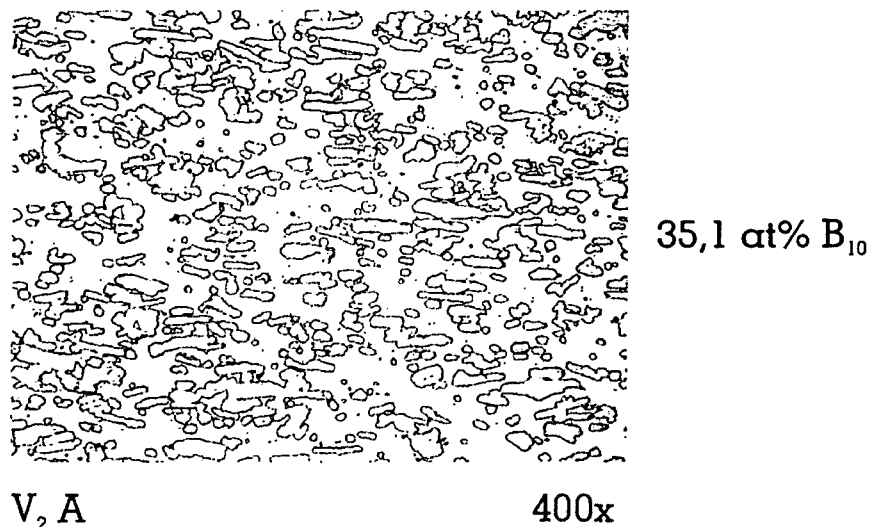
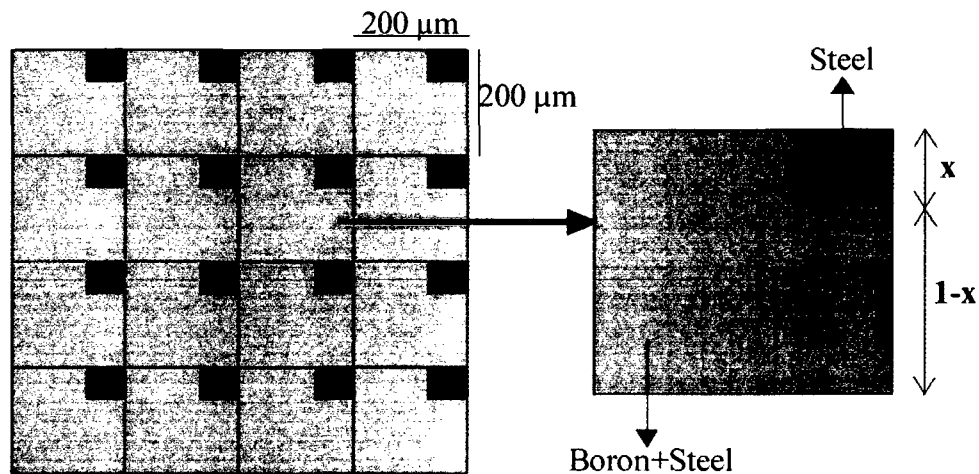


**Fig. 7.9:** A slice image, which shows the distribution of boron powders in boron – alloyed steel, was taken by SEM analysis; 1 mm was magnified with a factor of 400 [Boeh97].

The micro – heterogeneity can play a big role on the neutron transmission through a strong absorber material. Moreover, there is no fixed boron distribution in the plates, it distributes randomly in each sample depending on the manufacturing process. A simple and general model for all samples should describe the heterogeneity within the sample considering the random distribution. The better agreement between experimental data and MCNP simulations was found with an inhomogeneous composition like channel model. In this model, a specific description was used where the homogeneous and inhomogeneous boron areas were ordered. The distribution of boron powder in this micro – heterogeneous model was concentrated in one part of an unit cell, which has a size of  $200\ \mu\text{m} \times 200\ \mu\text{m}$  and keeps the total weight percent of natural boron constant in the sample (1.88 wt%). That means the heterogeneous unit cell is composed of two homogeneous sub cells where one of these sub cells does not contain any boron as depicted in Fig. 7.10. A measure for the level of the sample heterogeneity was the ratio of the volumes (steel sub cell to the unit cell). Therefore, one has to be cautious and certainly at the present stage, it is not possible to consider our MCNP model as the true physical model. Another crucial issue is the complete experimental verification of the model because it is difficult for the steel manufacturer to vary the distribution of the boron powder (in the form of boron carbides) in the steel.

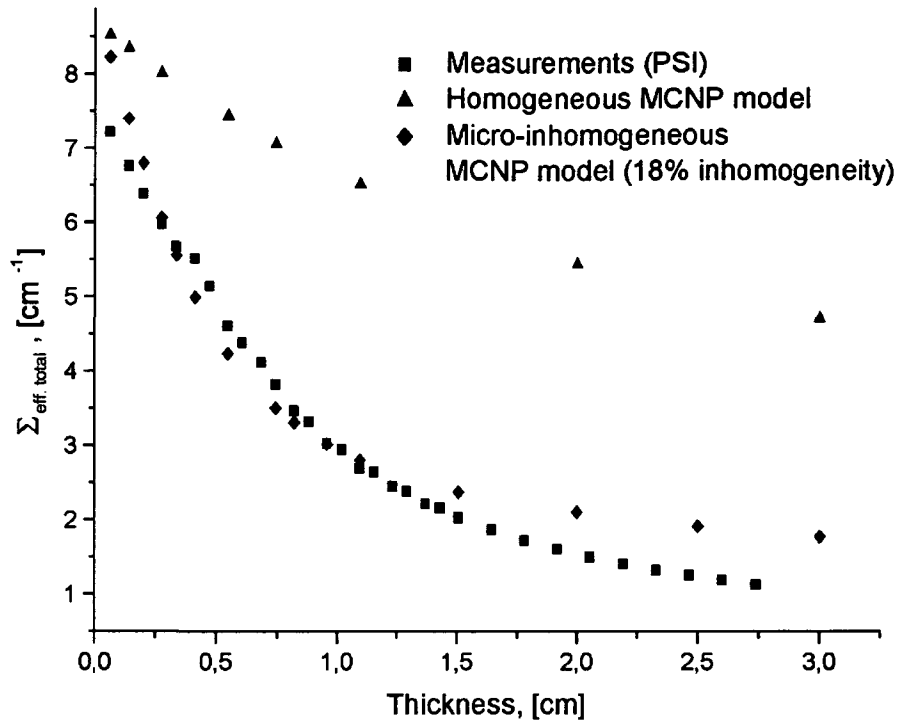
## 7. Quantitative Analysis of Shielding Materials

The size of the unit cell was chosen smaller than detector spatial resolution to measure the transmission from whole unit cell (micro – heterogeneous). That means measured intensity per one pixel is a combination of two unit cells. In the case of the channel model application, the neutron transmission will differ from the basic law of radiation attenuation [Bast02-1]. The best agreement between experimental data and MCNP simulations was found by changing the size of sub cells (e.g. changing  $x$  parameter) as represented in Fig. 7.9.



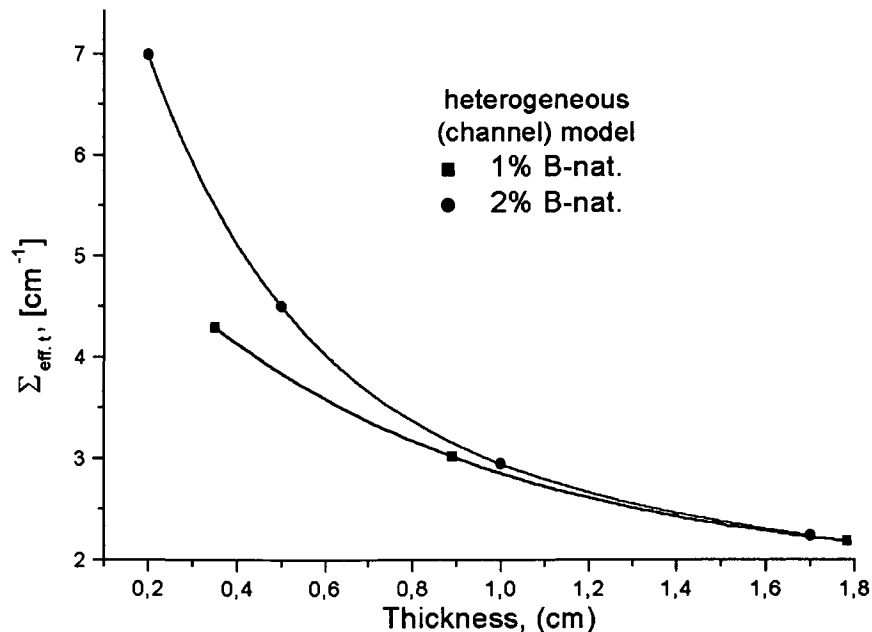
**Fig. 7.10:** A channel model representation used in the MCNP simulations to describe the boron – alloyed steel structure.

Fig. 7.11 shows a noticeable difference between homogeneous and inhomogeneous – channel model simulations. There is a thickness dependent deviation between MCNP structure models, which increases as a function of material thickness. Channel model assumption shows reasonable agreement with increasing material thickness, that shows the accuracy of the channel model, but it does not prove that this model is an optimal structure model for the investigated boron – alloyed steels. There are several possibilities to simulate geometrical structures; our model is probably the simplest one.



**Fig. 7.11:** The adaptation of the channel model simulations to the measurements of boron – alloyed steel as a function of material thickness.

Fig. 7.12 verifies the reliability of the beam hardening and heterogeneity assumption, because the boron content could not affect the results any more after a specific material thickness where the simulated macroscopic cross sections of 1wt % and 2 wt % natural boron – alloyed steel are nearly equal for heterogeneous material structure.



**Fig. 7.12:** Because of the beam hardening effect and heterogeneity problem, boron contents within the materials have no influence on the neutron attenuation after a specific material thickness.

It is a fact that JEN-3 system is not suitable for structure analysis of the materials, because it cannot detect the micro – heterogeneity in a material. In order to be sure of this assumption, we have used the same heterogeneous (channel) model for material structure in the MCNP simulations of JEN-3 transmission measurements. The simulations for a homogeneous and heterogeneous composition are in agreement as expected (Fig. 7.13). The reason is straightforward owing to the beam divergence in JEN-3 system. Considering the insensibility of JEN-3 system to the micro – heterogeneity within the material, further JEN-3 simulations have been performed using homogeneous boron distribution in order to reduce simulation time.

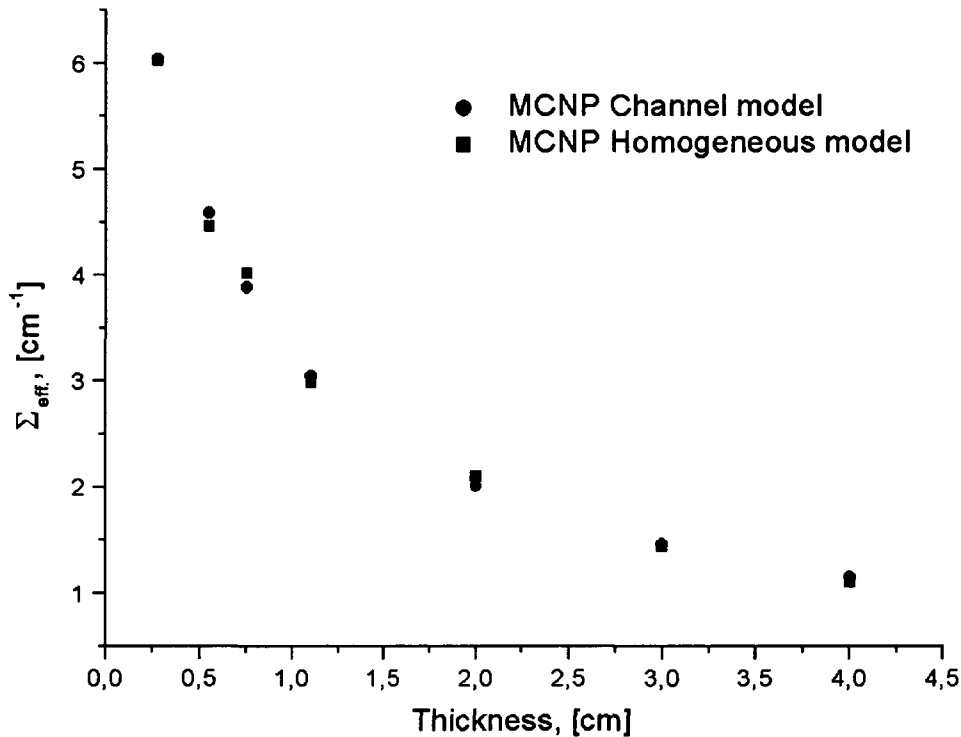


Fig. 7.13: The insensibility of the JEN-3 detection system to the material structure.

### 7.3.2.3 Background Effect

The results presented in Fig. 7.6 and Fig. 7.11, which show the effect of multiple scattered neutrons and deviation from MCNP model, indicate that the attenuation process cannot be described fully taking into account only the beam hardening and material heterogeneity. Obviously, there are still negative factors other than material heterogeneity, which have to be cleared up. Especially, the deviation between simulations and measurements after a specific material thickness should be considered. The deviation of measurements from the channel model simulations after a specific material thickness can be related to the existence of some uniform neutron background in the measurements, which cannot be simulated by MCNP code.

We assumed that background contribution to the transmission measurements is mainly scattered neutrons from the bunker walls and also from the experimental equipment such as detector etc. One can see from Fig. 7.6 and Fig. 7.11 that background is accessible from

## 7. Quantitative Analysis of Shielding Materials

measurements at larger sample thickness, where the signal from transmitted neutrons is negligible. The constant background becomes dominant after the detection limit and the measured signal levels cannot be explained with a MCNP model, where the background is not assumed. There is also a constant background from the electronic equipment such as noise etc., but this contribution is removed by the data handling in JEN-3 or image processing in NR as given in Eq. (7.1). The only way to simulate background effect in MCNP is to define an excess uniform neutron source in the input file. Since we do not know the exact background level at the facility, we cannot perform a reliable simulation. Instead of this, we tried to estimate the background level by the following assumption. If the investigated sample does not influence the spatial distribution of the background, then the background can be considered to be proportional to the initial beam intensity as in the Eq. (7.4) where  $k$  is a proportional coefficient representing the background contribution factor of the experimental set-up.

$$I_{BG} = k \cdot I_0 \quad (7.4)$$

Consequently, using this assumption, the following expression, Eq. (7.5), can be obtained for the measured transmission, where  $I_0$  and  $I$  are the incident and the transmitted neutron flux.

$$\frac{I_{exp}}{I_{0,exp}} = \frac{I + k \cdot I_0}{I_0 + k \cdot I_0} \quad (7.5)$$

For thicker absorbers, transmitted neutrons intensity will be very small ( $I \sim 0$ ), which gives directly the boundary condition as stated in Eq. (7.6). That means, there is a thickness limit for strong absorber materials, and over this limit, we can measure only background, not neutron transmission through the material.

$$\frac{I_{exp}}{I_{0,exp}} = \frac{k}{1+k}, \quad \text{at } I \sim 0 \quad (7.6)$$

In this way, the attenuation coefficient for thicker material can be obtained using Eq. (7.7) [Baec02-2].

$$\Sigma(d) = -\frac{1}{d} \cdot \ln\left(\frac{k}{1+k}\right), \quad (7.7)$$

This assumption was applied to measured data and rough background contributions of different facilities were compared as given in Fig. 7.14. The different neutron energy spectrum, background contribution, and other secondary effects peculiar to each NR facilities can explain the difference between PSI and ATI measurements. The background effect on the transmission measurements was determined as 5 % for NEUTRA – PSI where a fit yields  $k = 0.05$  ( $k = 0.05$  means 5 %). The deviation reason with increasing material thickness of the measurements performed at different NR facilities is the background factor. The 2 % background ( $k = 0.02$ ) at NR II – ATI is lower than the background (5 %) at NEUTRA. It can be related to the NR II set up, which is not in a closed room and the scattering effect from bunker walls is lower. In this case, a detection limit for a 1.88 wt % natural boron – alloyed steel can be defined where signal is still higher than the background level ( $d < 1.2$  cm). The

efficiency of JEN-3 system is below the NR facilities related to the higher background contribution ( $k = 0.08$  or 8 %) and different beam characteristics.

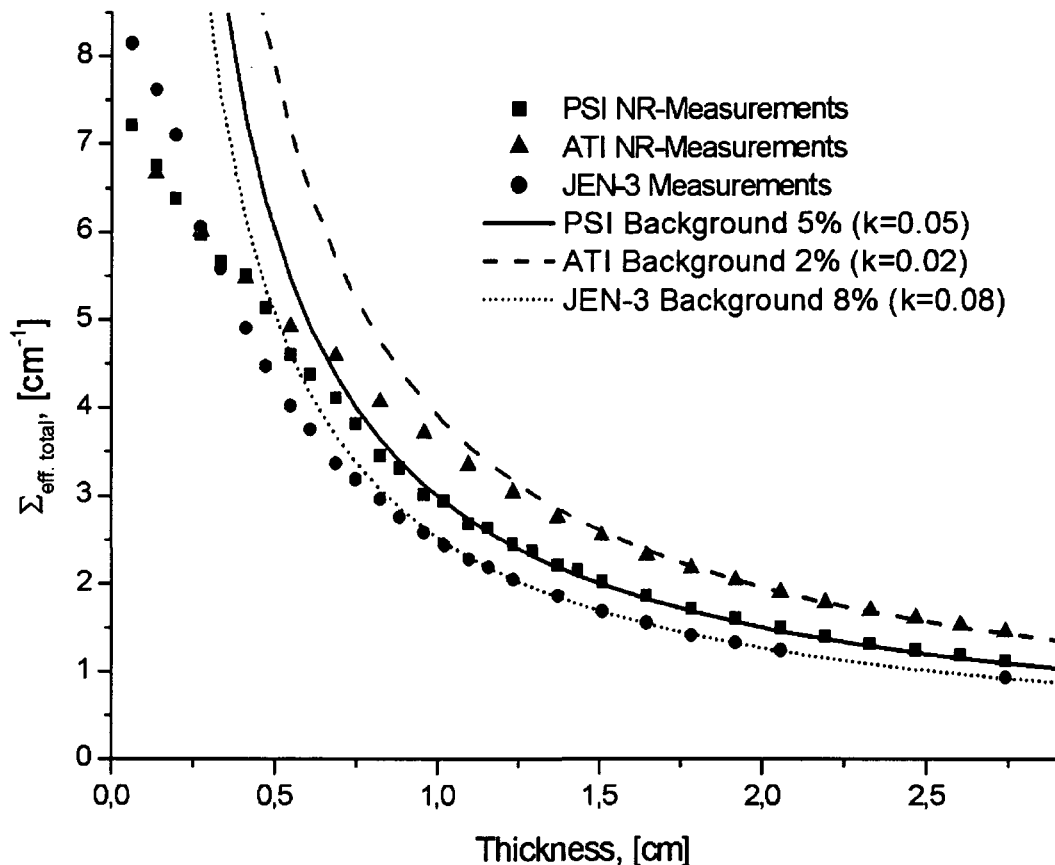


Fig. 7.14: The background contribution and the detection limit could be determined considering the intersection of the measurements with fit – function of the background contribution [Bast02-1].

#### 7.4 NT Investigations of Boron – alloyed Steel Rods

The aim of this study is the continuation of the quantitative analysis, and three – dimensional visualization of the  $^{10}\text{B}$  distribution within the boron – alloyed steel rods [Zawi03]. High thermal neutron flux is required to achieve sufficient counts behind the absorber. Here, we focus on the tomographic investigations with a well thermalized but rather weak ( $\approx 10^5 \text{ n.cm}^{-2}.\text{s}^{-1}$ ) neutron beams at the NR II facility, which was recently implemented [Koer00, Koer01]. Certainly, neutron tomography is the only method, which is able to analyze the complete isotope distribution in the material. The 3D image reconstruction is based on the common FBP (Filtered Back Projection) algorithm, which achieves good results with comparable image quality [Sear89, Herm80, Kak88]. Several difficulties are related directly to the FBP shortcomings. As explained in chapter 4, more projections are preferred for a good investigation to reduce reconstruction artifacts, if FBP algorithm is used. The low counts or intensity lead to a increasing of the statistical fluctuations, which get amplified in the FBP based image reconstruction. Therefore, one of the problems in the analysis of absorber materials is the reconstruction artifact depending on the few number of NT projections.

Poor reconstructed slices reduce the 3D image quality when not all artifacts can be corrected. Therefore, bad slices then have to be removed and/or replaced by neighboring slices, which affects the spatial resolution. The imaging quality depends also strongly on low background conditions. The detected neutrons come from the neighbor of the specimen or from the surrounding by scattering, which gives no information about the sample. The contribution of scattered neutrons, gamma rays, or light penetration in the light – tight detector box has to be suppressed as far as possible. Finally, an analytical correction, which can be applied only for simple geometrical objects, was developed for the negative factors such as background and beam hardening in the absorbing material investigations.

### 7.4.1 Measurements

All tomographic investigations have been performed using different camera – optics at the 250 kW TRIGA reactor of the ATI – Wien. In order to inspect the neutron shielding materials delivered from the BBG, high spatial resolution is necessary to visualize boron distribution. Cylindrical steel and boron – alloyed steel rods having different boron contents and radiuses were inspected with NT. The boron mass fraction in inspected rods actually changes from 0.0 to 1.88. The steel rods are ideal test objects for developing tomographic imaging, because the distribution of boron powders is expected homogeneously across the whole volume.

As mentioned in previous chapters, we have different camera lenses for different applications. The 180 mm F 2.8 lens is for small objects with high – resolution ( $\sim 170 \mu\text{m}$ ), and 58 mm F 1.2 is for wide – angle images with low – resolution ( $428 \mu\text{m}$ ) [App. II]. The disadvantage of the 180 mm lens is the longer exposure time ( $\sim 11$  times longer than 58 mm lens) to detect the same intensity in an image, but it can visualize small objects. Normal daily operation time of TRIGA Mark II research reactor at ATI is from 9:00 am to 4:00 pm. Under this condition, we have to consider projection number for a tomographic investigation of an object. Owing to the limited operation time, projection number is limited if we use high – resolution camera lens with longer exposure time. However, with the second lens 200 projections can be easily performed during this limited reactor operation time. The high – resolution optics was chosen for the measurements with a longer exposure time of 120 seconds and with a limited projection number of 60 for 3D reconstruction. An increase of the exposure time brings white spot problem, which increases with increasing the exposure time on an image and causes loss of information.

A 1.85 wt % natural boron – alloyed steel tube having 2 cm outer diameter and 1 cm inner diameter was filled by a 0.93 wt % enriched boron – alloyed steel rod having 1 cm diameter. 200 number of NT projections were performed using camera optics of 58 mm focal length for this inspection, and all NT projections were reconstructed 3 dimensionally basing on the FBP algorithm as represented in Fig. 7.15. Despite the 200 NT projections, the difference of the boron content within the steel rods could not be visualized. This camera optics is suitable for bigger samples, if high resolution is not demanded. In order to analyze the boron – alloyed steel rods with higher spatial resolution, we used other camera optics of 180 mm focal length for further NT inspections.

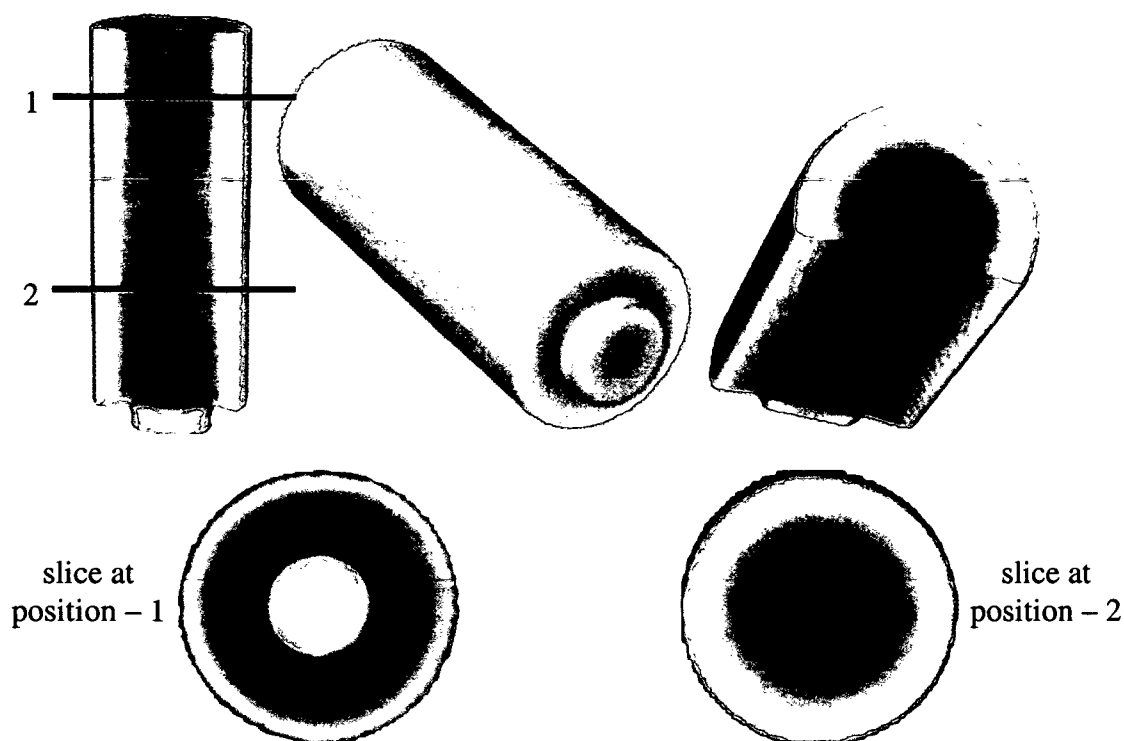


**Fig. 7.15:** The 3D reconstructed images of a 1.85 wt % natural boron – alloyed steel tube (outer) and a 0.93 wt % enriched boron – alloyed steel rod (inner), which was placed into another, taken with the camera optics of 58 mm focal length. The discrete slices are related to the positions 1 and 2.

#### 7.4.2 Correction of the Secondary Effects on the NT Measurements

For the detection of  $^{10}\text{B}$  within steel matrix, the energy dependence of the neutron attenuation has to be considered. If the incoming neutron spectrum, the sample geometry, and composition are known with sufficient precision, then the negative factors such as beam hardening and background can be corrected numerically. A small modification has been developed in the filtered back – projection based reconstruction program. The widely used IDL image – processing software (Research Systems Inc.) has been applied for the CT – reconstruction [Rive98]. Just before the evaluation of the sinogram, the corrected transmission has been calculated considering spectrum shift as given in Eq. (7.8) [Zawi02].

$$T_{\text{corr}} = T_{\text{eff}} / \exp \left[ \sum_i (\Sigma_i d_i) \delta\lambda / 2\lambda_{\text{th}} \right]^2 \quad (7.8)$$

According to the above expression the best corrections have been obtained with  $\delta\lambda = 0.08 - 0.09$  nm, which is in good agreement with recent measurements of the neutron spectrum at the thermal beam line [Haje01]. For a successful correction of beam hardening one needs some knowledge about the expected cross sections and their spatial extension. On the other hand, Eq. (7.8) can be used for an iterative approximation of the true composition, because beam hardening is very sensitively to the true macroscopic cross sections [Leli96, Zawi02, Zawi03]. When the exponent value, which is the multiplication of material thickness and macroscopic



## 7. Quantitative Analysis of Shielding Materials

---

cross section, becomes large, then any small deviations or fluctuations affect effective transmission,  $T_{\text{eff}}$ , and the beam hardening correction as well. The Gaussian model will fail if the exponent reaches a value of 4. However, even if the analytical correction is not perfect, it enables in many cases an essential improvement of the image quality.

In the NT inspection of a pure steel rod, no beam hardening is visible considering the contrast distribution. The grainy structure of the 3D pictures is caused by statistical intensity fluctuations and shortcoming of the filtered back – projection method. A median filter, which smoothes the images, was used at the expense the information loss or reduction of spatial resolution.



**Fig. 7.16:** 3D reconstructed images from 60 NT projections of a pure steel rod having 1.0 cm diameter (left image without smoothing and right image smoothing with median filter).

On the left side of the Fig. 7.17, the uncorrected reconstruction reveals artifacts in the boron – alloyed steel rod. The images of the macroscopic cross section distribution ( $^{10}\text{B}$  + steel) shows how the attenuator would act in a thermal neutron field and the uncorrected result is important for the application of the boron – alloyed steels. Then the negative factors were successfully corrected with the analytical formula, which are demonstrated at the right side of the Fig. 7.17. The corrected image is important for the steel manufacturer because it shows that no systematic  $^{10}\text{B}$  inhomogeneities are present in the boron – alloyed steels. The elevation of the effective transmission causes an apparent reduction of the macroscopic cross section towards the center of the rod.

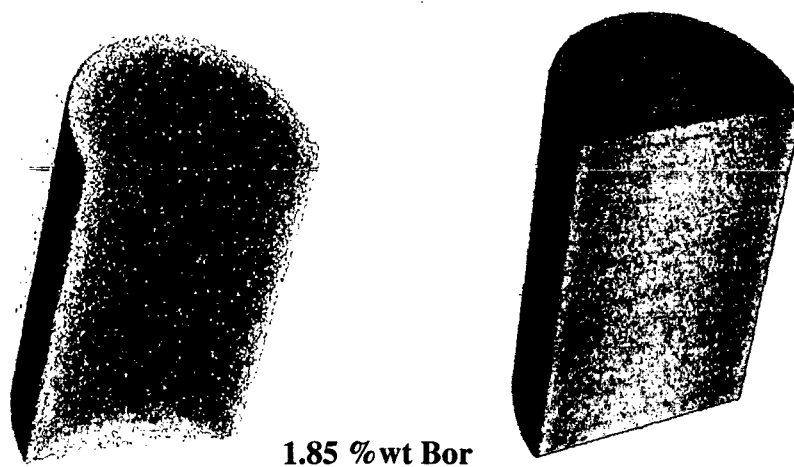
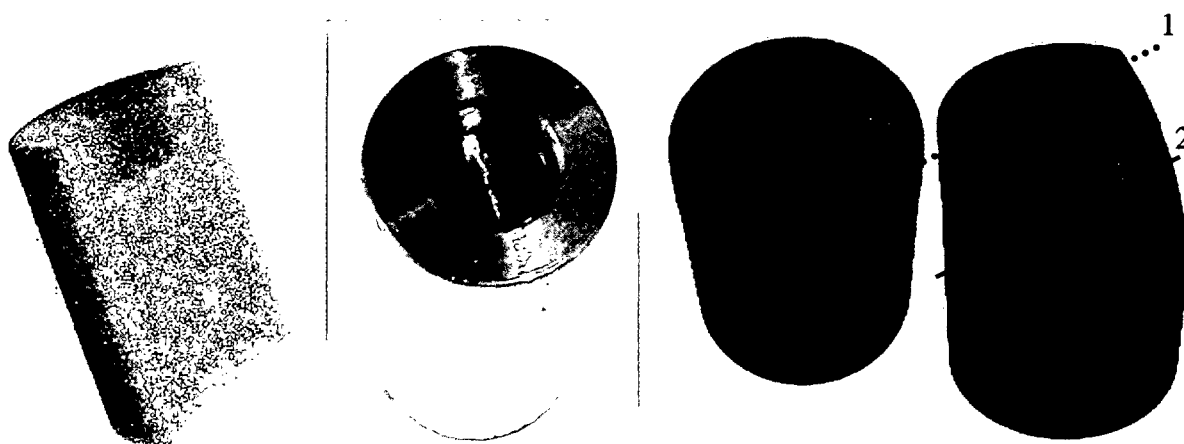
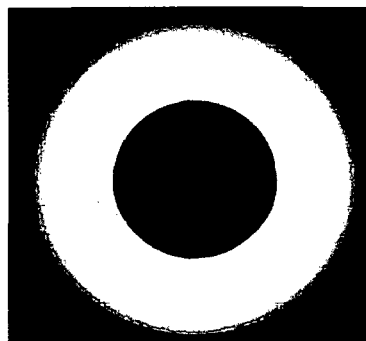
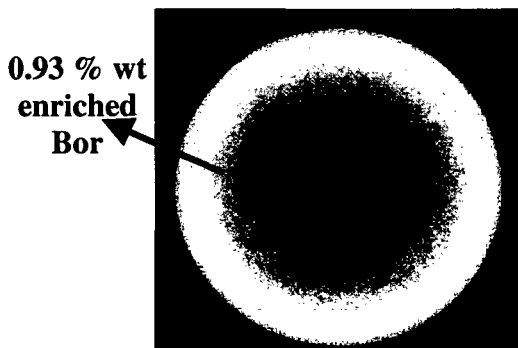


Fig. 7.17: 3D reconstructed images of a strong absorbing material having a diameter of 2 cm using 60 projections for 2 minutes exposure time,  $\Sigma_{\text{eff},t} = 7.4 \text{ cm}^{-1}$ , (left: uncorrected image, right: corrected image).

Fig. 7.18a, b and c show 3D reconstructed images of a 1.85 wt % natural boron – alloyed steel tube having 2 cm outer diameter and 1 cm inner diameter (hole), which was filled by a 0.93 wt % enriched boron – alloyed steel rod having 1 cm diameter. It demonstrates that this analytical correction can also be applied to the combination of materials having different boron contents.



a)



b)

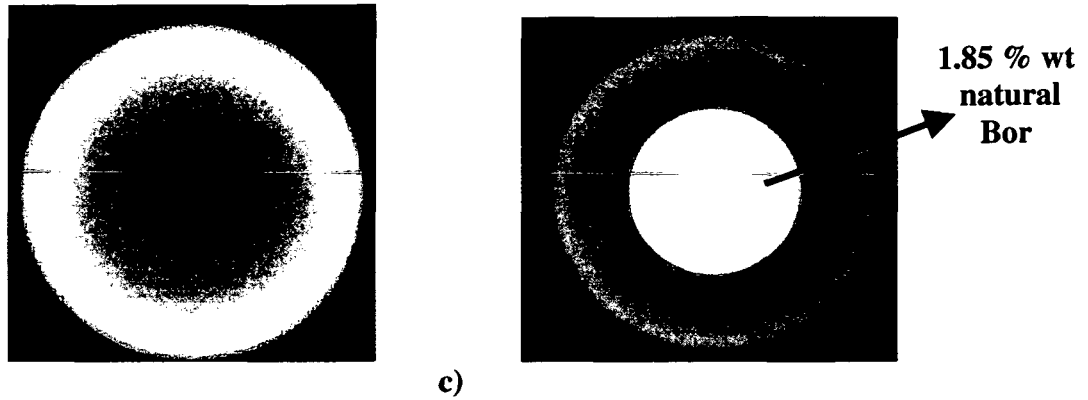


**Fig. 7.18:** a) 3D reconstructed images of cylindrical boron – alloyed steel rods, which was placed into one another. FBP method was used to reconstruct 60 projections for 2 minutes exposure time. Outer cylindrical rod of 2 cm diameter ( $\Sigma_t = 7.4 \text{ cm}^{-1}$ ) was partly filled with the second rod of 1 cm diameter ( $\Sigma_t = 4.4 \text{ cm}^{-1}$ ), b) reconstructed averaged slices at position – 1, without correction (left) and with correction (right), c) reconstructed averaged slice at position – 2, without correction (left) and with correction (right).

# 8

## Conclusion

Consequently, neutron radiography (NR) and neutron tomography (NT) are efficient tools to get information about the inner details of the materials nondestructively. The energy dependence of the neutron cross sections of elements was exploited in our material investigation with NR and NT. Developing three – dimensional image reconstruction program completed the NT facility at NR II at the Atominstitut of Austrian Universities. Surprisingly, different samples could be investigated successfully despite the weak neutron intensities of about  $10^5$  n/cm<sup>2</sup>s at NR facilities at ATI – Wien. Detection system at NR I facility is based on the X – ray film/Gd converter, and NR II facility on scintillator/digital CCD camera. Samples from different companies, such as shielding materials, structural and insulation materials for fusion reactor technology, manufacturing defects in TiAl turbine blade, ancient museum samples e.t.c., were investigated.

The porosity problem within fiber reinforced SiC/SiC ceramic composites and the quality of their bonding with metal pads was inspected with radiographic and tomographic methods. The inhomogeneous distribution of glue materials between SiC/SiC<sub>f</sub> composites and bonding with Cu metal pad could be visualized with thermal NR and NT. However, the thermal NR and NT fail in the investigations of 3 mm thick SiC/SiC<sub>f</sub> composites. Therefore, the specimens were examined at distinct neutron energies by using energy selective cold neutron radiography and tomography method, which gave more information about the inner structure than the commercial thermal neutron radiography. The ESNR measurements were carried out at PGA – PSI, which is based on the variation of the neutron spectrum using a mechanical neutron velocity selector.

The structural change like swelling within the insulation materials of toroidal field coils in ITER fusion device was investigated with NR and X – ray radiography. Because of the insufficient thickness, their tomographic inspections could not be realized. The Ansaldo and Alstom type fiber reinforced Kapton/R glass tapes showed different fiber structures and also

## 8. Conclusion

---

different neutron attenuation behaviors despite of the same material combination. Specially, the connection between fiber bundles and adhesive distribution yielded different contrasts in the radiographic inspections.

Strong absorbing material such as boron carbide should be distributed homogeneously to supply good shielding for neutrons. It is a fact that boron carbide cannot be distributed homogeneously by the present manufacturing methods. The distribution and size of boron carbide material within the steel matrix is a random process, which is dependent on the manufacturing process and manufacturer. Carrying out the NR measurements of boron – alloyed steels, which were produced by the Austrian Steel Production Company Böhler – Bleche GmbH, at NR II – ATI and NEUTRA – PSI gave a good opportunity to compare the quality of both facilities. The measured neutron attenuation coefficients showed clear differences from the expected values. The estimated effective secondary factors such as beam hardening effect, micro heterogeneous distribution of boron absorber within the shielding material, and background were analyzed with the help of the MCNP (Monte Carlo Neutron Particle) code. The good agreement between the experimental and simulated data allowed estimating the contribution of the beam hardening and also multiple scattered neutrons to the neutron transmission measurements. The strong influence of these factors on the attenuation coefficient of the boron – alloyed absorbing material was determined. The random distribution of boron in steel material (micro – heterogeneity) was simulated using a simple and general model in the MCNP input files. Beam hardening artifacts could be removed by an analytical correction for such simple geometric objects. The beam hardening correction presented two valuable effects. First, it has reproduced the correct macroscopic cross sections across the whole volume, and secondly, the image contrasts became dramatically enhanced at discontinuities. In order to verify this structural model and afore said factors, further experiments will be continued using different absorber materials and homogeneity distribution. Amazingly, neutron tomography of strong absorber materials is still possible with weak beam intensities noting the following difficulties:

- The low counts or intensity lead to increasing statistical fluctuations, which get amplified in the FBP (Filtered Back Projection) reconstruction. That means, in a NT investigation some difficulties can be related directly to the shortcomings of the FBP algorithm.
- Neutrons coming from the source enter sample and materials within the sample absorb and scatter some of them depending on their absorption and scattering cross sections. Some neutrons pass through the sample without any interaction with the materials. The image detector usually catches both (transmitted and scattered) neutrons; transmitted neutrons enter the detector directly from specimen, but the scattered neutrons come from the neighbor of the specimen, which carry no information about the sample. The contribution of background like scattered neutrons from the sample and the surrounding, gamma rays or light penetration in the light – tight detector box has to be suppressed as far as possible, because the imaging quality depends strongly on low background conditions

The commercial portable system JEN-3, which is used for routine material testing by Böhler – Bleche GmbH, was analyzed by means of MCNP code in order to describe its detection principle. The system performance of the JEN-3 system for the testing of shielding materials

## 8. Conclusion

---

such as boron – alloyed steels was also tested. The neutron radiography method was compared with the transmission data delivered from JEN-3 measurements. JEN-3 system is a very useful and portable system for routine material investigations with the appropriate beam optics especially for the analysis of shielding materials, which are used normally to shield scattered neutrons (fuel storage bins or transport baskets). The disadvantage of this system is the low neutron intensity, the impossibility for a localization of the inhomogeneities in the investigated samples and high background contribution on the neutron transmission measurements.

# 9

## Appendix I: 3D Image Reconstruction Program

In order to process neutron tomography (NT) projections and reconstruct 3 dimensionally, the following program was written using IDL software. The main program takes the name from the part of “*Pro RECONSTRUCTION*“, which was written in italic as shown in program below. On account of this, the file must be saved as “reconstruction.pro”. That means if you want to optimize this program, it must be saved in the same name of the program name (e.g. if the program is named “pro name”, then the program file should be saved “name.pro”). After compilation and running it, a special window appears on the monitor (see chapter 4). Some parameters have been given as a constant, which can be also added into this window using Widget functions (e.g. parameters for Flat Field correction).

The main program “Reconstruction.pro” contains 7 sub programs, which start with “pro” command, and 2 functions having following names respectively:

- Quit (sub-program to stop the process)
- Preview-Axis (sub-program to check rotation axis)
- Doall (sub-program)
- Wid\_base\_0\_event (to generate Preference window)
- Wid\_base\_0 (to generate preference window for input parameters)
- Shepp\_Logan (function for filtering)
- Remove\_negav\_treh (function to remove white spots and negative values)
- Menek (sub-program)
- Process (sub-program)

## 9. Appendix I: 3D Image Reconstruction Program

---

```
;*****  
; This special program for Atominstitut-Wien NT measurements processes and  
;reconstructs projections.  
; It was generated on 09.05.2001 by M. Bastürk  
;*****  
;  
Pro Quit, Event  
Widget_Control, Event.Top, /Destroy  
stop,'process.pro'  
End  
  
Pro Preview_Axis, Event  
  
;*****  
; Determination of preference window like left, right, top, botton, number of angles, image  
;names, file path and e.t.c.  
;*****  
  
Widget_Control, widget_info(Event.top, FIND_BY_UNAME='nangles'), $  
GET_VALUE=strnangles  
Widget_Control, widget_info(Event.top, FIND_BY_UNAME='cols'), GET_VALUE=strcols  
Widget_Control, widget_info(Event.top, FIND_BY_UNAME='rows'), $  
GET_VALUE=strrows  
Widget_Control, widget_info(Event.top, FIND_BY_UNAME='SizingTextOben'), $  
GET_VALUE=strop  
Widget_Control, widget_info(Event.top, FIND_BY_UNAME='SizingTextUnten'), $  
GET_VALUE=strbottom  
Widget_Control, widget_info(Event.top, FIND_BY_UNAME='SizingTextRechts'), $  
GET_VALUE=stright  
Widget_Control, widget_info(Event.top, FIND_BY_UNAME='SizingTextLinks'), $  
GET_VALUE=strleft  
Widget_Control, widget_info(Event.top, FIND_BY_UNAME='Pfad_original'), $  
GET_VALUE=pfad  
Widget_Control, widget_info(Event.top, FIND_BY_UNAME='Objectimages'), $  
GET_VALUE=name  
  
nangles=FIX(strnangles(0))  
cols=FIX(strcols(0))  
rows=FIX(strrows(0))  
oben=FIX(strop(0))  
unten=FIX(strbottom(0))  
links=FIX(strleft(0))  
rechts=FIX(stright(0))  
  
cd, pfad(0)  
  
lastnr=strcompress(nangles+1,/remove_all)  
print, lastnr
```



```

bild1=name(0)+'1'+'.raw'
bild201=name(0)+lastnr+'.raw'

print, 'cols=', cols, 'rows=', rows
    firstimage=make_array(cols,rows,/uint)
    openR,1,bild1
    bir=assoc(1,make_array(cols,rows,/uint))
    firstimage(*,*)=bir[0]
    close,1
lastimage=make_array(cols,rows,/uint)
openR,1,bild201
    iki=assoc(1,make_array(cols,rows,/uint))
    lastimage(*,*)=iki[0]
close,1
write_tiff,'firstimage.tif',firstimage,/short
write_tiff,'lastimage.tif',lastimage,/short
firstimage=read_tiff('firstimage.tif',/unsigned)
lastimage=read_tiff('lastimage.tif',/unsigned)
x=firstimage-reverse(lastimage)

;*****
; If contrast enhancement is necessary, use BytScl command
; mx=BytScl(x,Min=0,Max=8000,Top=1000)
;*****
window,1,title='0-180° without rotation axis correction'
tvsc1,x

;Check the matrix size
sizeinfo=size(firstimage)
cols=sizeinfo(1)
rows=sizeinfo(2)
print, 'cols=', cols, 'rows=', rows

;Image cutting from the sides to find rotation axis
change=firstimage(links:cols-rechts-1,unten:rows-oben-1)
lastimage=lastimage(links:cols-rechts-1,oben:rows-unten-1)
lastimage=Reverse(lastimage)
newbild=change-lastimage

;*****
; If you want to save the difference image in tiff format, use write_tiff command
; write_tiff,'lastimage_mask.tif',lastimage,/short
;To see images on the monitor, use tvsc1 command
;close,1
;window, 2, title = 'Original'
;tvsc1, firstimage
;window, 3, title = 'size changed'
;tvsc1, change

```

## 9. Appendix I: 3D Image Reconstruction Program

---

```

;*****

window, 4, title = 'Imageaxis corrected'
tvsc1, newbild
print,'size=',size(change)
End
;
Pro Doall
End
;
; IDL Widget Interface Procedures
;
Pro WID_BASE_0_event, Event

wWidget = Event.top

case Event.id of

Widget_Info(wWidget, FIND_BY_UNAME='SizingButtonPreview'): begin
    If( Tag_Names(Event, /STRUCTURE_NAME) eq 'WIDGET_BUTTON' )then $
        Preview_Axis, Event
End

Widget_Info(wWidget, FIND_BY_UNAME='AllButtonPerform'): begin
    If( Tag_Names(Event, /STRUCTURE_NAME) eq 'WIDGET_BUTTON' )then $
        menek, Event
End

Widget_Info(wWidget, FIND_BY_UNAME='ButtonQuit'): begin
    If( Tag_Names(Event, /STRUCTURE_NAME) eq 'WIDGET_BUTTON' )then $
        Quit, Event
End
    else:
        endcase
End

Pro WID_BASE_0, GROUP_LEADER=wGroup, _EXTRA=_VWBExtra_

Resolve_Routine, 'Doall' ; Load event callback routines

Resolve_Routine, 'process' ; Load event callback routines

WID_BASE_0 = Widget_Base( GROUP_LEADER=wGroup, UNAME='WID_BASE_0' $
,SCR_XSIZE=400 ,SCR_YSIZE=500 ,TITLE='Window of the Input parameters'+ $
' for the image reconstruction' ,SPACE=3 ,XPAD=3 ,YPAD=3)

SizingTextOben = Widget_Text(WID_BASE_0, UNAME='SizingTextOben' $
,XOFFSET=153 ,YOFFSET=150 ,SCR_XSIZE=38 ,SCR_YSIZE=20 $
```

## 9. Appendix I: 3D Image Reconstruction Program

---

```
/EDITABLE ,/ALL_EVENTS ,XSIZE=20 ,YSIZE=1)
```

```
SizingTextUnten = Widget_Text(WID_BASE_0, UNAME='SizingTextUnten' $  
,XOFFSET=153 ,YOFFSET=180 ,SCR_XSIZE=38 ,SCR_YSIZE=20 $  
,/EDITABLE ,XSIZE=20 ,YSIZE=1)
```

```
NumberSliceErst = Widget_Text(WID_BASE_0, UNAME='NumberSliceErst' $  
,XOFFSET=63 ,YOFFSET=210 ,SCR_XSIZE=38 ,SCR_YSIZE=20 $  
,/EDITABLE ,XSIZE=20 ,YSIZE=1)
```

```
NumberSliceLast = Widget_Text(WID_BASE_0, UNAME='NumberSliceLast' $  
,XOFFSET=153 ,YOFFSET=210 ,SCR_XSIZE=38 ,SCR_YSIZE=20 $  
,/EDITABLE ,XSIZE=20 ,YSIZE=1)
```

```
WID_LABEL_14 = Widget_Label(WID_BASE_0, UNAME='WID_LABEL_0' $  
,XOFFSET=21 ,YOFFSET=210 ,SCR_XSIZE=42 ,SCR_YSIZE=20 $  
,/ALIGN_LEFT ,VALUE='slicefirst')
```

```
WID_LABEL_15 = Widget_Label(WID_BASE_0, UNAME='WID_LABEL_0' $  
,XOFFSET=112 ,YOFFSET=210 ,SCR_XSIZE=42 ,SCR_YSIZE=20 $  
,/ALIGN_LEFT ,VALUE='slicelast')
```

```
WID_LABEL_0 = Widget_Label(WID_BASE_0, UNAME='WID_LABEL_0' $  
,XOFFSET=112 ,YOFFSET=150 ,SCR_XSIZE=36 ,SCR_YSIZE=20 $  
,/ALIGN_LEFT ,VALUE='top')
```

```
WID_LABEL_1 = Widget_Label(WID_BASE_0, UNAME='WID_LABEL_1' $  
,XOFFSET=112 ,YOFFSET=180 ,/ALIGN_LEFT ,VALUE='bottom')
```

```
SizingTextRechts = Widget_Text(WID_BASE_0, UNAME='SizingTextRechts' $  
,XOFFSET=63 ,YOFFSET=180 ,SCR_XSIZE=38 ,SCR_YSIZE=20 $  
,/EDITABLE ,XSIZE=20 ,YSIZE=1)
```

```
SizingTextLinks = Widget_Text(WID_BASE_0, UNAME='SizingTextLinks' $  
,XOFFSET=63 ,YOFFSET=150 ,SCR_XSIZE=37 ,SCR_YSIZE=20 $  
,/EDITABLE ,XSIZE=20 ,YSIZE=1)
```

```
WID_LABEL_2 = Widget_Label(WID_BASE_0, UNAME='WID_LABEL_2' $  
,XOFFSET=21 ,YOFFSET=180 ,SCR_XSIZE=36 ,SCR_YSIZE=20 $  
,/ALIGN_LEFT ,VALUE='right')
```

```
nangles = Widget_Text(WID_BASE_0, UNAME='nangles', XOFFSET=240 $  
,YOFFSET=28, SCR_XSIZE=38 ,SCR_YSIZE=16, /EDITABLE ,XSIZE=20 ,YSIZE=1)
```

```
cols = Widget_Text(WID_BASE_0, UNAME='cols', XOFFSET=240 ,YOFFSET=53 $  
,SCR_XSIZE=38 ,SCR_YSIZE=16, /EDITABLE ,XSIZE=20 ,YSIZE=1)
```

```
rows = Widget_Text(WID_BASE_0, UNAME='rows', XOFFSET=240, $
```

## 9. Appendix I: 3D Image Reconstruction Program

---

```
YOFFSET=78, SCR_XSIZE=38 ,SCR_YSIZE=16, /EDITABLE ,XSIZE=20 ,YSIZE=1)
```

```
WID_LABEL_12 = Widget_Label(WID_BASE_0, UNAME='WID_LABEL_12' $  
,XOFFSET=200 ,YOFFSET=53 ,SCR_XSIZE=38 ,SCR_YSIZE=20 $  
,/ALIGN_LEFT ,VALUE='cols')
```

```
WID_LABEL_13 = Widget_Label(WID_BASE_0, UNAME='WID_LABEL_13' $  
,XOFFSET=200 ,YOFFSET=78 ,SCR_XSIZE=38 ,SCR_YSIZE=20 $  
,/ALIGN_LEFT ,VALUE='rows')
```

```
WID_LABEL_16 = Widget_Label(WID_BASE_0, UNAME='WID_LABEL_16' $  
,XOFFSET=200 ,YOFFSET=28 ,SCR_XSIZE=38 ,SCR_YSIZE=20 $  
,/ALIGN_LEFT ,VALUE='nangles')
```

```
WID_LABEL_3 = Widget_Label(WID_BASE_0, UNAME='WID_LABEL_3' $  
,XOFFSET=21 ,YOFFSET=150 ,/ALIGN_LEFT ,VALUE='left')
```

```
WID_LABEL_4 = Widget_Label(WID_BASE_0, UNAME='WID_LABEL_4' $  
,XOFFSET=8 ,YOFFSET=130 ,SCR_XSIZE=250 ,SCR_YSIZE=20 $  
,/ALIGN_LEFT ,VALUE='Parameters for the image processing')
```

```
WID_LABEL_17 = Widget_Label(WID_BASE_0, UNAME='WID_LABEL_17' $  
,XOFFSET=8 ,YOFFSET=310 ,SCR_XSIZE=350 ,SCR_YSIZE=20, /ALIGN_LEFT $  
,VALUE='Parameters for FlatField (if you do not have middle mouse button)')
```

```
WID_LABEL_18 = Widget_Label(WID_BASE_0, UNAME='WID_LABEL_18' $  
,XOFFSET=21 ,YOFFSET=340 ,SCR_XSIZE=60 ,SCR_YSIZE=20, /ALIGN_LEFT $  
,VALUE='firstcolumn')
```

```
firstcolumn = Widget_Text(WID_BASE_0, UNAME='firstcolumn', XOFFSET=90 $  
,YOFFSET=340 ,SCR_XSIZE=40 ,SCR_YSIZE=20, /EDITABLE ,XSIZE=20 ,YSIZE=1)
```

```
WID_LABEL_19 = Widget_Label(WID_BASE_0, UNAME='WID_LABEL_19' $  
,XOFFSET=140 ,YOFFSET=340 ,SCR_XSIZE=60 ,SCR_YSIZE=20, /ALIGN_LEFT $  
,VALUE='lastcolumn')
```

```
lastcolumn = Widget_Text(WID_BASE_0, UNAME='lastcolumn', XOFFSET=210 $  
,YOFFSET=340 ,SCR_XSIZE=40 ,SCR_YSIZE=20, /EDITABLE ,XSIZE=20 ,YSIZE=1)
```

```
WID_LABEL_20 = Widget_Label(WID_BASE_0, UNAME='WID_LABEL_20' $  
,XOFFSET=21 ,YOFFSET=370 ,SCR_XSIZE=60 ,SCR_YSIZE=19, /ALIGN_LEFT $  
,VALUE='firstrow')
```

```
firstrow = Widget_Text(WID_BASE_0, UNAME='firstrow', XOFFSET=90 $  
,YOFFSET=370 ,SCR_XSIZE=40 ,SCR_YSIZE=20, /EDITABLE ,XSIZE=20 ,YSIZE=1)
```

```
WID_LABEL_21 = Widget_Label(WID_BASE_0, UNAME='WID_LABEL_21' $  
,XOFFSET=140 ,YOFFSET=370 ,SCR_XSIZE=60 ,SCR_YSIZE=20, /ALIGN_LEFT $
```

## 9. Appendix I: 3D Image Reconstruction Program

---

,VALUE='lastrow')

lastrow = Widget\_Text(WID\_BASE\_0, UNAME='lastrow', XOFFSET=210 \$  
,YOFFSET=370 ,SCR\_XSIZE=45 ,SCR\_YSIZE=20, /EDITABLE ,XSIZE=20,YSIZE=1)

WID\_LABEL\_22 = Widget\_Label(WID\_BASE\_0, UNAME='WID\_LABEL\_22' \$  
,XOFFSET=8 ,YOFFSET=400 ,SCR\_XSIZE=60 ,SCR\_YSIZE=20, /ALIGN\_LEFT \$  
,VALUE='resolution')

resolution = Widget\_Text(WID\_BASE\_0, UNAME='resolution', XOFFSET=70 \$  
,YOFFSET=400 ,SCR\_XSIZE=45 ,SCR\_YSIZE=20, /EDITABLE ,XSIZE=20 ,YSIZE=1)

WID\_LABEL\_23 = Widget\_Label(WID\_BASE\_0, UNAME='WID\_LABEL\_23' \$  
,XOFFSET=130 ,YOFFSET=400 ,SCR\_XSIZE=60 ,SCR\_YSIZE=20, /ALIGN\_LEFT \$  
,VALUE='kernelsize')

kernelsize = Widget\_Text(WID\_BASE\_0, UNAME='kernelsize', XOFFSET=190 \$  
,YOFFSET=400 ,SCR\_XSIZE=45 ,SCR\_YSIZE=20, /EDITABLE ,XSIZE=20 ,YSIZE=1)

WID\_LABEL\_24 = Widget\_Label(WID\_BASE\_0, UNAME='WID\_LABEL\_24' \$  
,XOFFSET=250 ,YOFFSET=400 ,SCR\_XSIZE=60 ,SCR\_YSIZE=20, /ALIGN\_LEFT \$  
,VALUE='filterwidth')

filterwidth = Widget\_Text(WID\_BASE\_0, UNAME='filterwidth', XOFFSET=310 \$  
,YOFFSET=400 ,SCR\_XSIZE=45 ,SCR\_YSIZE=20, /EDITABLE ,XSIZE=20 ,YSIZE=1)

WID\_LABEL\_25 = Widget\_Label(WID\_BASE\_0, UNAME='WID\_LABEL\_25' \$  
,XOFFSET=260 ,YOFFSET=240 ,SCR\_XSIZE=70 ,SCR\_YSIZE=20, /ALIGN\_LEFT \$  
,VALUE='open\_number')

open\_number = Widget\_Text(WID\_BASE\_0, UNAME='open\_number', XOFFSET=340 \$  
,YOFFSET=240 ,SCR\_XSIZE=27 ,SCR\_YSIZE=20, /EDITABLE ,XSIZE=20 ,YSIZE=1)

WID\_LABEL\_26 = Widget\_Label(WID\_BASE\_0, UNAME='WID\_LABEL\_26' \$  
,XOFFSET=21 ,YOFFSET=430 ,SCR\_XSIZE=30 ,SCR\_YSIZE=20, /ALIGN\_LEFT \$  
,VALUE='nair')

nair = Widget\_Text(WID\_BASE\_0, UNAME='nair', XOFFSET=70 ,YOFFSET=430 \$  
,SCR\_XSIZE=45 ,SCR\_YSIZE=20, /EDITABLE ,XSIZE=20 ,YSIZE=1)

WID\_LABEL\_27 = Widget\_Label(WID\_BASE\_0, UNAME='WID\_LABEL\_27' \$  
,XOFFSET=130 ,YOFFSET=430 ,SCR\_XSIZE=70 ,SCR\_YSIZE=20, /ALIGN\_LEFT \$  
,VALUE='reconvolume')

reconvolume = Widget\_Text(WID\_BASE\_0, UNAME='reconvolume', XOFFSET=210 \$  
,YOFFSET=430 ,SCR\_XSIZE=80 ,SCR\_YSIZE=20, /EDITABLE ,XSIZE=20 ,YSIZE=1)

WID\_LABEL\_28 = Widget\_Label(WID\_BASE\_0, UNAME='WID\_LABEL\_28' \$

## 9. Appendix I: 3D Image Reconstruction Program

---

```
,XOFFSET=130 ,YOFFSET=240 ,SCR_XSIZE=65 ,SCR_YSIZE=20, /ALIGN_LEFT $  
,VALUE='maxthreshold')
```

```
maxthreshold = Widget_Text(WID_BASE_0, UNAME='maxthreshold', XOFFSET=200 $  
,YOFFSET=240 ,SCR_XSIZE=40 ,SCR_YSIZE=20, /EDITABLE ,XSIZE=20 ,YSIZE=1)
```

```
WID_LABEL_29 = Widget_Label(WID_BASE_0, UNAME='WID_LABEL_29' $  
,XOFFSET=7 ,YOFFSET=240 ,SCR_XSIZE=60 ,SCR_YSIZE=20, /ALIGN_LEFT $  
,VALUE='minthreshold')
```

```
minthreshold = Widget_Text(WID_BASE_0, UNAME='minthreshold', XOFFSET=80 $  
,YOFFSET=240 ,SCR_XSIZE=40 ,SCR_YSIZE=20, /EDITABLE ,XSIZE=20 ,YSIZE=1)
```

```
selection = Widget_Text(WID_BASE_0, UNAME='selection', XOFFSET=260 $  
,YOFFSET=275 ,SCR_XSIZE=40 ,SCR_YSIZE=20, /EDITABLE ,XSIZE=20 ,YSIZE=1)
```

```
WID_LABEL_30 = Widget_Label(WID_BASE_0, UNAME='WID_LABEL_30' $  
,XOFFSET=8 ,YOFFSET=275 ,SCR_XSIZE=250 ,SCR_YSIZE=20, /ALIGN_LEFT $  
,VALUE='Enter 1 to determine the flat field with the mouse -->')
```

```
ButtonQuit = Widget_Button(WID_BASE_0, UNAME='ButtonQuit', XOFFSET=320 $  
,YOFFSET=160 ,SCR_XSIZE=50 ,SCR_YSIZE=30, /ALIGN_CENTER ,VALUE='Quit')
```

```
AllButtonPerform = Widget_Button(WID_BASE_0, UNAME='AllButtonPerform' $  
,XOFFSET=228 ,YOFFSET=180, SCR_XSIZE=80 ,SCR_YSIZE=30 ,/ALIGN_CENTER $  
,VALUE='Do all!')
```

```
WID_LABEL_7 = Widget_Label(WID_BASE_0, UNAME='WID_LABEL_7' $  
,XOFFSET=8 ,YOFFSET=6 ,SCR_XSIZE=99 ,SCR_YSIZE=20 ,/ALIGN_LEFT $  
,VALUE='Preferences')
```

```
openimages = Widget_Text(WID_BASE_0, UNAME='openimages', XOFFSET=100 $  
,YOFFSET=30 ,SCR_XSIZE=50 ,SCR_YSIZE=20 ,/EDITABLE , YSIZE=1)
```

```
darkimages = Widget_Text(WID_BASE_0, UNAME='Darkimages', XOFFSET=100 $  
,YOFFSET=49 ,SCR_XSIZE=50 ,SCR_YSIZE=20 ,/EDITABLE ,XSIZE=20, YSIZE=1)
```

```
objectimages = Widget_Text(WID_BASE_0, UNAME='OBJECTIMAGES' $  
,XOFFSET=100, YOFFSET=68 ,SCR_XSIZE=50 ,SCR_YSIZE=20 ,/EDITABLE $  
,XSIZE=20, YSIZE=1)
```

```
WID_LABEL_8 = Widget_Label(WID_BASE_0, UNAME='WID_LABEL_8' $  
,XOFFSET=7 ,YOFFSET=32 ,SCR_XSIZE=80 ,SCR_YSIZE=20 ,/ALIGN_LEFT $  
,VALUE='openimages')
```

```
WID_LABEL_9 = Widget_Label(WID_BASE_0, UNAME='WID_LABEL_9' $  
,XOFFSET=7 ,YOFFSET=51 ,SCR_XSIZE=80 ,SCR_YSIZE=20 ,/ALIGN_LEFT $  
,VALUE='darkimages')
```

## 9. Appendix I: 3D Image Reconstruction Program

---

```
WID_LABEL_10 = Widget_Label(WID_BASE_0, UNAME='WID_LABEL_10' $  
,XOFFSET=7 ,YOFFSET=70 ,SCR_XSIZE=85 ,SCR_YSIZE=20 ,ALIGN_LEFT $  
,VALUE='Objectimages')
```

```
pfad_original = Widget_Text(WID_BASE_0, UNAME='PFAD_ORIGINAL' $  
,XOFFSET=115,YOFFSET=105,SCR_XSIZE=250,SCR_YSIZE=20,/EDITABLE $  
,XSIZE=20 ,YSIZE=1)
```

```
WID_LABEL_11 = Widget_Label(WID_BASE_0, UNAME='WID_LABEL_11' $  
,XOFFSET=8 ,YOFFSET=105 ,SCR_XSIZE=95 ,SCR_YSIZE=20 $  
,ALIGN_LEFT ,VALUE='Pfad Originalimages')
```

```
SizingButtonPreview = Widget_Button(WID_BASE_0, $  
UNAME='SizingButtonPreview' ,XOFFSET=228 ,YOFFSET=150 $  
,SCR_XSIZE=80 ,SCR_YSIZE=20 ,ALIGN_CENTER ,VALUE='Preview')
```

```
Widget_Control, /REALIZE, WID_BASE_0
```

```
XManager, 'WID_BASE_0', WID_BASE_0
```

**End**

```
;  
;  
; RECONSTRUCTION ;  
;  
;  
;*****
```

```
PRO RECONSTRUCTION, GROUP_LEADER=wGroup, _EXTRA=_VWBExtra_  
WID_BASE_0, GROUP_LEADER=wGroup, _EXTRA=_VWBExtra_  
End
```

```
Function SHEPP_LOGAN,x,d  
d=!pi^2*d*(1-.4.*x^2)  
zeros=where(abs(d) le 1.0e-6,count)  
if(count ne 0) then d[zeros]=0.001  
return,2./d
```

**End**

```
Function Remove_negav_thres,image,dimen_size  
output=image  
threshold=1.1  
limit=0.0  
for i=0,dimen_size-1 do begin  
col=reform(output[i,*])  
bad=where(col le limit, count)  
if (count ne 0 ) then begin
```

```

col[bad]=limit
output[i,*]=col
endif
endfor
ratio=float(image)/smooth(image,3)
zinger=where(ratio gt threshold, count)
if(count gt 0) then $
output[zinger]=(output[zinger-2]+output[zinger+2])/2.
output=median(output,3)
return,output

```

**End**

**Pro menek, Event**

```

Widget_Control, widget_info(Event.top, FIND_BY_UNAME='PFAD_ORIGINAL'), $
GET_VALUE=pfad
Widget_Control, widget_info(Event.top, FIND_BY_UNAME='SizingTextOben'), $
GET_VALUE=strtop
Widget_Control, widget_info(Event.top, FIND_BY_UNAME='SizingTextUnten'), $
GET_VALUE=strbottom
Widget_Control, widget_info(Event.top, FIND_BY_UNAME='SizingTextRechts'), $
GET_VALUE=strright
Widget_Control, widget_info(Event.top, FIND_BY_UNAME='SizingTextLinks'), $
GET_VALUE=strleft
Widget_Control, widget_info(Event.top, FIND_BY_UNAME='NumberSliceErst'), $
GET_VALUE=strslicefirst
Widget_Control, widget_info(Event.top, FIND_BY_UNAME='nangles'), $
GET_VALUE=strnangles
Widget_Control, widget_info(Event.top, FIND_BY_UNAME='cols'), GET_VALUE=strcols
Widget_Control, widget_info(Event.top, FIND_BY_UNAME='rows'), $
GET_VALUE=strrows
Widget_Control, widget_info(Event.top, FIND_BY_UNAME='NumberSliceLast'), $
GET_VALUE=strslicelast
Widget_Control, widget_info(Event.top, FIND_BY_UNAME='OBJECTIMAGES'), $
GET_VALUE=name
Widget_Control, widget_info(Event.top, FIND_BY_UNAME='resolution'), $
GET_VALUE=strresolution
Widget_Control, widget_info(Event.top, FIND_BY_UNAME='kernelsize'), $
GET_VALUE=strkernelsize
Widget_Control, widget_info(Event.top, FIND_BY_UNAME='filterwidth'), $
GET_VALUE=strfilterwidth
Widget_Control, widget_info(Event.top, FIND_BY_UNAME='open_number'), $
GET_VALUE=stropen_number
Widget_Control, widget_info(Event.top, FIND_BY_UNAME='nair'), GET_VALUE=strnair
Widget_Control, widget_info(Event.top, FIND_BY_UNAME='openimages'), $
GET_VALUE=hell
Widget_Control, widget_info(Event.top, FIND_BY_UNAME='darkimages'), $
GET_VALUE=dunkle

```



## 9. Appendix I: 3D Image Reconstruction Program

---

```
Widget_Control, widget_info(Event.top, FIND_BY_UNAME='reconvolume'), $
GET_VALUE=recondat
Widget_Control, widget_info(Event.top, FIND_BY_UNAME='maxthreshold'), $
GET_VALUE=strmaxthres
Widget_Control, widget_info(Event.top, FIND_BY_UNAME='minthreshold'), $
GET_VALUE=strminthres
Widget_Control, widget_info(Event.top, FIND_BY_UNAME='selection'), $
GET_VALUE=strmaus
Widget_Control, widget_info(Event.top, FIND_BY_UNAME='firstcolumn'), $
GET_VALUE=strfirstcolumn
Widget_Control, widget_info(Event.top, FIND_BY_UNAME='lastcolumn'), $
GET_VALUE=strlastcolumn
Widget_Control, widget_info(Event.top, FIND_BY_UNAME='firstrow'), $
GET_VALUE=strfirstrow
Widget_Control, widget_info(Event.top, FIND_BY_UNAME='lastrow'), $
GET_VALUE=strlastrow
```

```
*****
; Input Parameters for the PROGRAM
*****
```

```
nangles=FIX(strnangles(0))
cols=FIX(strcols(0))
rows=FIX(strrows(0))
oben=FIX(strtop(0))
unten=FIX(strbottom(0))
links=FIX(strleft(0))
rechts=FIX(strright(0))
sliceErst=FIX(strSlicefirst(0))
sliceLast=FIX(strSlicelast(0))
mouse=FIX(strmaus(0))
kernelsize=FIX(strkernelsize(0)) ; determine the matrix size for the reconstruction
Auflösung=FIX(stresolution(0)) ; to eliminate some bad pixel values
width=FIX(strfilterwidth(0)) ; width of kernel size of median filter
dark_number=FIX(stropen_number(0))
open_number=dark_number
nair=FIX(strnair(0)) ; # of columns to normalize images from each side (left, right)
open=hell(0)
distance=1
dark=dunkle(0)
data_name=recondat(0) ; the file name for the output volume data
; 3D reconstructed data prepared for the VG STUDIOMAX
a=FIX(strfirstcolumn(0)) ;the begin of the cols for flat field area
b=FIX(strlastcolumn(0)) ;end of the cols
c=FIX(strfirstrow(0)) ;begin of the rows
d=FIX(strlastrow(0)) ;end of the rows
xz=FIX(strmaxthres(0)) ; max. threshold value max. intensity on a image
; for elimination of higher and lower values
```

```

yz=FIX(strminthres(0)) ; lower threshold value min. intensity on a image

;*****
;*****

;*****
; Descriptions of the used Matrix Elements
;*****

cd,pfad(0)

raw_data=make_array(cols,rows,/uint)
norm_data=make_array(cols,rows,/uint)
norm_data1=make_array(cols,rows,/float)
he_data=make_array(cols,rows,open_number,/uint)
du_data=make_array(cols,rows,dark_number,/uint)
hell=make_array(cols,rows,/float,value=0)
dunkel=make_array(cols,rows,/float,value=0)
volume=make_array(cols,rows,nangles,/uint)

;*****
; Cutting all projections according to the rotation axis
;*****
irow_min=unten
nrows=rows-unten-oben
irow_max=irow_min+nrows-1
icol_min=links
ncols=cols-icol_min-rechts
icol_max=icol_min+ncols-1

vol_mask=make_array(ncols,nrows,nangles,/uint)

;*****
; Determination of the first and last slice number for 3-D Demonstration
;*****

nslice=slicelast-sliceerst ;Total slice number to be reconstructed
recon_vol=make_array(ncols,nrows,nslice,/uint)
reconimage=fltarr(ncols,nrows)
sinogram=make_array(ncols,nangles,/float)
sinogcorr=make_array(ncols,nangles,/uint)
print,'ndime_recon_vol',size(recon_vol)

;*****
; ZERO - PADDING
;*****

np=fix(sqrt(2.)*ncols/distance+kernelsize+4)

```

## 9. Appendix I: 3D Image Reconstruction Program

---

```
print, 'np=', np
p=fltarr(np)
print, 'size_p=', size(p)
sinogramimage=fltarr(np, nangles)
convolvedsinogramimage=fltarr(np, nangles)
convolsinog=make_array(np, nangles, /uint)

;*****
; Reading input open beam images
;*****

for i=1, dark_number do begin
    close, 1
    fnr=strcompress(i, /remove_all)
    file_open=open+fnr+'.raw'
    openr, 1, file_open
    in_array=assoc(1, make_array(cols, rows, /uint))
    he_data[*, *, i-1]=remove_negav_thres(in_array[0], cols)
    close, 1

;*****
; Reading input dark beam images
;*****

    fnr=strcompress(i, /remove_all)
    file_dark=dark+fnr+'.raw'
    openr, 1, file_dark
    in_array=assoc(1, make_array(cols, rows, /uint))
    du_data[*, *, i-1]=remove_negav_thres(in_array[0], cols)
    close, 1
endfor
write_tiff, 'c:\transfer\schloss_280503\dark20s.tif', du_data[*, *, 3], /short
for i=0, open_number-1 do begin
    hell=hell+he_data[*, *, i]
    dunkel=dunkel+du_data[*, *, i]
endfor
hell=hell/5
; write_tiff, 'c:\tomo\motor\volume_open.tif', hell, /short
dunkel=dunkel/5

;***** determination of flat field area on the first objectimage *****

birinci=read_tiff('birinci.tif', /unsigned)
tvsc1, birinci
box_cursor, xair0, yair0, nxair, nyair, /message
print, 'xair0, yair0, nxair, nyair=', xair0, yair0, nxair, nyair
```

```

;*****
; Reading of the input object images
;*****

for i=0,nangles-1 do begin

    cd, pfad(0)
    file=name(0)
    fnr=strcompress(i+1,/remove_all)
    file=file+fnr+'.raw'
    openr,1,file
    ;print,format=('File:',a50),file
    in_array=assoc(1,make_array(cols,rows,/uint))
    raw_data=remove_negav_thres(in_array[0],cols)

;*****
; open and darkbeam correction over all objectimages
;*****

    norm_data1=20000*float(raw_data-dunkel)/(hell-dunkel)

; 20000 is scaling factor to visualize images on the monitor, you can also use maxthreshold
; value oder max intensity on an image instead of this scaling factor

    tvscl, norm_data1,0

;*****Flat-Field Correction*****

if (mouse eq 1) then begin
    a=xair0
    b=xair0+nxair
    c=yair0
    d=yair0+nyair
    field=fltarr(nxair+1,nyair+1)
    field(*,*)=norm_data1(a:b,c:d)
    flat=median(field)

endif else begin

    x=b-a+1 ;cols of the area from the images for flat field correction
    y=d-c+1 ;rows of the area from the images for flat field correction
    field=fltarr(x,y)
    field(*,*)=norm_data1(a:b,c:d)
    flat=median(field)

endelse

    norm_data=uint(20000*float(norm_data1/flat))

```

```

write_tiff,'volume.tif',norm_data,/short
endfor

;*****

tvsc1,norm_data,1
volume[*,* ,i]=norm_data[*,*]
close,1
Endfor

;*****
; removing lower and higher frequencies
;*****

vol=make_array(cols,rows,nangles,/uint)
for i=0, nangles-1 do begin
vol=reform(volume[*,* ,i])
bad=where(volume[*,* ,i] gt xz, count)
bad_1=where(volume[*,* ,i] lt yz,count_1)
if (count ne 0 ) then begin
vol[bad]=xz
volume[*,* ,i]=vol
endif
if (count_1 ne 0 ) then begin
vol[bad_1]=yz
volume[*,* ,i]=vol
endif
tvsc1,volume[*,* ,i],3
endfor
;*****
print,'volume_size',size(volume),'vol_mask_size',size(vol_mask)
vol_mask[0:ncols-1,0:nrows-1,*]=volume[icol_min:icol_max,irow_min:irow_max,*]
tvsc1,vol_mask[*,* ,0],3

;*****
; Creation of SINOGRAMS
;*****

for j=sliceerst,slicelast-1 do begin
raw_sin=reform(vol_mask[* ,j,*])
air_min_1=0
air_max_1=air_min_1+nair-1
air_min_2=ncols-nair
air_max_2=air_min_2+nair-1
air_vek=make_array(2*nair,nangles,/uint)
air_vek(0:nair-1,* )=raw_sin(air_min_1:air_max_1,* )
air_vek(nair:2*nair-1,* )=raw_sin(air_min_2:air_max_2,* )

```

## 9. Appendix I: 3D Image Reconstruction Program

---

```
for i=0,nangles-1 do begin
    air=total(air_vek[* ,i])/(2*nair)
    sinogram[* ,i]=-alog(raw_sin[* ,i]/air>1.e-5)
endfor
sinogram[where(sinogram LE 0)]=0
fnr=strcompress(j,/remove_all)
;window,4,title='raw_sinogram'
;tvsc1,raw_sin[* ,*],1

;*****
; FILTERUNG
;*****

x=findgen(2*kernelsize+1)-kernelsize
d=distance
ker=call_function('shepp_logan',x,d)
;plot,ker
window,5,title='ker,auswertung'
ker=ker/(total(ker)*nangles*sqrt(ncols))
;print,'nauswert_shepp_logan=new_ker', ker
;wset,1 & plot,ker
center=(icol_max-icol_min)/2
shiftvalue=(np-ncols)/2.
nshift=fix(shiftvalue)
center_value=center+shiftvalue

;*****
; REMOVE-RINGS
;*****

rem_width=3
ave=total(sinogram,2)/nangles
diff=ave-smooth(ave,rem_width)
for i=0,nangles-1 do sinogram(0,i)=sinogram(*,i)-diff

window,6,title='sinogconvolved'

for i=0,nangles-1 do begin

;*****
; CONVOULUTION (SHEPP-LOGAN FILTER)
;*****

p[*]=0.
p[nshift:nshift+ncols-1]=sinogram[* ,i]
sinogramimage[0,i]=p
convolvedsinogramimage[0,i]=convol(p,ker)
tvsc1, convolvedsinogramimage,2
```

## 9. Appendix I: 3D Image Reconstruction Program

---

```
;wset,3 & plot,convol(p,ker)

;*****
;BACKPROJECTION
;*****

rotation=i*!pi/nangles
riemann,convolvedsinogramimage,reconimage,rotation,$
/backproject,bilinear=bilinear,cubic=-3.,row=i,$
center=center_value
Endfor

;*****
;REMOVE DIFFRACTION
;*****

for i=0,ncols-1 do begin
  col=reform(reconimage[i,*])
  open=(total(col[0:10])/11.+total(col[ncols-11:ncols-1])/11.)/2.
  diffraction=where(col lt open, count)
  if (count ne 0) then begin
    col[diffraction]=open
    reconimage[i,*]=col
  endif
endfor

max_int=max(reconimage)
min_int=min(reconimage)
med_int=median(reconimage)
print,'max_int(reconimage)=' ,max_int,'min_int=' ,min_int,'med_int=' ,med_int

threshold=(max_int-min_int)/auflösung+min_int
threshold1=abs(max_int-abs((max_int-min_int)/auflösung))
for i=0,ncols-1 do begin
  for l=0,nrows-1 do begin
    col=reconimage[i,l]
    bad=where (col lt threshold, count)
    bad1=where(col gt threshold1,count1)
    if (count ne 0) then begin
      col[bad]=threshold
      reconimage[i,l]=col
    endif
    if (count1 ne 0) then begin
      col[bad1]=threshold1
      reconimage[i,l]=col
    endif
  endfor
endfor
```

## 9. Appendix I: 3D Image Reconstruction Program

---

```
imax_1=max(reconimage)
imin_1=min(reconimage)
imed_1=median(reconimage)
print,'MaxRecon_2=',imax_1,'Minrecon=',imin_1,'Medianrecon=',imed_1
recon_vol[*,*,(j-sliceerst)]=18000*reconimage
window,7,title='reconstructed slice'
tvsc1,recon_vol[*,*,(j-sliceerst)]
write_tiff,'recon.tif',recon_vol[*,*,(j-sliceerst)],/short
reconimage=fltarr(ncols,nrows)
print,'slice_number=',j,'total_slice_number=',nslice
Endfor
print,'size=',size(recon_vol)

;*****
;Write Volume Data
;*****

openw,2,data_name
writeu,2,recon_vol
close,2

imax_i=max(recon_vol)
imin_i=min(recon_vol)
imed_i=median(recon_vol)
print,'MaxRecon_vol=',imax_i,'Minrecon_vol=',imin_i,'Medianrecon_vol=',imed_i
print,'FINISHED!!!'
End

Pro process
End
```



# 10

## Appendix II: Further Applications of NR and NT at ATI –Wien

NR and NT has a wide application area in nuclear, aerospace, and industry as well as archaeology; such as quality insurance, visualization of defects, material inspection of being restored ancient samples, dynamic behaviors of the gas, liquid flows and multiphase flow patterns in tubes, flow cycles in the motors, refrigerant flow in refrigerators.

Despite low neutron flux and small beam size of NR II facility at ATI – Wien, radiographic and tomographic investigations are carried on routinely for neutron inspection of fuel elements such as enrichment analysis, absorber distribution within control rods, visualization of inner defects in fission or ionization chambers e.t.c. In the following, some applications are summarized and an outlook is given for further activities at the ATI – NR facilities.

### 10.1 Nuclear Applications

Specially, NR and NT are exploited in the nuclear technology to inspect radioactive materials. Uranium fuel elements with different U – 235 enrichments were inspected. The fuel elements having different enrichments show different neutron attenuation behavior.

**Table I:** The absorption cross section of the natural uranium and its isotopes [Lama83].

	$\sigma_a$ (barn)	$\sigma_f$ (barn)
<b>Natural Uranium</b>	7.59	4.19
<b>U – 238 (99.27 a/o)</b>	2.7	-
<b>U – 235 (0.72 a/o)</b>	680.8	582.2

The absorption cross section of an element is the sum of the fission and capture cross sections, and it depends strongly on the contribution of U – 235 isotope in uranium fuel element as seen in Table I. On this account, uranium fuel elements with different U – 235 enrichments give different image contrast; high – enriched uranium pellet attenuates more neutrons than low – enriched uranium pellet as shown in Fig. 10.1. For these measurements, uranium fuel elements of a BWR with 1.4, 2.05, and 2.5 % enrichments were used. Because of the limited beam size, we could inspect only both ends of the fuel elements. The deformation of the strings in one end of each fuel element could also be investigated (Fig. 10.1).

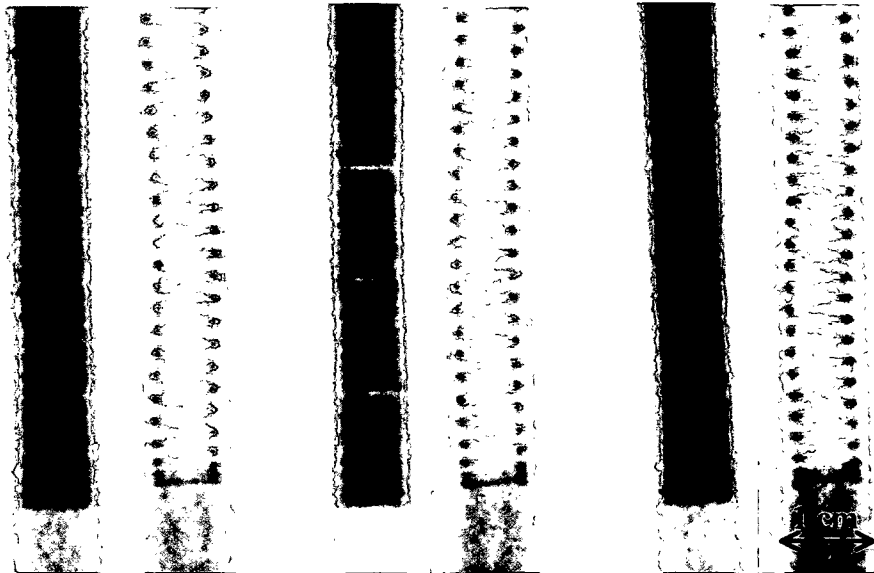


**Fig. 10.1:** NR images of BWR calibration fuel rods with different U – 235 enrichments; **left:** 1.4 %, **middle:** 2.05 %, **right:** 2.5 % (the length of fuel elements are longer than beam size, therefore NR images were taken only from beginning and end of the fuels).

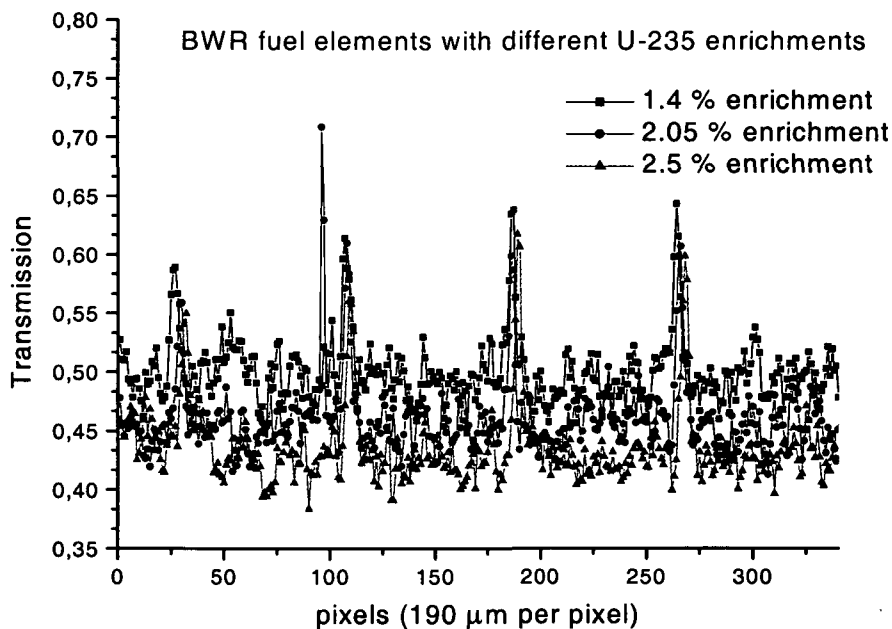


**Fig. 10.2:** Neutron transmission profiles along the length of the fuel elements.

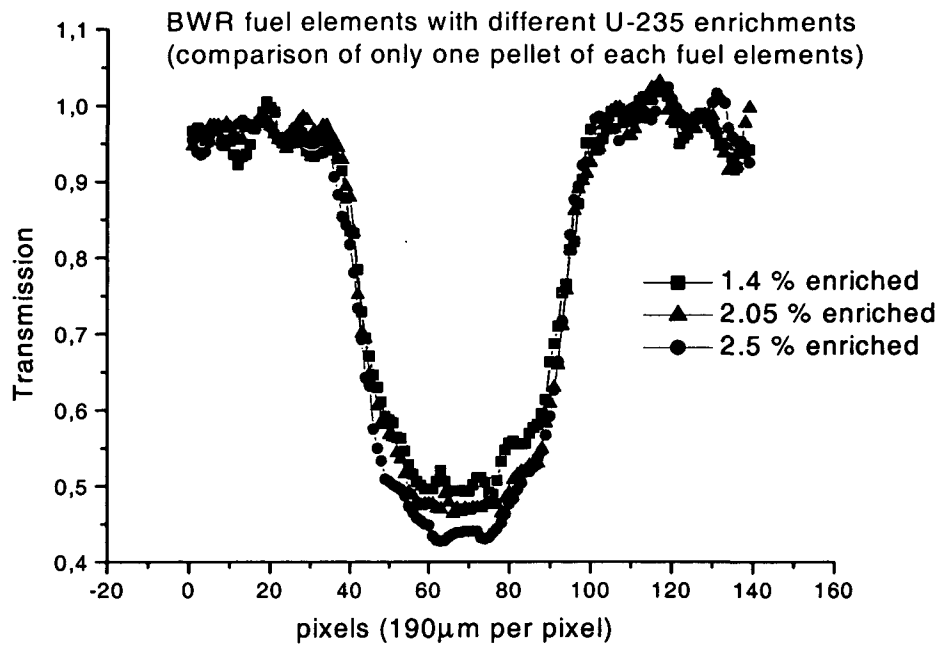


Fig. 10.3: Neutron transmission profiles on the cylindrical fuel pellet (horizontal line profile).

The chain reaction is controlled by inserting the control rod deeper into the reactor core or withdrawing it. Different reactors have different types of control rod.  $^{10}\text{B}$  is a strong neutron absorber and hence is the active material in this construction. The absorber content and distribution within a reactor control rod is very important to change reactivity fast and flat in the entire reactor core. In order to test the distribution of boron carbide, a cylindrical control rod was radiographed and a horizontal line profile was taken to calculate its neutron transmission. Fig. 10.4 shows a homogenous absorber distribution within this control rod.

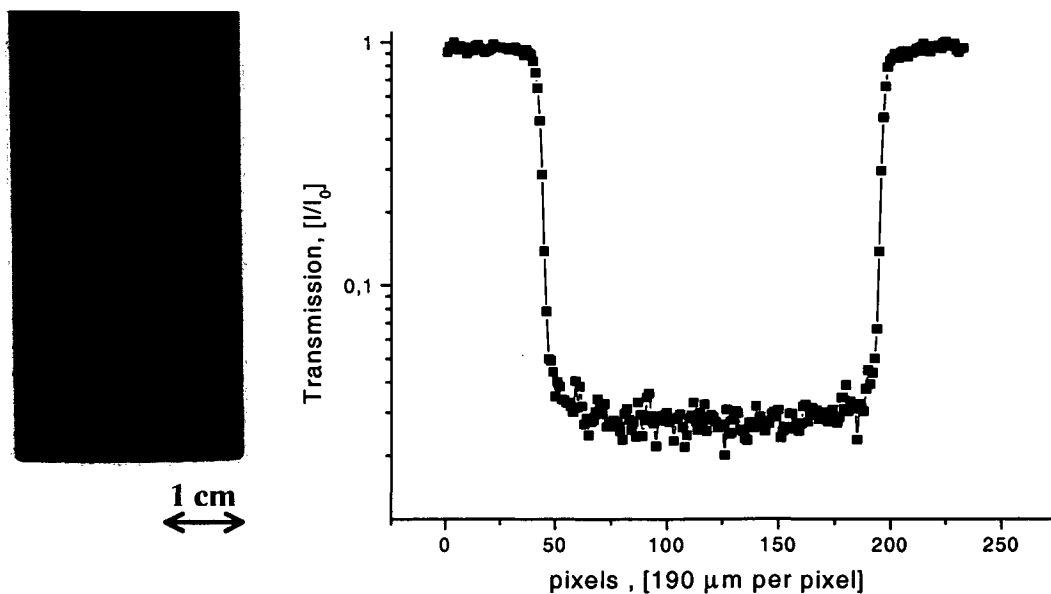


Fig. 10.4: NR inspection of a  $\text{B}_4\text{C}$  (boron carbide) control rod and neutron transmission profile horizontally.

Tomographic inspections could not be carried out for the fuel and control rods because of their size over our neutron beam size.

## 10.2 Ancient Samples from Austrian Museum of Natural History

The Austrian Museums are interested in the radiographic investigations of archaeological samples with neutrons. Before restoration of an ancient sample, radiographic imaging is necessary in order to define exactly where restoration is possible or required. The restoration quality can also be tested with radiographic methods. The suitable imaging method should be selected depending on being inspected sample materials. The usual imaging method in museums is X – ray radiography. However, some of interesting artifacts that are not suitable for X – ray inspection, can be inspected with NR.

A hand mirror and gold bowl were investigated by NR at ATI – Wien. The motivation of the hand mirror inspection was to visualize the corroded parts of the mirror – handle, which was covered with thin silver and filled with a hydrogenous material and hydrogenous materials are strong neutron attenuators on the contrary X – ray. So as to inspect the corrosion in the outer covering layer, neutron radiography was applied. The size of being inspected objects at NR II facility is limited with the beam size (8 cm diameter). Considering the length of the mirror handle, it was imaged in two steps (upper part and lower part) as seen in Fig. 10.5. The strong hydrogenous material did not allow that neutrons penetrate into the mirror – handle. Nevertheless, the corroded parts could be visualized enhancing image contrast using image histogram.

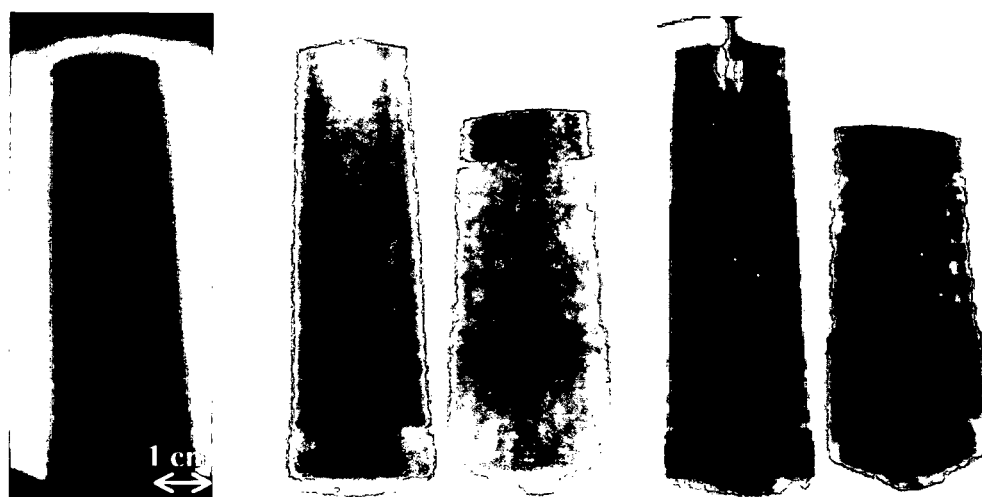


**Fig. 10.5:** NR images of the ancient hand-mirror were inspected at ATI – Wien (**left:** raw NR image of the upper part, **middle:** upper & lower parts from the front view, **right:** upper & lower from the side view).

Contrary to NR, the inner structure of mirror handle could be imaged easily with X – ray radiography as seen in Fig. 10.6. The important details about its structure, which X – ray

imaging gave, is that the metal support (mirror head) does not continue along the mirror – handle, the handle consists of two parts, which were connected mainly with a knitting needle.

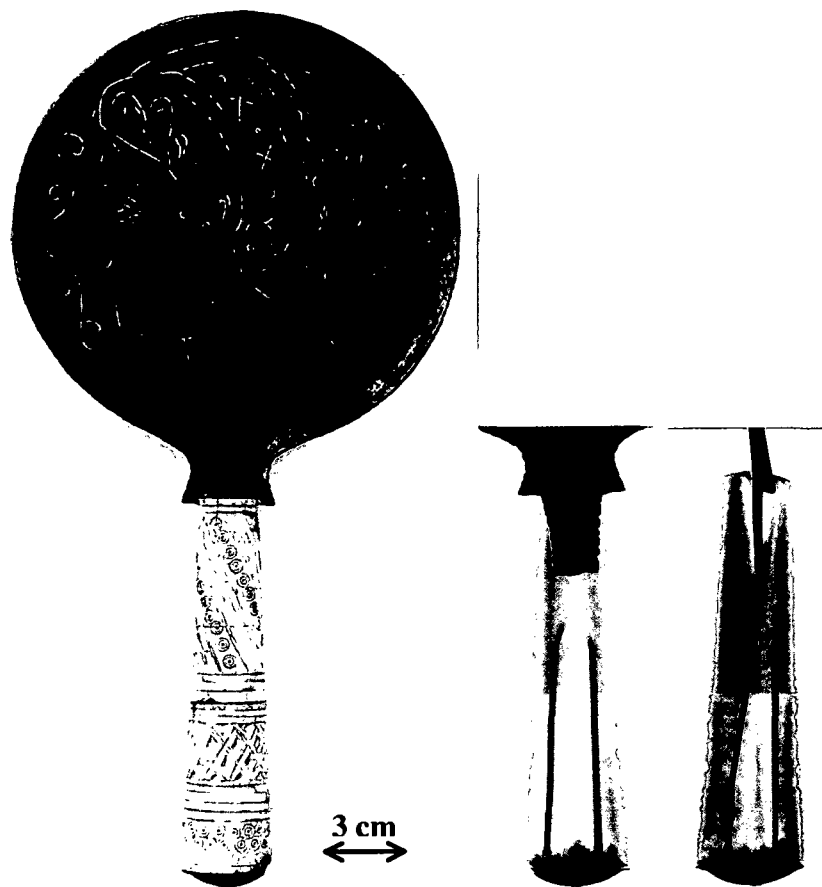


**Fig. 10.6:** X – ray radiography images (**left:** photo, **middle:** from the front view, **right:** from the side view) of the ancient hand-mirror made by Mongolians were taken at 80 kV and 3 mA for 1 minute by M. Schreiner at the Institute of the Natural Science in Arts.

In order to analyze the processing methods of Mongolians inspecting the hand-mirror, to verify the gold processing method (riveted gold dies) and also to test the restoration quality of an ancient gold bowl, NR was applied for the reason that NR distinguishes even some isotopes of elements. The restored gold parts (darker parts on image) attenuate more neutrons than original parts, which gave contrast difference as seen in Fig. 10.7 (left image). Some defects at the gold bowl – side shown in Fig. 10.7 (right image) and the relief figures in the middle part of the bowl could also be imaged.

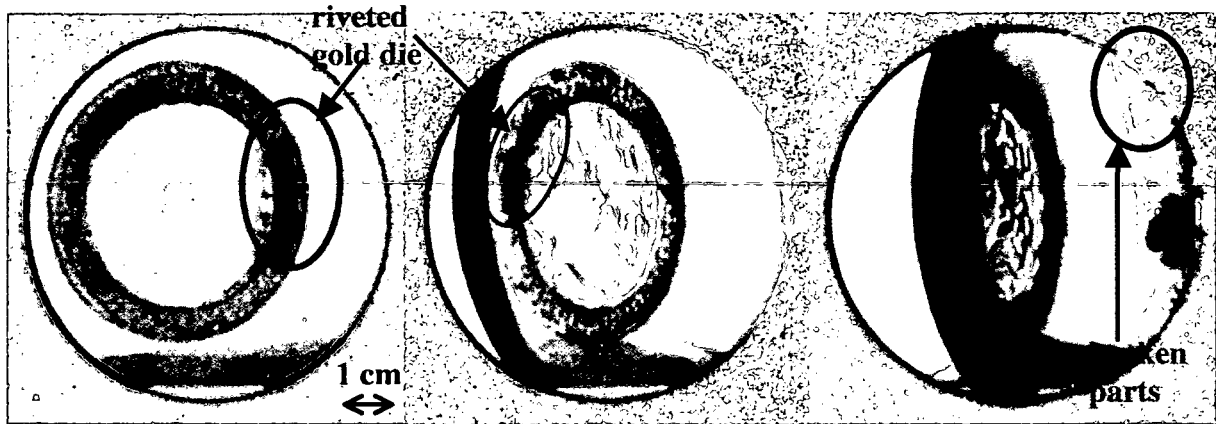


Fig. 10.7: NR images of the ancient gold bowl from different views were inspected at ATI –Wien using the 58 mm focal length camera lens for 20 seconds exposure time.

### 10.3 Electro Motors

Investigation of two different electro motors having each 4.0 cm diameter is a good example for the industrial application of NT. 200 projections with  $0.9^\circ$  degree angle step were taken with digital CCD camera based detector, each projection for 20 seconds exposure time.

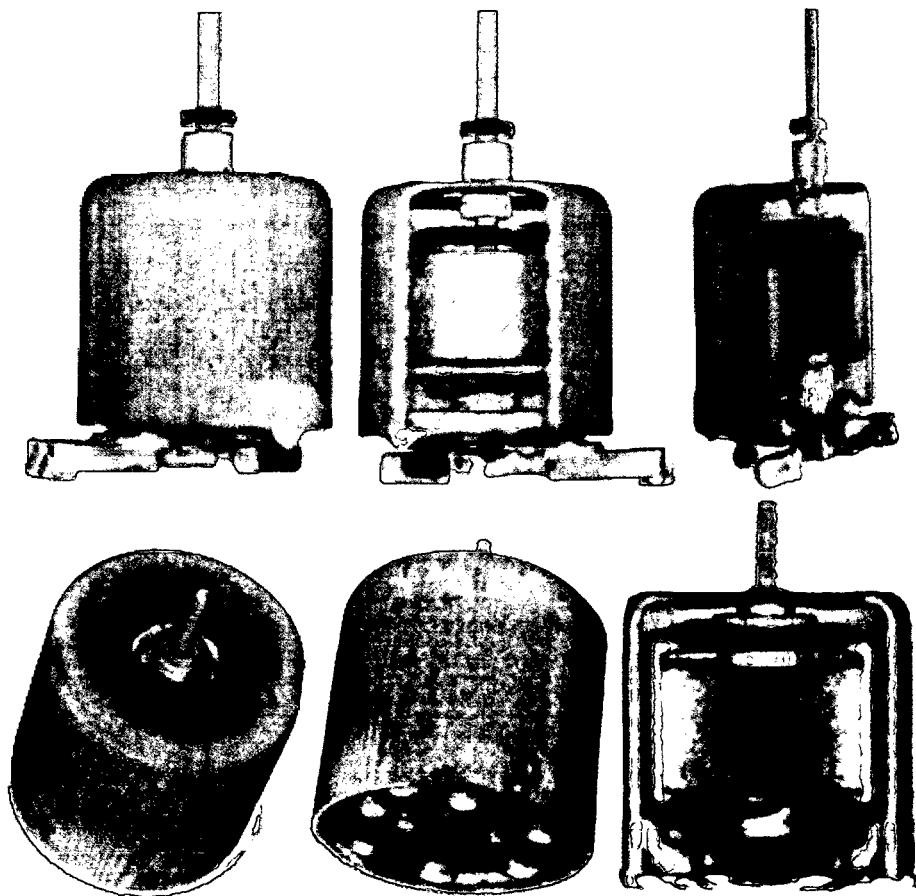
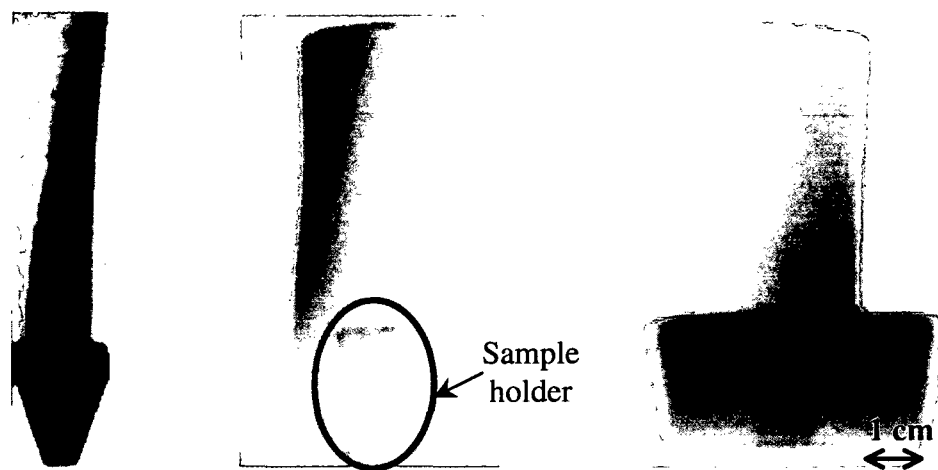


Fig. 10.8: Reconstructed NT images of two different electro motors using 58 mm focal length camera lens.

## 10.4 TiAl Turbine Blade

A new turbine blade material consisting of 47 at % Ti, 48 at % Al, 2 at % Cr, 2 at % Nb and 1 at % B elements, which was developed by the Institute of Physics of Materials in Czech republic has developed, was inspected with NR and NT at our institute. Boron is similar to carbon in that it has a capacity to form stable covalently bonded molecular networks. For this reason, they have used 1 at% natural boron in the manufacturing of the Titan – Aluminum turbine blades. The motivation of this study is to determine the homogeneity of the composition and manufacturing defects using NR method (quality insurance). According to the radiographic images from different views shown in Fig. 10.9, the TiAl blade seems homogeneous.



**Fig. 10.9:** NR images of TiAl turbine blade with 12 cm length from different views (minimum and maximum thicknesses are 2 mm and 2 cm).

However, for a complete imaging NT is necessary. For 3D image reconstruction of the turbine blade, 200 NT projections were taken with  $0.9^\circ$  angle step. Changing the contrast and cutting the images slice by slice, problem parts within the sample (low or high material concentration in some parts) could be determined as shown in Fig. 10.10. The inhomogeneity and some defects could be visualized enhancing the contrast of the reconstructed images.

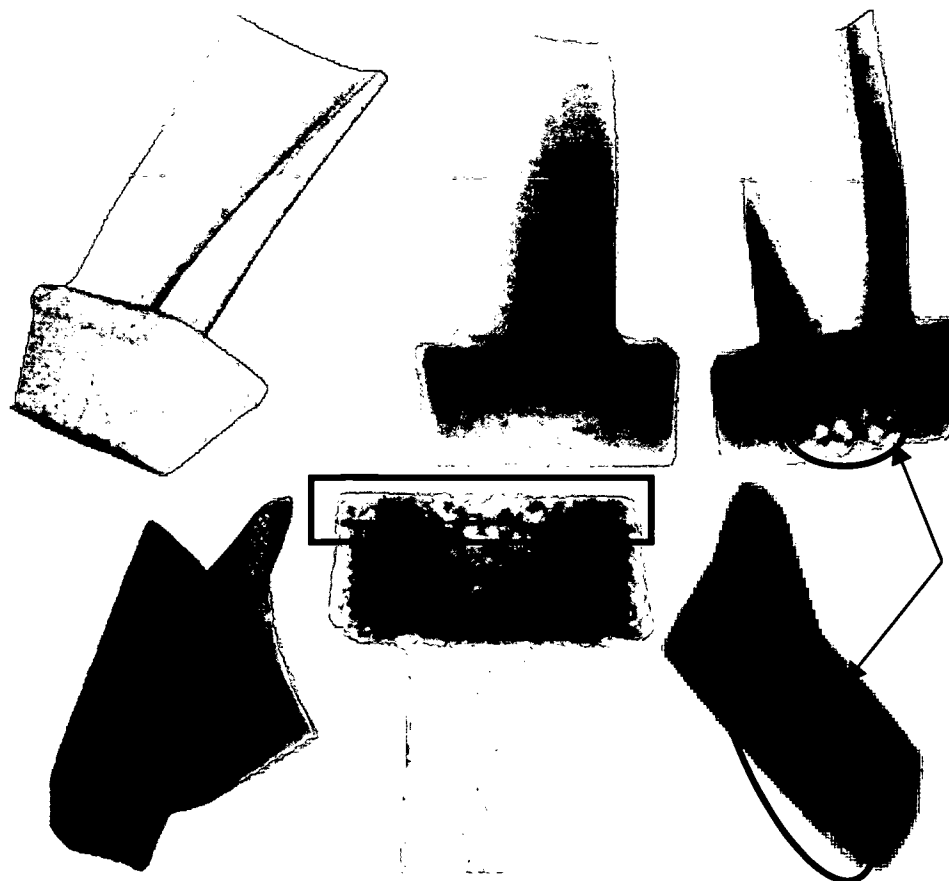


**Fig. 10.10:** 3D reconstructed NT images of the TiAl turbine blade with different opacity levels (inhomogeneous parts were shown on the images).

## 10.5 Upgrading of NR II Facility at ATI – Wien

A neutron beam shutter was installed at the collimator exit of NR II facility. After the installation of the beam shutter, sample – positioning problem was appeared because of insufficient place. As a result of this, the distance between detector and collimator exit was enlarged and a larger sample holder was installed. This allows also installing a sample – positioning device into (x, y, z) directions for the samples bigger than beam size. That means bigger samples could be radiographed changing their positions step by step. Then, in order to visualize the whole sample the generated NR images at different positions can be reconstructed, processing each image carefully.

As mentioned, we had two camera lenses. Using the first lens (58 mm focal length)  $\sim 21 \times 21 \text{ cm}^2$  object area can be imaged, which is over the 8 cm diameter beam size; second lens (180 mm focal length) can visualize only  $\sim 4 \times 4 \text{ cm}^2$  object area, which is smaller than the beam area. Therefore, a new camera lens with 105 mm focal length was installed to use the whole CCD chip with 8 cm diameter beam area. The MTF (Modulation Transfer Function) is an efficient tool to calculate spatial resolution of an image. The spatial resolutions of three camera lenses used at NR II facility were compared using a very thin Gd – edge as shown in Fig. 10.11. According to this comparison, it can be concluded that we can perform



measurements with the spatial resolutions from 170 to 428  $\mu\text{m}$ , which were measured setting the Gd foil direct on the scintillator screen.

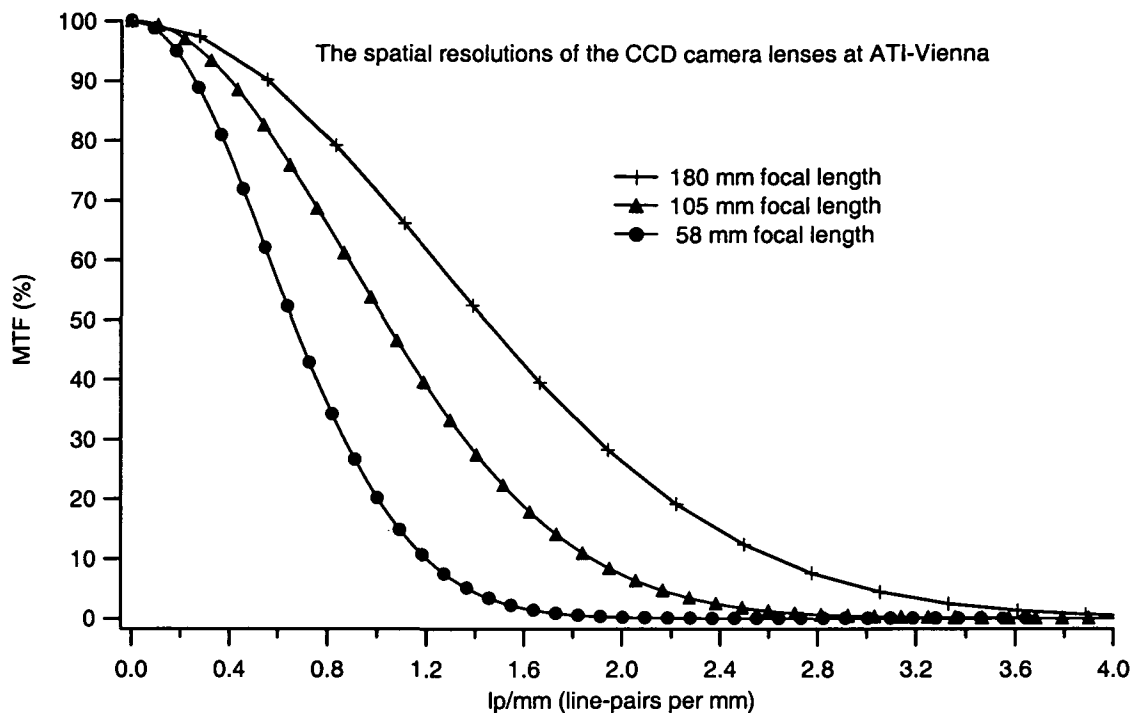


**Fig. 10.11:** Comparison of the spatial resolutions of the CCD camera lenses with different focal lengths, which are used at NR II facility at ATI – Vienna.

A personal dosimeter taken with 58 mm focal length (left image in Fig. 10.12), ionization chamber taken with 105 mm focal length (middle image in Fig. 10.12) and fiber reinforced silicon carbide ceramic composite taken with 180 mm focal length (right image in Fig. 10.12) were imaged using whole area of the CCD chip (512 x 512 pixels). The typical exposure times for each camera lenses were determined; 20 seconds for 58 mm focal length, 35 seconds for 105 mm focal length and 120 seconds for 180 mm focal length. The new lens with 105 mm focal length was determined as standard camera lens for our NR II facility considering its suitability to our beam size, and also spatial resolution.

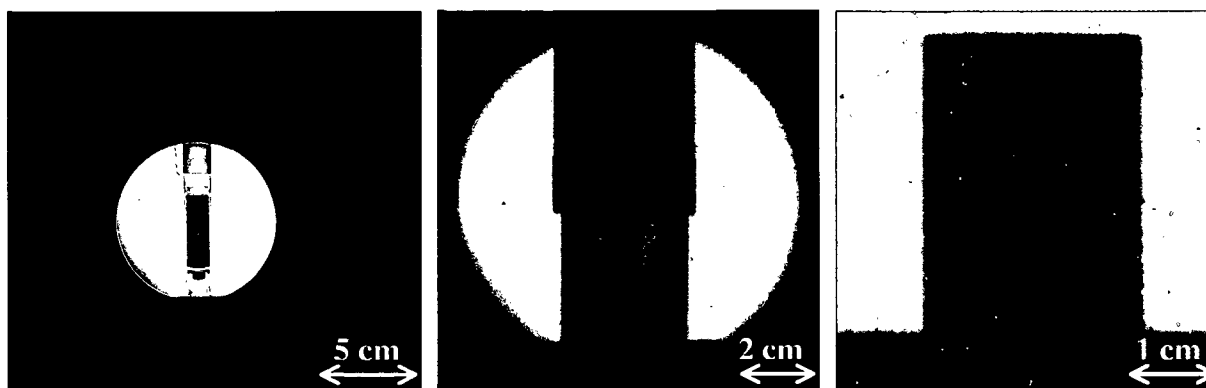


**Fig. 10.12:** NR images taken with lenses of 58 mm, 105 mm and 180 mm focal lengths in sequence (from left to right); the field of views of the lenses is approximately 22 x 22 cm, 10.5 x 10.5 cm and 4.5 x 4.5 cm in turn.

## 10.6 NR during TRIGA Mark II Reactor Pulse

TRIGA Mark II research reactor the fuel elements are in the form of a uniform mixture of 8 wt % uranium, 1 wt % hydrogen and 91 wt % zirconium, the zirconium – hydride, which is the main moderator. Since this moderator has the property of moderating less efficiently at high temperatures, TRIGA Mark II reactor in Vienna can also be operated in a pulsed mode (with a rapid power rise to 250 MW for roughly 40 milliseconds) with a maximal pulse rate of 8 –12 per hour. The boron carbide pulse rod with compressed air drive (5 bars) is utilized for the reactor pulse. The power rise is accompanied by an increase in the maximum neutron flux density from  $1.0 \times 10^{13} \text{ cm}^{-2} \cdot \text{s}^{-1}$  (at 250 kW) to  $1.0 \times 10^{16} \text{ cm}^{-2} \cdot \text{s}^{-1}$  (at 250 MW), which brings about the neutron flux at NR II facility from  $1.3 \times 10^5$  to  $1.3 \times 10^8 \text{ cm}^{-2} \cdot \text{s}^{-1}$ . The power decreases back to the normal condition (250 kW) owing to the negative temperature coefficient after the pulse. The temperature rise of the fuel elements during the reactor pulse from 200 °C to about 360 °C subjects the fuel elements to strong thermal stress.

As presented in Fig. 10.13, this very short pulse lifetime could be utilized for NR imaging at NR II facility with actually manual synchronization between CCD camera and reactor pulse. In comparison to NR image taken at the normal reactor operation for 20 seconds exposure time, the average intensity per pixel on an open beam is doubled. Nevertheless, it cannot be exploited to investigate dynamic samples with our present detection system owing to the longer read-out time (~ 2-3 seconds per NR image); more frames per second could be performed using a fast scan camera with intensifier.

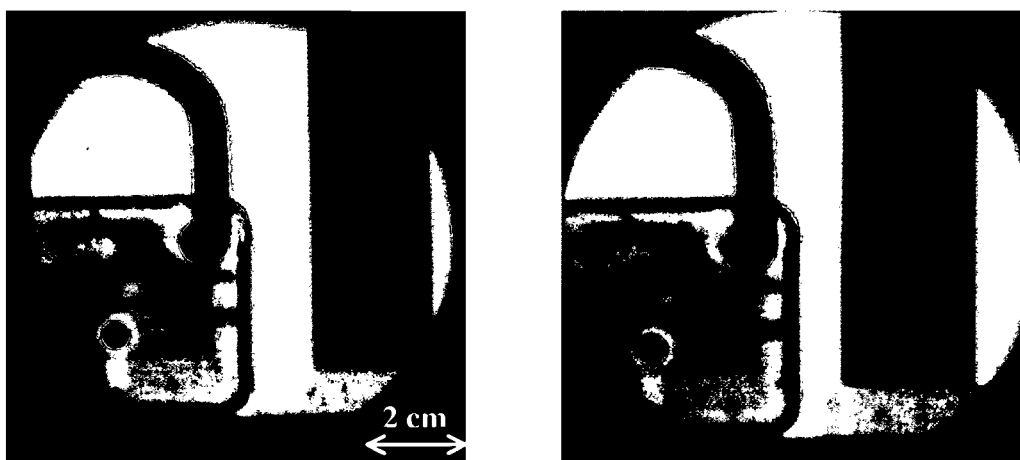


**Fig. 10.13:** Comparison of NR images taken at normal reactor operation at left side with 0.45 mm spatial resolution and ~ 17500 grey values (250 kW for 20 s exposure time with 58 mm focal length camera lens) and at reactor pulse at right side with 0.5 mm spatial resolution and ~ 36200 grey values (250 MW for 40 ms with the same camera lens).

# 11

## References

- [Aiel00] G. Aiello, H. Golfier, J. F. Maire, Y. Poitevin, J. F. Salavy, Modelling of SiC/SiC composite structures for nuclear components, *Fusion Engineering and Design*, vol. 51-52, pp.73-79, 2000.
- [Ayma01] R. Aymar, ITER R&D: Executive summary: Design overview, *Fusion Engineering and Design*, vol. 55, pp.107-118, 2001.
- [Astr98] UltraPlus™ Camera Control Software Manual, Version 1.0, Life Science Resources, AstroCam Camera System, 1998.
- [Baec02-1] S. Baechler, N. Kardjilov, M. Dierick, J. Jolie, G. Kühne, E. Lehmann, T. Materna, New features in cold neutron radiography and tomography, **Part I: Thinner scintillators and a neutron velocity selector to improve the spatial resolution**, *Nuclear Instruments and Methods*, vol. 491, pp. 481-491, October 2002.
- [Baec02-2] Baechler, B. Masschaele, P. Cauwels, M. Dierick, J. Jolie, T. Materna, W. Mondelaers, *Nucl. Instr. and Meth. A* 481, 38, 2002.
- [Bast02-1] M. Bastürk, N. Kardjilov, E. Lehmann, M. Zawisky, Radiography investigation and Monte Carlo simulation of neutron transmission of boron-alloyed steel, 7<sup>th</sup> World Conference on Neutron Radiography, Rome-Italy, 15-21 September 2002.
- [Bast02-2] M. Bastürk, N. Kardjilov, E. Lehmann, P. Vontobel, H. Rauch, Non-destructive neutron radiography and tomography inspection of the future

## 11. References

---

- nuclear fusion blanket material (SiC/SiC<sub>f</sub>), 7<sup>th</sup> World Conference on Neutron Radiography, Rome-Italy, 15-21 September 2002.
- [Bast03] M. Bastürk, N. Kardjilov, E. Lehmann, M. Zawisky, Monte Carlo simulation of neutron transmission of boron-alloyed steel, IEEE journal, in print, 2003.
- [Bate74] J. C. Bates and S. Roy: Neutron radiography with very cold neutrons, Nucl. Inst. And Meth. Vol. 120 Issue 2, pp.369-370, 1974.
- [Bitt02] K. Bittner-Rohrhofer, K. Humer, HW. Weber, K. Hamada, M. Sugimoto, K. Okuno, Mechanical strength of an ITER coil insulation system under static and dynamic load after reactor irradiation, Journal of Nuclear Materials, vol. 307-311, pp. 1310-1313, December 2002.
- [Brie97] J. F. Briesmeister, MCNP<sup>TM</sup>-A General Monte Carlo N-Particle Transport Code, Volume 1,2,3 and 4, Version 4B, March 1997.
- [Boeh97] Böhler Bleche GmbH, Archives on Böhler NEUTRONIT Boron-alloyed steel sheets, 1997, Mürrzuschlag, Austria, <http://www.boehler-bleche.at>.
- [Buch86] T. Buchberger, Neutronenradiographische Untersuchungen an Tantal-Tritium-Helium-Systemen, Dissertation, TU - Vienna, November 1986.
- [Buec93] T. Buecherl, C. Rausch, H. v. Seggern, Quantitative measurements on thermal neutron detectors based on storage phosphors, Nucl. Instr. And Meth. A 333, pp. 502-506, 1993.
- [Buec94] T. Bücherl, E. Steichele, Computerized tomography with thermal neutrons, International Symposium on Computerized Tomography for Industrial Applications, June 8-10, pp. 49-56, Berlin 1994.
- [Büyü98] O. Büyükoztürk, Imaging of concrete structures, NDT & E International, vol. 31, No 4, pp. 233-243, 1998.
- [Care01] Carel W. E. van Eijk, Inorganic-scintillator development, Nucl. Inst. And Meth. A V. 460 pp. 1-14, 2001.
- [Davi96] J. W. Davis, G. W. Wille and P. Heitzenroeder, "Use of titanium in the tokamak physics experiment (TPX)", J. Nuc. Mat., Vol. 233-237, p1, pp. 592-595, 1996.
- [Diet96] M. Dietze, J. Felber, K. Raum and C. Rausch, Intensified CCDs as position sensitive neutron detectors, Nuclear Instruments and Methods in Physics Research Section A: Accelerators, Spectrometers, Detectors and Associated Equipment, Volume 377, Issues 2-3, pp. 320-324, 1 August 1996.
- [Doma92] J. C. Domanus, Practical Neutron Radiography, Kluwer Academic Publishers, ISBN 0-7923-1860-9, The Netherlands, 1992.

## 11. References

---

- [Dona99] McDonald Jr, T.E. et al., 1999. Time-gated energy-selected cold neutron radiography, Nucl. Instr. and Meth. A 424, pp. 235-241, 1999.
- [Duke00] Duke University, Virtual-imaging Laboratory, [http://dukemil.egr.duke.edu/XRAY/CT/Simulation/ct\\_in.html](http://dukemil.egr.duke.edu/XRAY/CT/Simulation/ct_in.html).
- [Dove01] Edwin L. Dove, Notes on Computerized Tomography, Physics of medical Imaging, 51:060 Bioimaging Fundamentals, 10/24/01.
- [Elio99] F. Elio, et al., Engineering design of the ITER blanket and relevant research and development results, Fusion Engineering and Design 46, 159-175, 1999.
- [Esto99] U. von Estorff, L. M. Davies, P. prampus, (Eds.), NDT methods for monitoring degradation, Proceedings of the Joint EC – Specialists Meeting, European Commission (EUR 19718), International Journal of Pressure and Piping, 76, 965, 1999.
- [Feni98] P. Fenici, A.J. Frias Rebelo, R.H. Jones, A. Kohyama and L.L. Snead, “Current status of SiC/SiC composites R&D”, J. Nucl. Mater. 258-263, pp. 215-225, 1998.
- [Frie89] H. Friedrich, V. Wagner and P. Wille, A high-performance neutron velocity selector, Physica B 156&157, pp. 547-549, 1989.
- [Fuen59] E. Fünfer, H. Neuert, Zählrohre und Szintillationszähler, Verlag G. Braun 4091, Karlsruhe, Germany, 1959.
- [Gian98] L. Giancarli, et al., Design requirements for SiC/SiC composites structural material in fusion power reactor blankets, Fusion Engineering and Design 41, pp. 165-171, 1998.
- [Gian02] L. Giancarli, H. Golfier, S. Nishio, Raffray, C. Wong, R. Yamada, “Progress in blanket designs using SiC/SiC composites”, Fusion Engineering and Design, Vol. 61-62, pp.307/ 318, 2002.
- [Hain00] Martin Hainbuchner, Ultra-Kleinwinkelstreuung von Neutronen an strukturierten Materialien, Doctoral Thesis, TU – Vienna, 2000.
- [Haje01] M. Hajek, W. Schöner, Spectral distribution of neutron fluence at the thermal column of the TRIGA Mark II research reactor, AIAU 21313, April 2001.
- [Haje02] M. Hajek, Applied neutron spectrometry: Applications atop high-altitude mountains and onboard aircraft, Dissertation, TU – Vienna, April 2002.
- [Herm95] G. T. Herman, Image reconstruction from projections, Real-Time Imaging, vol.1, Issue 1, pp. 3-18, April 1995.
- [Herm80] G.T. Herman, Image reconstruction from projections: The fundamentals of computerized tomography, Academic Press, 1980, ISBN 0-12-342050-4.

## 11. References

---

- [Hume00-1] K. Humer, H.W. Weber, R. Hastik, H. Hauser, H. Gerstenberg, Dielectric strength, swelling and weight loss of the ITER Toroidal Field Model Coil insulation after low temperature reactor irradiation, *Cryogenics*, vol. 40, pp. 295-301, 2000.
- [Hume00-2] K. Humer, P. Rosenkranz, H.W. Weber, P.E. Fabian, J.A. Rice, Mechanical properties of the ITER central solenoid model coil insulation under static and dynamic load after reactor irradiation, *J Nucl Mater*, 283-287, pp.973-6, 2000.
- [IAEA] IAEA Nuclear Data Service, <http://www-nds.iaea.or.at/>.
- [Kak88] A. C. Kak, M. Slaney, Computerized tomographic imaging, IEEE Press, 1988.
- [Kard01] N. Kardjilov, B. Schillinger, E. Steichele, Energy selective neutron radiography and tomography at FRM, acc.p. *Applied Radiation and Isotopes* 2001.
- [Kard03-1] N. Kardjilov, S. Baechler, M. Bastürk, M. Dierick, J. Jolie, G. Kühne, E. Lehmann, T. Materna, B. Schillinger, New features in cold neutron radiography and tomography, **Part II: Applied energy-selective neutron radiography and tomography**, *Nuclear Instruments and Methods*, vol. 501, pp. 536-546, April 2003.
- [Kard03-2] N. Kardjilov, Further developments and applications of radiography and tomography with thermal and cold neutrons, Doctoral thesis, TU-Munich, Germany, June 2003.
- [Koer00] S. Koerner, Digital image processing in neutron radiography, Doctoral thesis, Technical University of Vienna, November 2000.
- [Koer01] S. Koerner, B. Schillinger, P. Vontobel, H. Rauch. A neutron tomography facility at a low power research reactor, *Nuclear Instr. and Methods in Physics Research A* 471 (2001) 69-74.
- [Kohy01] A. Kohyama, et. al., "Development of SiC/SiC Composite for Fusion", *FTP1/06(R)*, 18<sup>th</sup> Fusion Energy Conference, 4 - 10 October 2000, Sorrento, Italy, IAEA-CN-77 0, 2001.
- [Lama83] J. R. Lamarsh, Introduction to nuclear engineering, ISBN 0-201-142007, Addison-Wesley Publishing Company, New York, 1983.
- [Lehm96] E. Lehmann, H. Pleinert and L. Wiezel, Design of a neutron radiography facility at the spallation source SINQ, *Nuclear Instruments and Methods in Physics Research Section A: Accelerators, Spectrometers, Detectors and Associated Equipment*, vol. 377, Issue 1, 21, pp.11-15, July 1996.
- [Lehm00] E.H. Lehmann, Neutron Imaging, Proc. 18th Summer School on Neutron Scattering, Zuoz, Publ. World Scientific Publishing Co. Ltd, ISBN 981-02-4444-4, August 2000.

## 11. References

---

- [Leli96] C. J. Leliveld, A fast Monte Carlo simulator for scattering in x-ray computerized tomography, doctoral thesis, Zurich, Switzerland, 6 Jun 1996.
- [McDo99] T. E. McDonald Jr., et al., Time-gated energy-selected neutron radiography, Nuclear Instr. And Meth. in Physics A, vol. 424, pp. 235-241, 1999.
- [Mitc01] Mitchell N, Salpietro E., ITER R&D: Magnets: Toroidal field model coil, Fusion Engineering and Design, vol.55, pp.171-190, 2001.
- [Neut01] Paul Scherer Institute, PSI-Neutra, <http://neutra.web.psi.ch/What/detector.html>.
- [Niim94] N. Niimura, Y. Karasawa, I. Tanaka, J. Miyahara, K. Takahashi, H. Saito, S. Koizumi, M. Hidaka, An imaging plate neutron detector, Nucl. Instr. and Meth. A 349, pp. 521-525, 1994.
- [NNDC] National Nuclear Data Center, <http://www.nndc.bnl.gov/>.
- [Pere95] A. S. Pérez, et al., Progress on the Design of the Tauro breeding blanket concept, CEA/DMT Rept. (1995).
- [Plei97] H. Pleinert, et al., Design of a new CDD-camera neutron radiography detector, Nucl. Instr. and Methods A 399, pp.382-390, 1997.
- [Pere96] A. S. Pérez Ramírez, et al., Tauro:a ceramic composite structural material self-cooled Pb-17Li breeder blanket concept, Journal of Nuclear Materials 233-237, pp.1257-1261, 1996.
- [Rado17] J. Radon, Über die Bestimmung von Funktionen durch ihre Integralwerte längs gewisser Mannigfaltigkeiten, Berlin Sächsische Akademie der Wissenschaften 29, pp. 262-279, 1917.
- [Raus92] C. Rausch, T. Bücherl, R. Gähler, H. von Seggern, A. Winnacker, Recent developments in neutron detection, Neutrons, x-rays and gamma rays SPIE Proc. 1737, pp. 255-263, 1992.
- [Raus96] C. Rausch, M. Dietze, J. Felber, J. Hofmann, B. Schillinger, Position Sensitive Detectors for Thermal Neutrons using Image Intensifiers, CCDs and Image Plates, <http://www1.physik.tu-muenchen.de/lehrstuehle/E21/Projects/NNews/nnews.html>.
- [Raus99] C. Rausch, Neutron Detectors Using Slow Scan CCDs, J. Neutron Research Vol.4, pp.87-95, 1999.
- [Rive98] M. Rivers, Tutorial Introduction to X-ray Computed Microtomography, <http://www-fp.mcs.anl.gov/xray-cmt/rivers/diamonds.html>.
- [Rope00] Roper Scientific Germany, Signal to Noise Ratio (SNR), <http://www.roperscientific.de/>.

## 11. References

---

- [Sant01] J.R. Santisteban, et al., Strain imaging by Bragg edge neutron transmission, Nuclear Instr. and Methods in Physics A 0, pp. 1-4, 2001.
- [Schi99] B. Schillinger, Neue Entwicklungen zu Radiographie und Tomographie mit thermischen Neutronen und zu deren routinemäßigem Einsatz, Dissertation TU Munich, Mensch&Buch Verlag, Berlin, 1999, <http://www.menschundbuch.de/>.
- [Schi00] B. Schillinger, E. Lehmann, P. Vontobel. 3D neutron computed tomography: requirements and applications, Physica B 276-278, pp. 59-62, 2000.
- [Schi01-1] B. Schillinger, Improved radiography and 3D tomography due to better beam geometry, Nondestr. Test. Eval., vol. 16, pp. 277-285, Gardon & Breach, 2001.
- [Schi01-2] B. Schillinger, Estimation and measurement of L/D on a cold and thermal neutron guide, Nondestr. Test. Eval., vol. 16, pp. 141-150, Gardon & Breach, 2001.
- [Schi01-3] B. Schillinger, Neutron detectors using CCD cameras, Detector Workshop 2001 Berlin, [http://www.hmi.de/bensc/psnd2001/Talks/PSND2001\\_Schillinger/](http://www.hmi.de/bensc/psnd2001/Talks/PSND2001_Schillinger/).
- [Sear89] V.F. Sears, "Neutron Optics", Oxford University Press, Oxford, 1989.
- [Sear92] V.F. Sears, Neutron scattering lengths and cross sections, Neutron News, Vol. 3, No. 3, 26, 1992.
- [Silv01] A. X. da Silva and V. R. Crispim, Moderator-collimator-shielding design for neutron radiography systems using  $^{252}\text{Cf}$ , Applied Radiation and Isotopes, vol.54, Issue 2, pp.217-225, February 2001.
- [Smit95] D. L. Smith, H. M. Chung, B. A. Loomis, H. Matsui, S. Votinov and W. Van Witzenburg, Development of vanadium-base alloys for fusion first-wall – blanket applications, Fusion Engineering and Design, Vol. 29, pp.399-410, 1995.
- [Smit96] B. Smith, Thermography – a fast and reliable NDT method, NDT & E International, vol. 29, Issue 6, pp. 397, 1996.
- [Smit97] Steven W. Smith, California Technical Publishing, The Scientist and Engineer's Guide to Digital Signal Processing, ISBN 0-9660176-3-3, California, 1997.
- [Snea92] L. L. Snead, S. J. Zinkle, D. Steiner, Radiation induced microstructure and mechanical property evolution of SiC/C/SiC composite materials, Journal of Nuclear Materials, vol. 191-194, Part 1, pp.560-565, September 1992.
- [Taka96] K. Takahashi, S. Tazaki, J. Miyahara, Y. Karasawa, N. Niimura, Imaging performance of imaging plate neutron detectors, Nucl. Instr. and Meth. A, 377, pp. 119-122, 1996.



## 11. References

---

- [**Tayl01**] N. P. Taylor et al. The safety, environmental and economic implimantation of the use of silicon carbide in fusion power plant blankets, *Fusion Enginneering and Design*, vol. 58-59, pp.991-995, 2001.
- [**Thom97**] M. Thoms, M.S. Lehmann, C. Wilkinson, The optimization of the neutron sensitivity of image plates, *Nucl. Instr. And Meth. A* 384, pp. 457-462, 1997.
- [**Thom99-1**] M. Thoms, D. Myles, C. Wilkonson, Neutron detection with imaging plates **Part I: Image storage and readout**, *Nucl. Instr. And Meth. A* 424, pp. 26-33, 1999.
- [**Thom99-2**] M. Thoms, Neutron detection with imaging plates **Part II: Detector characteristics**, *Nucl. Instr. And Meth. A* 424, pp. 34-39, 1999.
- [**Tsuj01**] H. Tsuji, S. Egorov, J. Minervini, M. Martovetsky, K. Okuno, Y. Takahashi, R.J. Thome, ITER R&D:Magnets: Central solenoid model coil, *Fusion Engineering and Design*, vol. 55, pp.153 -170, 2001.
- [**Ultr00**] The web page of Ultramet, [http://http://www.ultramet.com/](http://www.ultramet.com/).
- [**Vict01**] M. Victoria, N. Baluc, P. Spätig, "Structural Materials for Fusion Reactors", *FTP1/13, 18<sup>th</sup> Fusion Energy Conference*, 4 - 10 October 2000, Sorrento, Italy, IAEA-CN-77 0, 2001.
- [**Vilp74**] K. O. Vilpponen and A. E. Salmela, Auto-radiographic determination of the distribution in some low-alloyed steels, *Scandinavian Journal of Metallurgy (Stockholm)*, 2, p. 298, 1974.
- [**Whit83**] W. L. Whittemore, H. Berger: Physics of NR using selected energy neutrons, *NR 1<sup>st</sup> Word Conf.*, pp.23-33, D. Reidel Publ. Co., 1983.
- [**Wilk92**] C. Wilkinson, A. Gabriel, M.S. Lehmann, T. Zemb, F. Né, *SPIE Proc.* 1737, 324, 1992.
- [**Wong02**] C.P.C. Wong, S. Malang, S. Nishio, R. Raffray, A. Sagara, Advanced high performance solid wall blanket concepts, *Fusion Engineering and Design*, vol. 61-62, pp. 283-293, 2002.
- [**Zink98**] S.J. Zinkle, H. Matsui, D.L. Smith, A.F. Rowcliffe, E. van Osch, K. Abe and V.A. Kazakov, "Research and development on vanadium alloys for fusion applications", *J. Nucl. Mater.* 258-263, pp. 205-214, 1998.
- [**Zawi02**] M. Zawisky, M. Bastürk, J. Rehacek, Z. Hradil, Neutron Tomographic investigations of strong absorbing materials, *7<sup>th</sup> World Conference on Neutron Radiography*, Rome-Italy, 15-21 September 2002.
- [**Zawi03**] M. Zawisky, M. Bastürk, R. Derntl, F. Dubus, E. Lehmann, P. Vontobel, Non-destructive <sup>10</sup>B Analysis in Neutron Transmission Experiments, *Journal of Applied Radiation and Isotopes*, in print, 2003.

# 12

## Acknowledgments

First of all, I would like to thank my dissertation father, Prof. Helmut Rauch, who gave me the honor to work at the Atominstitut of the Austrian Universities and for unending advices and essential support during this study. I want to give my best thanks to Prof. Helmuth Böck, without his supports I could not begin this study.

Next, I would like to thank all my colleges (DI Matthias Baron, DI Martin Jäkel, DI Martin Trinker, DI Hartmut Lemmel, Dr. Yuji Hasegawa, Babak Zamani) at the Institute for providing an excellent and friendly working atmosphere. Especially, I want to thank Dr. Erwin Jericha, Dr. M. Villa, and Dr. Martin Hainbuchner for the permanent scientific discussions and friendly conversations, spending nice time at the coffee automat and also for their helps to improve my German language. I would also like to thank to Dr. Michael Zawisky for his supports and providing me an interesting project on the shielding material analysis.

I would like to thank Dr. Sonja Körner, who helped me very much at the beginning of the study, and Prof. Peter Wobrauschek for his permanent supports in X – ray radiography measurements. I thank also our reactor operators Ernst Klappfer and Hans Schachner for their supports. I am very grateful to our secretaries (Eva, Maria, Brigitta and Friederike) and Dr. Gideon Rohr for their helps with administrative matters during this study.

I want to give my grateful thanks to Dr. Nikolay Kardjilov for his supports, his collaboration, and his valuable scientific discussions during this study. I am thankful to Dr. Burkhard Schillinger, Dr. Eberhard Lehmann and Dr. Peter Vontobel for continuing scientific discussions, essential experimental supports, exchanging of ideas and good collaborations between institutes, and also their close friendship during this study.

My special thanks go to Prof. Phil Beeley for English revision of my thesis.

## 12. Acknowledgments

---

Especially, I want to express my gratitude to my family, without whom I would never have been able to achieve so much, for always supporting my personal and academic advancement. Last, I want to thank to my husband for his infinite supports and patience during this work.

I thank also all cooperators from:

Institute of Physics of Materials, Czech Republic (Dr. Antonin Dlouhy)  
Austrian Museum of Natural History, Vienna (Mag. Karoline Zhuber-Okrog)  
Marketing and Quality Department - Böhler-Bleche GmbH, Mürzzuschlag-Austria (Dipl. Ing. Werner J. Jerlich)  
Plansee Incorporated, Tirol-Austria

This work was financially supported by the EURATOM-ÖAW UT4-Underlying Technology project, Neutron Inspection of Fusion Relevant Materials, European project COST Action 524 for Neutron Radiography Community and Böhler Bleche GmbH (Austrian Steel Production Company).